Variable turbulent Prandtl number model for high-speed flows with shock wave

Submitted in partial fulfillment of the requirements
for the degree of

Doctor of Philosophy

by

Subhajit Roy
(Roll No. 144016003)

Supervisor:
Prof. Krishnendu Sinha

Department of Aerospace Engineering
Indian Institute of Technology Bombay

2021

Acceptance Certificate

Department of Aerospace Engineering
Indian Institute of Technology Bombay

The thesis entitled "Variable turbulent Prandtl number model for high-speed flows with shock wave" submitted by Subhajit Roy (Roll No. 144016003) may be accepted for being evaluated.

Date: 2021

Prof. Krishnendu Sinha

Approval Sheet

This dissertation entitled “Variable turbulent Prandtl number model for high-speed flows with shock wave” by Subhajit Roy is approved for the degree of Doctor of Philosophy.

____

____

____

Examiners

____

____

____

Supervisor (s)

____

Chairman

Date: ____________

Place: ____________

Declaration

I declare that this written submission represents my ideas in my own words. Wherever ideas or words or figures have been included from published works/private communications are adequately cited and has been referred to their original sources. I also declare that I have adhered to all principles of academic honesty and integrity and have not misrepresented or fabricated or falsified data/idea/fact/source in my submission. I understand that any violation of the above will be the cause of disciplinary action by the institute and can also evoke penal action from the sources which have thus not been properly cited or from whom proper permission has not been taken when needed.

Subhajit Roy

Date: 2021 (Roll No. 144016003)

Abstract

Interaction of shock waves with turbulent boundary layers can enhance the surface heat flux dramatically. Reynolds-averaged Navier-Stokes simulations based on constant turbulent Prandtl number often give grossly erroneous heat transfer predictions in SBLI flows. This is due to the fact that the underlying Morkovin's hypothesis breaks down in the presence of shock waves; thus, the turbulent Prandtl number can not be assumed to be a constant. The interaction of a shock wave with turbulent flow is first studied to understand the effect of shock wave on the turbulent heat flux. Shock-turbulence interaction is a problem of interest where, the effects of the shock on the turbulence and vice versa could be studied in detail. A canonical case of one-dimensional mean flow convecting homogeneous isotropic turbulence across a normal shock wave provides a much cleaner environment for fundamental studies as it does not have any inhomogeneities or wall effects.

Direct numerical simulation data of shock-turbulence interaction is used to analyse the turbulent heat flux with varying Mach numbers and turbulence intensities. A dilatation based threshold method from literature is used to probe the DNS data at instantaneous shock wave to avoid any high jump at the shock wave due to shock oscillation. The threshold method is used to isolate the effect of instantaneous shock wave on turbulence and vice-versa. The upstream temperature fluctuation is found to play an important role to determine the post-shock variation of turbulent heat flux. The turbulent statistics is also calculated across the shock hole in broken shock regime. A turbulent heat flux model is developed based on the analysis from DNS data which accounts the variation of turbulent heat flux with turbulent Mach number also. The new model based on the DNS data predicts shock-generated turbulent heat flux better than existing models.

The new turbulent heat flux model is extended to supersonic shock-boundary layer interaction in terms of a turbulent Prandtl number for easy CFD implementation. The turbulent Prandtl number is a function of the shock strength and a shock function is proposed to identify the location and strength of shock waves. The shock function also simulates the post-shock relaxation of the turbulent heat flux, akin to that observed in canonical shock-turbulence interaction. The model is combined with the well-validated shock-unsteadiness k-ω model and is applied to the complex shock topology observed in oblique shock-turbulent boundary layer interactions. Comparison with experimental data shows significant improvement in the surface heat transfer rate in the interaction region, both for attached and separated SBLI cases. The shock function is also used to propose a robust form of the existing shock-unsteadiness k-ω model that simplifies the numerical implementation enormously.

The variable turbulent Prandtl number (Pr_T) model is next extended to hypersonic shock-boundary layer interaction with non-adiabatic walls. The extension is done by using the Huang's strong Reynolds analogy, Walz temperature distribution and the DNS data of a turbulent boundary layer. The primary advantage of the new variable Pr_T model is its algebraic form that makes it computationally efficient and numerically robust. It is applied in the region of shock waves and the model reverts back to the constant Pr_T version other wise. The new model can capture both the effects of shock wave and wall heating/cooling in a SBLI flow and is extensively tested against the available DNS and experimental data. The data covers a wide range of Mach number, Reynolds number, geometric configuration and wall heating/cooling ratio and for all the cases the variable Pr_T model predicts an improved surface heat transfer.

Keywords: Turbulence, turbulent heat flux, turbulent Prandtl number, direct numerical simulation, shock-turbulence interaction, shock wave, shock-boundary layer interaction.

Table of Contents

List of Figures

List of Tables

Chapter 1

Introduction

1.1 Background and Motivation

Shock-boundary layer interactions (SBLIs) are commonly observed in high-speed flows and they are characterized by a rise in surface pressure and high localized heat transfer. The aerothermodynamic heating has a large influence on the design of high-speed vehicles [8]. Thermal protection systems (TPSs) are often used to prevent the vehicle surface from overheating which can leads to disastrous accidents. To ensure the protection of such vehicles, these systems are specified with a large security factor, with the drawback of carrying extra weight. Thus, the accurate prediction of the aerodynamic heating in a high-speed flight is an important step in the design process, which can reduce the weight of the vehicle, increase the payload and enhance the fuel efficiency. SBLI associated with inlets and the inlet/isolator of supersonic combustion ramjet (SCRAMJET) engines can be a performance limiting feature due to the potential for triggering engine unstart by reducing the inviscid core flow. Additionally, SBLI can result in a decrease or complete loss of supersonic/hypersonic vehicle control surface effectiveness and premature failure of external aerodynamic components [7]. Shock-boundary layer interaction occurs in nearly every instance in which a body interacts with high-speed flow, and is therefore a common challenge for trans/super/hypersonic vehicle design engineers.

The interaction of homogeneous isotropic turbulence with a shock wave is a similar problem of fundamental interest in high-speed flows. It is rich with physical insights on the effects of shock on turbulence and vice-versa, and has been the focus of active research over the last couple of decades. Shock-turbulence interaction (STI) has implications in a variety of applications, to name a few, supersonic/hypersonic propulsion systems, inertial confinement fusion, shock wave lithotripsy, and astrophysical shock waves. It is often used as a model problem to understand shock-boundary layer interaction (SBLI) that are commonly observed in supersonic and hypersonic flows. SBLIs are characterized by high localized heat transfer, and the aerothermodynamic heating can have a large influence on the design of high-speed vehicles [8] and propulsion systems. The amplification of turbulent heat flux at shock waves can increase the surface heat transfer by up to 400% [73] at high Mach numbers. Turbulent heat flux is defined as the correlation between velocity and temperature fluctuations. In canonical STI, the streamwise component $\overline{u'T'}$ is of primary importance; here u is shock-normal velocity and T is temperature, prime denotes turbulent fluctuations and overbar represents Reynolds average.

Initial studies of shock-turbulence interaction were based on a theoretical tool called linear interaction analysis (LIA) [42, 55]. The theory was developed to study the interaction of acoustic and vorticity waves with a normal shock. Later the theory was used by many researchers to study the interaction between free turbulence and shock wave [20, 26, 32, 49, 53, 76]. Rapid distortion theory (RDT) is another theoretical tool used to study the STI [19, 24, 34, 41]. Although RDT supports sheared mean flow which replicates shock/boundary-layer interaction, it does not include the shock-distortion effect that are inherent in such flows. Several direct numerical simulations (DNS) [11, 14, 15, 27, 35, 44, 46, 48, 71] have also been carried out to study the canonical shock-turbulence interaction problem mainly to study the statistical quantities related to velocity fluctuations such as Reynolds stresses, vorticity variances and turbulent kinetic energy (TKE); purely driven by the need to understand mixing enhancement across the shock. Reynolds-averaged Navier-Stokes (RANS) framework [78, 86] is also used to develop advanced turbulence models for high-speed flow applications. A few experimental studies [4, 30] are reported, but they are limited due to difficulties in generating canonical shock-turbulence interaction in a laboratory environment without wall effects.

In the context of heat transfer, Quadros et al. [67] studied the post-shock turbulent energy flux correlation using LIA and DNS data. Turbulent energy transfer is quantified in terms of the turbulent energy flux $\overline{u'e'}$, which is related to the turbulent heat flux $\overline{u'T'}$ by a factor of c_v ($\overline{u'e'} = c_v\overline{u'T'}$). It is found that the turbulent energy flux attains a peak value immediately behind the shock and the post-shock variation is governed by the pressure-energy and pressure-dilatation source terms which are dominated by the acoustic mode and can be reproduced well by LIA [66]. The location of the peak turbulent energy flux is found to scale with the dissipation length scale that is characteristic of the acoustic disturbances in the flow. Quadros and Sinha [65] propose improvements to the modeling of turbulent energy flux in canonical shock-turbulence interaction. Scaling relations from LIA are used to propose a heat-flux limiter model for the turbulent energy flux at a shock wave. The model formulation is similar to the realizable $k-\epsilon$ model of [75] and matches

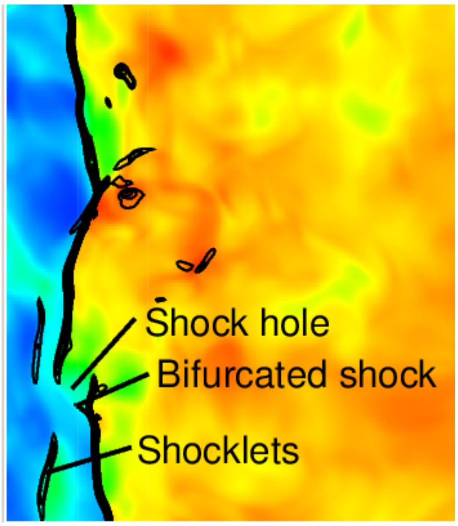

Figure 1.1: Shock-turbulence interaction at (M, M_t)=1.23,0.4. The figure shows the instantaneous temperature contour and the shock wave is identified by instantaneous dilatation contour. Shock hole and shocklets (ahead of the shock) are also visible in the figure. The DNS data is taken from [74].

the DNS values of the peak energy flux for a range of shock strengths. Quadros and Sinha [65] also develop a transport equation based model to bring in the history effect of the shock wave in the downstream flow. It includes the downstream decay in terms of the turbulent dissipation length scale and the model predictions match the DNS decay rate up to about one dissipation length behind the shock. However much of the work is limited to low turbulence intensity and the same analysis will hold for high turbulence fluctuation or not is questionable.

Chen and Donzis [11] study the amplification of turbulence across normal shock wave at high turbulence intensities (M_t up to 0.54). Here, the turbulent Mach number $M_t = \frac{\sqrt{2k}}{\overline{a}}$ is used as a measurement tool for turbulence intensity, k is the turbulent kinetic energy and $\overline{a}$ is the mean speed of sound. They study the effect of high turbulent Mach number on the mean flow quantities, like pressure, density. The amplification of mean flow variables are found to be a function of turbulent Mach number. Larsson et al. [44] also studied few STI cases at high M_t values. One of the important aspect at high M_t is the presence of shock holes. Due to the high turbulence intensity in the upstream region the local shock surface disappears and the turbulence passes without any significant change. This looks like a hole in the shock surface (visualized using density gradient or similar quantities) and is commonly known as shock holes; see Fig.1.1. In regions near shock holes, the normal shock is found to bifurcate into multiple shock waves. The analysis of turbulence statistics through the shock holes and bifurcated shock poses several challenge and none of the analytical models is tested across such regions. Recently Sethuraman et al. [74] studied various thermodynamic variances like temperature, pressure, density and entropy for high turbulence intensities (M_t up to 0.4) including cases with shock holes. They systematically varied the upstream turbulent Mach number M_t, and studied the changes in the downstream thermodynamic variances relative to the incoming turbulence. However, the analysis of turbulent heat flux at high turbulent Mach number is not available in their work.

In this work, direct numerical simulation data of STI is used to understand the behaviour of turbulent heat flux generated in canonical shock turbulence interaction, with a focus on high turbulence intensities and shock holes. The dilatation-based threshold method from [74] is used to probe the DNS data at instantaneous shock wave to avoid unphysical high jump in turbulence quantities due to unsteady shock oscillations. As shown in this work, the threshold method gives an unique advantage in directly comparing with theoretical formulation of the shock interaction. We extend the threshold method to shock holes and bifurcated shock waves, to study the variation of turbulence quantities in such scenarios. We also show a detailed sensitivity study of the method, by varying the shock edge detection technique proposed by [74]. Using the threshold method, we are able to obtain scaling of the non-linear effects in high M_t interactions. The insight into the shock-turbulence interaction physics obtained from analyzing DNS data is then used to build predictive models for the post-shock turbulence field. Both the peak turbulent heat flux behind the shock, and the downstream evolution are predicted well, and the effect of varying M_t is reproduced accurately by the model. The work presented in this dissertation demonstrates, possibly for the first time, a procedure to extend LIA-based turbulence models to high intensity turbulence interacting with strong shock waves.

The first observations of shock-boundary layer interaction (SBLI) were those of Ferri (1940) [21] who investigated the transonic flow over an airfoil in a high-speed wind tunnel. Since then SBLI has been widely studied to understand the physical mechanism and after 80 years of research also many aspects of SBLI are not fully understood. An excellent review of SBLIs occurring in varying conditions and configurations can be found in [23]. Numerically SBLI flows are widely studied using direct numerical simulation (DNS), large eddy simulation (LES), Reynolds-averaged Navier-Stokes simulation (RANS) and some hybrid methods such as detached eddy simulation (DES). Computational simulations through Reynolds-averaged Navier-Stokes (RANS) based turbulence models are popular in the aerospace industry owing to its low computational cost and time. Current turbulence models, however, over-predict the peak heat flux values by considerable margins [33, 50, 69] (see figure 1.2), and in this work this problem is systematically studied and tackled.

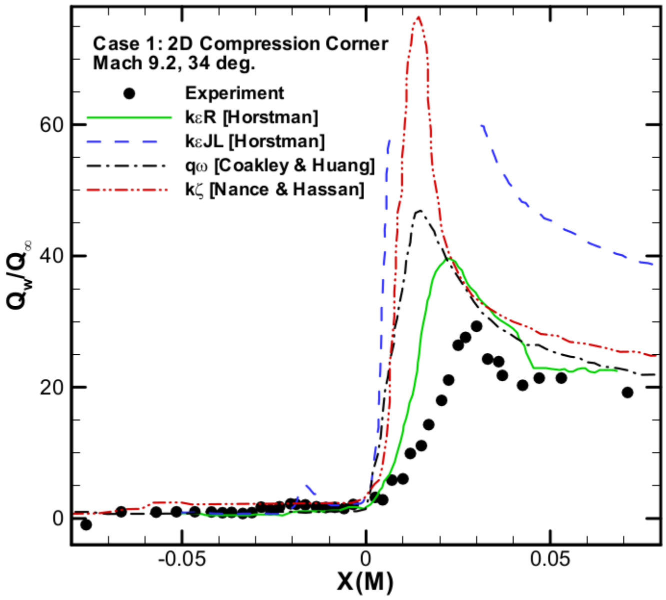

Figure 1.2: Comparison of surface heat flux using different turbulence models for a compression ramp geometry with 34 degree deflection angle at Mach 9.2 [69].

Transport of heat in standard turbulence models is modeled through temperature gradient approximation, with thermal conductivity having molecular and turbulent components. The turbulent part of thermal conductivity is usually written in terms of the turbulent Prandtl number (Pr_T), which is calculated based on Morkovin's hypothesis [56]. A direct mathematical implication of Morkovin's hypothesis is the Strong Reynolds Analogy (SRA). It states that the value of velocity-temperature correlation coefficient is -1, which leads to a theoretical value of $Pr_T = 1$. A value of 0.89 produces results that are in good agreement with the experimental data for turbulent boundary layers. This is not the case for SBLI flows, where the ability of the constant Pr_T approach has been called into question by several authors in the past [9, 92].

A natural progression in the modeling of turbulent heat flux is therefore to vary the Pr_T. Variable Pr_T models have shown improvement in the heat flux predictions in SBLI flows [13, 58, 95]. Most of the variable Pr_T models solve two additional transport equations for temperature variance and its dissipation rate. The turbulent Prandtl number is then calculated using the time scale of the temperature variance. The additional partial differential equations have a form similar to the k-ϵ or k-ω equations, and have a large number of source terms. The solution of extra equations thus requires more computational power and invariably increases the cost of computation. Algebraic Pr_T models have been devised to account the Pr_T variation in boundary layers, but they do not consider the effect of shocks [39]. In fact, recent studies of shock-turbulence interaction [66, 67] have revealed interesting and non-intuitive variation of the turbulent heat flux across shock waves.

The flow field of the SBLI becomes more complex with active wall heating/cooling which is the case for most real life application. Most of our current understanding of shock wave turbulent boundary layers interaction is based on the results of supersonic Mach numbers (M < 5) with adiabatic wall. There are very few works available in the literature which deal with non-adiabatic turbulent boundary layer and its interaction with the shock waves. The first investigation of the wall temperature effect on SBLI was done by [82] experimentally. They performed the experiment over a compression ramp geometry at Mach 2.9 with cold ($T_/T_r = 0.47$) and quasi adiabatic ($T_/T_r = 1.05$) wall conditions. [2] extended the experimental database by including an oblique shock wave impinging on a turbulent boundary layer at Mach 3.5 and deflection angle of 7 and 8 degrees. The wall to recovery temperature ratio (($T_/T_r$) was 0.44 for their experiment. Recently Jaunet et al. [36] carried out an experiment for an oblique shock and flat plate turbulent boundary layer interaction. They systematically varied the shock deflection angle from 3.5 to 9.5 degree at Mach 2.3 for heated and adiabatic wall conditions. All the experiments were done to check the wall temperature effect on separation bubble size. On the numerical side also, the data for non-adiabatic SBLI is very sparse [5, 87, 88]. Bernardini et al. [5] first systematically performed the simulations of SBLI at Mach 2.3 with different wall cond1ditions by means of direct numerical simulation (DNS). Volpiani et al. [87, 88] extended the database and included several deflection angles at supersonic and hypersonic Mach numbers. Both experimental and numerical results indicate that wall cooling minimizes the separation length and increases the surface heat transfer. The underlying physical mechanisms of shock wave and wall effect should, therefore, be considered for computing the turbulent Prandtl number in SBLI flows. This requirement motivated us to pursue this research to understand the physics of shock-turbulence and shock-boundary layer interactions.

1.2 Objective

The objective of the present study is to

- analyze the generation of turbulent heat flux at various inflow conditions across the shock wave using DNS data,
- investigate the dominant mechanisms behind the post shock evolution of turbulent heat flux,

- develop modeling strategies to capture the essential physics of the turbulent heat flux in shock-turbulence interaction (STI),
- extent this analysis to shock-boundary layer interaction problem in terms of a variable turbulent Prandtl number model,
- test the variable turbulent number model for different Mach number, configurations, Reynolds number and wall conditions.

A part of this work is also dedicated to fill in the gaps in existing literature to analyze the turbulent heat flux at high turbulent Mach number. A wide range of flow Mach numbers and turbulent Mach numbers, from 'wrinkled shock' to 'broken shock' regimes are considered from the data set of Sethuraman et al. [74]. The turbulent heat flux is also analysed across the shock hole.

1.3 Scope

This dissertation presents the numerical analysis of turbulent heat flux using DNS data of homogeneous turbulence interacting with normal shock waves of varying strengths (M = 1.23, 1.50, 2.50 and 3.50). The DNS data is taken from Ref. [74] in this dissertation for the analysis of turbulence statistics. A special focus is given to analyze the turbulent heat flux at high turbulent Mach numbers and across the shock hole which is first of its kind in the literature. The evolution of post shock turbulent heat flux is discussed in detail using the DNS data. Model for turbulent heat flux is developed using the DNS data which is able to capture the variation in turbulent intensity.

A new approach is proposed to vary Pr_T based on the physics of shock-turbulence interaction and subsequently extended to SBLI flows. The relationship between the fluctuating velocity and temperature behind a shock is used to develop an expression for Pr_T as a function of shock strength and a shock function is proposed to identify the location and strength of shock waves. The shock function also simulates the post-shock relaxation of the turbulent heat flux, akin to that observed in canonical shock-turbulence interaction. The shock function is also used to propose a robust form of the existing shock-unsteadiness k-ω model that simplifies the numerical implementation enormously. An analysis of cold/hot wall conditions is also performed based on the direct numerical simulation data and the effect of these wall conditions on surface heat flux is modeled using theoretical tools. Comparison of the new model with experimental and DNS data shows significant improvement in the surface heat transfer rate in the interaction region, both for attached and separated SBLI cases. Thus the new model will be very useful to get an quick estimation of surface heat flux and can help to design the thermal protection system of the vehicle.

1.4 Organization

This dissertation is organized as follows,

- Chapter 2 covers the basic analytical solutions for the turbulent boundary layer and the flow physics of different shock-boundary layer configurations. The governing equations for the compressible turbulent flow and a brief introduction of turbulence models including the turbulent heat flux closure are also included in this chapter.

- Numerical methods and the computational set up including the flow conditions and simulation parameters, initial and boundary conditions, test cases, grid convergence for the direct numerical simulations are described in chapter 3 The numerical method and boundary conditions used in the Reynolds-averaged simulations of SBLI flows are also discussed in this chapter.

- The fundamental study of various aspects of turbulent heat flux in shock-turbulence interaction problem is given in chapter 4 using the direct numerical simulation data. This analysis includes the post processing method to collect the statistics in instantaneous shock reference frame. The estimation of shock-speed and the shock hole statistics are also presented here. A closed form turbulent heat flux model is proposed at the end of this chapter based on the analysis.

- Application of turbulent heat flux model to supersonic SBLI configuration is presented in chapter 5. The variable turbulent Pradtl number (Pr_T) model development and its implementation to SBLI flows are discussed in detailed along with the test cases, computational set up, grid convergence and results. The sensitivity of the model parameter is also tested in this chapter.

- Chapter 6 presents the extension of the variable turbulent Prandtl number model to hypersonic flows. The model is tested against various SBLI configurations with varying Mach number and Reynolds number.

- The analysis and evaluation of the new model for non-adiabatic wall are carried out in chapter 7. The comparison of the new model for surface properties with available DNS and experimental data is also presented in this chapter and the conclusion is presented in chapter 8.

Chapter 2

Literature Review

The physics of turbulence amplification in fluids due to the presence of shocks has been a subject of study for several researchers, both in the past and in the present, and is expected to continue in the future also. This is entirely due to the complicated nature of both the shock wave and the turbulence itself. This chapter presents a brief review of turbulent boundary layer first followed by the flow physics of the interaction between the turbulent boundary layer and shock waves. In engineering predictions of shock-boundary layer interaction (SBLI) problems, Reynolds-averaged Navier-Stokes (RANS) approach is generally used. Brown [33], Roy et al. [69], and Gaitonde [23] reviewed the benefits and drawbacks of RANS turbulence models. Different configurations, such as compression ramps, sharp fins, and impinging shock interactions, have been extensively studied, and the numerical predictions have been compared with experimental data. Various turbulence models like the Spalart-Allmaras model, $k-\epsilon$, $k-\omega$, Reynolds stress models have been employed in the simulations with varying degree of success. Hence a discussion on turbulence modeling is also presented in this chapter followed by a special emphasis on turbulent heat flux closure.

2.1 Turbulent Boundary Layer

The efficient design of high-speed vehicles, including the prediction of skin friction and surface heat transfer, requires good understanding of the turbulent boundary layer, the layer of fluid in the immediate vicinity of the surface of vehicles. Most of the previous understanding of compressible turbulent boundary layers is based on results with moderate supersonic Mach numbers ($M \leq 3$) and adiabatic wall. At supersonic speeds, the surface temperature is essentially adiabatic; while at hypersonic speeds, due to considerable radiative cooling and internal heat transfer or due to necessary wall cooling to prevent melting, the surface temperatures are significantly lower than the adiabatic wall temperature. As a result, the conductive heat transfer between the boundary layer flow and the surface of hypersonic vehicles is enormous. This makes many of the scalings and models, which are obtained based on supersonic adiabatic flow data, for turbulent boundary inappropriate for non-adiabatic and hypersonic flows [16, 64, 89]. This subsection reviews few analytical solution and scaling of turbulent boundary layer.

2.1.1 Reynolds Analogy

Skin friction and surface heat trarsfer calculations are two major concern for high-speed flows. These two problem arise because of the presence of boundary layer. The physical mechanism for the heat transfer coefficient in a turbulent boundary layer is important because most aerospace vehicle applications have turbulent boundary layers. Very near the wall, the fluid motion is smooth and laminar, and molecular conduction and shear are important. As one moves away from the wall (but still in the boundary layer), the flow is turbulent. The fluid particles move in random directions and the transfer of momentum and energy is mainly through interchange of fluid particles. For the laminar region, the heat flux towards the wall is

$$q = -\kappa \frac{dT}{dy}, \tag{2.1}$$

where κ is the molecular thermal conductivity, T is the temperature and y is the wall normal distance. Dividing by the expression for the shear stress, $\tau = \mu du/dy$, the above expression yields

$$q = -\tau \frac{\kappa}{\mu} \frac{dT}{du}. \tag{2.2}$$

Here μ is the dynamic viscosity and u is the streamwise velocity. The same relationship is applicable in laminar or turbulent flow if $\kappa/\mu = c_p$ or the Prandtl number $\mu c_p/\kappa = 1$. A relation between the values at the wall (at which $T = T_w$ and $u = 0$) and those in the free stream can be obtained by integrating the equation 2.2 for dT from the wall to the free stream

$$-dT = \frac{1}{c_p} \frac{q}{\tau} du, \tag{2.3}$$

where the relation between heat transfer and shear stress has been taken as the same for both the laminar and the turbulent portions of the boundary layer. The assumption being made is that the mechanisms of heat and momentum transfer are similar. Equation 2.3

can be integrated from the wall to the freestream (denoted by ∞):

$$-\int_{w}^{\infty} dT = \frac{1}{c_p}\int_{w}^{\infty}\left(\frac{q}{\tau}\right)du, \tag{2.4}$$

where q/τ and c_p are assumed constant. Carrying out the integration yields

$$T_w - T_\infty = \frac{q_w}{\tau_w}\frac{u_\infty}{c_p} \tag{2.5}$$

where u_∞ is the velocity and c_p is the specific heat. In Equation 2.5, q_w is the heat flux to the wall and τ_w is the shear stress at the wall. The relation between the heat transfer and the skin friction coefficient

$$q_w = \frac{\tau_w c_p (T_w - T_\infty)}{u_\infty} \tag{2.6}$$

is known as the Reynolds analogy between shear stress and heat transfer. The Reynolds analogy is extremely useful in obtaining a first approximation for heat transfer in situations in where the shear stress is known. The non dimensional form of Eq. 2.6 is expressed as

$$St = \frac{c_f}{2}, \tag{2.7}$$

where $St = \frac{q_w}{\rho_\infty c_p u_\infty (T_w - T_\infty)}$ is the Stanton number and $c_f = \frac{2\tau_w}{\rho_\infty u_\infty^2}$ is the skin friction coefficient.

2.1.2 Morkovin's Hypothesis

The main assumption behind the Morkovin's hypothesis is that total temperature fluctuation is negligible in compressible turbulent boundary layers. Initially the analytical expression was derived by Morkovin [56] for a zero pressure gradient adiabatic turbulent boundary layer with Prandtl number equal to one. To derive the expression of Morkovin consider two dimensional steady boundary layer equations,

$$\frac{\partial}{\partial x}(\rho u) + \frac{\partial}{\partial y}(\rho v) = 0 \tag{2.8}$$

$$\rho u\frac{\partial u}{\partial x} + \rho v\frac{\partial u}{\partial y} = -\frac{\partial p}{\partial x} + \frac{\partial}{\partial y}(\mu\frac{\partial u}{\partial y}) \tag{2.9}$$

$$\frac{\partial p}{\partial y} = 0 \tag{2.10}$$

$$\rho u\frac{\partial h}{\partial x} + \rho v\frac{\partial h}{\partial y} = u\frac{\partial p}{\partial x} + \frac{\partial}{\partial y}(k\frac{\partial T}{\partial y}) + \mu(\frac{\partial u}{\partial y})^2 \tag{2.11}$$

The above equations are the conservation of mass, x and y momentum and energy equation respectively. Here ρ is the density, u and v are streamwise and wall normal velocity respectively, p is the pressure and $h = c_p T$ is the enthalpy of the gas. Across the boundary layer $v << u$ and $\frac{\partial}{\partial x} << \frac{\partial}{\partial y}$, so the $\frac{\partial}{\partial x}(\mu \frac{\partial u}{\partial x})$ term in the x-momentum equation is neglected. Now from the x-momentum equation the expression for the pressure gradient term is,

$$\frac{\partial p}{\partial x} = -\rho(u\frac{\partial u}{\partial x}) - \rho v\frac{\partial u}{\partial y} + \frac{\partial}{\partial y}(\mu\frac{\partial u}{\partial y}) \tag{2.12}$$

The energy equation can be written in terms of total enthalpy $H = h + \frac{u^2 + v^2}{2}$, as $v << u$ it can be simplified as $H = h + \frac{u^2}{2}$,

$$\rho\frac{DH}{Dt} = \rho u[\frac{\partial h}{\partial x} + u\frac{\partial u}{\partial x}] + \rho v[\frac{\partial h}{\partial y} + u\frac{\partial u}{\partial y}] \tag{2.13}$$

Again from energy equation,

$$\rho u\frac{\partial h}{\partial x} + \rho v\frac{\partial h}{\partial y} = u\frac{\partial p}{\partial x} + \frac{\partial}{\partial y}(k\frac{\partial T}{\partial y}) + \mu(\frac{\partial u}{\partial y})^2 \tag{2.14}$$

So,

$$\rho\frac{DH}{Dt} = u\frac{\partial p}{\partial x} + \frac{\partial}{\partial y}(k\frac{\partial T}{\partial y}) + \mu(\frac{\partial u}{\partial y})^2 + \rho u^2\frac{\partial u}{\partial x} + \rho uv\frac{\partial u}{\partial y} \tag{2.15}$$

Substituting the value of $\frac{\partial p}{\partial x}$ in the above equation yields

$$\rho\frac{DH}{Dt} = \frac{\partial}{\partial y}(k\frac{\partial T}{\partial y}) + \mu(\frac{\partial u}{\partial y})^2 + u\frac{\partial}{\partial y}(\mu\frac{\partial u}{\partial y}) \tag{2.16}$$

So the energy equation become,

$$\rho\frac{DH}{Dt} = \frac{\partial}{\partial y}(k\frac{\partial T}{\partial y} + \mu u\frac{\partial u}{\partial y}) \tag{2.17}$$

Replacing T with the total enthalpy H in the above equation and considering only the steady energy equation yields

$$\rho u\frac{\partial H}{\partial x} + \rho v\frac{\partial H}{\partial y} = \frac{\partial}{\partial y}(\frac{\mu}{Pr}\frac{\partial H}{\partial y}) + \frac{\partial}{\partial y}((1 - \frac{1}{Pr})\mu u\frac{\partial u}{\partial y}), \tag{2.18}$$

Where Pr is the laminar Prandtl number. This form of energy equation is also known as Crocco-Busemann Energy relation. Considering $Pr = 1$ in the above equation the last term will be zero. Hence the particular solution of this equation is $H =$ constant for a boundary-layer with adiabatic wall. So if the total instantaneous enthalpy is constant which is the sum of mean total enthalpy and fluctuation total enthalpy, it can be concluded that the fluctuation part of the total enthalpy should be zero as the mean of total enthalpy is also constant in a steady flow. So if the fluctuation of total enthalpy is zero than fluctuation of total temperature T_0'' is also zero which is the starting point of Morkovin's Hypothesis.

Now the total temperature is defined aw

$$T_0 = T + \frac{u^2}{2c_p},$$

which can be splitted as,

$$\widetilde{T}_0 + T_0'' = \widetilde{T} + T'' + \frac{1}{2c_p}[(\widetilde{u} + u'')^2 + (v'')^2].$$

Here the Favre decomposition is used to split the equation into mean and fluctuating parts given by $\widetilde{}$ and $''$ respectively.The mean and fluctuating part of the total temperature can be separated as,

$$\widetilde{T}_0 = \widetilde{T} + \frac{\widetilde{u}^2}{2c_p} + \frac{k}{c_p} \tag{2.19}$$

$$T_0'' = T'' + \frac{\widetilde{u}u''}{c_p}, \tag{2.20}$$

where k is the turbulent kinetic energy. Now for the boundary layer with adiabatic wall the total temperature fluctuation is zero. So from equation 2.20

$$T'' = -\frac{\gamma - 1}{\gamma R}\widetilde{u}u'',$$

as $c_p = \dfrac{\gamma R}{\gamma - 1}$. So from the above equation it can be modified as

$$\frac{T''}{\widetilde{T}} = -(\gamma - 1)M^2\frac{u''}{\tilde{u}}, \tag{2.21}$$

which can alternately express as,

$$\frac{\sqrt{\widetilde{T''^2}}}{\widetilde{T}} = (\gamma - 1)M^2\frac{\sqrt{\widetilde{u''^2}}}{\widetilde{u}}. \tag{2.22}$$

Also from equation 2.20, it can be written

$$\sqrt{\widetilde{T_0''^2}} = \sqrt{\overline{(T'' + \frac{\tilde{u}u''}{c_p})^2}}$$

,i.e.

$$\sqrt{\widetilde{T_0''^2}} = [\widetilde{T''^2} + \frac{\widetilde{u}^2\widetilde{u''^2}}{c_p^2} + 2\frac{\widetilde{u}}{c_p}\widetilde{u''T''}]^{1/2}. \tag{2.23}$$

Using equation 2.20 it can be further simplified as,

$$\sqrt{\widetilde{T_0''^2}} = [2\widetilde{T''^2} + 2\widetilde{T''^2}R_{uT}]^{1/2},$$

where $R_{uT} = \widetilde{u''T''}/(\sqrt{\widetilde{u''^2}}\sqrt{\widetilde{T''^2}})$ is the correlation factor between velocity and temperature fluctuations. Under the condition of total temperature fluctuation being zero

$$R_{uT} = -1, \tag{2.24}$$

Equations 2.20,2.22 and 2.24 belong to a set of equations termed as Strong Reynolds analogy (SRA), specified by Morkovin [56], and have been verified by experimental data of Bradshaw et al. [9], Smith and smits [80] for for moderate Mach numbers ($M \leq 3$) and adiabatic to mild cold wall flat plate turbulent boundary layers . Now from equation 2.20 one can express a correlation between wall normal velocity and temperature fluctuation as

$$\widetilde{v''T''} = -\frac{\widetilde{u}}{c_p}\widetilde{u''v''}. \tag{2.25}$$

Turbulent Prandtl number for the boundary layer can be written as

$$Pr_T = \frac{\nu_T}{\alpha_T} = \frac{\widetilde{u''v''}}{\widetilde{v''T''}}\left[\frac{\frac{\partial \widetilde{T}}{\partial y}}{\frac{\partial \widetilde{u}}{\partial y}}\right] \tag{2.26}$$

which represent the ratio of turbulent transport of heat to the turbulent transport of momentum. Here ν_T is the turbulent kinematic viscosity and α_T is the turbulent thermal diffusivity respectively. More discussion on this quantities can be found in the subsequent sections. Substituting $\widetilde{v''T''}$ correlation from equation 2.25 into the above equation yields,

$$Pr_T = -\frac{c_p(\frac{\partial \widetilde{T}}{\partial y})}{\widetilde{u}(\frac{\partial \widetilde{u}}{\partial y})} \tag{2.27}$$

Recalling the definition of mean total temperature,

$$\tilde{T}_0 = \widetilde{T} + \frac{\widetilde{u}^2}{2c_p} + \frac{k}{c_p} \tag{2.28}$$

and differentiating the above equation with respect to x gives

$$\frac{\partial \widetilde{T}_0}{\partial x} = 0 = \frac{\partial \widetilde{T}}{\partial x} + \frac{\widetilde{u}}{c_p}\frac{\partial \widetilde{u}}{\partial x} + \frac{1}{c_p}\frac{\partial k}{\partial x} \tag{2.29}$$

for a adiabatic turbulent boundary layer. Now the value of turbulent kinetic energy is much smaller than the mean velocity, so neglecting the last term of the above equation

$$\frac{(\frac{\partial \widetilde{T}}{\partial y})}{(\frac{\partial \widetilde{u}}{\partial y})} \approx -\frac{\widetilde{u}}{c_p} \tag{2.30}$$

which upon substitution to equation 2.27 gives $Pr_T = 1$. This is the direct consequence of the Morkovin's hypothesis [56] and constant value of $Pr_T = 0.89$ is found to be suitable for flat plate boundary layer computations.

2.1.3 Huang's Strong Reynolds Analogy (HSRA)

Strong Reynold's analogy (SRA), which is originally derived for adiabatic boundary layers, often found to deteriorate in high Mach number flows ($M \geq 3$) with cold/hot wall conditions [16, 64] which is measured in terms of the ratio of the wall temperature to the recovery temperature (defined as $T_r = T_\infty[1 + r_c\frac{\gamma-1}{2}M_\infty^2]$). Here $r_c \simeq \sqrt[3]{Pr}$ is the recovery factor for turbulent boundary layer and subscript ∞ represents the freestream condition. A more general form of the strong Reynold's analogy is proposed by Huang et al. [31] in 1995 almost three decades after the Morkovin's hypothesis. Huang et al. [31] defines the two length scale (velocity and temperature) of a turbulent boundary layer as per the mixing length assumption

$$l_u = \frac{u''}{\partial \widetilde{u}/\partial y} \tag{2.31}$$

$$l_T = \frac{T''}{\partial \widetilde{T}/\partial y}. \tag{2.32}$$

This can be combined to give

$$u''\frac{\partial \widetilde{T}}{\partial y} = cT''\frac{\partial \widetilde{u}}{\partial y} \tag{2.33}$$

where c is the scaling factor between the two length scale in boundary layers. Multiplying the above equation by $\rho v'$ and taking a time average at both sides yields

$$\bar{\rho}\widetilde{u''v''}\frac{\partial \widetilde{T}}{\partial y} = c\bar{\rho}\widetilde{v''T''}\frac{\partial \widetilde{u}}{\partial y}. \tag{2.34}$$

Hence c can be viewed as the ratio of

$$c = \frac{\widetilde{u''v''}\frac{\partial \widetilde{T}}{\partial y}}{\widetilde{v''T''}\frac{\partial \widetilde{u}}{\partial y}} = Pr_T \tag{2.35}$$

Thus the velocity and temperature fluctuations are expressed as

$$\frac{T''}{u''} = \frac{1}{Pr_T}\frac{\partial \widetilde{T}}{\partial \widetilde{u}} \tag{2.36}$$

The temperature gradient with respect to the mean velocity can be found from the total temperature definition assuming $\widetilde{u} >> \widetilde{v}$ and neglecting the contribution of turbulent kinetic energy with respect to the mean flow in boundary layer

$$\widetilde{T_0} = \widetilde{T} + \frac{1}{2c_p}\widetilde{u}^2 \tag{2.37}$$

$$\text{or,} \quad \frac{\partial \widetilde{T}}{\partial \widetilde{u}} = \frac{\widetilde{u}}{c_p}\left(\frac{\partial \widetilde{T_0}}{\partial \widetilde{T}} - 1\right)^{-1}. \tag{2.38}$$

The above relation simplifies the Eq. 2.36 as

$$\frac{T''}{u''} = \frac{1}{Pr_T}\frac{\overline{u}}{c_p}\left(\frac{\partial \widetilde{T_0}}{\partial \widetilde{T}} - 1\right)^{-1} \tag{2.39}$$

$$\text{or,} \quad \frac{T''}{\widetilde{T}} = \frac{(\gamma-1)M^2}{Pr_T}\frac{u''}{\widetilde{u}}\left(\frac{\partial \widetilde{T_0}}{\partial \widetilde{T}} - 1\right)^{-1}. \tag{2.40}$$

The above expression is an extended form the strong Reylond's analogy and often known as Huang's Strong Renolds's analogy (HSRA). There are other forms of SRA also but this form is found to match the direct numerical simulation (DNS) and experimental data[16, 64] better than any other forms.

2.1.4 Walz Temperature Distribution

Walz (1969)[91] found a relation of temperature field in a boundary layer as a function of streamwise velocity. The derivation is same as Morkovin's hypothesis [56] till equation 2.18. For $Pr = 1$, the reduced form of Eq. 2.18 will be

$$\rho u\frac{\partial H}{\partial x} + \rho v\frac{\partial H}{\partial y} = \frac{\partial}{\partial y}(\mu\frac{\partial H}{\partial y}) \tag{2.41}$$

To solve the above PDE, let $c_pT = f(u)$. Substituting this relation in the above equation yields

$$\begin{aligned}
&\rho u\frac{\partial f(u)}{\partial x} + \rho u^2\frac{\partial u}{\partial x} + \rho v\frac{\partial f(u)}{\partial y} + \rho uv\frac{\partial u}{\partial y} = \frac{\partial}{\partial y}(\mu\frac{\partial f(u)}{\partial y}) + \frac{\partial}{\partial y}(\mu u\frac{\partial u}{\partial y}) \\
\Longrightarrow &\rho u\frac{\partial u}{\partial x}\frac{\partial f(u)}{\partial u} + \rho u^2\frac{\partial u}{\partial x} + \rho v\frac{\partial u}{\partial y}\frac{\partial f(u)}{\partial u} + \rho uv\frac{\partial u}{\partial y} = \frac{\partial}{\partial y}(\mu\frac{\partial u}{\partial y}\frac{\partial f(u)}{\partial u}) + \frac{\partial}{\partial y}(\mu u\frac{\partial u}{\partial y}) \\
\Longrightarrow &\rho u\frac{\partial u}{\partial x}\frac{\partial f(u)}{\partial u} + \rho v\frac{\partial u}{\partial y}\frac{\partial f(u)}{\partial u} + \rho u^2\frac{\partial u}{\partial x} + \rho uv\frac{\partial u}{\partial y} = \frac{\partial f(u)}{\partial u}\frac{\partial}{\partial y}(\mu\frac{\partial u}{\partial y}) + \mu(\frac{\partial u}{\partial y})^2\frac{\partial^2 f(u)}{\partial u^2} \\
&\qquad + \frac{\partial}{\partial y}(\mu u\frac{\partial u}{\partial y})
\end{aligned}$$

Now multiplying the x-momentum equation 2.8 by $\dfrac{\partial f(u)}{\partial u}$ and subtracting from the above equation we have

$$-\frac{\partial p}{\partial x}\frac{\partial f(u)}{\partial u}+\rho u^2\frac{\partial u}{\partial x}+\rho uv\frac{\partial u}{\partial y}=\mu(\frac{\partial u}{\partial y})^2\frac{\partial^2 f(u)}{\partial u^2}+\mu(\frac{\partial u}{\partial y})^2+u\frac{\partial}{\partial y}(\mu\frac{\partial u}{\partial y}). \tag{2.42}$$

Again multiplying the x-momentum equation 2.8 by u and subtracting from the above equation yields

$$-\frac{\partial p}{\partial x}\frac{\partial f(u)}{\partial u}-u\frac{\partial p}{\partial x}=\mu(\frac{\partial u}{\partial y})^2\frac{\partial^2 f(u)}{\partial u^2}+\mu(\frac{\partial u}{\partial y})^2 \tag{2.43}$$

$$\Longrightarrow -\frac{\partial p}{\partial x}\left(\frac{\partial f(u)}{\partial x}+u\right)=\mu(\frac{\partial u}{\partial y})^2\left(\frac{\partial^2 f(u)}{\partial u^2}+1\right). \tag{2.44}$$

For a zero pressure gradient boundary layer this can be further simplified as

$$\mu(\frac{\partial u}{\partial y})^2\left(\frac{\partial^2 f(u)}{\partial u^2}+1\right)=0. \tag{2.45}$$

Now μ, and $(\dfrac{\partial u}{\partial y})^2$ can not be equal to zero. Hence

$$\frac{\partial^2 f(u)}{\partial u^2}+1=0 \tag{2.46}$$

$$\Longrightarrow\frac{\partial f(u)}{\partial u}=-u+B_1 \tag{2.47}$$

$$\Longrightarrow f(u)=A_1+B_1u-\frac{u^2}{2} \tag{2.48}$$

$$\Longrightarrow c_pT=A_1+B_1u-\frac{u^2}{2}, \tag{2.49}$$

where A_1 and B_1 are the integration constants. Now applying the boundary conditions $T=T_w$ at $u=0$ and $T=T_\infty$ at $u=u_\infty$

$$A_1=c_pT_w \tag{2.50}$$

and

$$c_pT_\infty=-\frac{u_\infty^2}{2}+B_1u_\infty+A_1 \tag{2.51}$$

$$\Longrightarrow c_pT_\infty=-\frac{u_\infty^2}{2}+B_1u_\infty+c_pT_w \tag{2.52}$$

$$\Longrightarrow 1=-\frac{u_\infty^2}{2c_pT_\infty}+B_1\frac{u_\infty}{c_pT_\infty}+\frac{T_w}{T_\infty} \tag{2.53}$$

$$\Longrightarrow B_1=(1-\frac{T_w}{T_\infty})\frac{c_pT_\infty}{u_\infty}+\frac{u_\infty}{2}. \tag{2.54}$$

Also from the one dimensional energy equation we have

$$T_\infty + \frac{u_\infty^2}{2c_p} = T_0 \tag{2.55}$$

$$\Longrightarrow 1 + \frac{u_\infty^2}{2c_pT_\infty} = \frac{T_0}{T_\infty} = 1 + \frac{\gamma-1}{2}M_\infty^2 \tag{2.56}$$

$$\Longrightarrow \frac{u_\infty^2}{2c_pT_\infty} = \frac{\gamma-1}{2}M_\infty^2, \tag{2.57}$$

where T_0 is the total temperature of the flow. Hence the temperature distribution will be,

$$c_pT = A_1 + B_1u - \frac{u^2}{2} \tag{2.58}$$

$$\Longrightarrow c_pT = c_pT_w + (1 - \frac{T_w}{T_\infty})\frac{c_pT_\infty u}{u_\infty} + \frac{u_\infty u}{2} - \frac{u^2}{2} \tag{2.59}$$

$$\Longrightarrow \frac{T}{T_\infty} = \frac{T_w}{T_\infty} + (1 - \frac{T_w}{T_\infty})\frac{u}{u_\infty} + \frac{u_\infty u}{2c_pT_\infty} - \frac{u^2}{2c_pT_\infty} \tag{2.60}$$

$$\Longrightarrow \frac{T}{T_\infty} = \frac{T_w}{T_\infty} + (1 - \frac{T_w}{T_\infty})\frac{u}{u_\infty} + \frac{u_\infty^2 u}{2c_pu_\infty T_\infty} - \frac{u^2}{2c_pu_\infty^2T_\infty}u_\infty^2 \tag{2.61}$$

$$\Longrightarrow \frac{T}{T_\infty} = \frac{T_w}{T_\infty} - (\frac{T_w}{T_\infty} - 1)\frac{u}{u_\infty} + \frac{u}{u_\infty}\frac{\gamma-1}{2}M_\infty^2 - \frac{u^2}{u_\infty^2}\frac{\gamma-1}{2}M_\infty^2 \tag{2.62}$$

$$\Longrightarrow \frac{T}{T_\infty} = \frac{T_w}{T_\infty} - (\frac{T_w}{T_\infty} - 1)\frac{u}{u_\infty} + \frac{\gamma-1}{2}M_\infty^2\frac{u}{u_\infty}(1 - \frac{u}{u_\infty}) \tag{2.63}$$

$$\Longrightarrow \frac{T}{T_\infty} = \frac{T_w}{T_\infty} + \left(\frac{T_0 - T_w}{T_\infty}\right)\frac{u}{u_\infty} + \left(\frac{T_\infty - T_0}{T_\infty}\right)\left(\frac{u}{u_\infty}\right)^2. \tag{2.64}$$

Practically nothing is perfectly insulated, so replacing T_0 with the recovery temperature T_r yields

$$\frac{T}{T_\infty} = \frac{T_w}{T_\infty} + \left(\frac{T_r - T_w}{T_\infty}\right)\frac{u}{u_\infty} + \left(\frac{T_\infty - T_r}{T_\infty}\right)\left(\frac{u}{u_\infty}\right)^2. \tag{2.65}$$

The above expression is known as the Walz temperature distribution equation [91] and it is valid for both laminar and turbulent boundary layer.

2.2 Shock-Boundary Layer Interaction

Shock-boundary layer interactions(SBLI) are well known phenomenon in high speed flows. Across shock wave boundary layer interaction, there is a jump in the static pressure due to the shock wave and affects the boundary layer, which is subjected to an adverse pressure gradient now. The shock waves also propagates through the boundary-layer (up to the sonic line). That means, both shock wave and boundary layer affects each other and change their shape accordingly when they interacts, this is commonly known as shock-boundary layer interaction or SBLI.

Shock-boundary layer interactions occur in many high-speed flow applications such as flow in intakes of scram-jets, rocket nozzles. The geometric complexity of practical applications make it difficult to understand and analyze the flow structure of such interactions. The complex configuration can be split into simpler geometries, which can isolate to understand the detail flow physics of shock/boundary-layer interactions. These simplified configurations are often known as canonical geometries. These include compression corner, oblique shock-wave impingement, cylinder-flare, cone-flare and three-dimensional configurations like single-fin, axial corner and double-fin. The flow structure of these interactions is determined by the shock strength. If the shock strength is high enough(specifically in the hypersonic flow regimes), the adverse pressure gradient produced by the shock will separates the boundary layer from the surface. This results into the formation of separation bubble and additional shock waves, expansion fans.

2.2.1 Oblique shock impingement on a flat plate

The application of oblique shock impingement case can be found in analysis of internal flows such as air intakes of high speed scram-jet engines. There is two kind of flow structure available depending on the strength of incident oblique shock wave. The flow structures are explained subsequently.

Flow without separation

The flow field organization of shock/boundary layer interaction(without separation) is illustrated in figure 2.1. Incident shock(shown as C_1) moves inside the inviscid part of the boundary layer. It also bends as it enters the boundary layer due to the local decrease of Mach number. Here δ is the boundary layer thickness. The shock intensity goes down and the shock disappears when it reaches the sonic line ($M = 1$) of the boundary layer. However the pressure rise because of this shock is experienced upstream of the flow. The same is visible in figure 2.1 where we can see subsonic pocket even before the shock impingement. The pressure rise caused by the shock wave is transmitted upstream through the subsonic part of the boundary layer. The subsonic pocket then acts as a ramp for incoming flow and thus a set of compression waves are produced which then combined to produce the reflected shock (C_2).

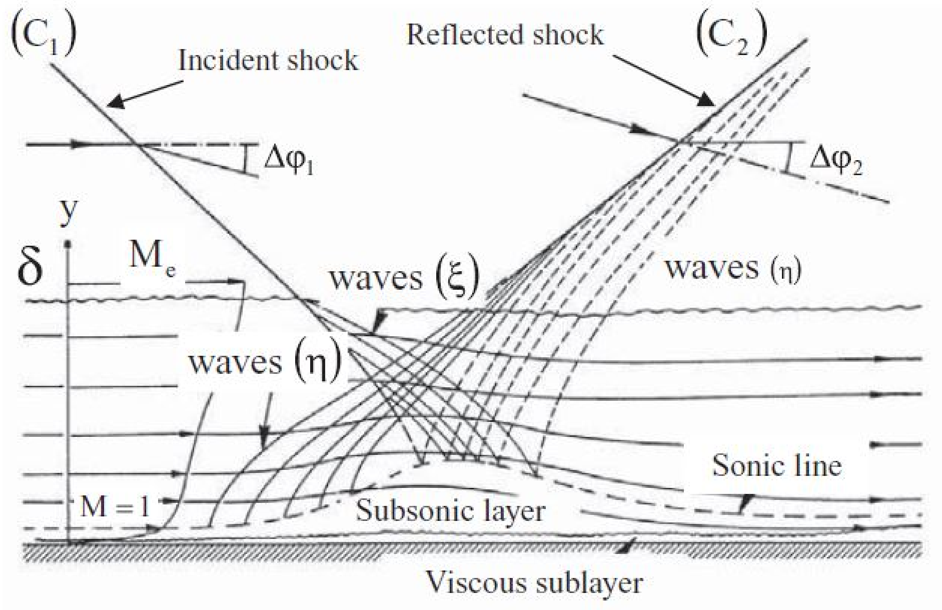

Figure 2.1: Shock/boundary-layer interaction without Separation[1].

Flow with separation

The complex flow field of the SBLI is illustrated in figure 2.2. Here S is the separation point and R is the reattachment point. The separation bubble is generated between this two points. The recirculating or reverse flow, inside the separation bubble, is separated from upstream to downstream flow by the dividing streamline (S).

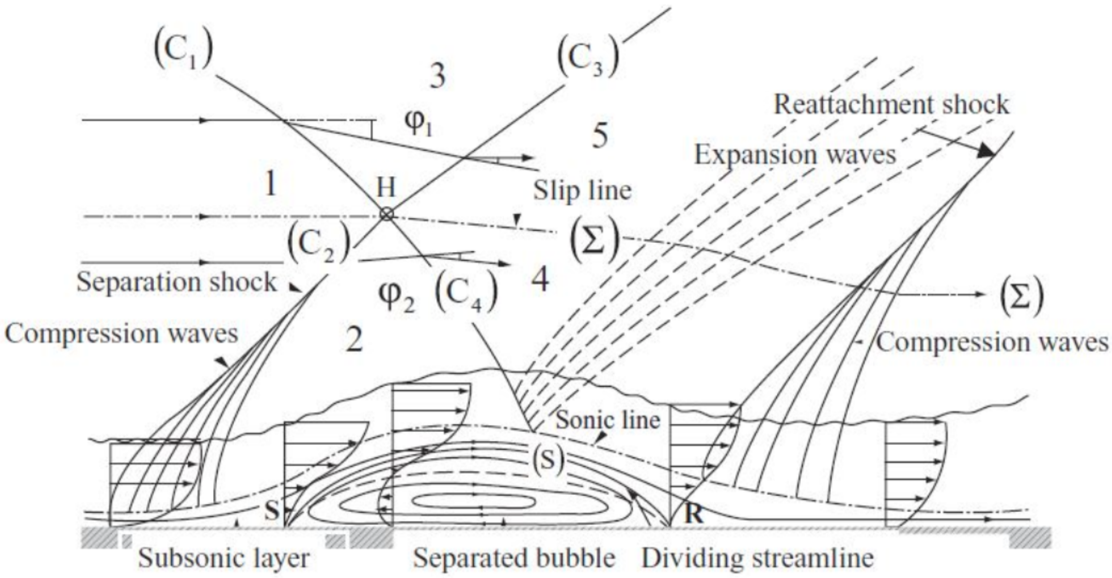

Figure 2.2: Shock/boundary-layer interaction with Separation[1].

The dividing streamline starts from the separation point S and ends at reattachment point R. The subsonic region ahead of the separation point acts as a compression ramp and generates the separation shock C_2. The separation shock interacts with the incident shock C_1 at point H where C_1 becomes C_4 and C_2 becomes C_3 after deflection. The deflected shock C_4 bends due to decrease in Mach number locally and meets the boundary layer at the sonic point where it is reflected as an expansion fan to match the isobaric nature of flow across the slip line. The flow is again reattached the surface at reattachment point R where a series of compression wave generates and together they form the reattachment shock.

2.2.2 Compression corner

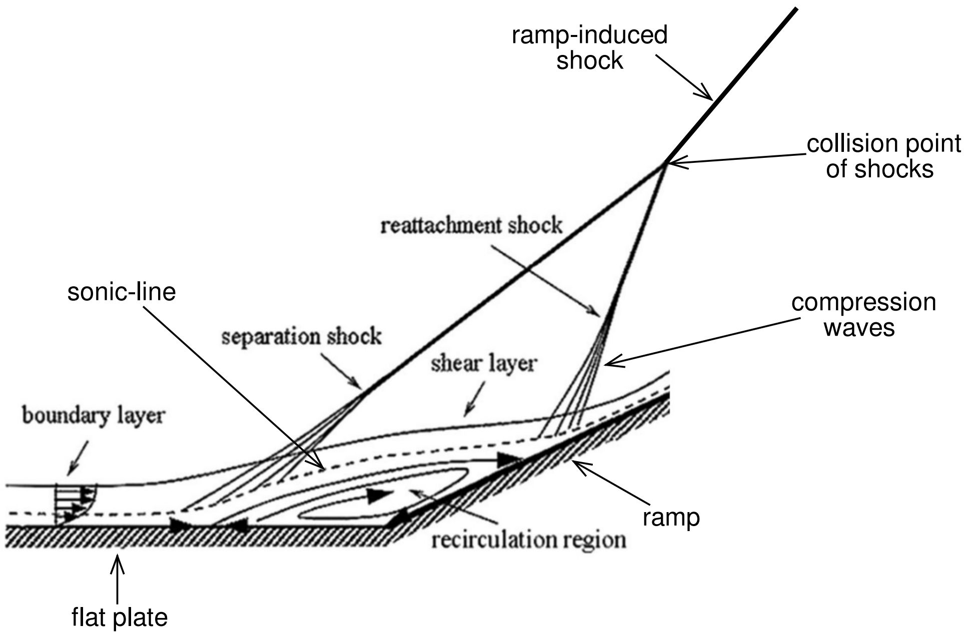

Figure 2.3: Shock/boundary-layer interaction over compression corner (reproduced from Wu et al. [94])

Two-dimensional compression corner finds application in many engineering areas, like flap controls, fuselage junctures, and scram-jet intake. It consists of a flat plate followed by a ramp inclined at an angle with respect to the flow direction. The flow over a compression corner contains complex structures like shear layers, separation, reattachment, shock waves. The interactions between shock wave and boundary-layer creates wall pressure oscillation which leads to noise mitigation and a performance degrade of aircraft control surfaces. Also large pressure oscillation can creates unwanted pressure drag on the vehicle surface due to the genaration of pressure fluctuation. Due to its importance in fundamental research of SBLI and engineering applications, several studies about ramp flow have been done in the past decades. As shown in Fig. 2.3, the turbulent boundary-layer on the flat plate interacts with the shock wave due to ramp compression. If the adverse pressure gradient created by shock wave exceeds the limit of boundary-layer to withstand the compression, flow separation occurs upstream of the compression corner. The re-circulation region is shown in Fig. 2.3 where the flow direction gets reversed due to the boundary-layer separation. The separation bubble acts as a blockage to the upstream flow and generates the separation shock. The boundary-layer now goes over the separation bubble to form a free shear layer. As the fluid-flow reattaches on the ramp, it generates a series of compression waves which coalesce to form a reattachment shock. The separation shock and the reattachment shock coalese at a point outside the boundary-layer to form the ramp-induced shock along with a weak oblique shock or expansion fan depending on the freestream conditions and shocks strength.

2.3 Governing Equations

The two-dimensional Reynolds averaged Navier-Stokes equations (RANS) are solved for the mean flow quantities. In the RANS method, the instantaneous variables are split into mean and fluctuating components as follows,

$$f = \overline{f} + f',$$

where over-bar denotes the Reynolds averaged quantities and prime represents the fluctuating component. If the flow is statistically steady, a time average of f can be taken over a finite interval T where T is large enough compared to the turbulent time scale t.

$$\overline{f}(x) = \lim_{T\to\infty} \frac{1}{T} \int_t^{t+T} f(x,t)dt,$$

where $x = (x, y, z)'$. In case of compressible flows, the flow variables are computed using a density-weighted Favre average procedure,

$$\widetilde{f} = \frac{\overline{\rho f}}{\overline{\rho}}.$$

Here, f is any flow dependent variable and tilde represents the Favre mass-averaged quantity. The Favre fluctuations are denoted by double-prime and given as

$$f = \widetilde{f} + f''.$$

The Favre fluctuations are related to Reynolds fluctuations as follow,

$$\overline{f''} = -\frac{\overline{\rho' f'}}{\overline{\rho}} \neq 0,$$

whereas $\overline{f'} = 0$. So from the mathematical simplification it can be concluded that the Favre averaging only eliminates the density fluctuation from the governing equations but it does not eliminate its effect on turbulence. So it's only a mathematical simplification not a physical one.

So applying the Reynolds averaged approach to the instantaneous Navier-Stokes equations with Favre decomposition, the compressible form of the Navier-Stokes equations are

$$\frac{\partial\overline{\rho}}{\partial t} + \frac{\partial}{\partial x_i}(\overline{\rho}\widetilde{u_i}) = 0 \tag{2.66}$$

$$\frac{\partial}{\partial t}(\overline{\rho}\widetilde{u_i}) + \frac{\partial}{\partial x_j}(\overline{\rho}\widetilde{u_j}\widetilde{u_i}) = -\frac{\partial\overline{p}}{\partial x_i} + \frac{\partial}{\partial x_j}(\overline{t_{ji}} - \overline{\rho u_j'' u_i''}) \tag{2.67}$$

$$\begin{aligned}&\frac{\partial}{\partial t}\left[\overline{\rho}(\widetilde{e} + \frac{\widetilde{u_i}\widetilde{u_i}}{2}) + \frac{\overline{\rho u_i'' u_i''}}{2}\right] + \frac{\partial}{\partial x_j}\left[\overline{\rho}\widetilde{u_j}(\widetilde{h} + \frac{\widetilde{u_i}\widetilde{u_i}}{2}) + \widetilde{u_j}\frac{\overline{\rho u_i'' u_i''}}{2}\right] \\ &= \frac{\partial}{\partial x_j}\left[-q_{Lj} - \overline{\rho u_j'' h''} + \overline{t_{ji} u_i''} - \overline{\rho u_j'' \frac{u_i'' u_i''}{2}}\right] + \frac{\partial}{\partial x_j}\left[\widetilde{u_i}(\overline{t_{ij}} - \overline{\rho u_i'' u_j''})\right].\end{aligned} \tag{2.68}$$

The above equations are known as compressible Reynolds averaged Navier-Stokes (RANS) equations. The above equations are almost similar to the instantaneous Navier-Stokes equations but here the instantaneous variables are replaced by the mean quantity and there are extra unclosed turbulent correlation terms in the averaged momentum and energy equations.

The first term in the left hand side of the above equations denoting the time rate of change of mean mass, momentum and total energy of the fluid. The total energy includes average internal energy, mean and turbulent kinetic energy. Turbulent kinetic energy is denoted by $\frac{\overline{u_i'' u_i''}}{2}$, k which is the contribution of turbulent fluctuation to the mean energy. The second term in the left hand side of the above equations represents the net flux of mass, momentum and total energy of the fluid which is also known as convective term.

The extra term $-\overline{\rho u_j'' u_i''}$ in the averaged momentum equation is the turbulent stress term. This extra term is denoted by τ_{ij} and is known as Reynolds stress tensor. This extra term came from the time average of convective term of the instantaneous momentum equation and it is responsible for the turbulent mixing. Here the turbulent momentum flux $\rho u_j''$ is being carried by the fluctuating velocity u_i'' , so the stress is induced by the turbulent momentum flux.

The terms on the right hand side of the averaged energy equation like $\frac{\partial q_{Lj}}{\partial x_j}$, $\frac{\partial}{\partial x_j}(\widetilde{u_i}\overline{t_{ij}})$ reflects rate of mean heat conduction and work done by viscous stresses respectively. The viscous stresses and the mean heat conduction are important in the region very close to the wall where turbulent fluctuations can be neglected. The terms are given as

$$\overline{t_{ij}} = \mu\left(\frac{\partial\widetilde{u_i}}{\partial x_j} + \frac{\partial\widetilde{u_j}}{\partial x_i}\right) - \frac{2}{3}\mu\frac{\partial\widetilde{u_k}}{\partial x_k}\delta_{ij}$$
$$q_{Lj} = -\kappa\frac{\partial\widetilde{T}}{\partial x_j},$$

where μ, κ are the viscosity and thermal conductivity of the fluid respectively. The term denoted by $\overline{\rho u_j^{''} h^{''}}$ is known as turbulent heat flux which represent the mixing of turbulent heat,i.e. convection of turbulent enthalpy $h^{''}$ by the fluctuating velocity. The term involving the triple correlation $\overline{\rho u_j^{''} u_i^{''} u_i^{''}}/2$ represent the turbulent mixing of turbulent kinetic energy, here turbulent kinetic energy is transported by fluctuating velocity, therefore diffused the turbulent kinetic energy. The term containing $\overline{t_{ij} u_i^{''}}$ represent the molecular turbulent diffusion here the viscous stress tensor is transported by the fluctuating velocity.

In terms of mean variables the fluid is assumed to be an ideal gas with gas constant R,

$$\overline{p} = \overline{\rho} R\widetilde{T}.$$

The unclosed term in the Reynolds averaged governing equations are the Reynolds stress, τ_{ij}, the turbulent heat flux vector, $\overline{\rho u_j^{''} h^{''}}$, and the turbulent transport and viscous diffusion of the turbulent kinetic energy. Modeling of these unclosed terms are discussed in the next section.

2.4 Turbulence Models

The RANS methodology introduces new turbulent correlations in the mean flow governing equations, which need to be modeled in order to solve the equations. As there are 6 equations, i.e. one continuity, three momentum, one energy and perfect gas equations. In these equations there are six unknown mean variables; $\widetilde{u_i}$, $\overline{\rho}$, $\overline{p}$, $\widetilde{T}$ and additional turbulent terms need to be calculated. These turbulent terms are modeled in terms of turbulent and mean variable which can be easily solved, thus closing the governing equations. The 'n-equation' turbulent model means that n extra turbulent transport equations are solved apart from mean conservation equations. Some of the examples are zero, one and two equation turbulent models.

2.4.1 Boussinesq Hypothesis

Mostly turbulence models are based on the Boussinesq hypothesis. Boussinesq believes that the momentum transfer occurs in a turbulent flow by the fluid lumps the so

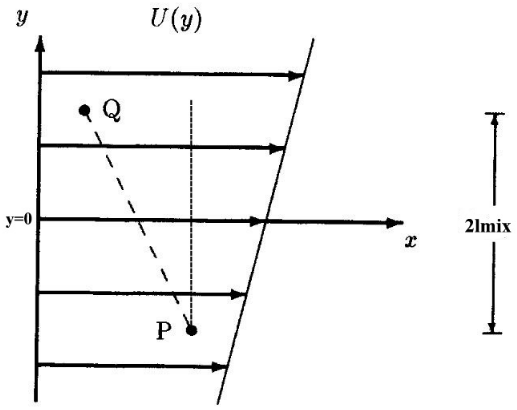

Figure 2.4: Shear flow profile between molecules[92]

called turbulent eddies can be modeled with an eddy viscosity. The same thing is happening when the fluid particles in motion transfer their momentum by the molecular viscosity. From this analogy Boussinesq states that Reynolds Stress tensor τ_{ij} is proportional to the mean Strain-rate tensor S_{ij}. Mathematically it can be expressed as

$$\tau_{ij} = 2\mu_T(S_{ij} - \frac{1}{3}\frac{\partial \widetilde{u}_k}{\partial x_k}\delta_{ij}) - \frac{2}{3}\bar{\rho}k\delta_{ij} \tag{2.69}$$

where

$$S_{ij} = \frac{1}{2}(\frac{\partial \widetilde{u}_i}{\partial x_j} + \frac{\partial \widetilde{u}_j}{\partial x_i}) \tag{2.70}$$

is the strain rate tensor and δ_{ij} is the Kronecker delta. So any stress which is governed from the momentum flux transport can be expressed in this from. Hence Reynolds Stress is calculated from the eddy viscosity μ_T and the strain rate tensor. Turbulence models are required to compute this Eddy viscosity in order to compute the Reynolds stress tensor.

2.4.2 Zero Equation Model

Turbulence model in which the eddy viscosity μ_T is determined as the function of local mean flow variables, i.e. there is no extra transport equation being used rather than the conservation equations, is known as the zero equation model or the algebraic equation model. Prandtl(1925) first postulated this zero equation method which is often known as Prandtl's mixing length hypothesis. Physically the mixing length can be defined as the average distance that a small mass of fluid travels before it exchanges its momentum with another mass of fluid. Prandtl relates this eddy viscosity with the molecular mixing phenomenon. Figure 2.4 shows the shear flow profile between two molecules. Now when the molecules move from one place to another,it will transfer the momentum in it. If the momentum transport take place in the perpendicular direction it will give rise to the shear stress or the momentum flux. Now it can be shown that the viscous stress $t_{xy} = \overline{-\rho u''v''}$, this similarity is the basis of the Prandtl's mixing length Hypothesis.

Though molecular viscosity and eddy viscosity are fundamentally different, i.e. molecular viscosity is a property of the fluid and eddy viscosity is a property of flow. Prandtl relate the molecules with the lump of fluids or eddies which carry the momentum, energy in a turbulent flow. This is main reason why eddy viscosity and mixing length are specified in terms of a algebraic equation:

$$\mu_T = \rho l_{mix}^2 |\frac{\partial \widetilde{u_i}}{\partial y}|, \tag{2.71}$$

where l_{mix} is the mixing length which is similar to the mean free path of the molecules in the molecular mixing. Baldwin-lomax, Cebeci-Smith are the most common algebraic model. The main problem in this model is that mixing length vary for each flow and must be known in advance to obtain a solution and this model is also not suitable for separated flow.

Advantages Of Zero Equation Model

- Easy implementation.
- Low economic cost in term of CPU usage.
- Predict well enough for attached boundary flow.

2.4.3 One equation model

The basic extra transport equation for the one equation turbulence model is the turbulent kinetic energy equation. The turbulent kinetic energy (TKE) is associated with the eddies in a turbulent flow and mathematically it can be quantified by measuring the root mean square (RMS) velocity fluctuations. Taking moment of the instantaneous momentum equation and after that taking the trace of that equation, will give the turbulent kinetic energy equation. The Reynolds averaged turbulent kinetic energy equation is given by,

$$\bar{\rho}\frac{\partial k}{\partial t} + \bar{\rho}\widetilde{u_j}\frac{\partial k}{\partial x_j} = \tau_{ij}\frac{\partial \widetilde{u_j}}{\partial x_j} - \bar{\rho}\epsilon + \frac{\partial}{\partial x_j}[\mu\frac{\partial k}{\partial x_j} - \frac{\overline{\rho u_i'' u_i'' u_j''}}{2} - \overline{p' u_j''}], \tag{2.72}$$

where $k = \frac{1}{2}\overline{u_i'' u_i''}$ is the turbulent kinetic energy and $\epsilon = \nu\overline{\frac{\partial u_i''}{\partial x_k}\frac{\partial u_i''}{\partial x_k}}$ is the dissipation rate of the turbulent kinetic energy per unit mass.

The first term in the left hand side is the time rate of change of the turbulent kinetic energy k, whereas the second term in the left hand side represent change of net turbulent kinetic energy flux.

The first term in the right hand side $\tau_{ij}\frac{\partial\widetilde{u_i}}{\partial x_j}$ denotes work done by the velocity gradient or the mean strain rate against the turbulent stress, i.e kinetic energy is transformed from the mean flow to the turbulent flow which is the main source of the turbulence. That is why this term is often called as turbulence production term. The second term in the right hand side signifies the work done by the fluctuating velocity gradient against the viscous stress. It transfer the turbulent kinetic energy into thermal internal energy and often known as the dissipation of turbulence. The term in the right hand side denoting by $\mu\frac{\partial k}{\partial x_j}$ represent the diffusion or transfer of turbulent kinetic energy from one fluid lump to another by the molecular transport and known as molecular diffusion. The term with the triple velocity fluctuation correlation signifies transport rate of the turbulent kinetic energy by the fluctuating velocity or the transport of Reynolds stress by the turbulent fluctuating velocity. The last term in the right hand side represent the pressure diffusion by the turbulent fluctuating velocity.

All the turbulent models use gradient diffusion analogy to close the turbulent correlation terms. The gradient diffusion analogy states that turbulent transport of any scalar quantity in a turbulent flow can be represent as the mean gradient of that scalar quantity. The physical idea behind this analogy is that the stress created by the molecular transport is directly proportional to the mean velocity gradient, so the turbulent transport of scalar quantity can be mathematically written as,

$$\overline{u'_j\phi'} \propto \frac{\partial\overline{\phi}}{\partial x_j}, \tag{2.73}$$

Boussinesq used this analogy and hypothesized that the Reynolds Stress tensor τ_{ij} is proportional to the mean strain-rate tensor S_{ij} . He also states that the momentum transfer occurs in a turbulent flow by the fluid lumps, the so called turbulent eddies, can be modeled with an eddy viscosity μ_T. The same thing is happening when the fluid particles in motion transfer their momentum by the molecular viscosity. Mathematically it is given by the following expression.

$$\tau_{ij} = 2\mu_T(S_{ij} - \frac{1}{3}\frac{\partial\widetilde{u_k}}{\partial x_k}\delta_{ij}) - \frac{2}{3}\overline{\rho}k\delta_{ij}, \tag{2.74}$$

where,

$$S_{ij} = \frac{1}{2}(\frac{\partial\widetilde{u_i}}{\partial x_j} + \frac{\partial\widetilde{u_j}}{\partial x_i})$$

Any stress which is governed from the momentum flux transport can be expressed in this from. The turbulent transport of turbulent kinetic energy (TKE) in the energy and

TKE equation and the viscous diffusion term in the energy equation are modeled as,

$$\overline{\rho u_j'' \frac{u_i'' u_i''}{2}} = \frac{\mu_T}{\sigma_k}\frac{\partial k}{\partial x_j}$$
$$\overline{t_{ji} u_i''} = \mu \frac{\partial k}{\partial x_j}$$

where σ_k is the closure constant coefficient. The last term in the turbulent kinetic energy represents the pressure diffusion in the flow. As per recent direct numerical simulation (DNS) data this term is very small in turbulent flow and hence neglected in TKE equation. So the simplified form of the turbulent kinetic energy is given as,

$$\bar{\rho}\frac{\partial k}{\partial t} + \bar{\rho}\widetilde{u}_j\frac{\partial k}{\partial x_j} = \tau_{ij}\frac{\partial \widetilde{u}_i}{\partial x_j} - \bar{\rho}\epsilon + \frac{\partial}{\partial x_j}\left[(\mu + \frac{\mu_T}{\sigma_k})\frac{\partial k}{\partial x_j}\right] \tag{2.75}$$

Although the early development of one-equation model is based on turbulent kinetic energy equation, the most popular one-equation model of Spalart-Allmaras rely on the empirical transport equations for the eddy viscosity.

Advantages of one equation model

- Give better prediction than the zero equation model.
- Mainly used for aerodynamic flow with adverse pressure gradient.

2.4.4 Two Equation Model

The two equation turbulent model is most popular in engineering applications. Zero and one equation models are the incomplete model as they do not give us any clue about the turbulent length scale and for this reason one has to depend on the flow history. Whereas two equation turbulence models are complete and do not need any prior knowledge of the flow history. Two extra transport equations are used to solve the following turbulent flow field quantities,

- One equation is used to calculate the turbulent kinetic energy k.
- Another equation is for turbulence length scale.

The choice of the second equation to calculate length scale is quite frequent, but the most popular ones are as follows,

- ϵ -Dissipation rate of turbulence
- ω -Rate of dissipation of energy per unit volume and time

- τ - turbulence time scale = $\frac{1}{\omega}$

The turbulence models based on k-ω framework are only discussed in this report because of their popularity in wall bounded flows.

2.4.5 k- ω model

The k-ω model of Wilcox [92] is a well known and widely tested [3, 59, 69] two equation eddy viscosity model. This model is referred to here as the standard k-ω model. The k-ω model of Wilcox demonstrates superior performance for wall-bounded and low Reynolds number flows. The standard k-ω model has proven to be superior in transitional flows. In the logarithmic region of boundary layer, the model gives good agreement with experimental results for mild adverse pressure gradient flows. The two extra convective transport equation are solved apart from conservation equations.

- One equation describes the turbulent kinetic energy k.
- Another equation is for turbulence length scale in terms of ω which is the rate of dissipation of energy per unit volume and time.

The standard k-ω model is approximated as follows,

$$\bar{\rho}\frac{\partial k}{\partial t} + \bar{\rho}\widetilde{u}_j\frac{\partial k}{\partial x_j} = \tau_{ij}\frac{\partial \widetilde{u_i}}{\partial x_j} - \beta^*\bar{\rho}k\omega + \frac{\partial}{\partial x_j}\left[(\mu + \frac{\mu_T}{\sigma_k})\frac{\partial k}{\partial x_j}\right] \tag{2.76}$$

$$\bar{\rho}\frac{\partial \omega}{\partial t} + \bar{\rho}\widetilde{u}_j\frac{\partial \omega}{\partial x_j} = \alpha\frac{\omega}{k}\tau_{ij}\frac{\partial \widetilde{u_i}}{\partial x_j} - \beta\bar{\rho}\omega^2 + \frac{\partial}{\partial x_j}\left[(\mu + \frac{\mu_T}{\sigma})\frac{\partial \omega}{\partial x_j}\right], \tag{2.77}$$

where α,β,β^* are the closure coefficient. The values of the closure co-efficient, which have been found from the experimental date, are: $\alpha = \frac{5}{9}$, $\beta = \frac{3}{40}$,$\beta^* = \frac{9}{100}$, $\sigma = 2$, $\sigma_k = 1$.

The turbulent kinetic energy equation is described in the previous section. The terms on left hand side of Eq. 2.77 represents the unsteady and convective transport terms respectively. The first term on right hand side represents the rate of production of specific dissipation rate ω. The second term represents the destruction of specific dissipation rate and the third and fourth terms on right hand side represent the molecular and turbulent diffusion.

2.4.6 Shock-unsteadiness modification

The accuracy of standard RANS turbulence models, like k-ϵ and k-ω, is limited in high-speed flows involving strong shock waves. This is due to the over-amplification of turbulent kinetic energy across the shock wave by standard models. The over estimation of TKE leads to a more energized boundary layer, which is able to sustain the adverse pressure gradient created by the shock waves for longer, thus delaying flow separation. The over-amplification of TKE is partly due to the fact that the standard models do not consider the unsteady nature of shock wave while interacting with turbulence. Upstream turbulence makes the shock oscillate about a mean position and the amplification of turbulence across an unsteady shock is less compared to its amplification across a steady shock wave. Sinha et al. [78] model the unsteady effect of shock waves in the otherwise steady RANS framework and include the unsteady shock physics into standard turbulence models. The shock-unsteadiness modified turbulence models are found to improve the flow topology significantly, thereby giving better predictions for surface pressure and separation bubble size, in flows with shock-shock and shock-boundary layer interactions [60, 61, 79]. In this section, we briefly outline the key features of shock-unsteadiness k-ω model.

The production term of the turbulent kinetic energy in the standard k-ω model is given as:

$$P_k = \mu_T \left(2S_{ij}S_{ji} - \frac{2}{3}S_{ii}^2 \right) - \frac{2}{3}\bar{\rho}kS_{ii} \tag{2.78}$$

where $S_{ij} = \frac{1}{2}\left(\partial\widetilde{u_i}/\partial x_j + \partial\widetilde{u_j}/\partial x_i\right)$ and $\widetilde{u_i}$ is the component of the Favre-averaged velocity in the i-direction. Here, the overbar and tilde represent the Reynolds and Favre-averaged quantities respectively and the turbulent eddy viscosity is modeled as $\mu_T = \bar{\rho}k/\omega$.

Sinha et al. [78] develop a new transport equation of the TKE with an extra source term to account for the shock-unsteadiness damping effect and it is combined with the production term to get

$$P_k^{'} = -\frac{2}{3}\bar{\rho}kS_{ii}\left(1 - b_1^{'}\right), \tag{2.79}$$

where μ_T is set to zero in Eq. 2.78 so as to limit the very high values of $P_k \sim \mu_T(\partial\widetilde{u_i}/\partial x_j)^2$ obtained in shock waves. Here,

$$b_1^{'} = \max.[0, 0.4\left(1 - e^{1-M_{1n}}\right)] \tag{2.80}$$

represents the damping effect of unsteady shock oscillations, and is prescribed using Linear interaction analysis (LIA) results for canonical shock-turbulence interaction. In spite of the limitations of LIA, the shock-unsteadiness model has worked well in SBLI flows [60, 61, 79]. The shock-unsteadiness damping parameter is a function of the upstream shock-normal Mach number M_{1n}, which brings in the physical effect of the shock strength. It takes a value of 0.4 in the hypersonic limit and vanishes for very weak shock waves. Additional details of the shock-unsteadiness model development are given in [79].

The shock-unsteadiness modification is applied in the k-ω framework by multiplying the production term of the standard k-ω model by the factor,

$$c_\mu^{'} = 1 - f_s \left[1 + \frac{b_1^{'} \omega}{\sqrt{3} S} \right] \tag{2.81}$$

where $S = \left[2S_{ij}S_{ji} - \frac{2}{3}S_{ii}^2 \right]^{1/2}$ and f_s is an empirical function of the non-dimensional mean dilatation $S_{ii}\delta_0/U_\infty$ [60],

$$f_s = \frac{1}{2} - \frac{1}{2} tanh \left[12 \left(S_{ii}\delta_0/U_\infty \right) + 4 \right] \tag{2.82}$$

It takes a value of one in shocks and high compression regions, such that $c_\mu^{'} = -b_1^{'}\omega/\sqrt{3}S$ and we get the modified production $P_k^{'}$. Otherwise, it is zero and the standard form of k-ω model is recovered outside of shock waves.

2.5 Turbulent Heat Flux Model

In the previous section the modeling approach of Reynold's stress tensor is discussed. Another important unclosed term in the Reynolds averaged energy equation turbulent heat flux $q_{T_j} = -\overline{\rho u_j^{''} h^{''}}$ will be discussed here. Conventionally it is modeled by the gradient diffusion hypothesis and the strong Reynolds analogy (SRA) relates the turbulent heat flux with the Reynolds stress via turbulent Prandtl number.

$$q_{T_j} = -\overline{\rho u_j^{''} h^{''}} = -\frac{\mu_T c_p}{Pr_T} \frac{\partial \widetilde{T}}{\partial x_j}. \tag{2.83}$$

Generally a constant value of $Pr_T = 0.89$ is used for the simulations. A constant Pr_T gives very good prediction of surface heat transfer for turbulent boundary layer but it does not perform well with flows dominated by shock waves. Some times the conventional heat flux modeling overpredicts the wall heat flux by a factor of 2 [95] in high-speed flows where strong viscous interaction or shock-shock interaction take place. Some recent developments in this area shows an improvement to surface heat flux by calculating the turbulent Prandtl number as part of the solution instead of taking a constant value. In this section few advanced turbulent heat flux model is discussed for reference of the readers.

2.5.1 Algebraic model

Golberg et al. [25] developed a turbulent heat flux model based on variable turbulent Prandtl number. The velocity-temperature fluctuation correlation is defined as,

$$\widetilde{u_i^{''} T^{''}} = \frac{\tau_t}{C_{\theta 1} + \frac{1}{2}(P_k/\epsilon - 1)} \left[\overline{u_i^{''} u_j^{''}} \frac{\partial \widetilde{T}}{\partial X_j} - \frac{C_{\theta 2}}{6R} f_\theta \sqrt{(\overline{u_i^{''} u_j^{''}})(\overline{u_i^{''} u_j^{''}})(\frac{\partial \widetilde{T}}{\partial x_i}\frac{\partial \widetilde{T}}{\partial x_i})} \right]. \tag{2.84}$$

In the above equation f_θ is a function of turbulent Reynolds Number, τ_t is the turbulence time scale of temperature fluctuation, ϵ is the dissipation of k, P_k is the production of k which is given by $\tau_{ij}\frac{\partial \widetilde{u_i}}{\partial x_i}$ and transfer the energy from mean flow to turbulent flow. $C_{\theta 1}, C_{\theta 2}, R$ are the model constants. The turbulent thermal diffusivity is given as

$$[\alpha_t]^{-1} = \sqrt{\frac{(\frac{\partial \widetilde{T}}{\partial X_i}\frac{\partial \widetilde{T}}{\partial X_i})}{(\widetilde{u_i''T''}\widetilde{u_i''T''})}} \tag{2.85}$$

Once the value of $\widetilde{u_i''T''}$ is calculated from equation 2.84, α_t can be calculated from the above equation. This model calculate the value of turbulent Prandtl number Pr_T as,

$$Pr_T = \max\left[2Pr_{T,constant} - 4.75\sigma_t\right] \tag{2.86}$$

where $\sigma_t = \frac{\nu_t}{\alpha_t}$. Recently Quadros et al. [67] developed a turbulent heat flux model for shock dominated flows which is discussed in chapter 4.

2.5.2 Differential Equation Based Model

Xiao et al [95] presents a model for better prediction of heat flux value in high-speed flows. The turbulent Prandtl number Pr_T is calculated as a part of the solution instead of keeping it constant. This is basically a $k-\zeta$ two equation model where k represents the turbulent kinetic energy(TKE) and ζ represents the enstrophy, a variance of vorticity. This model compute the heat flux for separated flow better than the conventional turbulence model. There are two extra transport equations apart from Navier-Stokes and turbulence model $(k-\zeta)$ equations,

- one equation describe the variance of enthalpy.
- Another one describe the dissipation rate of enthalpy variance.

The enthalpy variance equation is given as,

$$\begin{aligned}
\frac{\partial}{\partial t}\left(\bar{\rho}\frac{\widetilde{(h'')^2}}{2}\right) + \frac{\partial}{\partial x_j}\left(\bar{\rho}\widetilde{u}_j\frac{\widetilde{(h'')^2}}{2}\right) &= \frac{\partial}{\partial x_j}\left[\rho(\gamma\alpha + \alpha_T C_{h,2})\frac{\partial \widetilde{(h'')^2}/2}{\partial x_j}\right] \\
&+ 2\mu\gamma\left[\frac{\partial}{\partial x_j}(q_{T,i}/\rho) + \frac{\partial}{\partial x_i}(q_{T,j}/\rho)\right] - \frac{4}{3}\mu\gamma\widetilde{S}_{kk}\frac{\partial}{\partial x_i}(q_{T,j}/\rho) \\
&- (\gamma-1)\bar{\rho}\widetilde{h''^2}\frac{\partial \widetilde{u_i}}{\partial x_i} - q_{T,i}\frac{\partial \widetilde{h}}{\partial x_i} + 2C_{h,4}\gamma\mu\sqrt{\widetilde{(h'')^2}}\zeta - \gamma\bar{\rho}\epsilon_h,
\end{aligned} \tag{2.87}$$

where,

$$q_{T,j} = -\bar{\rho}\alpha_T \frac{\partial \widetilde{h}}{\partial x_j}$$
$$\alpha_T = 0.5[C_h k\tau_h + \nu_t/0.89]$$
$$\tau_h = \widetilde{h''^2}/\epsilon_h$$
$$\epsilon_h = \alpha\overline{(\frac{\partial h''}{\partial x_j})^2}$$

In the above equations $q_{T,j}$ is turbulence heat flux vector, α_T is the turbulent eddy thermal diffusivity, τ_h is time scale of enthalpy fluctuation, C_h is the model constant, ϵ_h is the dissipation rate of enthalpy variance, α is the molecular diffusivity. Also turbulent kinematic viscosity ν_T is given by,

$$\nu_T = \frac{C_\mu k^2}{\nu\zeta} = C_\mu k\tau_k, \tag{2.88}$$

where C_μ is the model constant, τ_k is the time scale for turbulent velocity fluctuations and given by

$$\tau_k = \frac{k}{\epsilon}$$

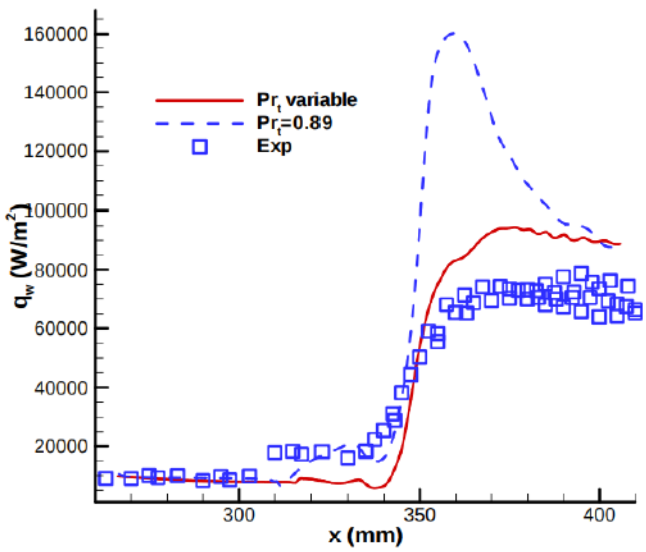

Figure 2.5: Computed surface heat transfer distribution for 14 degree oblique shock impingement case of Schulein [73] for Mach 5 from Xiao et al. [95]

The model equation for dissipation rate of enthalpy variance is expressed as

$$
\begin{aligned}
&\frac{\partial}{\partial t}(\overline{\rho}\epsilon_h) + \frac{\partial}{\partial x_j}(\overline{\rho}\widetilde{u}_j\epsilon_h) = -\overline{\rho}\epsilon_h(C_{h,5}b_{jk} - \frac{\delta jk}{3})\frac{\partial \widetilde{u}_j}{\partial x_k} \\
&- C_{h,6}\overline{\rho}k\frac{\partial\sqrt{(\widetilde{h''})^2}}{\partial x_j}\frac{\partial \widetilde{h}}{\partial x_j} + \frac{\partial}{\partial x_j}\left[(\gamma\alpha + C_{h,7}\alpha_T)\frac{\partial \epsilon_h}{\partial x_j}\right] \\
&+ C_{h,8}\frac{q_{T,j}}{\tau_h}\frac{\partial \widetilde{h}}{\partial x_j} - \gamma\rho\epsilon_h\left[\frac{C_{h,9}}{\tau_h} + \frac{C_{h,10}}{\tau_k}\right] \\
&C_{h,11}\epsilon_h\left[\frac{D\overline{\rho}}{Dt} + \frac{\overline{\rho}}{\overline{P}}\max(\frac{D\overline{p}}{Dt}, 0.0)\right]
\end{aligned}
\tag{2.89}
$$

where

$$b_{ij} = \frac{\tau_{ij}}{\overline{\rho}k} + \frac{2}{3}\delta_{ij}$$

and $\tau_{ij} = -\overline{\rho u_i'' u_j''}$ is the Reynolds Stress tensor. The constants from C_h to $C_{h,11}$ are the model constants. Equations 2.87 and 2.89 are the governing equation for the Xiao et al. [95] model. Now the turbulent Prandtl no. Pr_T is given by

$$Pr_T = \frac{\nu_T}{\alpha_T} \tag{2.90}$$

This differential equation based models are computationally expensive and rarely used for large practical applications. Figure 2.5 shows the surface heat transfer distribution for 14 degree oblique shock impingement case from Xiao et al. [95]. The experiment data was taken from Schulein et al. [73].

2.6 Summary

A brief review of available analytical solutions for velocity and temperature field of a turbulent boundary layer are discussed in this chapter. The flow physics of weak and strong interaction of a turbulent boundary layer and shock wave is also explained here. The Reynolds-averaged Navier-Stokes equations govern the compressible turbulent flow with additional equations for the Reynolds stress tensor, turbulent heat flux. Various turbulence models with ample assumptions and limitations are presented for engineering applications.

Chapter 3

Methodology

A description of the numerical method and the simulations carried out are provided in this chapter. The work is divided into two parts: a) shock-turbulence interaction (STI) and b) shock-boundary layer interaction (SBLI). First, the interaction of isotropic turbulence with a normal shock wave is used to study the effect of shock wave on the turbulence and vice-versa. This model problem is often referred as canonical shock-turbulence interaction because of its simplicity and complexities such as mean shear, streamline curvature, real gas effects, magnetic effects, etc. have been removed from this model problem. Next, shock-boundary layer interactions have studied for different configurations and flow conditions. The numerical methodology for these two problems are explained separately.

3.1 Shock-Turbulence Interaction

3.1.1 Direct Numerical Simulation

Computations are performed by Sethuraman et al. [74] for the interaction of a temporally decaying homogeneous isotropic turbulence with a normal shock wave using the shock-capturing methodology. The turbulence database is generated in a separate precursor simulation. All the simulations are carried out by Sethraman et al. [74] and here the post-processing is done for the turbulent heat flux analysis. The physical insights gain from this analysis is used to develope a predictive model for turbulent heat flux in the susequent chapter.

Governing equations

The governing equations are the three-dimensional, unsteady, compressible Navier-Stokes (NS) equations with the assumption of perfect gas. The equations are solved in the Cartesian coordinates for the conservative variables ρ, $\rho\, u_i$, $\rho\, E_0$ as shown below,

$$\frac{\partial \rho}{\partial t} + \frac{\partial(\rho\, u_k)}{\partial x_k} = 0, \tag{3.1}$$

$$\frac{\partial(\rho\, u_i)}{\partial t} + \frac{\partial(\rho\, u_i u_k)}{\partial x_k} + \frac{\partial p}{\partial x_i} = \frac{\partial \sigma_{ik}}{\partial x_k}, \tag{3.2}$$

$$\frac{\partial(\rho\, E_0)}{\partial t} + \frac{\partial(\rho\, u_k\, E_0)}{\partial x_k} + \frac{\partial(p\, u_k)}{\partial x_k} = \frac{\partial(u_i\, \sigma_{ik})}{\partial x_k} - \frac{\partial q_k}{\partial x_k}, \tag{3.3}$$

where, ρ is density, u_i is the velocity vector, p is the pressure, E_0 is the total energy, σ_{ik} is the viscous stress tensor and q_k is the heat conduction vector. The viscous stresses and the heat flux are modeled using Stokes hypothesis and Fourier's law of heat conduction, respectively. They are expressed as follows,

$$\sigma_{ik} = \mu \left(\frac{\partial u_i}{\partial x_k} + \frac{\partial u_k}{\partial x_i} - \frac{2}{3}\frac{\partial u_m}{\partial x_m}\,\delta_{ik} \right), \tag{3.4a}$$

$$q_k = -\frac{\mu\, c_p}{Pr}\frac{\partial T}{\partial x_k}. \tag{3.4b}$$

State equation for the perfect gas holds and thus pressure, $p = \rho R T$. The thermal conductivity, κ is related to molecular viscosity, μ through the assumption of constant Prandtl number $Pr = \mu\, c_p/\kappa$, with c_p being the gas specific heat at constant pressure. The molecular viscosity varies as a function of temperature, which according to a power law is given as, $\mu_{ref}(T/T_{ref})^{3/4}$. Here, μ_{ref} and T_{ref} are the reference viscosity and temperature of the gas, respectively. The compressible NS equations are solved using a solution-adaptive finite difference method for the perfect gas. The inviscid fluxes near the shock are calculated using a fifth order accurate weighted essentially non-oscillatory (WENO) numerical scheme with Roe flux splitting. The fluxes in the remainder of the domain are calculated using a sixth order accurate central difference scheme in the split form proposed by Ducros *et al.* [18]. The use of the split form is known to improve the nonlinear numerical stability, and no de-aliasing filter is required. The shock wave(s) are identified as regions where the negative dilatation is greater than the low pass-filtered vorticity magnitude i.e., where $-\frac{\partial u_k}{\partial x_k} > \sqrt{\omega_k\, \omega_k}$. Having identified the grid points occupied by the shock wave(s), the WENO scheme is applied to the narrow region comprising those points as well as three additional grid points in every direction. This is carried out in order to ensure that the central scheme is never used across any shock wave(s). The switching between the WENO and central differencing schemes, introduces internal 'interfaces' in the domain. The method devised by Pirozzoli [63] is used to ensure proper conservation across these interfaces and the linear stability of these interfaces has been verified by Larsson and Gustafsson [45]. Any spurious oscillations introduced due to the solution-adaptive switching of the numerical schemes are thus bounded. The entire system of equations is integrated in time using a fourth order accurate explicit Runge-Kutta (RK4) scheme.

This numerical procedure has been verified and validated on several problems of interest [37, 43, 44, 46, 74]. It was also identified that the solution-adaptive method has no effect on the results provided that there is sufficient grid resolution [44]. The present study uses the term 'DNS' in the extended sense, where all scales of the turbulence are computed but the shock waves are captured numerically. This implies that the methodology assumes that there is sufficient separation between the turbulence length scale (usually η) and the shock length scale (its physical thickness δ_s). In the shock-capturing framework, the interaction problem is accurately described if the numerical shock thickness, δ_n is sufficiently small than the Kolmogorov length scale, η. Larsson [43] has shown that any error induced by the shock-capturing scheme is of the $O(\Delta x_1^2)$ with Δx_1 being the grid spacing in the streamwise direction. When the streamwise grid spacing is sufficiently refined, the numerical errors in the statistics are found to decrease considerably.

Initial Conditions

The governing equations are solved in the dimensional form itself with upstream mean density, $\bar{\rho}_1$ being set at a value of 1. In essence, the upstream values are setup in the non-dimensional form instead of the governing equations. The mean temperature in the turbulence database initially kept at 1 but as the turbulence develops in the temporal simulation, the temperature increased due to viscous dissipation. The results are always presented in the normalized sense and thus the present approach is acceptable to describe the shock-amplified turbulence quantities. The value of $\mu_{ref} = 0.002$ yields a Taylor-scale Reynolds number of $Re_{\lambda,db} = 34$ in the turbulence database. The specific gas constant R is varied in order to get the desired upstream turbulent Mach numbers., and shown in table 3.1. The Prandtl number and the ratio of specific heats are kept at a constant value of $Pr = 0.7$ and $\gamma = 1.4$, respectively for the perfect gas. The mean pressure in the turbulence database is calculated according to the equation of state. The upstream mean sound speed and the Mach number are used to calculate the upstream streamwise mean velocity $\bar{u}_1$. The downstream mean values are specified using the laminar RH relations.

Table 3.1: Initial flow conditions for all the cases considered in the present study.

M	M_t	$\overline{\rho}_1$	$\overline{T}_1$	$\overline{u}_1$	$\overline{p}_1$	R
1.23	0.05	1.0	1.0043	15.81	118.01	117.5
1.50	0.05	1.0	1.0043	19.28	118.01	117.5
2.50	0.05	1.0	1.0043	32.13	118.01	117.5
3.50	0.05	1.0	1.0043	44.99	118.01	117.5
1.23	0.15	1.0	1.0380	5.40	13.75	13.25
1.50	0.15	1.0	1.0380	6.58	13.75	13.25
2.50	0.15	1.0	1.0380	10.97	13.75	13.25
3.50	0.15	1.0	1.0380	15.36	13.75	13.25
1.23	0.25	1.0	1.1043	3.32	5.19	4.7
1.50	0.25	1.0	1.1043	4.04	5.19	4.7
2.50	0.25	1.0	1.1043	6.74	5.19	4.7
3.50	0.25	1.0	1.1043	9.43	5.19	4.7
1.23	0.40	1.0	1.2595	2.22	2.33	1.85
1.50	0.40	1.0	1.2595	2.71	2.33	1.85
2.50	0.40	1.0	1.2595	4.51	2.33	1.85
3.50	0.40	1.0	1.2595	6.32	2.33	1.85

Numerical Domain Setup

The physical domain is a rectangular box with a dimension of 2.25π in the streamwise direction (denoted as x) and $(2\pi, 2\pi)$ in the transverse directions (denoted as y and z), as shown in Fig. 3.1. The normal shock is initially placed at $x = \pi/4$. An artificial sponge is used at the end of the computational domain from 2.25π to 5π to eliminate reflecting waves. Periodic boundary conditions are used in the transverse directions as the flow is assumed to be periodic and homogeneous in these directions. Pre-generated decaying homogeneous isotropic turbulence database is then superimposed on the mean flow using Taylor's hypothesis and allowed to develop into a more realistic turbulence state before reaching the shock wave.

Inflow and outflow Conditions

The turbulence immediately upstream of the shock is needed to be realistic, fully developed and well-characterized. For this, the inflow turbulence is generated in several steps essentially following the technique proposed by Xiong et al. [96]. First, several independent but statistically identical fields of isotropic turbulence in periodic boxes are

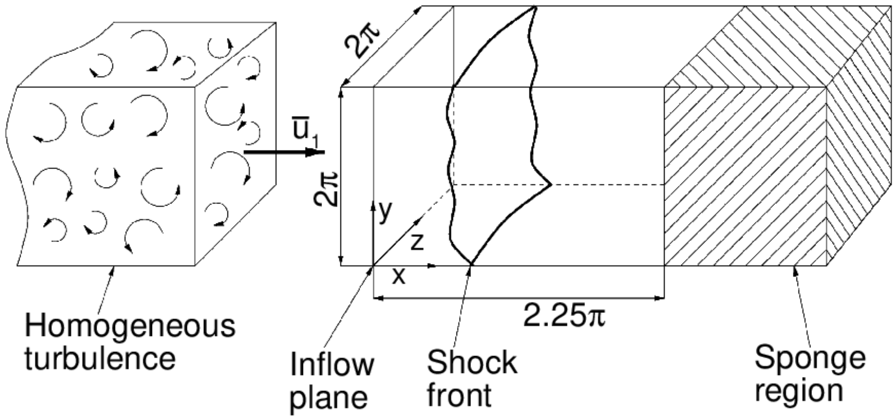

Figure 3.1: Schematic of the shock-turbulence interaction computational domain modified from [74].

generated using the methodology proposed by Ristorcelli and Blaisdell [68]. These fields have been generated with initial energy spectra of the form similar to the von Kármán energy spectrum [43] with peak energy at wavenumber $\kappa_0 = 4$ and Taylor length scale Reynolds number of $Re_{\lambda,t=0} = 114$. They are then allowed to decay temporally in periodic boxes for approximately $1-2$ units of the dissipation time scale, t_ϵ, which ensures that the turbulence is fully developed and realistic. These independent realizations (or flow fields) of turbulence are then blended together into a longer inflow database [46], which is then used together with Taylor's hypothesis to specify the time-dependent inflow turbulence. This technique leads to very accurate spatially decaying turbulence immediately behind the inlet [45, 96].

The resolved (or useful) part of the computational domain ends at an arbitrary length. A sponge region is appended beyond this length to gently damp disturbances before reaching the outlet, thus minimizing spurious reflections towards the shock. In the sponge layer, source terms in the form of,

$$-\sigma_0 \left(\frac{x_1 - x_{sp}}{L_{sp}}\right)^2 \left(f - \overline{f}_{y,z}\right), \tag{3.5}$$

are added to the RHS of Eqs. (3.1) - (3.3), where f denotes the conserved variable in each equation. Here, σ_0 is the strength coefficient, x_{sp} is the location in the computational domain where the sponge begins, and L_{sp} is the length of the sponge. The target state, $\overline{f}_{y,z}$ for all quantities is taken as the post shock state obtained from laminar Rankine-Hugeniot (RH) shock relations, except for pressure. The target state for pressure is taken as the back pressure specified at the outlet, and is usually closer to the RH value for pressure.

The back pressure is specified such that the shock is stationary in the mean. The RH relations are only valid instantaneously (near the shock), but not in the far field region in a turbulent flow. Lele [51] used RDT to develop approximate shock relations for turbulent flow, and found that the density and pressure jumps decrease in the presence of turbulence for a given shock Mach number. Thus, the value of back pressure that yields a stationary shock for a given M and M t should be slightly lower than that predicted by the laminar RH relations. Larsson et al. [44], however, showed that there is one additional effect that counteracts this decrease in jump across the shock. The decay of turbulence kinetic energy in the downstream region implies a spatially increasing internal energy, which causes the outlet state to be different from the state immediately downstream of the shock. More specifically, it suggests that the back pressure value which yields a stationary shock is slightly higher than that given by the turbulent shock jump. These two effects make it nearly impossible to find the exact back pressure value that yields a stationary shock a priori. Multiple runs, possibly on a coarser grid, are required to identify the correct value of back pressure that keeps the shock nearly stationary.

Homogeneous isotropic turbulence database

Decaying isotropic turbulence fields were generated with using the gas properties, $R = (117.5, 13.25, 4.7, 1.85)$ and $\mu_{ref} = 0.002$ for the cases provided here in a precursor simulation. First, initial fields of turbulence are generated as per the steps given below,

1. generate a random velocity field with chosen peak energy wavenumber and a decaying velocity spectra in Fourier space. We consider the von Kármán spectrum [43] with peak energy wavenumber of $k_0 = 4$.

2. filter to avoid aliasing errors. When the product of two Fourier modes (say, $\hat{f} * \hat{g}$) with different wavenumber k_f and k_g is discretized, the resultant would have modes with wavenumbers of $k_f + k_g$, which are not resolved. On the discrete grid points, these modes will be identical to modes that lie within the range of resolved wavenumbers, leading to ‘aliasing’ errors [6].

3. normalize the velocity field such that the isotropic condition is satisfied. We now have a solenoidal isotropic turbulence.

4. solve a Poisson equation for pressure (see Eq. (3) in Ref. [68]) and ensure positive pressure by using limiter functions. The pressure field needs to be transformed to the physical space to check for positiveness.

5. solve a Poisson equation for time-derivative of pressure and use it in conjunction with the isentropic mass equation (see Eqs. (10) and (11) in Ref. [68]) to obtain the fluctuations of dilatation.

6. extract the irrotational velocity field from the fluctuations of dilatation and add them to the solenoidal velocity field. We now have the compressible velocity field in the wavenumber space.

7. transform to physical space by means of inverse Fourier transforms.

8. add the pressure fluctuations and the isentropic density fluctuations in physical space to the velocity field.

The initial field of compressible turbulence generated as mentioned above allows the flow to develop more naturally as the pressure field is associated with the vortical motions. The compressible NS equations are solved with these initial fields in a triply periodic box of length 2π to generate the isotropic turbulence fields. There are no forcing mechanisms added to the governing equations and the fields are allowed to decay temporally. The fluxes are solved using sixth-order central differencing scheme and the time integration is by the RK4 method. The boundary conditions are periodic in all directions. For the high M_t cases, eddy shocklets are found in the turbulence fields [72], which are captured using the fifth-order accurate WENO scheme.

Simulations are carried out for four different upstream Mach numbers (M = 1.23, 1.50, 2.50, 3.50) and the turbulent Mach number (M_t) for each of the upstream conditions is varied from 0.05 to 0.40 comprising a total of 16 cases. The turbulent Mach number is defined as $M_t = \sqrt{R_{kk}}/\overline{a}$, where R_{kk} represents twice the turbulence kinetic energy and $\overline{a}$ denotes the Reynolds averaged speed of sound. The Reynolds number based on Taylor length scale is $Re_\lambda = \overline{\rho}_1 \sqrt{R_{kk}/3}\lambda/\overline{\mu} \simeq 33$ for all the cases. Here λ is the Taylor length scale and $\overline{\mu}$ is the Reynolds averaged dynamic viscosity which is calculated using the power law with an exponent of 0.75. The mean density and temperature are initially set at a value of 1. As the flow develops, temperature rises to a higher value due to viscous dissipation and pressure is calculated using the equation of state. The specific gas constant R is varied in order to get the desired upstream turbulent Mach numbers.

Grid Convergence Study

A grid convergence test was performed by Sethuraman et al. [74] to ensure that all the turbulence length scales were well resolved. Here we summarize these results for completeness along with additional convergence results for turbulent heat flux. The computational grid is stretched in the streamwise direction to facilitate finer grid sizes near the shocks and relatively coarser sizes away from the shock. A uniform grid spacing is used for the transverse directions. Figure 3.2 shows the turbulent heat flux $\overline{u'T'}$ as a function of normalized streamwise distance $\kappa_0 x$. The solution for turbulent heat flux shows convergence with successive grid refinement in all three directions , proving the numerical accuracy. Due to the limitations in computational resource, the grid convergence test is only performed for M_t = 0.15 data sets and the same grid resolution is used for other M_t cases. The converged grid resolution for M_t = 0.15 cases are : 882×384^2 (M = 1.23), 1042×384^2 (M = 1.50), 1142×384^2 (M = 2.50), 1313×384^2 (M = 3.50). The maximum ratio between upstream Kolmogorov length scale (η_1) and numerical shock thickness (δ_n) is 1.30 which is sufficient to resolve the interaction between numerical shock and small-scale turbulent motion. Other details of grid resolution and turbulent length scales can be found in [74].

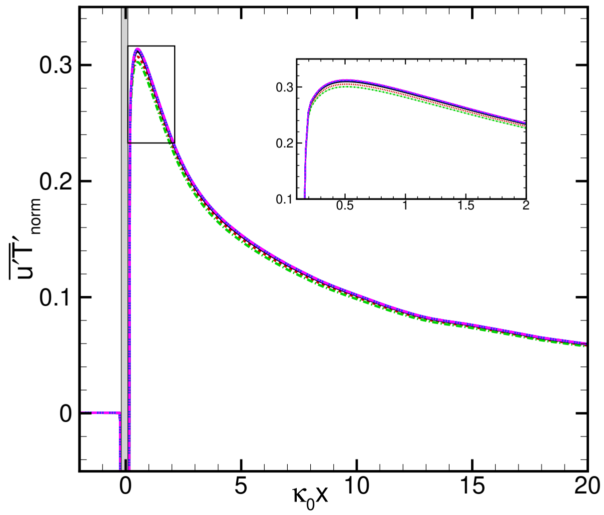

Figure 3.2: Grid convergence result for the case of M = 3.50, M_t = 0.15. Streamwise variation of turbulent heat flux is shown. The data is normalized by upstream mean velocity and downstream mean temperature. The turbulent heat flux correlation is additionally scaled by the upstream normalized turbulence kinetic energy ($0.5\overline{u'^2_{i,1}}/\overline{u}_1^2$). The streamwise distance is normalized by the peak energy wave number κ_0. The grids detail for the convergence study are 875×256^2 (Red dashed), 658×384^2 (Green dash-dotted), 1313×384^2 (Black solid), 1844×384^2 (Blue dotted), 1750×512^2 (Pink dash-double dotted).The region of unsteady shock movement is shown in grey. The inset figure shows the variation in the short region enclosed by the rectangle.

3.2 Shock-Boundary Layer Interaction

To compute a compressible turbulent flow, one needs to solve the Reynolds-averaged Navier-Stokes equations (RANS) for the mean flow along with the transport equations for the turbulence quantities. The standard k-ω model of Wilcox [92] and the shock unsteadiness modified k-ω models of Sinha et al. [78] and Veera and Sinha [85] are used for turbulence closure. The turbulence models do not include any compressibility corrections, as they are found to deteriorate model predictions in the undisturbed boundary layer upstream of the interaction [12, 22]. Compressibility corrections of the form of dilatational dissipation reduce the turbulent kinetic energy in the boundary layer, and thus decrease the skin friction coefficient compared to well-established correlations for zero pressure-gradient turbulent boundary layers. In this chapter we will discuss the simulation methodology to solve the governing equations.

3.2.1 Numerical method

The RANS equations govern the flow features of any fluid flow. The exact analytical solutions of these equations are difficult to obtain for complex flows such as shock-wave turbulent boundary-layer interactions. As an engineering approach, these partial differential equations are discretized into system of algebraic equations. Generally the Taylor series expansion is used to approximate the partial differential equations to system of algebraic linear equations. There are different discretization method available like finite difference, finite element and finite volume. In this section, we restrict ourselves to the finite volume technique only. We use Reynolds-Averaged Navier-Stokes (RANS) equations to solve the high-speed flows. Basically the terms in RANS equations can be split into three categories, the inviscid or convective terms, the viscous terms and the source terms.

The shock-boundary layer interaction flows includes different high gradient regions such as separation bubble, shock-waves, expansion waves, shear-layer and boundary-layer flow separation point and reattachment point and, all of these physical features in the flow field has to be captured accurately using appropriate CFD techniques. For the steady-state solution of high speed flows the hyperbolic and elliptic nature of the equations dominate the flow. For high speed steady flows the convective terms dominate in the inviscid regions and the flow is hyperbolic in nature in space. For boundary-layer flows and separated flows the diffusive terms dominate. In a separation bubble the flow is diffusive in nature hence the information can flow in all the directions and the flow posses elliptic nature in this confined region. The central differencing scheme can be used to discretize the viscous terms.

A finite volume formulation is used to discretize the governing mean flow equations fully coupled with turbulence model equations. The inviscid fluxes are solved using a modified, low-dissipation form of the Steger-Warming flux splitting method [52]. This method reduces the numerical dissipation which is very useful for high speed flows with strong shock waves and viscous-inviscid interactions with boundary layers. As a result, very thin and well defined shock waves are captured over minimal grid cells. The discretization method is second-order accurate in space. The details of the formulation can be found in Ref. [77]. The viscous fluxes and the turbulent source terms are calculated using second-order accurate central difference method. The implicit Data Parallel Line Relaxation (DPLR) method of Wright et al. [93] is used to integrate the equations in time to reach a steady-state solution.

In the following, we briefly discuss about the finite volume formulation and flux-vector splitting scheme of Steger-Warming [83] and modified Steger-Warming [52], for solving RANS equations using shock-unsteadiness modified k-ω model for perfect gas.

Conservation form

The in-house CFD code is used to solve the test case. The in-house code is capable of parallel computing and it has been well validated for several high speed applications [60, 61, 79]. We use the two-dimensional RANS equations along with shock-unsteadiness modified k-ω model to calculate the eddy viscosity. we solve for one continuity, two momentum, one energy, one turbulent kinetic energy, and one dissipation of turbulent kinetic energy equations. A total of six equations are solved simultaneously to obtain six conservative variables $\overline{\rho}$, $\overline{\rho}\widetilde{u}$, $\overline{\rho}\widetilde{v}$, $\overline{\rho}\widetilde{E}$, $\overline{\rho}k$, $\overline{\rho}\omega$. Here $\widetilde{E}$ is the total mean flow energy. From these conservative variables, the six primitive mean flow quantities are calculated as, streamwise and wall normal velocities $\widetilde{u}, \widetilde{v}$ respectively, density $\overline{\rho}$, temperature $\widetilde{T}$, TKE k and the dissipation of turbulent kinetic energy ω. The mean pressure $\overline{p}$ is obtained from perfect gas equation. The two-dimensional RANS system of equations can be written in conservation form as,

$$\frac{\partial U}{\partial t} + \nabla.\left(\vec{F} + \vec{G}\right) = Q, \tag{3.6}$$

where U is the set of conservative variable, $\vec{F}$ is the flux vector in streamwise direction, $\vec{G}$ is the flux vector in flow normal direction and Q is the source term. The total fluxes are split into inviscid and viscous part. The subscripts I and V represent the inviscid and viscous terms. These equations are written in Cartesian form as,

$$\frac{\partial U}{\partial t} + \nabla .\, (F + G) = Q, \tag{3.7}$$

where

$$F = F_I - F_V; \qquad G = G_I - G_V \tag{3.8}$$

$$U = \left[\; \overline{\rho} \quad \overline{\rho}\widetilde{u} \quad \overline{\rho}\widetilde{v} \quad \overline{\rho}\widetilde{E} \quad \overline{\rho}k \quad \overline{\rho}\omega \; \right]^T, \tag{3.9}$$

where superscript T stands for the transpose of the matrix.

$$F_I = \begin{bmatrix} \overline{\rho}\widetilde{u} \\ \overline{\rho}\widetilde{u}^2 + \overline{p} + \frac{2}{3}\overline{\rho}k \\ \overline{\rho}\widetilde{u}\widetilde{v} \\ \left(\overline{\rho}\widetilde{E} + \overline{p} + \frac{2}{3}\overline{\rho}k\right)\widetilde{u} \\ \overline{\rho}\widetilde{u}k \\ \overline{\rho}\widetilde{u}\omega \end{bmatrix}; \qquad G_I = \begin{bmatrix} \overline{\rho}\widetilde{v} \\ \overline{\rho}\widetilde{u}\widetilde{v} \\ \overline{\rho}\widetilde{v}^2 + \overline{p} + \frac{2}{3}\overline{\rho}k \\ \left(\overline{\rho}\widetilde{E} + \overline{p} + \frac{2}{3}\overline{\rho}k\right)\widetilde{v} \\ \overline{\rho}\widetilde{v}k \\ \overline{\rho}\widetilde{v}\omega \end{bmatrix} \tag{3.10}$$

$$F_V = \begin{bmatrix} 0 \\ \overline{t_{xx}} + \tau_{xx} \\ \overline{t_{xy}} + \tau_{xy} \\ \left(\overline{t_{xx}} + \tau_{xx}\right)\widetilde{u} + \left(\overline{t_{xy}} + \tau_{xy}\right)\widetilde{v} + (\kappa + \kappa_T)\,\frac{\partial \widetilde{T}}{\partial x} + \left(\mu + \frac{\mu_T}{\sigma_k}\right)\frac{\partial k}{\partial x} \\ \left(\mu + \frac{\mu_T}{\sigma_k}\right)\frac{\partial k}{\partial x} \\ \left(\mu + \frac{\mu_T}{\sigma}\right)\frac{\partial \omega}{\partial x} \end{bmatrix} \tag{3.11}$$

$$G_V = \begin{bmatrix} 0 \\ \overline{t_{xy}} + \tau_{xy} \\ \overline{t_{yy}} + \tau_{yy} \\ \left(\overline{t_{xy}} + \tau_{xy}\right)\widetilde{u} + \left(\overline{t_{yy}} + \tau_{yy}\right)\widetilde{v} + (\kappa + \kappa_T)\,\frac{\partial \widetilde{T}}{\partial y} + \left(\mu + \frac{\mu_T}{\sigma_k}\right)\frac{\partial k}{\partial y} \\ \left(\mu + \frac{\mu_T}{\sigma_k}\right)\frac{\partial k}{\partial y} \\ \left(\mu + \frac{\mu_T}{\sigma}\right)\frac{\partial \omega}{\partial y} \end{bmatrix} \tag{3.12}$$

$$Q = \left[\; 0 \quad 0 \quad 0 \quad 0 \quad (P_k - \beta^* \overline{\rho} k \omega) \quad \left(\alpha \frac{\omega}{k} P_k - \beta \overline{\rho} \omega^2\right) \; \right]^T \tag{3.13}$$

Here $\overline{\rho}$ is the mean density of the fluid, $\widetilde{u}$, $\widetilde{v}$ are the mean velocities in streamwise and wall normal direction, $\overline{p}$ is the mean pressure, $\overline{t_{xx}}$, $\overline{t_{xy}}$, $\overline{t_{yy}}$ are the mean viscous stresses acting on fluid particles, τ_{xx}, τ_{xy}, τ_{yy} are the Reynolds stresses, $\widetilde{E}$ is the mean total energy of the flow, P_k represents the production term of the turbulent kinetic energy as per shock-unsteadiness modification. The conservation equation 3.6 is integrated over the control surface area (CS) of control volume (CV) to give:

$$\frac{\partial}{\partial t}\iiint\limits_{CV} U\,dV + \iint\limits_{CS}\left[\left(\vec{F_I}+\vec{G_I}\right)+\left(\vec{F_V}+\vec{G_V}\right)\right].(\hat{n}dS) = Q \tag{3.14}$$

$$\frac{\partial U}{\partial t} = -\frac{1}{V_{i,j}}\left[\vec{F}_{i+1/2,j}.\vec{S}_{i+1/2,j}+\vec{F}_{i-1/2,j}.\vec{S}_{i-1/2,j}+\vec{G}_{i,j+1/2}.\vec{S}_{i,j+1/2}+\vec{G}_{i,j-1/2}.\vec{S}_{i,j-1/2}\right]+Q, \tag{3.15}$$

where

$$\begin{aligned}\vec{S}_{i+1/2,j} &= \left(y_{i+1,j+1}-y_{i+1,j}\right)\hat{i}-\left(x_{i+1,j+1}-x_{i+1,j}\right)\hat{j}\\ \vec{S}_{i-1/2,j} &= -\left(y_{i,j+1}-y_{i,j}\right)\hat{i}+\left(x_{i,j+1}-x_{i,j}\right)\hat{j},\end{aligned} \tag{3.16}$$

and

$$\begin{aligned}V_{i,j} = [|&\left(x_{i,j}-x_{i+1,j}\right)y_{i+1,j+1}+\left(x_{i+1,j}-x_{i+1,j+1}\right)y_{i,j}+\left(x_{i+1,j}-x_{i,j}\right)y_{i+1,j}|\\ +|&\left(x_{i,j}-x_{i+1,j+1}\right)y_{i,j+1}+\left(x_{i+1,j+1}-x_{i,j+1}\right)y_{i,j}+\left(x_{i,j+1}-x_{i,j}\right)y_{i+1,j+1}|]\end{aligned} \tag{3.17}$$

Here $\hat{n}$ is unit normal vector to surface area dS as shown in Fig. 3.3 and $\vec{S}_{i+1/2,j}$, $\vec{S}_{i-1/2,j}$ are the the surface area vectors and $\hat{i}$, $\hat{j}$ are unit vectors in i and j direction respectively. x and y are the coordinates of the grid points and $V_{i,j}$ is the control volume. The calculation of $\vec{S}_{i,j-1/2}$ is explained in Fig. 3.3. The vector $\vec{DC} = \left(x_{i+1,j}-x_{i,j}\right)\hat{i}+\left(y_{i,j+1}-y_{i,j}\right)\hat{j}$. Hence the normal vector is evaluated as $\vec{S}_{i,j-1/2} = \left(y_{i,j+1}-y_{i,j}\right)\hat{i}-\left(x_{i+1,j}-x_{i,j}\right)\hat{j}$. The normal vector $\vec{S}_{i,j+1/2}$ is calculated in a similar way.

Steger-Warming method

The Steger-Warming method is used for high speed inviscid flows to capture shock waves by taking the advantage of the hyperbolic nature of the Euler equations. The basic requirement for hyperbolic flow is that the eigen values should be real, distinct and positive. The upwind discretization method is used to solve the governing equations. In an upwind scheme spatial differencing is done on the mesh points on the side from which the information or wind flows. Upwind schemes use information of the local wave propagation explicitly. The eigen values provide the direction of information in the flow. To demonstrate the Steger-Warming method the case of one dimensional Euler equations are taken

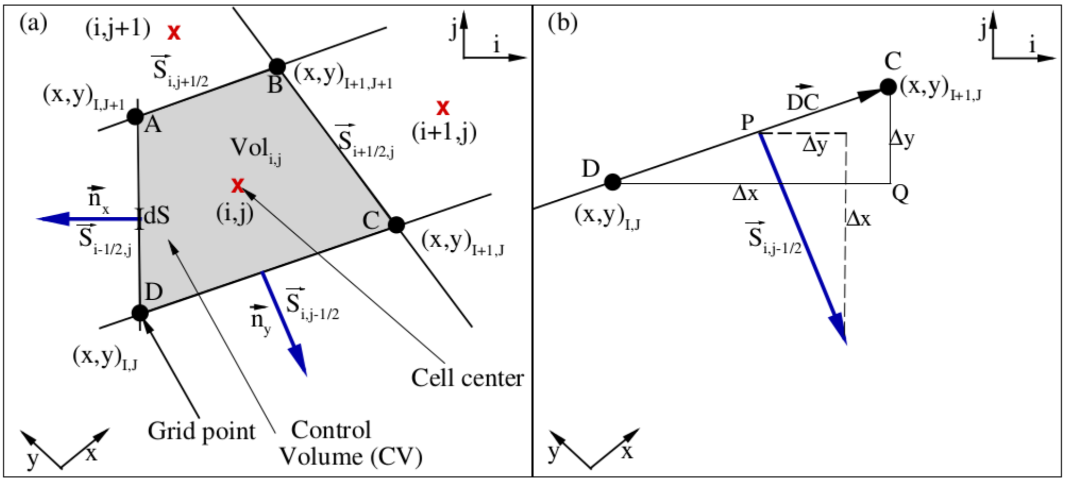

Figure 3.3: (a) Two-dimensional control volume used in finite volume formulation, where the grid points are represented by black solid circles with capital indices of I and J and cell centers are shown by crosses represented by small indices of i and j and (b) Calculation of normal surface vector $\vec{S}_{i,j-1/2}$. [28]

for simplicity. The same methodology can be extended to the two- and three-dimensional flows.

$$U = \begin{bmatrix} \rho & \rho u & E \end{bmatrix}^T = \begin{bmatrix} U_1 & U_2 & U_3 \end{bmatrix}^T, \tag{3.18}$$

$$F_I = \begin{bmatrix} \rho u & \left(\rho u^2 + p\right) & (Eu + pu) \end{bmatrix}^T = \begin{bmatrix} F_1 & F_2 & F_3 \end{bmatrix}^T, \tag{3.19}$$

where $E = \rho u + \frac{1}{2}\rho u^2$ is the total energy and $e = c_v T$ is the internal energy. The flux vector is function of the conservative variable vector and is evaluated as,

$$[F] = [A]\,[U] \tag{3.20}$$

where A is the Jacobian matrix and U is the conserved variables vector. The Jacobian matrix, A is calculated by taking the partial derivative of the flux-vector with respect to the vector of conserved variables.

$$A = \begin{bmatrix} \frac{\partial F_1}{\partial U_1} & \frac{\partial F_1}{\partial U_2} & \frac{\partial F_1}{\partial U_3} \\ \frac{\partial F_2}{\partial U_1} & \frac{\partial F_2}{\partial U_2} & \frac{\partial F_2}{\partial U_3} \\ \frac{\partial F_3}{\partial U_1} & \frac{\partial F_3}{\partial U_2} & \frac{\partial F_3}{\partial U_3} \end{bmatrix} = \begin{bmatrix} 0 & 1 & 0 \\ (\gamma-3)\,u^2/2 & (3-\gamma)\,u & (\gamma-1) \\ (\gamma-1)\,u^3 - \gamma e u/\rho & \gamma e/\rho - 3\,(\gamma-1)\,u^2/2 & \gamma u \end{bmatrix} \tag{3.21}$$

With this Jacobian matrix we write the characteristic equation to find the eigen values.

$$det\,[A - \lambda I] = 0 \tag{3.22}$$

where I is the identity matrix. The three eigen values of the above matrix are

$$\Lambda = \begin{bmatrix} u & 0 & 0 \\ 0 & u + a & 0 \\ 0 & 0 & u - a \end{bmatrix} \tag{3.23}$$

Here u is speed of the flow and a corresponds to the speed of the sound. The corresponding left eigen vector matrix and right eigen vector matrix is evaluated as T and T^{-}. For each eigen value the corresponding eigen vectors are calculated as,

$$[A]\left[r_1^1 r_1^2 r_1^3\right] = \lambda_1 \left[r_1^1 r_1^2 r_1^3\right]^T \tag{3.24}$$

$$[A]\left[r_2^1 r_2^2 r_2^3\right] = \lambda_2 \left[r_2^1 r_2^2 r_2^3\right]^T \tag{3.25}$$

$$[A]\left[r_3^1 r_3^2 r_3^3\right] = \lambda_3 \left[r_3^1 r_3^2 r_3^3\right]^T \tag{3.26}$$

Each of the these single column 1×3 matrix of eigen vectors are arranged in three columns of a 3×3 square matrix to form a right eigen vector matrix T as given by Eqs. 3.27.

$$[T] = \left[|r_k^p||r_k^p||r_k^p|\right] \tag{3.27}$$

Here r is a 1×3 single column eigen vector with $p = (1, 2, 3)$ and $k = (1, 2, 3)$. $|r_k^p|$ corresponds to the right eigen vector single column matrix formed by calculating the three eigen vectors in Eqs. 3.26, for corresponding eigen values. The left eigen vector matrix is calculated by taking the inverse matrix of the right vector matrix. Using T and T^{-} the negative and positive Jacobian matrices are calculated. The Jacobian is splitted into positive and negative parts by splitting the eigen values into positive and negative parts. The diagonal matrix Λ_+ contains only positive eigen values and diagonal matrix Λ_-

has only negative eigen values.

$$A = A_+ + A_- \tag{3.28}$$

$$\lambda_k = \lambda_{k+} + \lambda_{k-} \tag{3.29}$$

$$\lambda_{k+} = \frac{\lambda_k + |\lambda_k|}{2} \tag{3.30}$$

$$\lambda_{k-} = \frac{\lambda_k - |\lambda_k|}{2} \tag{3.31}$$

$$\Lambda = \Lambda_+ + \Lambda_- \tag{3.32}$$

$$\Lambda_+ = diag\left(\frac{\lambda_k + |\lambda_k|}{2}, \frac{\lambda_k + |\lambda_k|}{2}, \frac{\lambda_k + |\lambda_k|}{2}\right) \tag{3.33}$$

$$\Lambda_- = diag\left(\frac{\lambda_k - |\lambda_k|}{2}, \frac{\lambda_k - |\lambda_k|}{2}, \frac{\lambda_k - |\lambda_k|}{2}\right) \tag{3.34}$$

$$A_+ = T\Lambda_+T^-; \quad A_- = T\Lambda_-T^- \tag{3.35}$$

The fluxes are then split according to the sign of the Jacobians as positive and negative parts as below.

$$F = F_+ + F_- \tag{3.36}$$

$$F_+ = F_+U \quad F_- = F_-U \tag{3.37}$$

The above fluxes are evaluated for subsonic flows. For supersonic flows the information flows in downstream direction and there is no information flows is upstream direction. Hence for supersonic flows $F_+ = F$ and $F_- = 0$. The information in a flow can come from upstream or downstream direction and depending on it, the discretization is done to the fluxes. In a control volume these fluxes are calculated at the cell faces with the help of the Jacobian and the values of conservative variables are taken from the cell center. The first order fluxes are given as

$$F_{+_i} = A_{+i}U_i \tag{3.38}$$

$$F_{-_{i+1}} = A_{-_{i+1}}U_{i+1} \tag{3.39}$$

For hyperbolic nature of the Euler equations, the eigen values are real and distinct. In the Steger-Warming method, the modification is made to the eigen values when they become either zero or one. This can happen when the flow becomes sonic for local Mach number = 1 or stagnant for $M = 0$ in some regions.

Modified Steger-Warming method

The Steger-Warming method when applied to the viscous flows results in large numerical dissipation [52] across the boundary-layer. Also it creates fictitious pressure gradient which causes the unrealistic convection within the layer. It has similar problems across free shear-layers. MacCormack and Candler [52] modified the Steger-Warming method to reduce the excessive numerical mixing in the boundary-layer and free shear-layer flows. In the Steger-Warming method the evaluation of Jacobians at the cell centers resulted in excessive numerical dissipation in the boundary-layer. In the modified Steger-Warming method the Jacobians are modified and are calculated at cell-interfaces (see Fig. 3.4) and from these values the first order fluxes were calculated as given by Eq. 3.40

$$\begin{aligned}
F_{+_i} &= A_{+_{i+1/2}} U_i \\
F_{-i+1} &= A_{-_{i+1/2}} U_{i+1} \\
A_{\pm_{i+1/2}} &= A_{\pm}\left[\frac{1}{2}\left(U_i + U_{i+1}\right)\right]
\end{aligned} \tag{3.40}$$

The explicit time integration is carried out by

$$U_i^{n+1} = U_i^n - \frac{\Delta t}{\Delta x}\left[\left(F_{+_i} + F_{-i+1}\right) - \left(F_{+_{i-1}} + F_{-i}\right)\right]^n, \tag{3.41}$$

where n is the current time step and n+1 is the next time step. The first-order upwind schemes are less accurate as they contain less number of points in a stencil. They are more dissipative and do not give any oscillations across the high gradient regions such as shock waves. The second order central differencing schemes are more accurate than first order upwind schemes and are less dissipative, but they are unstable across the shock waves. The second order upwind schemes possess less numerical dissipation compared to the upwind first order schemes and are more accurate because of more points in the cell face. By increasing the number of points minute details of flow physics can be accurately captured by the numerical method.

Second order Steger-Warming method

$$\begin{aligned}
F_{+_i} &= A_{+_i} U^L_{i+1/2} \\
F_{-_{i+1}} &= A_{-_{i+1}} U^R_{i+1/2}
\end{aligned} \tag{3.42}$$

$$\begin{aligned}
U^L_{i+1/2} &= \frac{3}{2} U_i - \frac{1}{2} U_{i-1} \\
U^R_{i+1/2} &= \frac{3}{2} U_{i+1} - \frac{1}{2} U_{i+2}
\end{aligned} \tag{3.43}$$

Second order modified Steger-Warming method [52]

$$\begin{aligned}
F_{+_i} &= A_{+_{i+1/2}} U^L_{i+1/2} \\
F_{-_{i+1}} &= A_{-_{i+1/2}} U^R_{i+1/2}
\end{aligned} \tag{3.44}$$

$$
\begin{aligned}
U^L_{i+1/2} &= \frac{3}{2}U_i - \frac{1}{2}U_{i-1} \\
U^R_{i+1/2} &= \frac{3}{2}U_{i+1} - \frac{1}{2}U_{i+2}
\end{aligned}
\tag{3.45}
$$

Here U_L and U_R correspond to the left and right states. Fig. 3.4 gives the physical interpretation for evaluating the fluxes using second order scheme. The fluxes are extrapolated to the interfaces defining the flux equal to the numerical scheme. Fig. 3.4 shows that at cell inter- face i + 1/2 the flux is evaluated as summation of the contribution from first order scheme and contribution from second order from left and right states. The second order

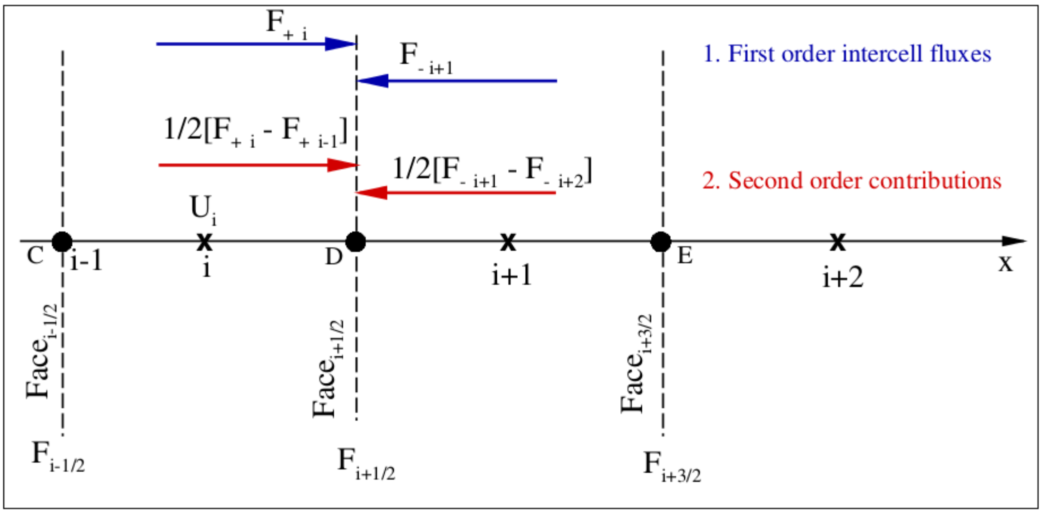

Figure 3.4: Physical interpretation for evaluation of fluxes for the second-order method. [28]

schemes produce non-physical oscillations across high gradients such as shock waves. To avoid these oscillations they are converted to first order schemes across the shock waves. The flux limiters are used to avoid high oscillations or wiggles across the shocks. The second order modified Steger-Warming method is converted to first order method by applying the pressure limiter . Flux limiters are used to limit the spatial derivatives to physically realistic values. They come in to operation when sharp gradients like shocks occur. For smooth gradient regions these flux limiters are not active. The shock-wave regions are detected if the pressure jump is greater than 50% across grid points. The modified Steger-Warming method [52] gives less dissipation in the boundary-layers and result in oscillations in the high gradient regions such as shock waves. Whereas the standard Steger-Warming gives more numerical dissipation in the boundary-layers and is stable across the shock-waves. To take the advantage of both the methods, a hybrid scheme is used to evaluate the fluxes and the pressure limiter is used to switch from modified Steger-Warming scheme to the standard Steger-Warming scheme across the shock-waves. When the pressure gradient is more than 50% across the shock waves the scheme is reverted to Steger-Warming method and when the pressure gradient is less the scheme is reverted to modified Steger-Warming method in the boundary-layer regions. The pressure jump across high gradients is detected with the use of pressure limiter.

Boundary Conditions

Dummy cells are used to impose the boundary conditions. They are constructed in such a way that the average of the value at dummy cell and first interior cell gives the value of the variables at the boundaries. Dummy cells are assigned appropriate values to obtain the required flow condition at the boundaries. We refer to the dummy cell as the 1^{st} cell and the interior cell adjacent to the boundary as 2^{nd} cell.

The viscous boundary condition (no-slip condition) needs the velocity at wall to be zero. This is done by setting velocity value negative of the 2^{nd} cell. For isothermal boundary condition, we need a constant temperature at the wall. This is done by extrapolating the value at the 1^{st} cell from the 2^{nd} cell, such that the wall will have a specified temperature. For inviscid boundary condition, we need to calculate the wall normal velocity component at the 2^{nd} cell. Then we put the value at the dummy cell in such a way that this wall normal component becomes zero. The symmetry boundary condition is similar with an added clause that the gradients of all the variables should be zero. The extrapolation boundary condition at exit plane physically means that the mass flux should be balanced and the diffusion fluxes for all the variables should be zero. This means that the dummy cells do not affect the interior in this case. For the inlet boundary, the dummy cell values are always set to freestream values.

Boundary condition	**Physical condition**	**Implementation in code**
No-slip condition	$V_{wall} = 0$	$V_1 = -V_2$
Isothermal condition	T_{wall} =constant	$T_1 = 2T_{wall} - T_2$
Slip condition	$\vec{V}.\hat{n} = 0$	$V_1 = V_2 - 2\left(\vec{V_2}.\hat{n}\right)$
Symmetry condition	$dU/d\eta = 0$ & $\vec{V}.\hat{n} = 0$	$V_1 = V_2 - 2\left(\vec{V_2}.\hat{n}\right)$
Extrapolation	$\dot{m}_1 = \dot{m}_2$	$U_1 = U_2$

Here, U is the matrix of conserved variables. η is the wall normal direction. V is velocity in the wall normal direction.

3.3 Summary

A brief description of the DNS methodology is provided in this chapter. Temporally decaying homogeneous isotropic turbulence databases are generated separately and blended together to form a sufficiently long database for statistical convergence. The discretized governing equations are solved using a solution adaptive finite difference method with fifth order accurate WENO scheme in the shock region and sixth order accurate central differencing scheme with Roe flux splitting form for the rest of the domain. Time advancement is done by explicit fourth order Runge-Kutta scheme. Non-reflecting boundary conditions are used at the outflow with periodic boundary conditions on the shock-parallel directions. Grid-convergence study shows that the computational domain with 384 grid points in each of the transverse directions to be sufficient for the statistics of interest. Reynolds-averaged Navier stokes equations are used for the shock-boundary interaction. A finite volume based numerical method is described to discretise the governing equations of RANS framework. It uses modified Steger-Warming flux splitting approach for computing the inviscid fluxes, and second order central differencing for the viscous fluxes and turbulent source terms.

Chapter 4

Direct Numerical Simulation of Shock-Turbulence Interaction

The study of a turbulent flow interacting with a shock wave is an active area of research, where various methods and techniques are employed to provide a description of the specific problem under consideration than the complete physics of the problem itself. The case of homogeneous isotropic turbulence interacting with a normal shock wave is considered in this work. This configuration albeit being simple, is still not fully understood and has been studied by many using theoretical [20, 26, 32, 49, 53, 76], numerical [11, 14, 15, 44, 46, 71], and experimental methods [4, 30]. The interaction of isotropic turbulence with a normal shock wave is the most fundamental problem to study the effect of shock wave on the turbulence and vice-versa. This model problem is often referred as canonical shock-turbulence interaction because of its simplicity and complexities such mean shear, streamline curvature, real gas effects, magnetic effects, etc. have been removed. In earlier studies, computations for this canonical problem were done for statistical quantities related to velocity fluctuations such as shock-normal Reynolds stresses, vorticity variances and turbulent kinetic energy (TKE). Quadros et al. [67] studied the post-shock turbulent energy flux correlation using linear interaction analysis (LIA) and direct numerical simulation (DNS) data up to a turbulence intensity of $M_t \leq 0.2$. They showed that the turbulent energy flux correlation is governed by the pressure-energy and pressure-dilatation source terms, which are dominated by the acoustic mode and can be reproduced well by LIA. [11] study the amplification of turbulence across normal shock wave at high turbulence intensities (M_t up to 0.54). They study the effect of high turbulent Mach number on the mean flow quantities, like pressure, density. The amplification of mean flow variables are found to be a function of turbulent Mach number. Larsson et al. [44] also studied few cases at high M_t values but both of their anlysis are limited to low supersonic Mach numbers ($M \leq 1.5$) for high turbulence intensity. What happened to turbulence at high Mach number and high turbulence intensities is still an open question in the literature. Recently Sethuraman et al. [74] studied various thermodynamic variances like temperature, pressure, density and entropy for high turbulence intensities ($M_t \leq 0.4$). They systematically tuned the upstream turbulent Mach number M_t, and studied the changes in the downstream thermodynamic variances relative to the incoming turbulence. But the analysis of turbulent heat flux at high turbulent Mach number is not available in the current literature. The analysis of turbulent heat flux is presented in this chapter with a description of the data extraction methodology at the beginning.

4.1 Instantaneous shock statistics

Conventional averaging procedure is usually employed over the homogeneous shock parallel directions for a number of flow realizations. This averaging procedure gives a mean shock thickness which encompasses the region of shock wrinkling and oscillations. Statistics computed at a fixed x location inside the mean shock therefore includes the effect of the jump in mean flow quantities across an unsteady shock wave. This gives very large values of the fluctuating quantities, as documented by [44] and [74]. It is therefore difficult to isolate the turbulence fluctuations in the close vicinity of the interaction. On the other hand, turbulence statistics collected with respect to the instantaneous shock position, can be a useful tool to isolate and analyse the physical effects of shock-turbulence interaction. As we will see, this gives a direct comparison with theoretical approaches based on shock discontinuity on either side of the instantaneous shock.

We use the threshold method proposed by [74] to compute turbulence statistics across an instantaneous shock wave. The shock location is identified based on the value of the instantaneous dilatation. A threshold value of 1% of the most negative dilatation is employed to identify the upstream $x_{s,1}$ and downstream $x_{s,2}$ extent of the instantaneous shock wave. Figure 4.1 shows the graphical representation of the above method for the case of $M = 3.50$ and $M_t = 0.15$. The data corresponds to a single x-line (at constant y, z and t), and the flow variables are interpolated at the points $x_{s,1}$ and $x_{s,2}$. The process is repeated for each grid line passing through the shock, and the flow variables obtained at $x_{s,1}$ and $x_{s,2}$ are averaged over all y, z and t to arrive at the turbulence statistics conditioned to the instantaneous shock. The upstream and downstream quantities are denoted by subscript 1 and 2 respectively, and they do not correspond to fixed x location. This is unlike conventional Reynolds averaging described by [11], where the shock upstream and downstream locations are identified in terms of the local minima and maxima in the Reynolds

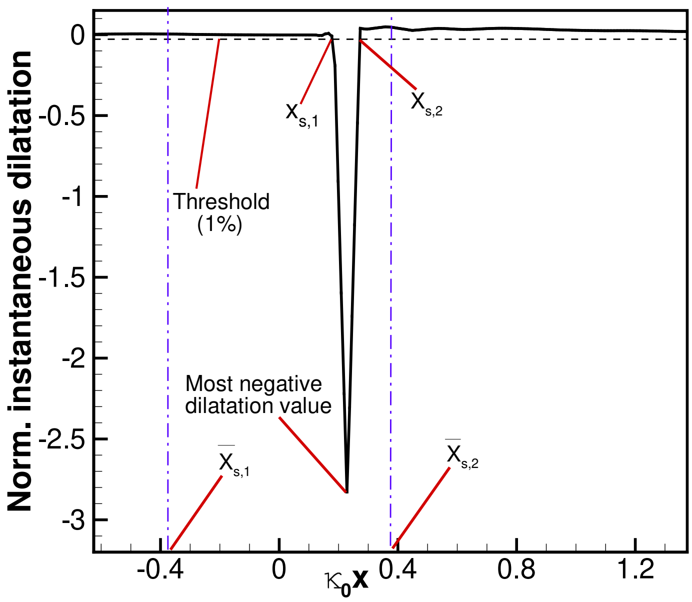

Figure 4.1: Identification of instantaneous shock locations using instantaneous dilatation. The data corresponds to a single x-line (at constant y, z and t) for the case of $M = 3.50$ and $M_t = 0.15$. Dilatation is normalized by $\kappa_0 \overline{u}_1$ and the streamwise distance is normalized by κ_0. The extent of the mean shock is identified by the dash-dotted lines and are given by $\overline{x}_{s,1}$ and $\overline{x}_{s,2}$ as upstream and downstream values respectively. Here the mean shock is centered at $\kappa_0 x = 0$.

stresses. The instantaneous shock thickness obtained from the threshold method is much smaller than the mean shock thickness computed using conventional Reynolds averaging (by up to 10 times).

The shock wave undergoes unsteady motion in response to the fluctuations in a turbulent flow. The deviation of the shock from its mean position is taken as $\xi(y, z, t)$, such that the temporal derivative ξ_t represents the instantaneous shock speed in the streamwise direction, see Fig. 4.2. We use the conservation of mass across the oscillating normal shock wave in the frame of reference of shock to compute the instantaneous shock speed ξ_t

$$(\overline{\rho}_1 + \rho_1') (\overline{u}_1 + u_1' - \xi_t) = (\overline{\rho}_2 + \rho_2') (\overline{u}_2 + u_2' - \xi_t) . \tag{4.1}$$

Here ρ and u are the density and streamwise velocity of the flow respectively. The above equation after some mathematical simplification (neglecting the higher order fluctuations with respect to first order fluctuation and mean quantities) yields

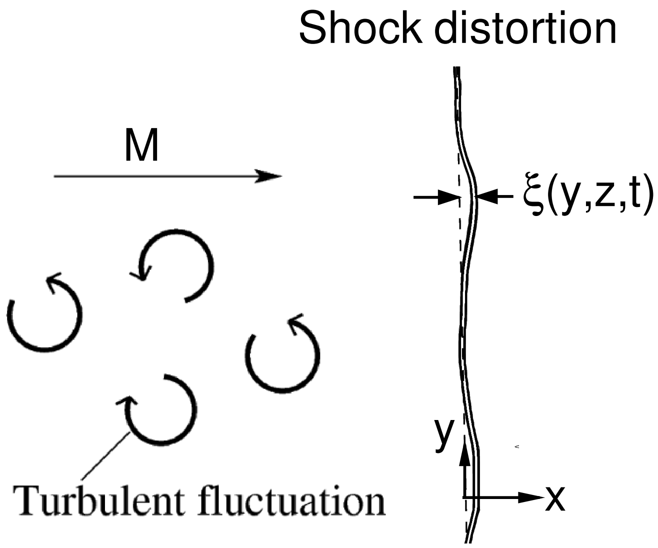

Figure 4.2: Schematic of a distorted shock while interacting with upstream turbulent fluctuations and the dashed line represents the mean shock location.

$$\xi_t = \frac{1}{r-1}\left[r u_2' - u_1' + \overline{u}_1 \left(\frac{\rho_2'}{\overline{\rho}_2} - \frac{\rho_1'}{\overline{\rho}_1} \right) \right], \tag{4.2}$$

where r is the mean density ratio across the shock wave. The corresponding root mean square (rms) value of the shock speed is

$$\begin{aligned} \xi_t^{rms} \quad = \quad & \frac{1}{r-1}\left[r^2\overline{u_2'^2} + \overline{u_1'^2} - 2r\overline{u_1'u_2'} + \overline{u}_1^2 \left(\frac{\overline{\rho_2'^2}}{\overline{\rho}_2^2} + \frac{\overline{\rho_1'^2}}{\overline{\rho}_1^2} - 2\frac{\overline{\rho_1'\rho_2'}}{\overline{\rho}_1\overline{\rho}_2} \right) \right. \\ & \left. + 2\overline{u}_1 \left(\frac{\overline{\rho_2'u_2'}}{\overline{\rho}_1} - \frac{r}{\overline{\rho}_1}\overline{\rho_1'u_2'} - \frac{\overline{\rho_2'u_1'}}{\overline{\rho}_2} + \frac{\overline{\rho_1'u_1'}}{\overline{\rho}_1} \right) \right]^{0.5}. \end{aligned} \tag{4.3}$$

We compute the upstream and downstream correlations on the right hand side across the instantaneous shock wave using the threshold method. The rms shock speed thus obtained is listed for all the M and M_t cases in table 4.1. Note that the shock speed, normalised by upstream mean velocity, decreases with increase in Mach number, indicating that stronger shocks are more stable to incoming turbulent fluctuations. For a given Mach number, $\xi_t/\overline{u}_1$ increases with M_t, as expected. Overall, the ratio of the shock speed to the upstream rms velocity is found to be order one for all the cases considered in this work (see table 4.1).

Table 4.1: Variation of *rms* shock speed computed from direct numerical simulation data.

M	M_t	$\frac{\xi_t^{rms}}{\overline{u}_1}$	$\frac{\xi_t^{rms}}{u_1^{rms}}$
1.23	0.05	0.0100	0.43
1.50	0.05	0.0093	0.49
2.50	0.05	0.0087	0.76
3.50	0.05	0.0080	0.96
1.23	0.15	0.022	0.32
1.50	0.15	0.020	0.34
2.50	0.15	0.015	0.42
3.50	0.15	0.012	0.47
1.23	0.25	0.030	0.26
1.50	0.25	0.027	0.28
2.50	0.25	0.021	0.36
3.50	0.25	0.016	0.38
1.23	0.40	0.036	0.19
1.50	0.40	0.032	0.21
2.50	0.40	0.024	0.26
3.50	0.40	0.019	0.29

We next use the threshold method to compute the following upstream and downstream correlations and these will be useful for next section 4.2.

$$\begin{aligned}
\overline{u_1'\xi_t} &= \frac{1}{r-1}\left[r\overline{u_1'u_2'} - \overline{u_1'^2} + \overline{u}_1\left(\frac{\overline{u_1'\rho_2'}}{\overline{\rho}_2} - \frac{\overline{u_1'\rho_1'}}{\overline{\rho}_1}\right)\right] \\
\overline{T_1'\xi_t} &= \frac{1}{r-1}\left[r\overline{T_1'u_2'} - \overline{T_1'u_1'} + \overline{u}_1\left(\frac{\overline{T_1'\rho_2'}}{\overline{\rho}_2} - \frac{\overline{T_1'\rho_1'}}{\overline{\rho}_!}\right)\right] \\
\overline{u_2'\xi_t} &= \frac{1}{r-1}\left[r\overline{u_2'^2} - \overline{u_1'u_2'} + \overline{u}_1\left(\frac{\overline{u_2'\rho_2'}}{\overline{\rho}_2} - \frac{\overline{u_2'\rho_1'}}{\overline{\rho}_1}\right)\right] \\
\overline{T_2'\xi_t} &= \frac{1}{r-1}\left[r\overline{T_2'u_2'} - \overline{T_2'u_1'} + \overline{u}_1\left(\frac{\overline{T_2'\rho_2'}}{\overline{\rho}_2} - \frac{\overline{T_2'\rho_1'}}{\overline{\rho}_1}\right)\right]
\end{aligned} \tag{4.4}$$

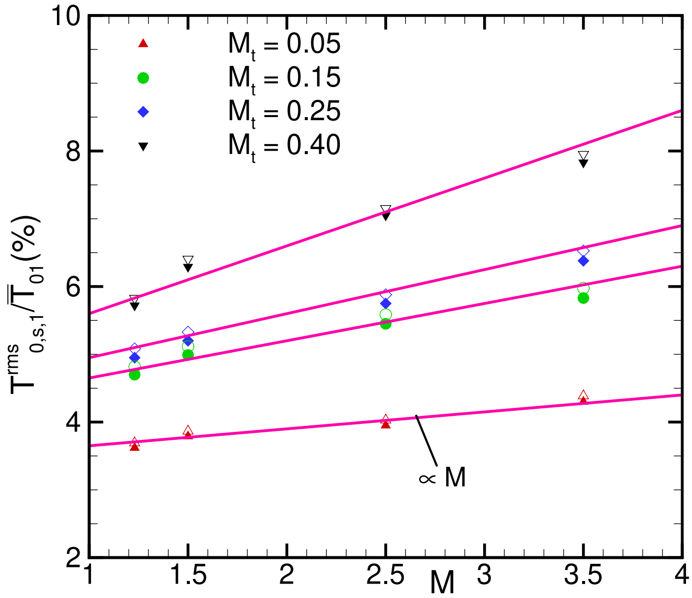

Figure 4.3: Variation of upstream total temperature *rms* with flow Mach number using direct numerical simulation data. The data is normalized with the upstream mean total temperature. Here the hollow symbols represent the *rms* of Eq. 4.6 and the solid symbols denote the rms of first two terms of Eq. 4.6 for different upstream turbulent Mach numbers.

4.2 Total temperature fluctuations

Total enthalpy is a quantity of fundamental interest in high-speed flows. It represents the overall energy content of the gas, and is conserved across an (adiabatic) shock wave. Conservation of total enthalpy is true for a stationary shock, and we transform to a frame of reference attached to the unsteady oscillating shock wave. We investigate the fluctuations in total temperature with respect to the shock wave, and relate it to the temperature fluctuations generated by the shock. This leads to an expression for the turbulent heat flux dowsntream of the shock wave.

The instantaneous total temperature in the shock reference frame is written as

$$T_{0,s} = \overline{T} + T' + \frac{(\overline{u} + u' - \xi_t)^2 + v'^2 + w'^2}{2c_p}. \tag{4.5}$$

Here, u,v,w are the velocity components and subscript s represents the shock reference frame. The mean flow is one-dimensional (only streamwise direction), while the turbulence is three-dimensional in this model problem. Subtracting the mean value from the above equation we will get the fluctuating total temperature, once again in the frame of reference of the unsteady shock wave.

$$T'_{0,s} = T' + \frac{\overline{u}}{c_p}(u' - \xi_t) + \frac{u'^2 + v'^2 + w'^2}{2c_p} + \frac{\xi_t^2}{2c_p} - \frac{u'\xi_t}{c_p}. \tag{4.6}$$

The root mean square (*rms*) total temperature fluctuation is computed from DNS data using the difference between instantaneous and mean total temperature and then taking appropriate *rms*.

Fig. 4.3 shows that the *rms* of total temperature increases with upstream flow and turbulent Mach numbers (M, M_t). As we increase the upstream flow Mach number M keeping mean temperature constant, mean upstream velocity $(\overline{u}_1)$ increases and this will increase the kinetic energy contribution of total temperature fluctuations. An increase in upstream turbulent Mach number M_t will give rise to higher u_1^{rms}, hence the kinetic energy contribution of total temperature fluctuation increases. In both the cases the variation of total temperature *rms* is highly dependent on the linearized kinetic energy of the flow, which is a linear function of M and M_t via the second term in Eq. 4.6 and is given by the pink solid lines in Fig. 4.3.

The linear component of the total temperature fluctuation can be computed using the first first two terms of Eq. 4.6 and the corresponding *rms* is given by

$$T_{0,s}^{rms} = \left[(T^{rms})^2 + \frac{\overline{u}^2}{c_p^2}\left((u^{rms})^2 + \xi_t^2 - 2\overline{u'\xi_t} \right) + \frac{2\overline{u}}{c_p}\left(\overline{u'T'} - \overline{T'\xi_t} \right) \right]^{0.5} \tag{4.7}$$

where the correlations are calculated using Eqs. 4.3 and 4.4 at the upstream location of the instantaneous shock wave identified using threshold method . The hollow symbols in the Fig. 4.3 represent the *rms* of Eq. 4.6, whereas the data for the solid symbols are computed using linear component from Eq. 4.7. Since the difference between the two is less than 0.5%, we will approximate the total temperature fluctuation

$$T'_{0,s} \simeq T' + \frac{\overline{u}}{c_p}(u' - \xi_t) \tag{4.8}$$

with the first two terms of Eq. 4.6 from now on for simplicity.

4.2.1 Conservation of energy in total temperature fluctuation

Conservation of energy contained in total temperature fluctuation across an unsteady normal shock forms the basic tenet for the heat flux analysis.

$$T'_1 + \frac{\overline{u}_1}{c_p}(u'_1 - \xi_t) = T'_2 + \frac{\overline{u}_2}{c_p}(u'_2 - \xi_t). \tag{4.9}$$

We probe the DNS data across the instantaneous shock using the method discussed in subsection 4.1 to compute the upstream and downstream total temperature fluctuation (as

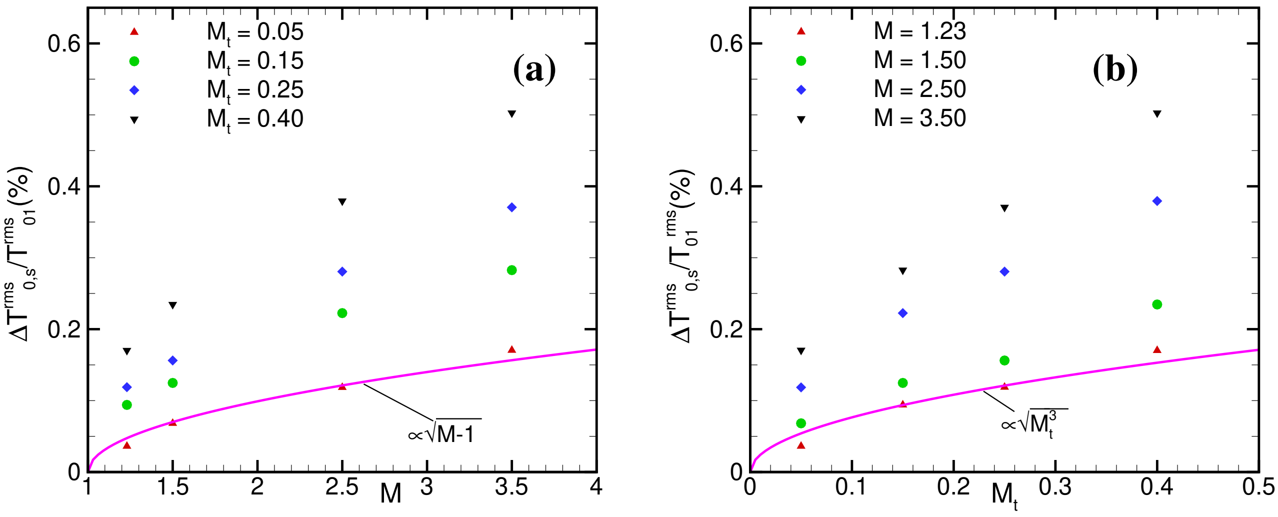

Figure 4.4: Statistical error analysis of total temperature *rms* as a function of flow and turbulent Mach numbers from DNS data. An approximate scaling is highlighted by the pink solid line.

per Eq. 4.8), $T'_{01,s}$ at $x_{s,1}$ and $T'_{02,s}$ at $x_{s,2}$. The root mean square of the total temperature difference across the instantaneous shock is given by

$$\Delta T_{0,s}^{rms} = \sqrt{\overline{\left(T'_{02,s} - T'_{01,s}\right)^2}} \tag{4.10}$$

and is plotted as a function of flow and turbulent Mach number in Figure 4.4. The data is normalized with the upstream total temperature *rms* T_{01}^{rms}. The error or difference of total temperature *rms* across the instantaneous shock wave increases with both flow and turbulent Mach numbers. This is due to an increase in kinetic energy contribution to the higher order terms neglected in Eq. 4.8.

$$\frac{\overline{T'_1 u'^2_1}}{c_p} + \frac{\overline{u}_1 \overline{u'^3_1}}{c_p^2} - \frac{\overline{u}_1 \overline{u'^2_1 \xi_t}}{c_p^2} + \ldots$$

The dominant higher order error terms can be scaled as

$$\sqrt{\frac{\overline{u}_1 \overline{u'^3_1}}{c_p^2}} \sim \sqrt{\frac{\overline{u}_1 \overline{u'^2_1 \xi_t}}{c_p^2}} \sim \sqrt{M M_t^3}$$

The effect of $\sqrt{\frac{\overline{T'_1 u'^2_1}}{c_p}}$ will be small as T'_1 is small in the upstream region (see next subsection). This scaling approximation is shown in Fig. 4.4 by the pink solid line, and it is found to match the trend in the DNS data. We note that the scaling for Mach number $\sqrt{M}$

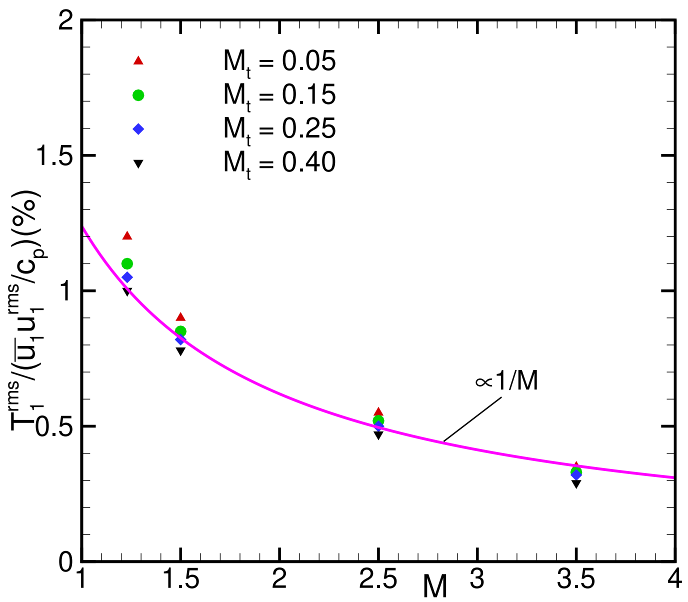

Figure 4.5: The contribution of upstream static temperature *rms* relative to the upstream linearized kinetic energy computed using DNS data. The approximate scaling of the ratio with flow Mach number M is shown by the pink solid line.

is replaced by $\sqrt{M-1}$ to bring the difference to zero at Mach 1 instead of $M = 0$; shock waves are not present below Mach 1.

As the difference between upstream and downstream total temperature rms is within 0.6% for all the 16 cases in the present DNS study, the conservation of the linearized total temperature fluctuation across an instantaneous shock wave is assumed to be true for M_t up to 0.4.

4.2.2 Upstream temperature fluctuation

The upstream fluctuation of total temperature has two dominant sources in Eq. 4.8, namely, the static temperature fluctuation T_1' and the linearized kinetic energy contribution from mean and turbulence velocity fluctuation $\frac{\overline{u}_1}{c_p}u_1'$. Figure 4.5 shows the variation of T_1^{rms} and $\overline{u}u_1^{rms}/c_p$ ratio with flow Mach number M for four different turbulent Mach numbers. As we increase the upstream M or M_t, the effect of the second term increases significantly and thus the ratio of this two term decreases with M and M_t.

The method prescribed by [68] is used to generate the upstream compressible turbulence, according to which a small perturbation in velocity field will generate pressure, density, temperature and dilatation fluctuations. The analysis done by [68] shows a scaling of temperature fluctuation as $(\gamma - 1)M_t^2$. Although the amplitude of upstream static temperature fluctuation is very small in most of the DNS study, it is found to be an important parameter to analyse the post shock turbulent heat flux. Data in Fig. 4.5 shows that the error encountered by neglecting T_1' can be higher than the error from neglecting higher order terms in the total temperature fluctuations. This is especially true for the cases with intense upstream temperature fluctuation , e.g. turbulent boundary layer with cold wall.

The value of T_1^{rms} is 1.2% or less of the linearized kinetic energy $(\overline{u}u_1^{rms}/c_p)$ and this ratio can be approximately scaled as

$$\frac{c_p T_1^{rms}}{\overline{u}_1 u_1^{rms}} \sim \frac{c_p T_1^{rms}}{M M_t(\gamma R \overline{T}_1)} \sim \frac{M_t}{M} \tag{4.11}$$

where $T_1^{rms} \sim M_t^2$. The scaled ratio is plotted in Fig. 4.5 by the pink solid line and all the data approximately follow this scaling.

4.2.3 Shock hole statistics

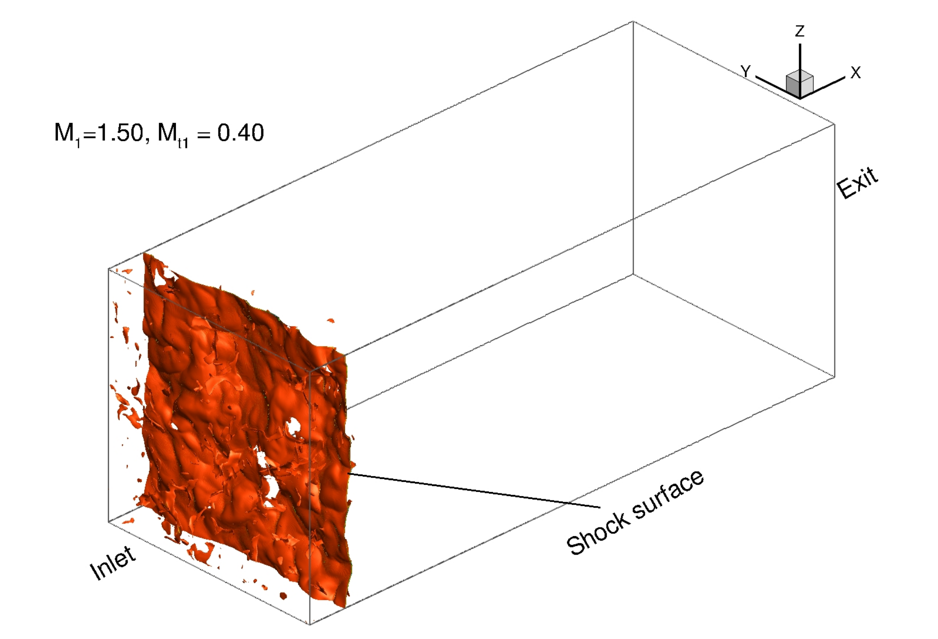

Figure 4.6: Shock-turbulence interaction for $M = 1.5$ and $M_t = 0.4$. The figure also highlighted the shock hole on the shock surface. The flow is coming from left to right direction.

Shock-turbulence interaction (STI) problems are usually divided into 'wrinkled' and 'broken' regimes based on the criterion provided by [44]. They proposed the criterion, $M_t > 0.6(M_1 - 1)$, for which the shocks are found to be extinguished locally. They termed such interactions as the 'broken' shock regime, where the local shock surface disappears (shock holes 4.6) and through which the turbulence passes without any significant

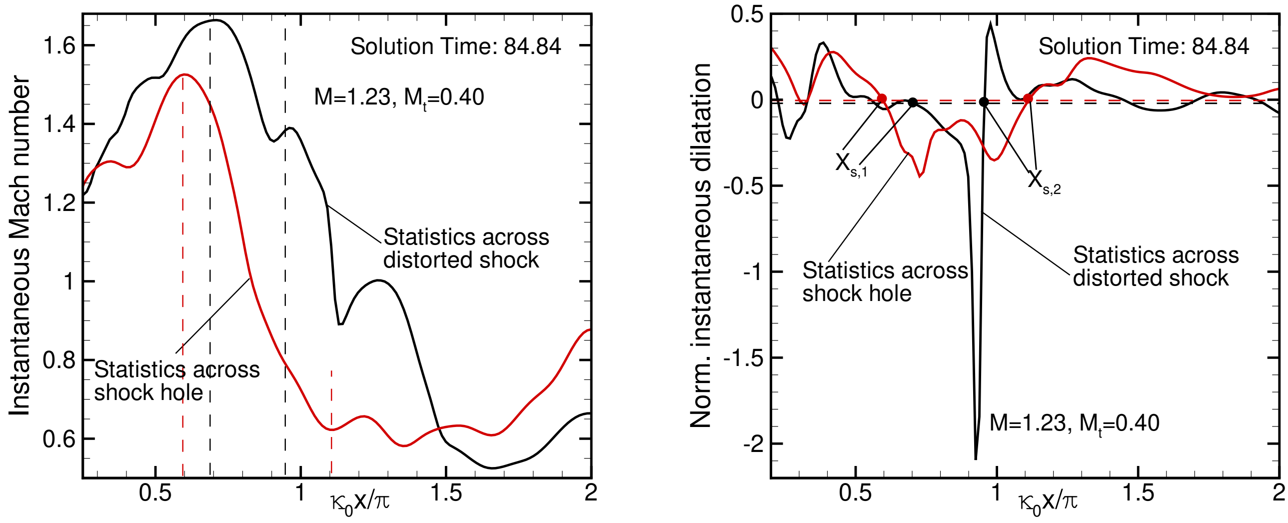

Figure 4.7: Instantaneous Mach number and dilatation distribution across the distorted (black line) and shock hole surface (red line) for $M = 1.23$ and $M_t = 0.40$. The instantaneous dilatation is normalized by $\kappa_0 \overline{u}_1$.

change. The 'wrinkled' shock regime is identified for $M_t < 0.6(M_1 - 1)$. There are no local extinguishing of the shock surface, but the shock could be strongly distorted in this regime. Recently [11] found a new shock regime where they did not find any amplification in Reynolds stresses but the mean quantities still followed a shock-like behavior. They named it as 'vanished' shock regime. In this present study, we did not find the presence of 'vanished' zone. Probably a higher turbulence intensity than those considered in this work will give 'vanished' shock, which is not in the scope of current work.

We calculate the turbulence statistics, relevant to the turbulent heat flux analysis described in the previous subsections, across shock holes. The shock hole regions are identified based on the two criterion [11, 14, 44]: subsonic or near sonic Mach number ahead of the shock hole and multiple peaks in the instantaneous dilatation profile which creates bifurcated shock structure in the shock hole region; see Fig. 4.7. The above two criterion are integrated along with the threshold method [74] to get the (y, z) co-ordinates for the shock holes. The corresponding upstream x_s, 1 and downstream x_s, 1 locations are identified (see Fig. 4.7) and the statistics are calculated by taking appropriate average over (y, z, t) corresponding to shock holes.

The results from the statistical analysis and the statistical convergence details are given in table 4.2. The three M, M_t cases that satisfy the broken shock condition given above are listed. For each case, results are compared between shock holes and the distorted parts of the shock wave. The shock holes are present in less than 1% region of

Table 4.2: Statistical analysis across shock hole and distorted regions.

M	M_t	$\frac{\Delta T^{rms}_{0,s}}{T^{rms}_{01}}\%$		$\frac{c_p T^{rms}_1}{\bar{u}_1 u^{rms}_1}\%$		$\frac{\xi^{rms}_t}{u^{rms}_1}$	
		Hole	Distorted	Hole	Distorted	Hole	Distorted
1.23	0.25	0.099	0.119	1.24	1.05	0.059	0.26
1.23	0.40	0.136	0.170	1.20	1.00	0.027	0.19
1.50	0.40	0.210	0.235	0.90	0.78	0.043	0.21

the total shock surface, and the number of points considered for shock hole statistics are listed in the table.

The difference between the upstream and downstream total temperature fluctuation in shock reference frame across the shock hole is comparatively lower than the distorted or wrinkled shock surface for the same freestream Mach number. It is proportional to $\sqrt{MM_t^3}$. The flow Mach number is either subsonic or lower than the freestream Mach number ahead of the shock hole. This is due to the presence of small shocklets, which are generated by intense turbulence fluctuations upstream of shock holes. Hence, $\Delta T^{rms}_{0,s}/T^{rms}_{01}$ is up to 20% lower at shock holes for the same M and M_t; see table 4.2.

As per Eq. 4.11 the temperature-velocity ratio is inversely proportional to M. The presence of a lower (subsonic or close to sonic) Mach number ahead of the shock hole will increase this temperature-velocity ratio. The *rms* of the temperature fluctuation will also increase across the shocklets and the flow may not be isentropic ahead of a shock hole. A higher temperature fluctuation will increase the temperature-velocity ratio upstream of the shock hole. Overall the ratio is 15-20% higher than the corresponding distorted surface for each case listed in table 4.2.

The shocklets extinguished the shock surface and replace it with a series of weak compression waves. The effective speed of these compression waves can be found from the mass conservation relation of Eq. 4.4 where the upstream and downstream locations are considered ahead of the first compression wave and after the last compression wave respectively. The effective oscillation speed of weak compression waves is found to be much lower than a distorted normal shock wave (75 to 85% lower speed) and is tabulated in table 4.2.

The compression waves in the shock hole region create a wider instantaneous dilatation peak instead of a sharp peak found in a distorted shock wave. In local bifurcated shock multiple peaks are observed in the instantaneous dilatation profile; see Fig. 4.7.

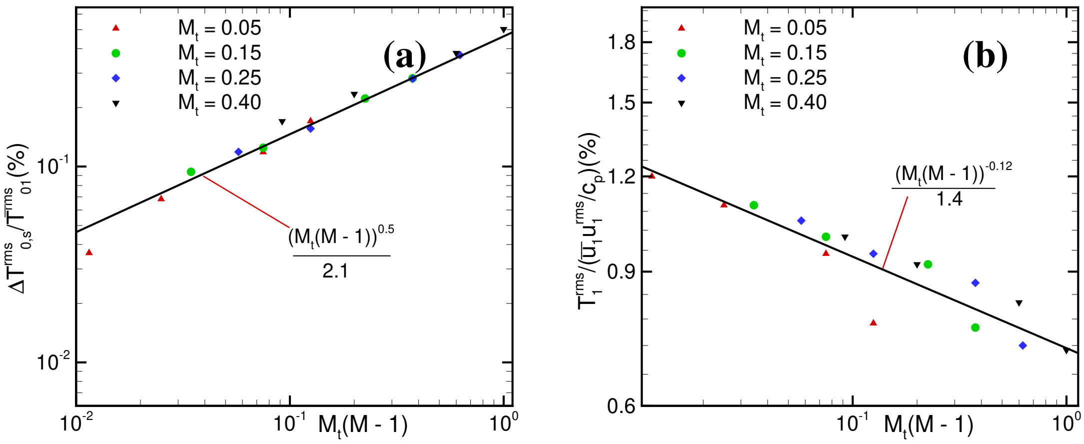

Figure 4.8: Empirical scaling analysis using DNS data and threshold method (subsection 4.1).

The presence of weak compression wave in shock hole decreases the non-linear effect of total temperature fluctuation compared to a shock surface. Hence the turbulent heat flux analysis based on Eqs. 4.8 and 4.9 is expected to be equally valid for shock wave and compression wave. The amplification of all the turbulence quantities is much smaller across the shock hole compared to a normal shock at identical freestream conditions. A weaker compression across the shock hole reduces the amplification factor of turbulence quantities.

4.2.4 Scaling of error

In previous subsections we analyse the variation of the total temperature fluctuations across a shock wave as a function of Mach number and turbulent Mach number. We also present the contribution of the upstream temperature fluctuations to $T_{0,s}^{rms}$, relative to the kinetic energy component, for different M and M_t cases. These higher-order effects are found to be small in magnitude and are often neglected from turbulent heat flux models developed using linear interaction analysis [65]. Here, we quantify the error caused by these approximations and propose a combined scaling in terms of the mean and turbulent Mach numbers of the flow. The error or difference due to linear approximation of total temperature fluctuation is studied as a function of the product of the mean and turbulent Mach numbers, to bring in the combined effect of the shock wave and the turbulence intensity. As earlier, we use $M - 1$ in stead of M as the physically relevant parameter describing shock strength.

Figure 4.8 presents the data on logarithmic axes, and all the 16 cases with varying M and M_t are included in the plots. We find the following empirical curve fits,

$$\begin{aligned} \frac{\Delta T_{0,s}^{rms}}{\overline{T}_{01}} &\sim (M_t(M-1))^{0.5} \\ \frac{c_p T_1^{rms}}{\overline{u}_1 u_1^{rms}} &\sim (M_t(M-1))^{-0.12} \end{aligned} \tag{4.12}$$

Note that the variation of total temperature fluctuations across the shock is found to increase with both flow Mach and turbulent Mach number, matching with the trend shown in Fig. 4.4. On the other hand, the ratio of upstream temperature fluctuations to the upstream linearized kinetic energy is found to decrease with $M_t(M-1)$. Thus the highest magnitude are observed at low Mach and turbulence intensity. Also note that the T_1^{rms} effect is much larger than $\Delta T_{0,s}^{rms}$ across the shock (by an order of magnitude). Thus the dominant error (due to neglecting the upstream temperature fluctuations) is found to reduce with M and M_t, indicating that the approximations are progressively more valid for stronger shock waves. This is in line with the linear analysis framework, where the shock effect becomes stronger than nonlinear turbulence interaction at higher Mach number.

A decrease of the upstream temperature fluctuations, relative to the linearized kinetic energy of the flow, at higher M_t brings out another interesting point. It shows that neglecting the T_1' term in Eq. 4.9 is progressively more valid at higher turbulence intensities. Thus, heat flux models based on linear interaction analysis (ideally valid for$M_t \to 0$) are also valid for finite M_t cases. The data shows that they are expected to hold even in the broken shock regime. Although the term $c_p T_1^{rms}/\overline{u}_1 u_1^{rms}$ is slightly higher in shock holes than distorted shock (see Table 4.2), the magnitudes are small enough to neglect the contribution of T_1' in the overall balance equation for total temperature fluctuations across an instantaneous shock wave.

4.3 Sensitivity study of threshold method

A threshold value of 1% of the most negative instantaneous dilatation is used in the original method of [74] to identify the upstream and downstream edges of the instantaneous shock wave. In this section the sensitivity of the method on shock edge detection is studied, where the threshold limit is systematically varied up to 10% to analyse the effectiveness of the method to identify the instantaneous shock edges.

Figure 4.9 shows the graphical representation of different threshold values with respect to the most negative instantaneous dilatation. An increase in threshold limit moves

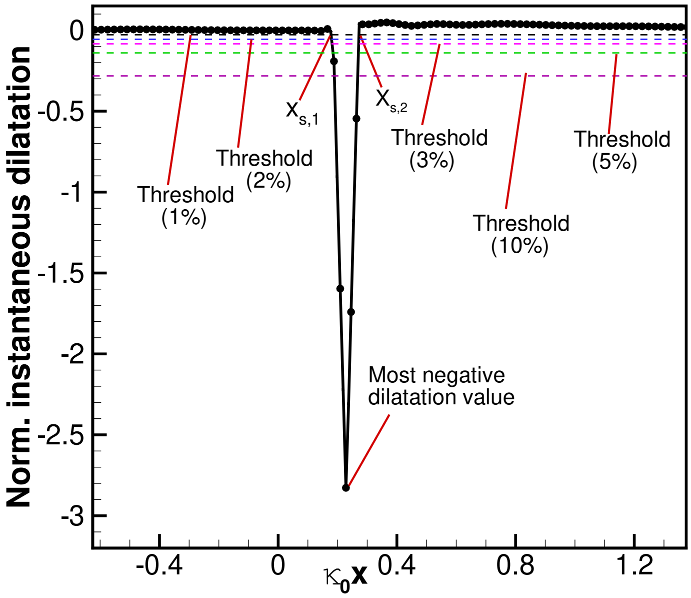

Figure 4.9: Sensitivity study of the threshold values (1,2,3,5,10%) to identify the instantaneous shock locations using instantaneous dilatation. The data corresponds to a single x-line (at constant y, z and t) for the case of $M = 3.50$ and $M_t = 0.15$. Dilatation is normalized by $\kappa_0 \overline{u}_1$ and the streamwise distance is normalized by κ_0. The mean shock is centered at $\kappa_0 x = 0$ and the symbol represents the grid points for N = 1,2,3$\cdots$. Every second grid point is showing here.

the upstream and downstream shock locations toward the center of the shock (most negative dilatation value) and instead of detecting the shock edges, the points are located inside the shock wave. The apparent upstream fluctuation level also increases accordingly as the threshold limit is increased. This is due to the fact that the upstream point is already inside the shock wave and a part of the shock amplification contributes to the mean and fluctuating values. The unphysical high prediction of the upstream turbulence statistics also produces an error in the downstream calculation. Further increase of the threshold limit will create a point where the upstream and downstream locations will coincide and there will be no amplification in the turbulence quantities across the shock wave, which signifies a presence of an artificial shock hole.

The distribution of the upstream total temperature *rms* calculated with different threshold limit is shown in Fig. 4.10(a) for different Mach numbers, at $M_t = 0.4$. The value increases with threshold limit as the upstream point moves inside the shock wave and we get a higher upstream turbulence statistics. Data obtained for a fixed threshold value of 1% (Fig. 4.3) shows an increase in $T_{0,s}^{rms}/\overline{T}_{01}$ with Mach number and turbulent

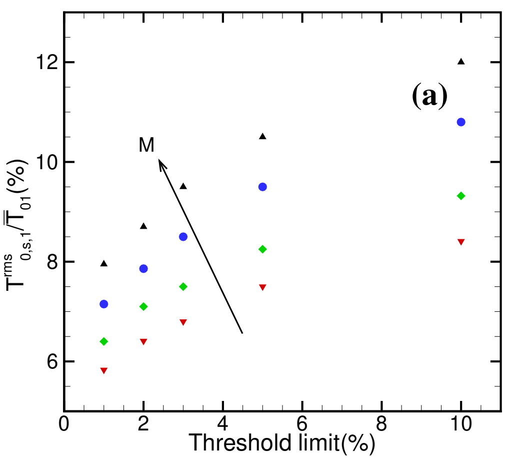

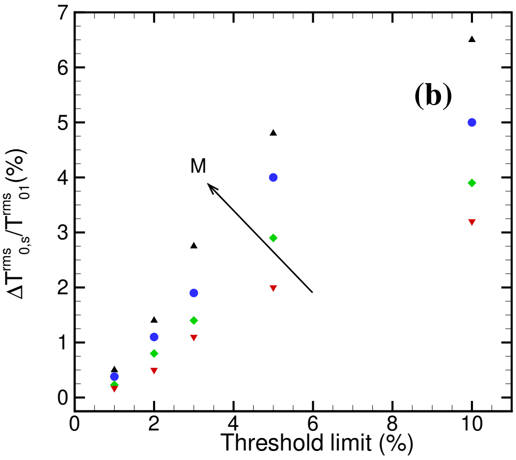

Figure 4.10: Sensitivity of threshold limit on different turbulence statistics with increasing Mach number and $M_t = 0.4$.

Table 4.3: Variation of turbulence statistics with a threshold limit of 5%.

	$\frac{c_p T_1^{rms}}{\overline{u}_1 u_1^{rms}}(\%)$				$\frac{\Delta T_{0,s}^{rms}}{T_{01}^{rms}}(\%)$			
M $\quad M_t =$	0.05	0.15	0.25	0.40	0.05	0.15	0.25	0.40
1.23	4.28	4.07	3.84	3.61	1.00	1.30	1.75	2.00
1.50	4.09	3.89	3.62	3.49	1.45	2.00	2.50	2.90
2.50	3.91	3.75	3.55	3.31	2.50	2.80	3.40	4.00
3.50	3.78	3.59	3.43	3.18	3.10	3.50	4.00	4.80

Mach number. The same trend is present at other threshold values as well, except for the fact that the magnitude of the total temperature *rms* is higher for a higher threshold limit.

The threshold limit also increases the contribution of the higher-order terms by increasing the level of turbulence fluctuations. The difference between the total temperature fluctuations upstream and downstream of the shock is quantified by $\Delta T_{0,s}^{rms}$, and it represents the magnitude of the second-order terms in Eq. 4.10. As expected, $\Delta T_{0,s}^{rms}/T_{01}^{rms}$ increases with the threshold limit; see Fig. 4.10(b). Also, the data follows the same trend as that presented for 1% threshold limit in Fig. 4.4, and match the scaling obtained for varying M and M_t. Thus the results presented in the previous section, in terms of the total temperature fluctuations and the scaling relations for the higher-order terms are valid irrespective of the threshold value used to identify the shock edge.

The data presented in Fig. 4.10 corresponds to different Mach numbers at $M_t = 0.4$, and the same trend is observed at other values of turbulent Mach number. Table B.4

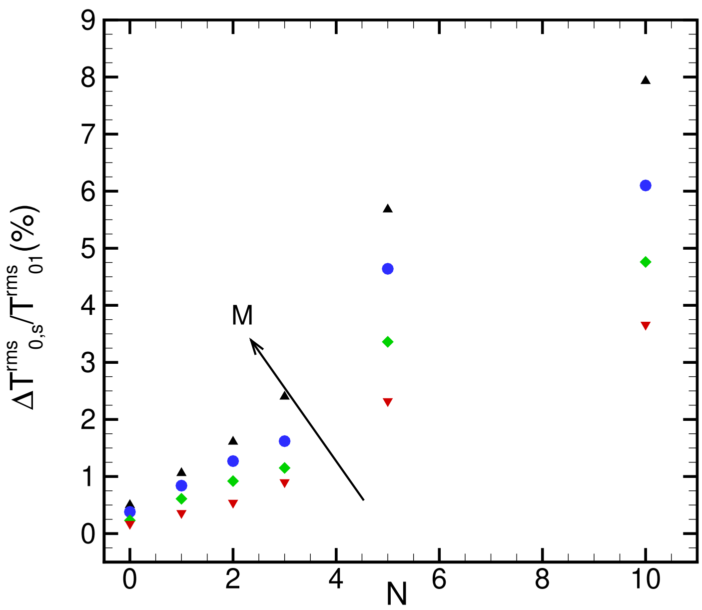

Figure 4.11: Effect of varying the number of grid points (N) away from the shock edge used in threshold method on the higher order turbulence statistics for increasing Mach number at $M_t = 0.4$

lists the value of $\Delta T^{rms}_{0,s}/T^{rms}_{01}$ for all the 16 cases, obtained using a 5% threshold limit. A monotonic increase in the effect of non-linear terms is evident with increase in M as well as M_t, as noted earlier. More important, the highest value is 4.8% for (M, M_t) = (3.5,0.40). Thus the error due to the non-linear terms is within 5%, and can be considered to be acceptable. A threshold value between 1 and 5% can therefore be expected to give negligible error in the heat flux analysis presented above.

Table B.4 also lists the magnitude of upstream temperature-velocity fluctuations ratio for the different Mach number and turbulent Mach number cases. Once again, the data is computed using a 5% threshold limit and follow the same trend with M and M_t, as those in Fig. 4.5 (for 1% threshold limit). Here, the highest value is observed at the weakest shock and turbulence (M, M_t) = (1.23,0.05), and $c_p T^{rms}_1/\overline{u}_1 u^{rms}_1$ is within 4.3%; corroborating the fact that shock edge detected using a threshold value between 1% and 5% of the peak dilatation in the shock wave is acceptable.

Instead of going inside the shock wave (by increasing the threshold limit), if the upstream and downstream locations $x_{s,1}$ and $x_{s,2}$ move away from the instantaneous shock edges by few grid points, i.e. move towards the mean shock edge ($\overline{x}_{s,1}$ and $\overline{x}_{s,2}$ in figure 4.1). Here, N = 1, 2, ... represent the first, second, etc. grid points moving outward in both directions from the edges of the instantaneous shock detected by the threshold

Table 4.4: Variation of turbulence statistics obtained by using N = 5 in the threshold method.

		$\frac{c_p T_1^{rms}}{\overline{u}_1 u_1^{rms}}(\%)$				$\frac{\Delta T_{0,s}^{rms}}{T_1^{rms}}(\%)$			
M	M_t =	0.05	0.15	0.25	0.40	0.05	0.15	0.25	0.40
1.23		4.65	4.14	3.88	3.40	1.16	1.51	2.03	2.32
1.50		3.93	3.38	3.08	2.85	1.74	2.32	2.90	3.36
2.50		3.31	3.14	2.90	2.70	2.39	2.95	3.64	4.14
3.50		2.95	2.92	2.66	2.40	3.06	3.52	3.97	4.68

method. A threshold value of 1% is used to get the instantaneous shock boundaries and the corresponding statistics are marked as N=0.

The magnitude of higher-order terms, as quantified by $\Delta T_{0,s}^{rms}/T_{01}^{rms}$ increases with the shock boundary locations $x_{s,1}$ and $x_{s,2}$ moving outward from the instantaneous shock wave; see Fig. 4.11. Table B.7 lists the value for all the 16 cases, obtained using N=5; similar trends are observed for other values of N as well; see Appendix B. For each N, the variation of $\Delta T_{0,s}^{rms}/T_{01}^{rms}$ follows the scaling obtained earlier in section 4.2.1, and the highest value occurs for highest M and M_t combination. Table B.7 also lists the ratio of the upstream temperature and velocity fluctuations, and their qualitative behaviour is akin to that observed in Table B.4. Overall, the error reported in Table B.7 are within about 5% for N up to 5, and it quantifies the sensitivity of the results to the variations in the original threshold method proposed by [74].

4.4 Turbulent heat flux model

Next, we use the insight gained from the DNS data to develop a predictive model for the turbulent heat flux generated by a shock wave. We start with the conservation of total temperature in the frame of reference of the unsteady shock wave. For the turbulence field, it gives the relation 4.9 for the post-shock temperature fluctuations in terms of the velocity fluctuations upstream and downstream of the shock wave, and the instantaneous shock speed.

An equation for shock downstream (station 2) turbulent heat flux can be obtained by multiplying eq. 4.9 by u_2' and then taking Reynolds average

$$\overline{u_2'T_2'} = -\frac{\overline{u}_2}{c_p}\overline{u_2'^2} + \frac{\overline{u_2'\xi_t}}{c_p}(\overline{u}_2 - \overline{u}_1) + \frac{\overline{u}_1}{c_p}\overline{u_1'u_2'}, \tag{4.13}$$

where the velocity temperature correlation $\overline{T_1' u_2'}$ is neglected as the upstream temperature fluctuation is found to be negligible. The post-shock turbulent heat flux (at $x_{s,2}$, which is identified using the threshold method explained in subsection 4.1), depends on the streamwise shock normal Reynolds stress ($\overline{u_2'^2}$), shock unsteadiness correlation ($\overline{u_2' \xi_t}$) and the two-point velocity correlation ($\overline{u_1' u_2'}$). A similar equation is presented in [70] based on linear analysis results, which is ideally valid in the limit $M_t \to 0$. The earlier model is only a function of the shock strength, and independent of the turbulence intensity. Here, we show the limitations of the earlier model, and propose new closure approximations for high M_t cases. Comparison with DNS data shows a significant advantage over earlier models based on linear interaction analysis.

4.4.1 Two-point velocity correlation

The two-point velocity correlation ($\overline{u_1' u_2'}$) in Eq. 4.13 is not readily available in Reynolds averaged Navier-Stokes simulations (RANS). In our previous work [70] we modeled the two-point velocity correlation in terms of a modeling parameter $\alpha = \frac{\overline{u_1' u_2'}}{\overline{u_2'^2}}$, where the post-shock normal Reynolds stress can be easily computed in a RANS simulation. A constant value of 0.6 for the parameter α is used for simplicity. The current analysis shows if we take $\alpha = 0.6$ the error due to upstream turbulence increases compared to Fig. 4.8. This is specially significant at lower M and M_t values. Here we model the parameter α using the DNS data across the instantaneous shock.

The current analysis from DNS data shows the model parameter α saturates to a value of 0.6 for higher Mach numbers ($M > 3$), see Fig. 4.12 and $\alpha \to 1$ for vanishing shock waves ($M \to 1$), i.e. there will be no amplification of turbulence fluctuations without a shock wave. A suitable curve fit is obtained from the DNS data

$$\alpha = \frac{\overline{u_1' u_2'}}{\overline{u_2'^2}} = 0.6 + 0.4 \exp(1 - M). \tag{4.14}$$

The effect of turbulent Mach number is not very significant on α and the model coefficient is only a function of upstream Mach number which represents the shock strength.

4.4.2 Shock unsteadiness damping parameter

The shock unsteadiness correlation $\overline{u_2' \xi_t}$ brings in the effect of the unsteady shock oscillations on the turbulent heat flux. It has an opposite sign to the Reynolds stress term in Eq. 4.13, and hence represents a damping effect of the shock unsteadiness [78] on temperature fluctuations. We introduced a new modeling parameter b_2 using the DNS data to model the post-shock unsteadiness correlation $\overline{u_2' \xi_t}$. The variation of the new

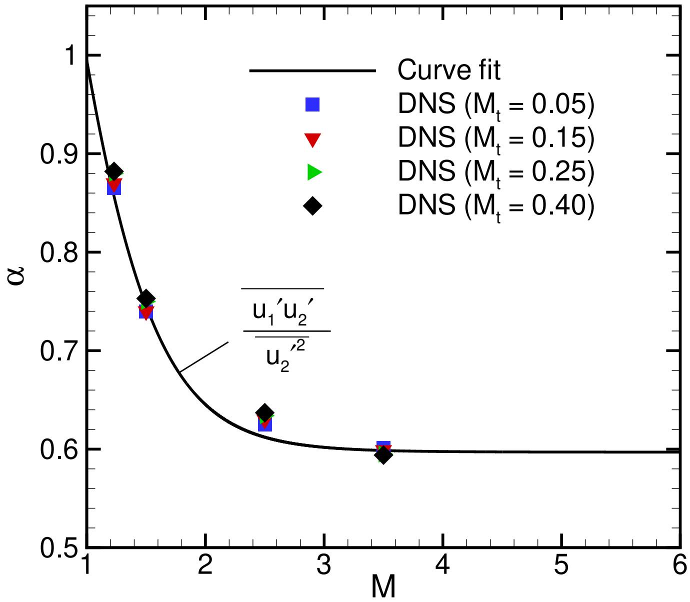

Figure 4.12: Variation of model parameter $\alpha = \frac{\overline{u_1'u_2'}}{\overline{u_2'^2}}$ with upstream Mach number for different M_t cases.

model parameter with Mach number is shown in Fig. 4.13 and the data fit model equation is written as

$$b_2 = \frac{\overline{u_2'\xi_t}}{\overline{u_2'^2}} = (0.5 + M_t^2)(1 - \exp(1 - M)). \tag{4.15}$$

The new post-shock damping parameter is a function of the flow and turbulent Mach numbers. It is affected by both the shock strength and the upstream turbulence intensity. The current DNS data helps us to bring the effect of M_t in the modeling parameter which is not possible with the linear analysis based model in [70]. In the earlier work, the shock unsteadiness effect was modeled using the shock unsteadiness parameter b_1 from [78]. Figure 4.13 shows the damping effect due to shock oscillation increases with upstream turbulence intensity M_t, and the coefficient b_2 is able to capture the effect accurately.

4.4.3 Turbulent kinetic energy amplification

We also analysed the amplification of turbulent kinetic energy (TKE) across the instantaneous shock wave for different turbulence intensities. The turbulent kinetic energy is directly related to the shock normal Reynolds stresses and an improvement in TKE amplification can affect the post-shock turbulent heat flux, see Eq. 4.13. The amplification in turbulent kinetic energy is given as per [78]

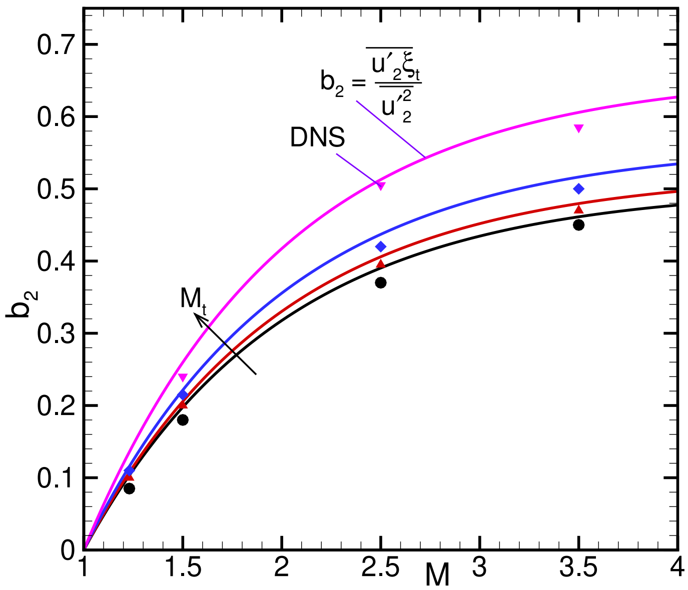

Figure 4.13: Variation of model parameter b_2 as a function of flow Mach number M. The effect of turbulent Mach number is also included in the figure with different symbols: Black circle – $M_t = 0.05$, Red delta – $M_t = 0.15$, Blue diamond – $M_t = 0.25$, Pink gradient – $M_t = 0.40$. The solid lines represent the corresponding modeling prediction (Eq. 4.15) for different M_t.

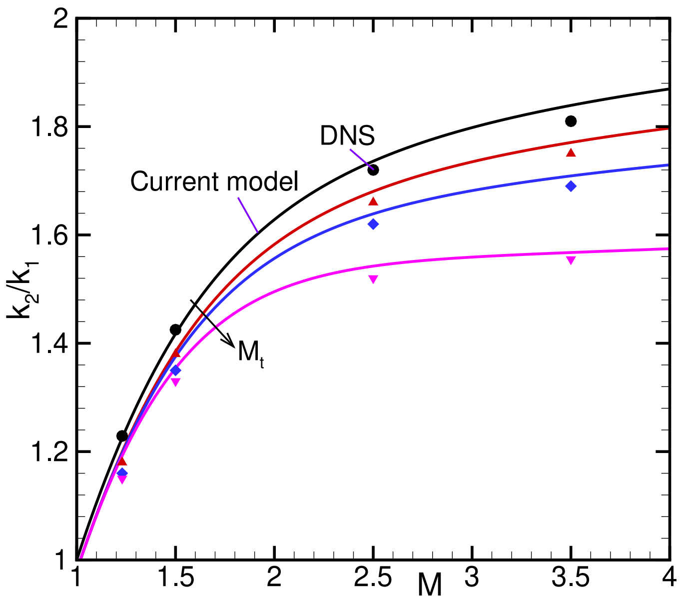

Figure 4.14: Variation in turbulent kinetic energy amplification with upstream Mach number. The amplification in the DNS data is obtained as per threshold method across an instantaneous shock wave. The effect of turbulent Mach number is also included in the figure with different symbols and solid lines. The symbolic representation is same as Fig. 4.13.

$$\frac{k_2}{k_1} = \left(\frac{\overline{u}_1}{\overline{u}_2}\right)^{2/3(1-b_1')} = r^{2/3(1-b_1')}, \tag{4.16}$$

where r is the mean density ratio across the shock wave and b_1' is the shock unsteadiness damping parameter with low Mach number correction.

Figure 4.14 shows that the amplification in TKE is affected by the upstream turbulence intensity and the jump in TKE across an instantaneous shock reduces with M_t increment. This is consistent with the findings of [14, 44, 71]. The damping parameter b_1' [78] based on linear analysis does not include the effect of turbulent Mach number and it will give same amplification of TKE for all turbulence intensities. We update the model parameter b_1' using the direct numerical simulation data to include the effect turbulent Mach number and the modified form is given as

$$b_1' = (0.4 + M_{t1}^2)(1 - \exp(1 - M)). \tag{4.17}$$

The formulation of the parameter b_1' is very similar to the original work [78] except the M_t term. The damping parameter is found to scale with M_t^2 and it increases with upstream turbulence intensity causing a reduction in TKE jump.

4.4.4 Model evaluation

Incorporating the closure approximations described above , we obtain a model to predict the turbulent heat transfer generated behind a shock wave.

$$\overline{u_2' T_2'} = -\frac{\overline{u}_2}{c_p}\overline{u_2'^2}\left(1 + b_2(r-1) - \beta\right), \tag{4.18}$$

where $\beta = \alpha r$ and r is the mean density ratio across the shock wave. The shock normal Reynolds stress is calculated as per the model given by [86]. The model parameters b_2, α and b_1' are a function of upstream shock-normal Mach number. This makes the CFD implementation of the model non-local in nature for flows involving multiple shock interactions. Following the work of [70], the upstream shock normal Mach number is replaced by local density ratio r and the model parameters are recast as a function of r.

$$\begin{aligned} \alpha &= \quad 0.6 + 0.4\left(\tfrac{6-r}{5}\right)^{5.2} \\ b_2 &= \quad (0.5 + M_t^2)\left(\tfrac{r-1}{5}\right)^{0.3} \\ b_1' &= \quad (0.4 + M_t^2)\left(\tfrac{r-1}{5}\right)^{0.3} \end{aligned} \tag{4.19}$$

Here the exponents are obtained by a curve fitting to Eqs. 4.14,4.15,4.17. Figure 4.15 shows the variation of peak turbulent heat flux with upstream flow Mach number M, for

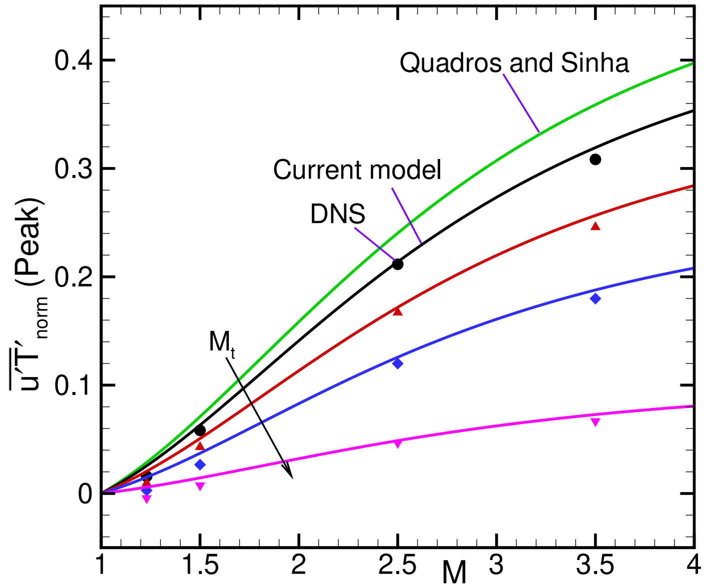

Figure 4.15: Variation of normalized peak turbulent heat flux with upstream Mach number. The peak in the DNS data is obtained as per threshold method. Symbols: Black circle – $M_t = 0.05$, Red delta – $M_t = 0.15$, Blue diamond – $M_t = 0.25$, Pink gradient – $M_t = 0.40$. The turbulent heat flux is normalized with upstream mean velocity $\overline{u}_1$ and downstream mean temperature $\overline{T}_2$. The correlation is further scaled with upstream normalized TKE $k_1/\overline{u}_1^2$.

different M_t. The threshold method of [74], see subsection 4.1, is used to get the post-shock turbulent heat flux from DNS data. The data is normalized by upstream mean velocity $\overline{u}_1$ and downstream mean temperature $\overline{T}_2$. The data is further scaled with upstream normalized TKE $k_1/\overline{u}_1^2$.

The current model matches DNS data well for all M and M_t cases and gives a better prediction compared to the model of [65]. Notably, it can predict the effect of turbulent Mach number, which is missing in the earlier model, as described below. The model of [65] is based on linear interaction analysis and realizable constraints

$$\overline{u'T'} = \frac{\beta' k \overline{u}}{c_p} \tag{4.20}$$

where β' is a model constant. The post-shock normalized heat flux is then given as

$$\overline{u'T'}|_{norm} = \frac{\beta' k \overline{u}}{c_p \overline{u}_1 \overline{T}_2 \frac{k_1}{\overline{u}_1^2}}. \tag{4.21}$$

Following the work of [65] we set k and $\overline{u}$ with upstream values to simplify the above equation

$$\overline{u'T'}|_{norm} = \frac{\beta'(\gamma-1)M_1^2}{T_r}, \tag{4.22}$$

where T_r is the mean temperature ratio across the shock. Thus, the post-shock turbulent heat flux is a function of upstream Mach number; it is not able to predict the M_t variation and gives identical result for all turbulent Mach number cases.

4.4.5 Post-shock evolution

In this subsection, we propose a differential equation based model to predict the turbulent heat flux in shock-turbulence interaction problem. The differential form of the model also enable us to calculate the post-shock variation of turbulent heat flux. Similar to algebraic model (Eq. 4.18) the differential model is also based on total energy conservation across an instantaneous shock wave

$$\frac{\partial T'_{0,s}}{\partial x} = 0. \tag{4.23}$$

Here subscript s denotes the shock reference frame. Next we substitute Eq. 4.8 to expand the above equation

$$\frac{\partial T'}{\partial x} + \frac{\overline{u}}{c_p}\frac{\partial u'}{\partial x} + \frac{u'-\xi_t}{c_p}\frac{\partial \overline{u}}{\partial x} = 0 \tag{4.24}$$

where the derivative of instantaneous shock speed ξ_t is set to zero as it is a function of (y, z, t). Taking a moment with u' and Reynolds averaging yields a differential equation for turbulent heat flux

$$\frac{\partial}{\partial x}\overline{u'T'} = -\frac{\overline{u'^2}}{c_p}\frac{\partial \overline{u}}{\partial x} + \frac{\overline{u'\xi_t}}{c_p}\frac{\partial \overline{u}}{\partial x} - \frac{\overline{u}}{2c_p}\frac{\partial \overline{u'^2}}{\partial x} + \overline{T'\frac{\partial u'}{\partial x}}. \tag{4.25}$$

Here the first term in the RHS represents the production of turbulent heat flux due to the mean compression by the shock and second term brings the effect of unsteady shock oscillation. The streamwise convection of the Reynolds stress by mean flow contributes to the turbulent heat flux by the third term in RHS. The last term denotes a correlation between temperature fluctuation and streamwise change of velocity fluctuation across the shock. Following the modeling convention of [78] we write $\overline{u'\xi_t} = b_1\overline{u'^2}$ where the modeling parameter $b_1 = (0.4 + M_t^2) + 0.6\exp(2(1-M_1))$ is updated with the current DNS data to include the upstream turbulence intensity effect. The streamwise change in shock normal Reynolds stress is modeled as per [86] to get a simplified form

$$\frac{\partial}{\partial x}\overline{u'T'} = -C_{uT}\frac{\overline{u'^2}}{c_p}\frac{\partial \overline{u}}{\partial x} \tag{4.26}$$

where $C_{uT} = b_1 - b_1' - \frac{2}{3}C_2$ and $C_2 = 0.55$ are the model coefficients and the last term of Eq. 4.25 has been dropped for a closed form solution.

The second part of the model deals with the post-shock decay of the turbulent heat flux, where we follow the work of [65]. The decay in turbulent heat flux behind the shock wave is found to be due to an acoustic relaxation mechanism [67], which is modeled as an exponential profile. The final differential form of the turbulent heat flux model is given by

$$\frac{\partial}{\partial x}\overline{u'T'} = C_{ut}\frac{\overline{u'^2}}{c_p}\frac{\partial \overline{u}}{\partial x} - C_d\frac{\overline{u'T'}}{L_\epsilon}. \tag{4.27}$$

Here $C_d = (0.25 + M_t^2) + 4\exp(1 - M_1)$ is a decay coefficient obtained from the current DNS data and $L_\epsilon = k^{3/2}/\epsilon$ is the turbulence dissipation length scale representing acoustic decay.

We solve the above equation and the model prescribed by [86] to obtain the unclosed Reynolds stress term. The shock is specified as a hyperbolic tangent profile of the mean flow variables and it is centered at $x/L_\epsilon = 0$, with the thickness obtained from the DNS data. The Lax-Friedrich scheme is used to evaluate the inviscid fluxes at the cell faces and the turbulence source terms are calculated at the cell centers. The first order accurate Lax-Friedrich method is highly dissipative in nature but it can match higher order results by using a larger number of points [86]. A much higher grid count can be used in these one-dimensional flows. A constant Courant-Friedrichs-Lewy (CFL) number of 0.8 is used for all the simulated results.

Figure 4.16 shows the streamwise variation of turbulent heat flux and the results are compared with the DNS data for different M and M_t. The data is obtained using the conventional averaging (over transverse planes and time for a fixed-x location), instead of the threshold method of [74]. The threshold method is conditioned at the shock wave and is able to predict the upstream and downstream variables across an instantaneous shock; it does not give the streamwise variation behind the shock wave.

There are two prominent effects of turbulent Mach number in Fig. 4.16. First, the peak turbulent heat flux and its downstream evolution in a strong function of M_t. Second, the thickness of the mean shock, as obtained by conventional averaging, increases dramatically for higher M_t. The heat flux correlation takes large negative values in the region of the mean shock thickness. This is an artifact of the unsteady shock oscillations and not captured by the model. Instead, the solution to Eq. 4.27 varies smoothly, and the heat flux correlation increases from zero upstream of the shock to the post-shock peak value. The incoming turbulent heat flux is set to zero in the numerical simulation as the upstream temperature fluctuation is very small.

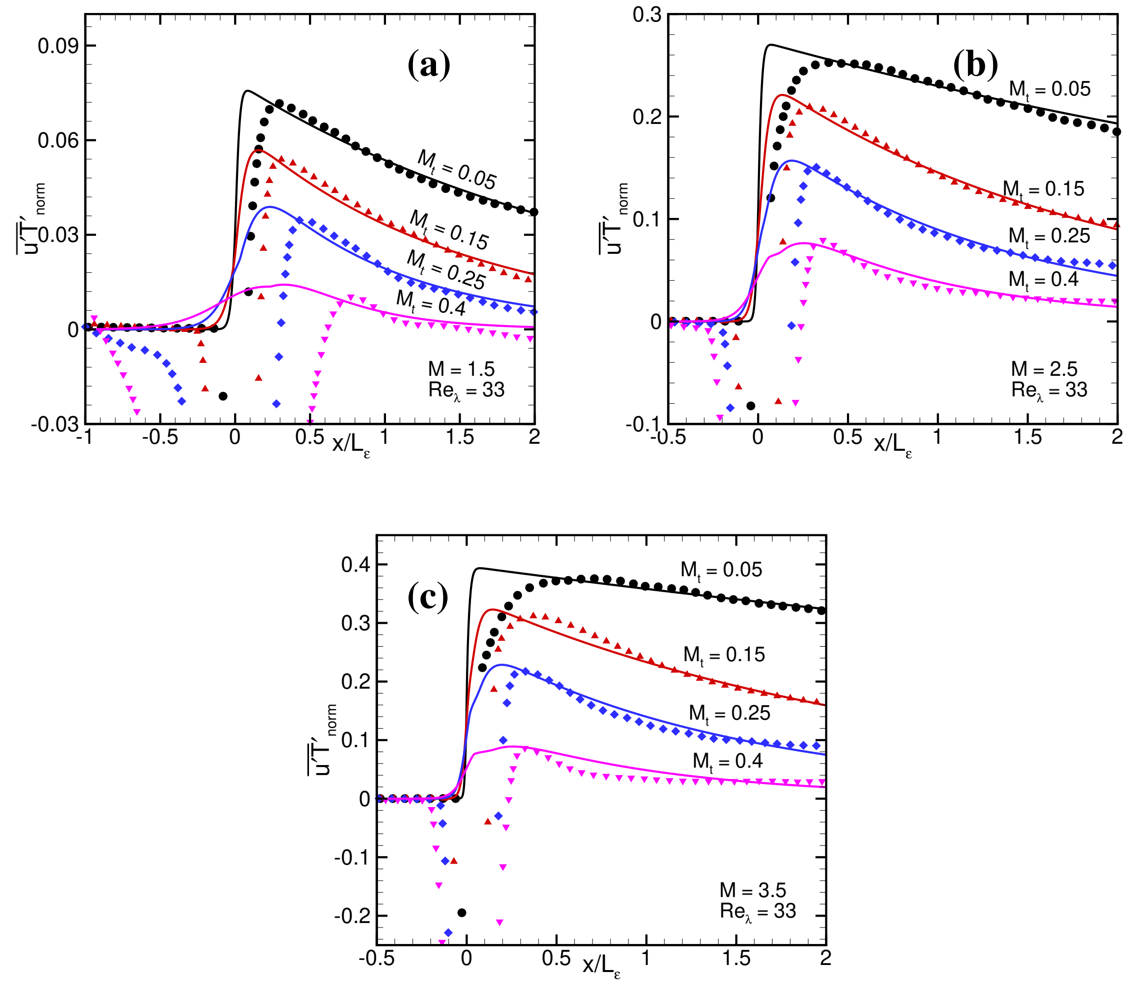

Figure 4.16: Streamwise variation normalized turbulent heat flux for different upstream flow and turbulent Mach numbers. The heat flux normalization is done as per figure 4.15 and the streamwise distance is normalized with the dissipation length scale $L_\epsilon = k^{3/2}/\epsilon$. The shock thickness in the numerical simulation is given as per DNS data. The symbolic representation of the DNS data is same as Fig. 4.15.

The peak turbulent heat flux is predicted well by the model for all M and M_t cases presented in Fig. 4.16. The M = 1.23 cases have low value of $\overline{u'T'}$ and they are not included in the figure. For a fixed Mach number, the positive peak decreases with the turbulence intensity. This trend is similar to turbulent kinetic energy (Fig. 4.4.3) and it is due to the increased damping effect of the shock oscillations at high turbulence intensity. Also, the location of the peak is closer to the shock wave than the DNS data, and this is due to the rapid non-monotonic variation of $\overline{u'T'}$ immediately behind the shock wave; see [67] for additional details. numbers.

4.5 Summary

Direct numerical simulation data is used to analyse the turbulent heat flux across a normal shock wave. The data is also used to analyse the turbulent statistics across the shock hole for high turbulence intensities at low Mach numbers. The data is also used to close the turbulent heat flux equation. The upstream temperature fluctuation is found to be important to find the post shock turbulent heat flux. An evaluation of the peak and post shock variation of the heat flux highlighted the efficacy of the new model equation based on the DNS data.

Chapter 5

Turbulent Heat Flux Model for Supersonic Flows

When applied to turbulent boundary layers and shock-boundary layer interaction at high Reynolds numbers, the computational cost of DNS becomes highly prohibitive. Moser and Moin [57] and Kim et al. [40] showed that the grid points required to accurately resolve the Kolmogorov length scales of a turbulent flow in three dimensions scaled as $Re^{9/4}$ and that temporal resolution of the Kolmogorov time scale was also required. Wall bounded turbulence is a multi-scale phenomena in which the energetic motions of the inner layer (closest to the wall) become progressively smaller in size as the Reynolds number increases, thus increasing the resolution requirements to resolve smaller and smaller structures. To overcome the limitation imposed by the cost and computational time of DNS, Reynolds-averaged Navier-Stokes (RANS) simulations are used for engineering applications where a quick prediction of the surface properties are often required. In this chapter a variable turbulent Prandtl number (Pr_T) based heat flux model is applied to oblique shock wave impingement SBLIs. The model development is very similar to that presented in chapter 4 with few more engineering assumptions, like gradient diffusion hypothesis and Boussinesq assumption.

5.1 Test cases

Experiments were conducted by Schulein [73] in the DLR Gottingen Ludwieg tube wind tunnel for oblique shock wave/turbulent boundary layer interaction flows with three different shock deflection angles of 6^o, 10^o and 14^o. All the test cases were performed at Mach 5 for 0.3s in the tunnel. The experimental configuration, shown in figure 5.1, consists of a flat plate and a shock generator with deflection angle β. The flat plate was kept in the center of test section, while the shock generator was placed axially above the plate. The position of the deflector was varied for each test case to impinge the inviscid shock at a fixed location of 350 mm from the plate leading edge. The incident shock strength increases with higher deflection angle, resulting in a stronger interaction with the turbulent boundary layer developed over the flat plate. The inflow unit Reynolds number, static pressure and temperature are 37×10^6 m^{-1}, 4008.5 N/m^2 and 68.3 K respectively. The flat plate surface temperature is 300 K. Dry air was taken as the test medium with perfect gas assumption. Initially, the experiments were performed for flow over flat plate to develop the undisturbed turbulent boundary layer and the boundary layer properties like δ, δ^*, θ and c_f were measured at different locations. Surface properties like pressure, skin friction and heat transfer rates were obtained along the flat plate in the interaction region.

5.2 Computational method

In order to compute a compressible turbulent flow using two-equation turbulence model, one needs to solve the Reynolds-averaged Navier-Stokes equations (RANS) for the mean flow along with the transport equations for the turbulence quantities. The standard k-ω model of Wilcox [92] and the shock unsteadiness modified k-ω model of Sinha et al. [79] are used for turbulence closure. The turbulence models do not include any compressibility corrections, as they are found to deteriorate model predictions in the undisturbed boundary layer upstream of the interaction [12, 22]. Compressibility corrections of the form of dilatational dissipation reduce the turbulent kinetic energy in the boundary layer, and thus decrease the skin friction coefficient compared to well-established correlations for zero pressure-gradient turbulent boundary layers.

The detailed description of the numerical method is given in chapter 3 and a brief summary of that is presented here. A finite volume formulation is used to discretize the governing mean flow equations fully coupled with turbulence model equations. The inviscid fluxes are solved using a modified, low-dissipation form of the Steger-Warming flux splitting method [52]. This method reduces the numerical dissipation, and is found to be useful for high-speed flows with strong shock waves and viscous-inviscid interactions with boundary layers. As a result, very thin and well-defined shock waves are captured over a few grid cells. The discretization method is second-order accurate in space; the details of the formulation can be found in Ref. [77]. The viscous fluxes and the turbulent source terms are calculated using second-order accurate central difference method. The implicit Data-Parallel Line Relaxation (DPLR) method of Wright et al. [93] is used to integrate the equations in time to reach a steady-state solution.

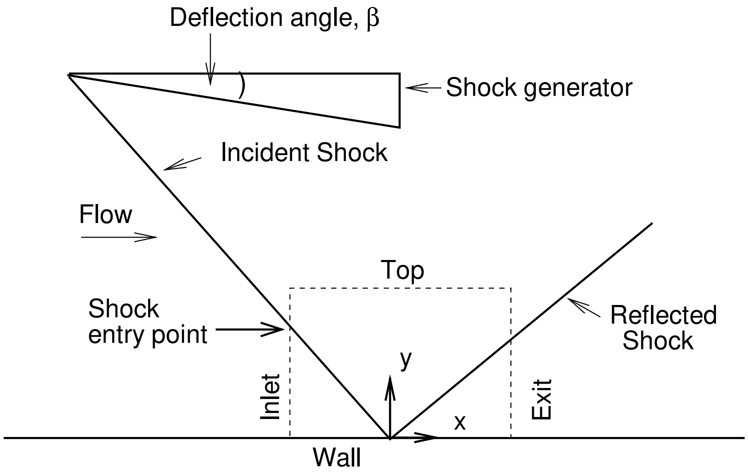

Figure 5.1: Experimental configuration of Schulein [73] to study the interaction of an oblique shock with a turbulent boundary layer. Dashed line represents the computational domain, with the boundary conditions marked in the figure.

The computational domain is shown in figure 5.1 by dashed line and it extends to about 14 δ_0 upstream and 25 δ_0 downstream of the shock impingement point. Here δ_0 = 5.9 mm is boundary layer thickness upstream of the shock impingement. No slip and isothermal boundary conditions are used at the wall, while extrapolation condition is applied at the exit boundary of the domain. Inlet profiles are obtained from separate flat plate simulation; the details can be found in Pasha et al. [60]. For the turbulence quantities, the boundary conditions at the wall [54] are prescribed as $k = 0$ and $\omega = 60\nu_w/\beta_1\Delta y_1^2$, where ν_w is kinematic viscosity at the wall, $\beta_1 = 3/40$ and Δy_1 is the normal distance to the grid point nearest to the wall. Following Menter [54], the freestream conditions used for the flat plate simulations are $\omega_\infty = 10U_\infty/L = 8.28 \times 10^3 s^{-1}$ and $k_\infty = 0.01\nu_\infty\omega_\infty = 1.87 \times 10^{-3} m^2/s^2$ where L = 1 m is a characteristic length of the flat plate. For the SBLI simulations, k and ω values at the boundary layer edge in the inlet profile are taken as the freestream conditions at the top boundary.

5.3 Variable turbulent Prandtl number model

The turbulent mode of heat transfer is an important unclosed term in the Reynolds averaged energy equation. In general, the turbulent heat flux vector $q_{T,j}$ is modeled using the gradient diffusion hypothesis

$$q_{T,j} = -\kappa_T \frac{\partial \overline{T}}{\partial x_j}, \tag{5.1}$$

where κ_T is the turbulent conductivity of heat. It is related to eddy viscosity via the turbulent Prandtl number Pr_T and the specific heat of the gas at constant pressure c_p.

$$\kappa_T = \frac{\mu_T c_p}{Pr_T} \tag{5.2}$$

Strong Reynolds analogy relates the turbulent heat flux to the Reynolds stress in a boundary layer and thus prescribes a constant value of the turbulent Prandtl number. This framework is used to propose an alternate model for the turbulent heat flux at shock waves in terms of a variable turbulent Prandtl number formulation.

Shock waves enhance turbulence, and lead to a jump in Reynolds stresses, turbulence kinetic energy, vorticity variances and the turbulent dissipation rate. Shock waves also generate large fluctuations in entropy, total temperature and other thermodynamic quantities. The Morkovin's hypothesis [56], based on the assumption of negligible total temperature fluctuations in a flow, therefore breaks down behind a shock wave. Consequently, the velocity temperature correlation coefficient and the equivalent turbulent Prandtl number may vary significantly from their values prescribed by Morkovin's hypothesis. Traditional modeling of the turbulent heat flux in terms of a constant Pr_T thus becomes fundamentally incorrect in regions of shock waves.

Quadros et al. [67] study the turbulent energy transfer when homogeneous isotropic turbulence interacts with a nominally normal shock wave. This is the most fundamental shock-turbulence interaction and it isolates the effects of shock wave on the turbulent transport of heat and momentum. Turbulent energy transfer is quantified in terms of the turbulent energy flux, which is proportional to the turbulent heat flux $q_{T,j}$. It is found that the turbulent energy flux attains a peak value immediately behind the shock, and the post-shock variation is governed by the acoustic decay behind the shock. The location of the peak turbulent energy flux is found to scale with the dissipation length scale that is characteristic of the acoustic disturbances in the flow.

Quadros and Sinha [65] propose improvements to the modeling of turbulent heat flux in canonical shock-turbulence interaction. Scaling relations from Linear Interaction Analysis (LIA) are used to propose a heat-flux limiter model for the turbulent energy flux at a shock wave. The model formulation is similar to the realizable k-ϵ models [75] and matches the DNS values of the peak heat flux for a range of shock strengths. However, being an algebraic model based on the local mean flow properties, it is not able to reproduce the downstream decay in the post-shock flow. Quadros and Sinha [65] also develop a transport equation based model to bring in the history effect of the shock wave in the downstream flow. It includes the downstream decay in terms of the turbulent dissipation length scale and the model predictions match the DNS decay rate up to about one dissipation length behind the shock. This region is expected to be crucial in predicting the wall heat transfer rates, especially in the case of strong SBLI with large separation bubble.

In the current work, a simpler approach than [65] is used to model the turbulent heat flux in terms of a variable turbulent Prandtl number. This is unlike the previous paper, where the turbulent heat flux is modeled directly in the form of an algebraic or differential equation [65]. Being a scalar formulation, the Pr_T approach is easily extendable from one-dimensional canonical shock-turbulence interaction to multi-dimensional SBLI flows. It can also be easily integrated in existing CFD codes, which are traditionally based on constant Prandtl number formulation. In the following, we cast the shock-induced turbulent heat flux into an equivalent turbulent Prandtl number, and propose a variable Pr_T model based on shock-turbulence interaction physics. The variation of Pr_T across a shock wave, if estimated correctly, could improve the heat flux prediction capabilities of the standard turbulence models.

The model is initially developed for a one-dimensional flow through a normal shock, and then extended to two- and three-dimensional flows with oblique and multiple shock waves. The mean flow gradients in the shock-normal direction are very high compared to those in the shock parallel directions. Hence, only the shock-normal component of the velocity and temperature gradients are considered for evaluating the turbulent Prandtl number. The shock-normal Reynolds stress is given in terms of the Boussinesq approximation.

$$-\overline{u'^2} = \frac{4}{3}\nu_T \frac{\partial \overline{u}}{\partial x} - \frac{2}{3}k, \tag{5.3}$$

where ν_T is the turbulent kinematic viscosity. The first part is proportional to the mean strain rate across a shock and it is much larger than the turbulent kinetic energy contribution to the Reynolds stress. One can thus write

$$\nu_T = -\frac{3}{4}\overline{u'^2}\left(\frac{\partial \overline{u}}{\partial x}\right)^{-1}. \tag{5.4}$$

Here, the Reynolds averaging procedure is used over Favre averaging, as the difference between the two methods is found to be negligible for Mach numbers up to 6 [67]. Similarly, we can write the thermal eddy diffusivity by applying the gradient-diffusion hypothesis across the shock.

$$\alpha_T = -\overline{u'T'}\left(\frac{\partial \overline{T}}{\partial x}\right)^{-1}, \tag{5.5}$$

where $\overline{u'T'}$ represents the shock-normal component of the turbulent heat flux vector. The turbulent Prandtl number is thus given by

$$Pr_T = \frac{\nu_T}{\alpha_T} = \frac{3}{4}\frac{\overline{u'^2}}{\overline{u'T'}}\frac{\partial \overline{T}}{\partial x}\left(\frac{\partial \overline{u}}{\partial x}\right)^{-1} \tag{5.6}$$

The mean flow gradients are computed as part of a RANS solution, and several models are available for the Reynolds stresses, for example, k-ω, k-ϵ, SST, etc. The turbulent heat flux at a shock is estimated as follows.

The conservation of total enthalpy is considered for a turbulent flow passing through a shock wave. It is written in terms of the total temperature in the frame of reference of the shock wave, which undergoes unsteady motion in response to the fluctuations in a turbulent flow. The deviation of the shock from its mean position is taken as $\xi(y, z, t)$, such that the temporal derivative ξ_t represents the instantaneous shock speed in the streamwise direction [76]. The total temperature is written as

$$T_0 = \overline{T} + T' + \frac{(\overline{u} + u' - \xi_t)^2 + v'^2 + w'^2}{2c_p}, \tag{5.7}$$

by assuming that the shock wave distorts by small angles from its planar mean position. Here, u,v,w are the velocity components, overbar represents mean flow quantity and primes denote turbulent fluctuations. The total temperature is being equated between the shock upstream 1 and downstream 2 locations.

$$T_1' + \frac{\overline{u_1}(u_1' - \xi_t)}{c_p} = T_2' + \frac{\overline{u_2}(u_2' - \xi_t)}{c_p}, \tag{5.8}$$

where the shock speed and the fluctuations are assumed to be small compared to the jumps in the mean flow quantities across the shock. Terms containing squares of fluctuations are therefore neglected. Rearranging the above equation gives

$$T_1' + \frac{\overline{u_1}u_1'}{c_p} = T_2' + \frac{\overline{u_2}u_2'}{c_p} + \frac{\xi_t}{c_p}(\overline{u_1} - \overline{u_2}), \tag{5.9}$$

where the left hand side represents the linearized form of the total temperature fluctuations upstream of the shock wave. As per Morkovin's hypothesis [56], it can be expected that the total temperature fluctuations in the upstream flow to be negligible, and this results in

$$T_2' + \frac{\overline{u_2}u_2'}{c_p} = -\frac{\xi_t}{c_p}(\overline{u_1} - \overline{u_2}), \tag{5.10}$$

which gives an expression for the turbulent heat flux behind the shock wave.

$$c_p\overline{u'T'} = -\overline{u}\left(\overline{u'^2} + \overline{u'\xi_t}(r-1)\right), \tag{5.11}$$

where r is the mean density ratio across the shock wave and the subscripts are dropped for convenience.

The above expression relates the turbulent heat flux to the streamwise Reynolds stress and can be used to obtain a value of the turbulent Prandtl number. To achieve this, the shock-unsteadiness model of Sinha et al. [78] (see subsection 2.4.6) is employed, where the unclosed $\overline{u'\xi_t}$ correlation is written in terms of the shock-normal Reynolds stress component.

$$\overline{u'\xi_t} = b_1\overline{u'^2}, \quad \text{with} \quad b_1 = 0.4 + 0.6e^{2(1-M_{1n})} \tag{5.12}$$

This is based on the assumption that the unsteady shock motion is caused by the incoming turbulent velocity fluctuations, and the closure coefficient b_1 is obtained from the linear interaction analysis. The above model for the shock unsteadiness damping correlation accounts for the shock motion at frequencies comparable to that of the incoming turbulence. Additional low-frequency shock oscillations, observed in SBLI, has vanishingly small correlation with the turbulent velocity fluctuations in the boundary layer. Such low frequency shock motion does not contribute to the damping effect in the current framework. Thus the turbulent heat flux equation become

$$\overline{u'T'} = -\frac{\overline{u}}{c_p}\overline{u'^2}\left(1 + b_1(r-1)\right), \tag{5.13}$$

which on substitution in Eq. (5.6) gives the turbulent Prandtl number relation for canonical shock-turbulence interaction.

$$Pr_T = \frac{3}{4}\left(\frac{1}{1 + b_1(r-1)}\right) \tag{5.14}$$

Here, we have used the mean flow energy conservation to relate the mean temperature and velocity gradients at the shock, assuming minimal contribution from the turbulent kinetic energy to the total enthalpy of the flow.

Figure 5.2 shows the variation of Pr_T with shock strength represented in terms of the mean density ratio across the shock. The shock unsteadiness parameter b_1 is also a function of the shock strength, via the shock-normal mean flow Mach number. The turbulent Prandtl number at the shock is lower than the conventionally accepted boundary layer $Pr_{T,0} = 0.89$ and it decreases for stronger shocks. This is consistent with the shock physics, where a stronger interaction has a larger effect on the turbulent transfer of heat and momentum.

DNS data shows that the turbulent energy flux increases dramatically at a shock wave [67]. It attains a peak in magnitude immediately behind the shock and then exponentially decays with distance from the shock wave. In a similar vein, it is reasonable to expect

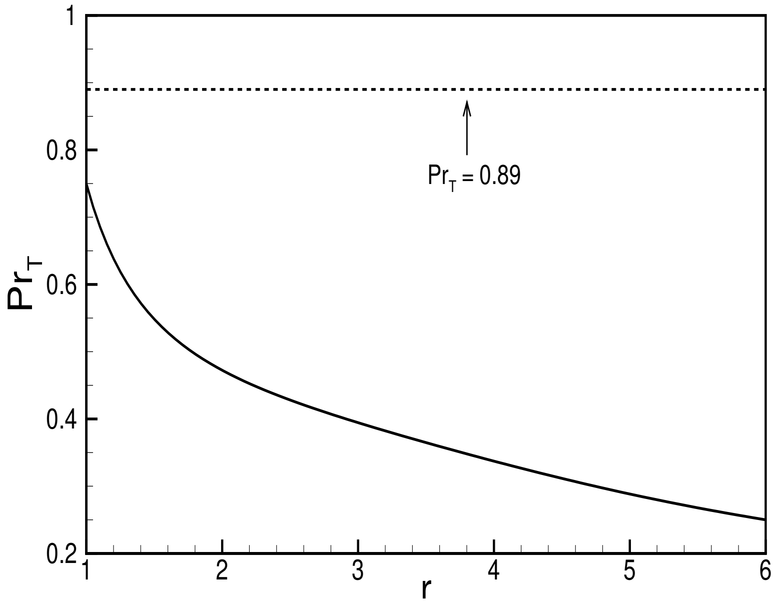

Figure 5.2: Turbulent Prandtl number as a function of the density ratio across a shock wave.

that the turbulent Prandtl number relaxes from its shock value to the conventional value of 0.89 away from the shock, such that the low Pr_T values attained at the shock persists for some finite distance in the downstream flow. Note that a lower Pr_T is equivalent to higher κ_T and higher turbulent heat flux. The post-shock behaviour can be modeled by a differential equation that has an exponentially varying solution behind the shock. The approach is similar to the differential equation model proposed for turbulent energy flux in Ref. [65].

5.3.1 Scalar Shock function

Instead of writing a transport equation for the turbulent Prandtl number, a scalar shock function ψ is introduced and a transport equation is written for the same. The objective is that ψ should identify the regions of shock wave in a flow and bring in the history effect of the shock in the downstream flow. The turbulent Prandtl number can then easily be modeled in terms of ψ. The transport equation for ψ is such that it deviates from its undisturbed value ψ_0 only in the regions of strong compression and gradually relaxes back from the shock value to the reference value.

$$\frac{\partial(\bar{\rho}\bar{u}\psi)}{\partial x} = \bar{\rho}\psi\frac{\partial \bar{u}}{\partial x} - \bar{\rho}(\psi - \psi_0)\frac{\bar{u}}{L_\epsilon} \tag{5.15}$$

Here, the left hand side represents the convection in the shock-normal direction x, the first term on the right-hand side brings in the effect of one-dimensional mean compression, and

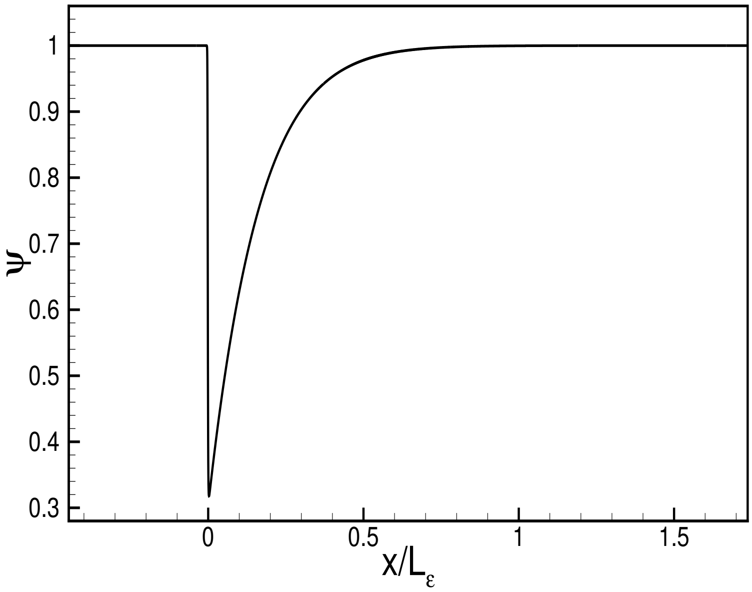

Figure 5.3: Streamwise variation of the shock function ψ across a Mach 2.5 normal shock located at x$/L_\epsilon = 0$.

the second term results in the exponential post-shock variation. Dropping the last term, and integrating across the shock yields

$$\frac{\psi_s}{\psi_0} = \frac{\overline{u_2}}{\overline{u_1}} = \frac{1}{r}, \tag{5.16}$$

where the shock value ψ_s is an indicator of the shock strength and an upstream undisturbed value of $\psi_0 = 1$ ensures that it gets $\psi_s = 1/r$ at the shock location. Figure 5.3 shows the variation of ψ in a Mach 2.5 canonical shock-turbulence interaction. The ψ equation is integrated with the shock unsteadiness modified k-ϵ model [38] applied to the one-dimensional mean flow through the normal shock, and the dissipation length $L_\epsilon = \sqrt{k^3}/\epsilon$ is computed using the local values of turbulent kinetic energy and its dissipation rate ϵ. A minimum value of $\psi_s = 0.31$ is observed for a density ratio of 3.33 across the shock wave, and it relaxes back to the reference value by $x/L_\epsilon \simeq 1$.

Next, a substitution of $r = 1/\psi$ in Eq. (5.14) gives an expression for turbulent Prandtl number

$$Pr_T = \frac{3}{4}\frac{\zeta}{1 + b_1(\frac{1}{\psi} - 1)}, \tag{5.17}$$

where an additional factor ζ is introduced to make the formulation consistent with the conventionally accepted Pr_T value of 0.89 in boundary layers without shock waves. Thus, ζ is defined as

$$\zeta = 1 + \left(\frac{0.89}{0.75} - 1\right) exp\left(\chi(1 - \frac{1}{\psi})\right) \tag{5.18}$$

such that it is equal to 0.89/0.75 in the absence of strong compression ($\psi \rightarrow 1$) and approaches 1 in the presence of shock waves. Figure 5.4 plots the results for ψ ranging from 1/6 (for $M_1 \rightarrow \infty$) to 1 (vanishingly weak shock wave), for a few different values of χ. The parameter χ decides how fast or slow the transition between the shock value of Pr_T and its reference value $Pr_{T,0}$ takes place.

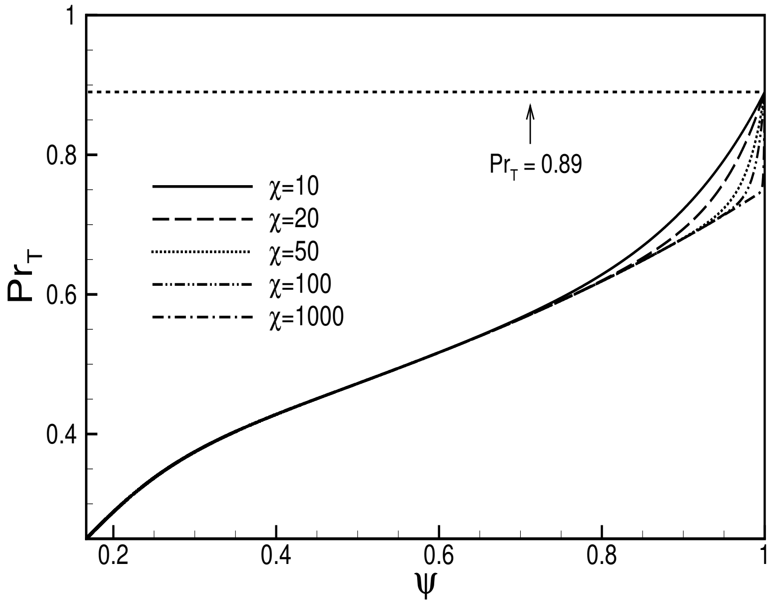

Figure 5.4: Effect of the model parameter χ on the variation of the turbulent Prandtl number Pr_T with shock function ψ.

Figure 5.5 shows the Pr_T computed as a function of streamwise distance for a Mach 2.5 shock wave. It drops from its undisturbed value of 0.89 to about 0.35 at the shock wave, and then exponentially increases back to its reference value. Results are plotted for different values of χ, and it shows the transition from $Pr_{T,shock}$ prescribed by the shock physics to $Pr_{T,0}$. The turbulent Prandtl number approaches the reference level faster for $\chi = 10$, whereas it follows the $Pr_{T,shock}$ values longer for $\chi = 1000$ and switches back to $Pr_{T,0}$ around x $\sim L_\epsilon$. The effect of these differences on the predicted wall heat transfer rate is reported subsequently.

5.3.2 Application to canonical shock-turbulence interaction

The current model is applied to the turbulent heat flux generated across a shock wave in canonical shock-turbulence interaction, for which LIA and DNS data is available in Refs. [44, 65–67]. Quadros et al. [67] study the shock-normal component of the turbulent energy flux $\overline{u'e'}$ in canonical STI. Here, $e = c_v$T is the specific internal energy of the fluid,

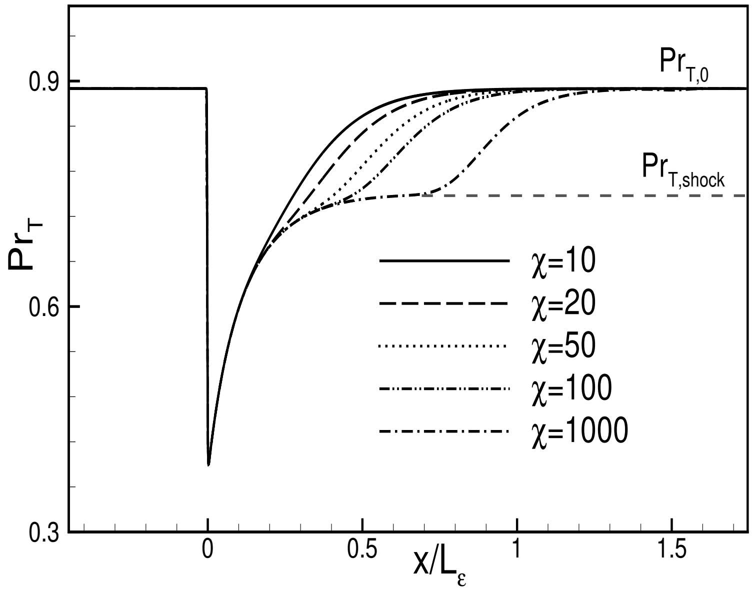

Figure 5.5: Variation of turbulent Prandtl number with streamwise distance for a Mach 2.5 shock wave, computed using different values of the model parameter χ.

c_v is the specific heat at constant volume and specific enthalpy $h = \gamma e$. We thus have

$$q_{T,x} = \overline{u'h'} = \gamma\overline{u'e'}. \tag{5.19}$$

In a subsequent work, Quadros and Sinha [65] propose physics-based models for the $\overline{u'e'}$ generated behind the shock wave. The algebraic heat flux limiter model is of particular interest in the current context and will be considered here. The model is developed using results from linear interaction analysis applied to canonical shock-turbulence interaction, and has a form similar to the realizable Reynolds stress models [84]. The model predicts the peak energy flux behind the shock wave and is able to match well with the DNS data of Larsson et al. [44].

The canonical STI cases considered in the previous works [65–67] have purely vortical turbulence field upstream of the shock. The same is true for the extensive DNS database of Larsson et al. [44, 46], where magnitude of thermodynamic fluctuations are negligible before the shock wave. For such flows, $T_1' = 0$ in Eq. (5.9) but the contribution of u_1' has to be retained in the derivation.

A variable Pr_T model is developed for canonical shock turbulence interaction where a homogeneous isotropic disturbance field interacts with a normal shock. The initial development is similar to that presented in section 5.3 and it relates the change in total temperature fluctuations across the shock to the unsteady shock oscillation speed ξ_t. Starting with Eq. 5.9

$$T_1' + \frac{\overline{u_1}u_1'}{c_p} = T_2' + \frac{\overline{u_2}u_2'}{c_p} + \frac{\xi_t}{c_p}(\overline{u_1} - \overline{u_2}) \tag{5.20}$$

For purely vortical turbulence upstream of the shock wave, we have $T_1' \to 0$, which leads to

$$T_2' + \frac{\overline{u_2}u_2'}{c_p} = \frac{\overline{u_1}u_1'}{c_p} - \frac{\xi_t}{c_p}(\overline{u_1} - \overline{u_2}) \tag{5.21}$$

Compared to Eq. (5.10) in section 5.3, the right-hand side has the additional contribution from the upstream velocity fluctuation u_1'. On taking a moment with u_2' yields

$$\overline{u_2'T_2'} = -\frac{\overline{u_2}}{c_p}\left(\overline{u_2'^2} + \overline{u_2'\xi_t}(r-1) - r\overline{u_1'u_2'}\right) \tag{5.22}$$

The unclosed correlation between the upstream and downstream velocity fluctuations is modeled in terms of the parameter α.

$$\overline{u_1'u_2'} \sim \alpha\overline{u_2'^2}$$

and unsteady shock speed is modeled as per Eq. (5.12) to get

$$\overline{u'T'} = \frac{\overline{u}}{c_p}\overline{u'^2}\left[(r\alpha - 1) - (r-1)b_1\right], \tag{5.23}$$

where the subscript 2 is dropped for convenience. The above form is identical to Eq. (5.13) except for α. Substitution into Eq. (5.6) leads to,

$$Pr_T = \frac{3}{4}\left(\frac{1}{b_1(r-1) - (r\alpha - 1)}\right) \tag{5.24}$$

The turbulent energy flux is modeled in terms of the turbulent heat flux

$$\overline{u'e'} = \frac{\overline{u'h'}}{\gamma} = -\frac{\kappa_T}{\gamma\overline{\rho}}\frac{\partial\overline{T}}{\partial x} = -\frac{\mu_T c_p}{\gamma\overline{\rho}Pr_T}\frac{\partial\overline{T}}{\partial x}, \tag{5.25}$$

where the eddy viscosity μ_T is obtained from a realizable turbulence model [84]. For a normal shock, we have

$$\mu_T = \frac{\sqrt{3c_\mu^o}}{2}\overline{\rho}k\left|\frac{\partial\overline{u}}{\partial x}\right|^{-1} \tag{5.26}$$

which on substitution in Eq. (5.25) yields

$$\overline{u'e'} = \widetilde{\beta}\frac{k\overline{u}}{\gamma}. \tag{5.27}$$

The form is very similar to that proposed by Quadros and Sinha [65], where $\widetilde{\beta}$ is given by

$$\widetilde{\beta} = \beta_0\left(1 - \exp(1 - M_1)\right) \quad \text{and} \quad \beta_0 = \frac{2}{3}\sqrt{3c_\mu^o}\left[(\mathrm{r}\alpha - 1) - \mathrm{b}_1(\mathrm{r} - 1)\right]. \tag{5.28}$$

Note that the modeling parameter $\widetilde{\beta}$ in the heat flux limiter model [65] is obtained from the hypersonic limiting value of the $\overline{u'e'}$ as per LIA. By comparison, the modeling parameter β_0 is directly derived from the governing equation. It is a function of α which relates the upstream and downstream velocity fluctuations, and is expected to be of order 1. A value of $\alpha = 0.6$ matches the DNS data fairly well over the entire range of Mach numbers. This value is the same as the high Mach number ($M \geq 3$) value obtained in chapter 4.

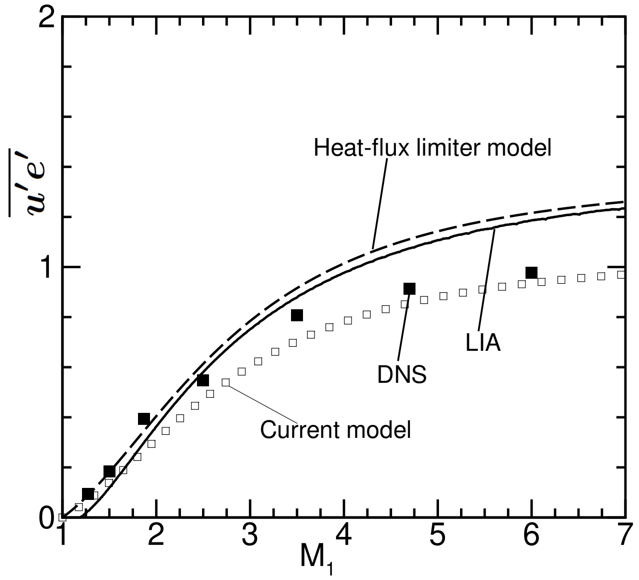

Figure 5.6: Peak turbulent energy flux generated in canonical shock-turbulence interaction [67]. The current model is compared with DNS data, LIA predictions and the heat-flux limiter model [65].

5.3.3 Extension to shock-boundary layer interaction

For application to real life flows involving multiple shock waves and boundary layer, the transport equation of ψ (Eq. 5.15) can be written in a general frame-invariant tensor form as,

$$\frac{\partial(\overline{\rho}\psi)}{\partial t} + \frac{\partial(\overline{\rho}\widetilde{u}_i\psi)}{\partial x_i} = \overline{\rho}\psi S_{ii} - \overline{\rho}(\psi - \psi_0)\frac{\sqrt{\widetilde{u}_i\widetilde{u}_i}}{L_\epsilon}, \tag{5.29}$$

where $\sqrt{\widetilde{u}_i\widetilde{u}_i}$ is the mean velocity magnitude and $L_\epsilon = \sqrt{k}/\omega$ is the dissipation length scale in the k-ω framework. Here, the Reynolds and Favre averaged quantities are used in a way that is consistent with the RANS equations, and the temporal derivative is added for unsteady flows. Further, ψ is artificially kept under the maximum limit of 1 in regions where S_{ii} is positive, such as expansion fans. The transport equation for ψ is solved using the Lax-Friedrich method with explicit time integration. The ψ-solver is decoupled from the main solver for the mean and turbulence model equations described in chapter 3. A constant CFL of 0.2 is used to update the ψ-function at each time step, and it evolves to attain steady state values in every grid cell, as the flow field converges to its steady state solution.

The shock function is expected to identify the high compression regions in an SBLI flow. These would include the incident shock, separation shock, reflected shock and others, most of which are oblique in nature. The ψ function computed using Eq. (5.29) will yield the density jump across the oblique shocks. This corresponds to the strength of the equivalent normal shock. The current model developed for a normal shock wave is thus extended to oblique shocks, as per the local ψ value. This is based on the assumption that the gradients in the shock-normal direction and the corresponding heat flux component plays a dominant role at the shock wave. A more general derivation for oblique shocks will involve transverse velocity fluctuations, and the turbulent Prandtl number will have contributions of the Reynolds shear stresses. The canonical STI problem does not provide information on Reynolds shear stresses, and the current approach will be limited in shock waves that are highly oblique to the incoming flow. An alternate approach would be to extend the current model using Reynolds shear stress data from DNS of SBLI flows. The theoretical framework presented in Ref. [86] to compute post-shock Reynold stresses can be used.

The canonical STI assumes uniform mean flow upstream and downstream of the shock wave. The presence of incoming boundary layer gradients in an SBLI flow can result in a curved shock wave. The shock curvature is governed by the transverse gradient of Mach number, and is expected to be high for hypersonic conditions (see, for example, SBLI flow computations in Ref. [61]). There is a minimal effect of shock curvature in the Mach 5 SBLI cases considered in this chapter; see section 5.4 for further details.

The linear interaction analysis of canonical STI models a shock wave as a well-defined discontinuity. The linear theory is based on the assumption that the turbulent fluctuations are small compared to the jump in mean properties across the shock. The assumption is compromised in transonic flows (M $\rightarrow$ 1) and near the sonic line in a supersonic or hypersonic boundary layer. It can be physically argued that the effect of the shock is negligible in the limit of Mach number approaching unity, and the turbulence quantities, including the turbulent heat flux, tends to its upstream undisturbed value. This is built into the current model, Eq. (5.17), where $Pr_T \rightarrow Pr_{T,0}$ when $\psi \rightarrow 1$ for vanishingly weak shock waves.

Further, the LIA framework is based on inviscid flow with a homogeneous isotropic turbulence field upstream of the shock wave. These assumptions are not valid in the near-wall region of a turbulent boundary layer, where low Reynolds number corrections, with damping functions, are often used. In the present context, experimental data suggest that the turbulent Prandtl number is lower than the conventionally accepted value of 0.89 in the log-region of a turbulent boundary layer. A log-layer value of 0.85 is reported for zero pressure gradient boundary layers [39]. Using this value as $Pr_{T,0}$, instead of 0.89, will result in a further reduction of Pr_T across the shock, leading to a lower wall heat flux prediction. This can also be incorporated into the model in the form of a low Reynolds number damping function that will be active in the near-wall region of a turbulent boundary layer.

5.3.4 Local formulation of Shock-unsteadiness model

The physics of shock-turbulence interaction is highly dependent on shock strength and the parameter b'_1 brings in this effect in terms of the shock normal upstream Mach number M_{1n}; see Eq. (2.80). This makes the CFD implementation of the shock-unsteadiness model non-local in nature. The flow variables at upstream points of the shock wave are used to evaluate b'_1 required to solve the turbulent kinetic energy equation at points in the shock region. Computing M_{1n} is not trivial for flows involving multiple shock interactions [60, 61], where the shock topology is not known a priori. Preliminary simulations are done to get an estimate of the shock location, shape and strength, which are then used to compute b'_1 in a subsequent simulation. This increases the computational time and human effort to obtain the final results using shock-unsteadiness model.

In this work, the non-local nature of the shock-unsteadiness model is eliminated. The upstream shock-normal Mach number dependence of the model parameter is replaced by the local density ratio r, which is used to represent the shock strength. The shock-unsteadiness parameter is recast as

$$b'_1 = 0.4\left(\frac{r-1}{5}\right)^{0.3} = 0.4\left(\frac{1-\psi}{5\psi}\right)^{0.3}, \tag{5.30}$$

where the exponent is obtained using least square curve fitting to the original b'_1 in Eq. (2.80), and the local density ratio is written in terms of the shock function ψ. In the undisturbed flow ahead of shock waves, $\psi = \psi_0 = 1$, which implies $b'_1 = 0$ and the shock unsteadiness correction is not applied. At shock waves, ψ takes the value $1/r$, as per Eq. (5.16), and it captures the shock strength for computing the local value of b'_1. Thus the flow-physics of the original shock-unsteadiness model remain unchanged. The exponential decay of ψ in the post-shock flow does not affect the shock-unsteadiness model correction, as $f_s \to 0$ outside of shock waves.

The local shock-unsteadiness model produces similar results to those of the original non-local version of the model [60, 79]. Figure 5.7 presents the surface properties computed for a 10 degree oblique shock impinging on a turbulent boundary layer. The current results obtained using the local SU k-ω model are almost identical to earlier results of the non-local SU k-ω model [60]. In the earlier study, the variation of the shock-unsteadiness parameter b'_1 was computed manually along the different shock waves in the interaction region, and a mean value of the parameter was used to obtain the final predictions. By

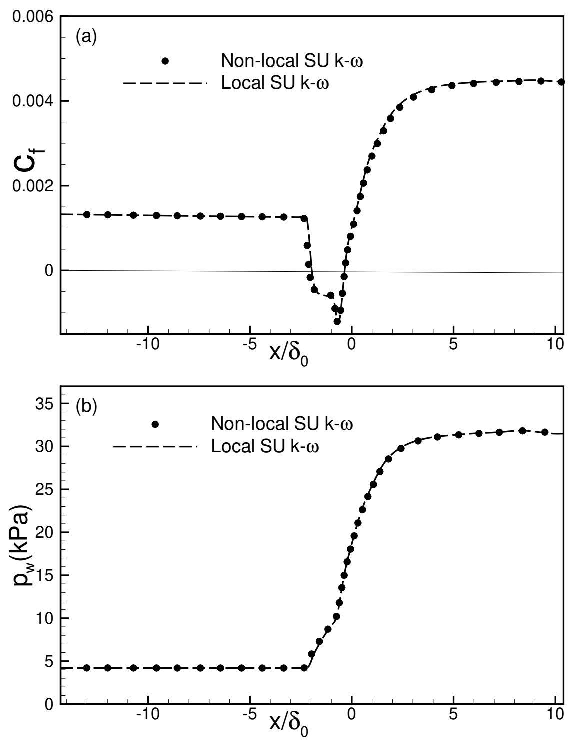

Figure 5.7: Comparison of (a) skin friction coefficient and (b) surface pressure for $\beta = 10^o$ oblique shock turbulent boundary layer interaction at $M_\infty = 5$, computed using the non-local SU k-ω [60] and the current local SU k-ω models.

comparison, in situ computation of b_1' in terms of the shock-function ψ gives the variation of the model parameter as part of the solution and is directly used in the on-going computation. This results in a 20% reduction in the computational time of the simulation on identical grid. The results obtained for the other cases with 14 and 6 degree shock generators are similar to those presented in Fig. 5.7 and are not repeated here.

The model parameter b_1 in Eq. (5.12) is also recast as

$$b_1 = 0.4 + 0.6\left(\frac{6-r}{5}\right)^{5.2} = 0.4 + 0.6\left(\frac{6\psi-1}{5\psi}\right)^{5.2}, \tag{5.31}$$

in terms of local mean density ratio across the shock wave and the shock function ψ. The coefficient 0.4 and 0.6 in the above equation are retained from the original form of b_1 given in Eq. (5.12). Similarly, the coefficient 0.4 in Eq. (5.30) is matched to that in Eq. (2.80). The original form of the model parameters b_1 and b_1' were proposed in Ref. [78] to match LIA data for canonical shock-turbulence interaction. They have been found to work well in SBLI flows over a range of Mach number for different geometric configurations [60, 61, 79], and are therefore incorporated into the current model. The exponents in Eqs. (5.30) and (5.31) are obtained by curve fitting to the original model coefficients b_1 and b_1' from [78].

It should be noted that the above formulation is for the SU k-ω model. We can develop local formulation of the shock-unsteadiness corrected k-ϵ and SA models, in a similar way. Also, the variable Pr_T model proposed in this work can be implemented in the k-ϵ framework, using the alternate form of $L_\epsilon = k^{3/2}/\epsilon$. The definition of the dissipation length scale is not trivial for the SA model, and further work is required in this direction.

5.4 Results

The variable Pr_T model is next applied to oblique shock impingement SBLI flows. Three cases with progressively increasing shock strength are presented, and the predictions of the variable Pr_T model are compared with those of existing turbulence models. The simulations are performed on 300×400 computational grids, and a detailed grid refinement study is presented below.

5.4.1 Grid Convergence Study

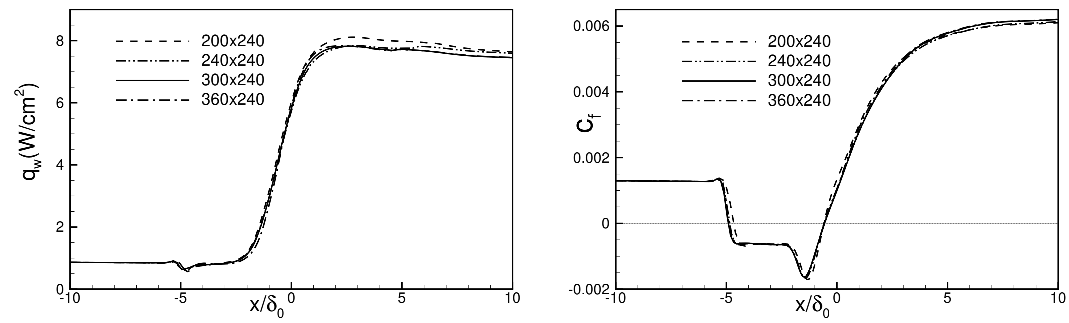

Figure 5.8: Effect of varying number of wall parallel grid points on computed (a) wall heat flux and (b) skin friction coefficient for $\beta = 14^o$ and $M_\infty = 5$.

A structured Cartesian grid is used to capture the strong shock waves, expansion fans and separated flow region. The mesh is stretched exponentially in both wall normal and streamwise directions. The grid points are clustered at $x/\delta_0 = 0$ (point of inviscid shock impingement) and exponential stretching is applied upstream and downstream of the interaction zone. A careful grid refinement study is done by systematically varying the number of grid points in each direction, as well as refining the cell size in the wall-normal direction. The skin friction coefficient is found to be most sensitive to the computational mesh and is used to identify a grid independent solution. Note that the current simulations are done using the local form of the SU k-ω model. A similar grid-refinement study is reported in [60] for the original non-local SU k-ω model applied to identical SBLI cases.

The grid refinement study for the $\beta = 14^o$ strongest interaction is shown here. The variable turbulent Prandtl number model is used to study the grid converged solution. The number of points in the wall parallel direction is refined first. The skin friction and wall heat flux plots in figure 5.8 indicate that 300 grid points are sufficient for an accurate solution. Next, the number of points in the wall-normal direction is increased until the two finest grid, 300×400 and 300×460, give overlapping solutions in figure 5.9. Finally, the normal distance of the first cell center from the wall is successively reduced. Figure 5.10 shows that the first cell center distance of 1×10^{-6} m is sufficient to obtain a grid converged solution. This corresponds to a y_2^+ value of 0.5 or lower in the interaction region. Based on the above grid refinement study, the solution obtained from 300×400 grid points with first cell center distance of 1×10^{-6} m from the wall is considered as grid converged. The same grid is used to generate all the results presented in this chapter, including the weaker interaction cases.

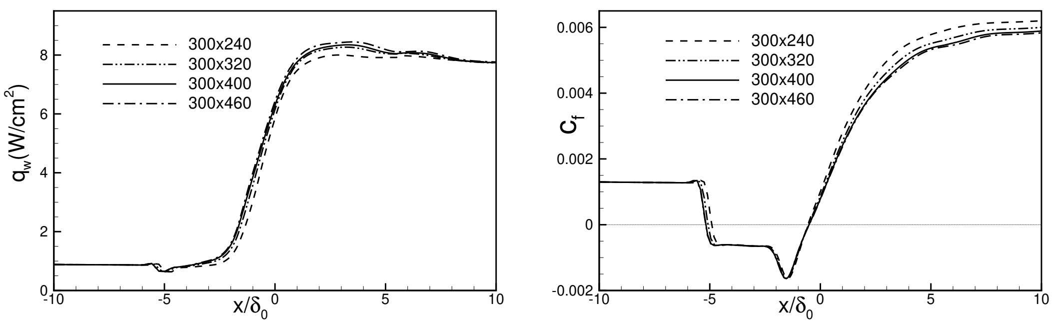

Figure 5.9: Effect of varying number of wall normal grid points on computed (a) wall heat flux and (b) skin friction coefficient for $\beta = 14^o$ and $M_\infty = 5$.

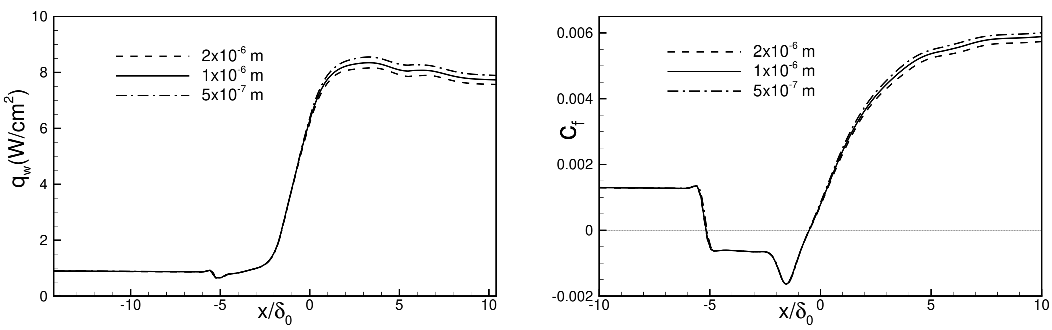

Figure 5.10: Effect of varying wall normal spacing on computed (a) wall heat flux and (b) skin friction coefficient for $\beta = 14^o$ and $M_\infty = 5$.

5.4.2 6 degree case

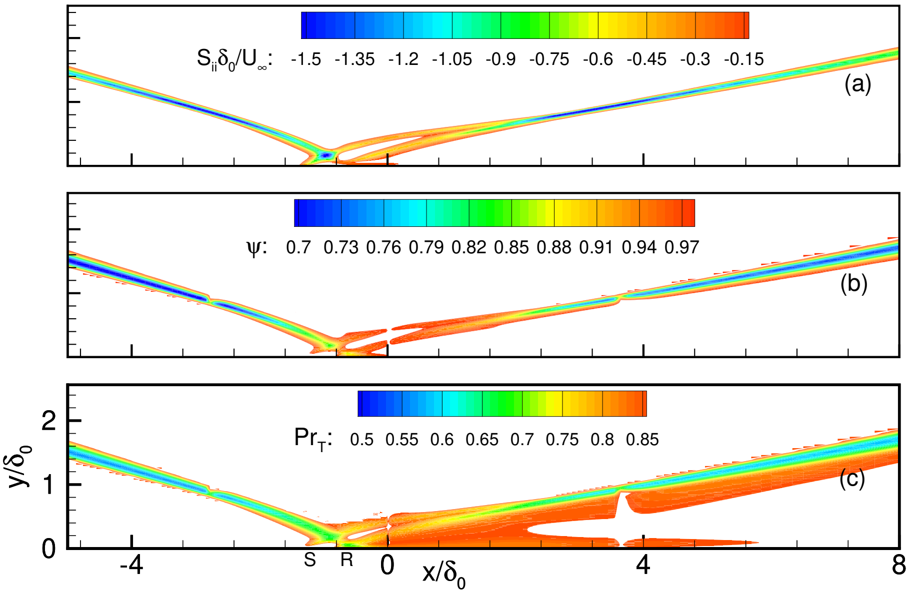

Figure 5.11: Distribution of (a) shock function ψ and (b) turbulent Prandtl number for $\beta = 6^o$ and $M_\infty = 5$ shock-boundary layer interaction.

Figure 5.11 shows the shock structure for an SBLI generated by the 6 degree shock deflector, where the streamwise and wall-normal distances are normalized by δ_0. The solution corresponds to the SU k-ω turbulence model with the variable Pr_T formulation. Figure 5.11(a) shows the distribution of dilatation. Here the dilatation contour is normalized by the upstream boundary layer thickness δ_0 and the freestream velocity U_∞. Figure 5.11(b) shows that ψ deviates from its reference value of 1 in the regions of shock waves. The same is true for the turbulent Prandtl number; see Fig. 5.11(c). The regions with $\psi <$ 0.97 and $Pr_T < 0.85$ are highlighted in the plots. In the interaction region, ψ is around 0.85 and it results in a Pr_T value of about 0.67. This is about 25% lower than the conventional value of 0.89. Even lower values of Pr_T, in the range of 0.5, are observed in the incident and reflected shocks, but they do not affect the surface heat flux predictions directly.

Figure 5.12 compares the computed surface properties with the experimental data reported by Schulein [73]. Three turbulence models are used in the simulations, namely, the standard k-ω model, the shock-unsteadiness k-ω and the variable Pr_T formulation added to the shock-unsteadiness k-ω model. All the three turbulence models predict almost identical surface pressure, with a small deviation in the vicinity of the shock impingement point. There is a dip in c_f due to incipient separation in k-ω solution, while the shock-unsteadiness model gives a finite, but small separation bubble. This is because of

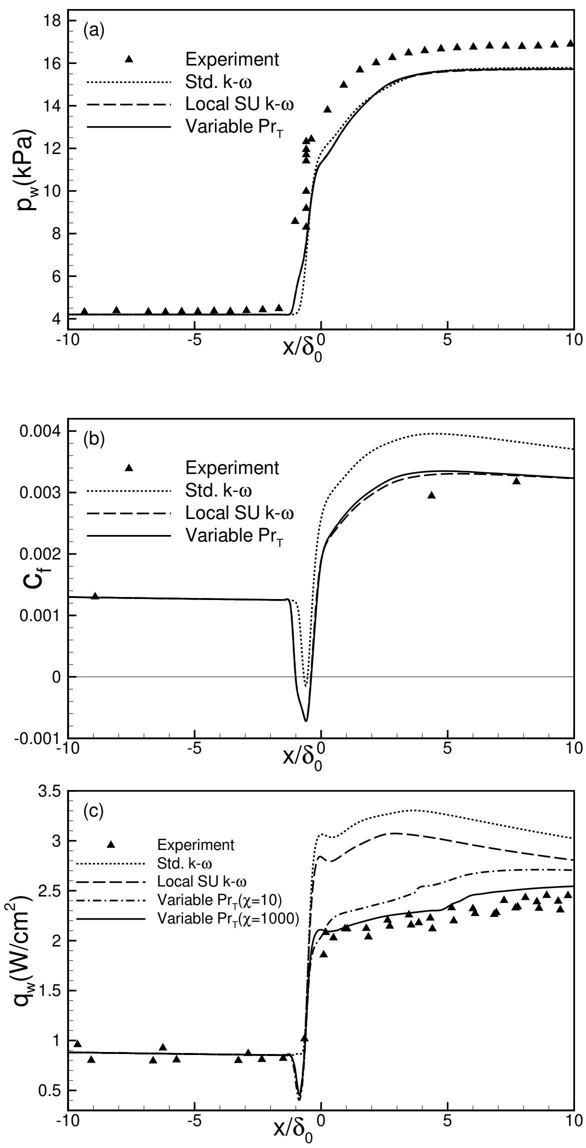

Figure 5.12: Comparison of (a) surface pressure, (b) skin friction coefficient and (c) wall heat flux for $\beta = 6^o$ and $M_\infty = 5$ using standard k-ω, shock-unsteadiness modified k-ω and variable Pr_T models with the experimental data of Schulein [73].

a lower amplification of the turbulent kinetic energy, which enhances flow separation at shock waves. The variable Pr_T form of the SU k-ω model predicts almost identical c_f as that of the constant Pr_T version. Downstream of the interaction region, the SU k-ω results (both constant Pr_T and variable Pr_T versions) are comparable to the experimental c_f measurements; and the results are identical to those presented in Ref. [60].

The heat flux data in Fig. 5.12(c) shows a trend similar to the skin friction coefficient, with a constant value in the undisturbed boundary layer and a dip in the heat transfer rate at the shock impingement point. The dip is because of the small separation bubble in the SU k-ω solution and is not seen in case of the standard k-ω model. The experimental data has a sudden jump in surface heat flux, and all three models reciprocate this trend. The standard k-ω model, however, overpredicts the heat flux by about 50%. The shock-unsteadiness correction is found to reduce the surface heat transfer rate, but the results are still substantially higher than the experiment. On the other hand, the variable Pr_T model brings down the post-shock heat transfer dramatically and the results are close to the experiments.

The majority of the data reported in Figs. 5.11 and 5.12 correspond to $\chi = 1000$. The only exception is the $\chi = 10$ curve in Fig. 5.12(c). Using a lower value of χ gives higher surface heat flux, especially in the recovering boundary layer downstream of the interaction region. The heat flux in the vicinity of the reflected shock ($x/\delta_0 \simeq 0$) is relatively unaffected by the change in χ. This is in line with the normal shock data presented in Fig. 5.5, where all the different values of χ give identical Pr_T near the shock wave. Further downstream, a higher χ retains the low Pr_T values for a longer distance in the downstream flow. For the SBLI configuration, this translates to a lower surface heat flux in the boundary layer recovery region, up to $x/\delta_0 = 10$, as shown in the figure. The Pr_T value in this region ($x/\delta_0 = 10$) lies between 0.8 to 0.86 which is lower the the conventional value of 0.89 and thus gives a lower surface heat flux

Also, note that the standard and shock-unsteadiness k-ω models give a qualitatively different heat flux variation in the recovering boundary layer. There is a peak in the surface heat flux prediction, followed by gradual decrease to levels comparable to the experimental measurements far downstream of the interaction. By comparison, the variable Pr_T model predicts a jump comparable to the measurements, and then a further increase in the recovering boundary layer, akin to what is seen in the experiments.

5.4.3 10 degree case

Experimental data for the 10 degree shock generator shows clear indication of flow separation and the shock-unsteadiness k-ω model reproduces this effect [60]. There are multiple shock waves in the interaction region, with the separation and reattachment points marked as S and R, respectively. Additional details can be found in [60]. The variation of Pr_T, shown in Fig. 5.13(a) follows the shock pattern closely. There is a region of low Pr_T (in the range of 0.68) in the vicinity of the reattachment point, and it varies along the plate to reach 0.8 at $x \simeq 2\delta_0$.

The surface heat flux is directly influenced by the variation of Pr_T in the reattachment region and in the recovering boundary layer. Reducing the Pr_T value results in a higher turbulent conductivity as per Eq. (5.2). An elevated turbulent conductivity leads to a higher diffusion of heat away from the wall, leading to a lower surface heat transfer rate.

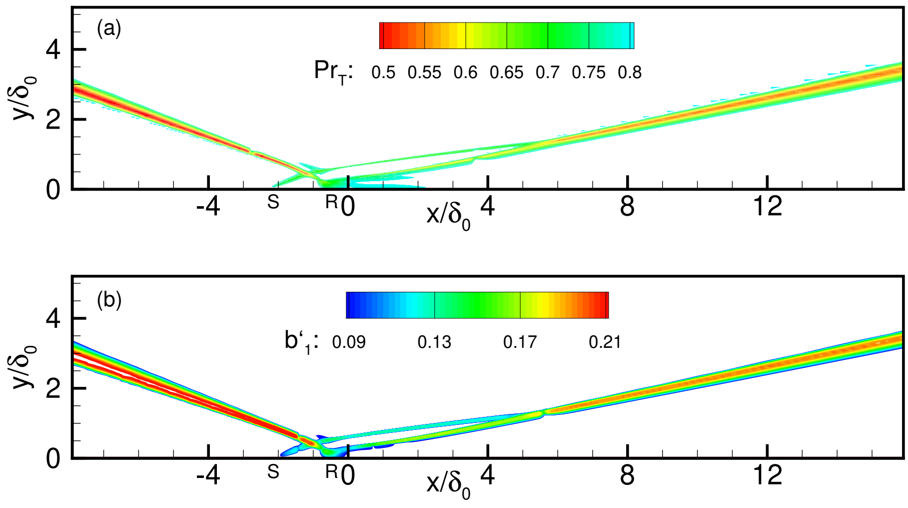

Figure 5.13: Distribution of (a) turbulent Prandtl number and (b) shock-unsteadiness parameter b'_1 for $\beta = 10^o$ and $M_\infty = 5$ shock-boundary layer interaction.

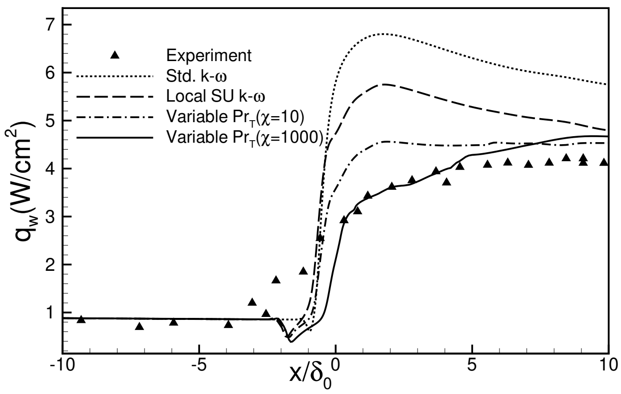

Figure 5.14: Comparison of wall heat flux for $\beta = 10^o$ and $M_\infty = 5$ using standard k-ω, shock-unsteadiness modified k-ω and variable Pr_T models with the experimental data [73].

The model predictions ($\chi = 1000$) match the experimental measurements, both qualitatively and quantitatively, in this region; see Fig. 5.14. By comparison, the standard and SU k-ω models with constant turbulent Prandtl number predict too high a jump in heat flux at the reattachment point, and they overpredict the data further downstream. None of the models reproduce the increase in surface heat transfer rate at the separation point, and thus under predict the experimental data in the separation bubble.

The surface heat flux predictions in Fig. 5.14 show a higher sensitivity to the value of the model parameter χ, as compared to the weaker 6 degree interaction. This is because of the presence of a bigger separation bubble in the 10 degree case that moves the shock waves away from the wall; see the description of shock topology in Fig. 5.15(a). In such a scenario, the parameter χ plays a crucial role in bringing the effect of the shock waves to the near-wall region. A higher χ results in a lower Pr_T near the surface, and thus a lower surface heat flux is predicted, compared to $\chi = 10$, around $x/\delta_0 = 2$.

The surface pressure and skin friction coefficient are identical to those presented in Fig. 5.7, as they are not affected by the variation of Pr_T in the interaction region. The SU k-ω model predictions show fair comparison with the measurements, and a detailed comparison with experimental data is presented in [60]. The results are based on the shock-unsteadiness parameter b_1' computed locally in terms of the shock function ψ. The b_1' values are between 0.13 and 0.17 in the interaction region, and increase to 0.21 in the incident shock wave; see Fig. 5.13(b). The values are indicative of the local shock strength, and b_1' goes to zero outside of shock waves.

5.4.4 14 degree case

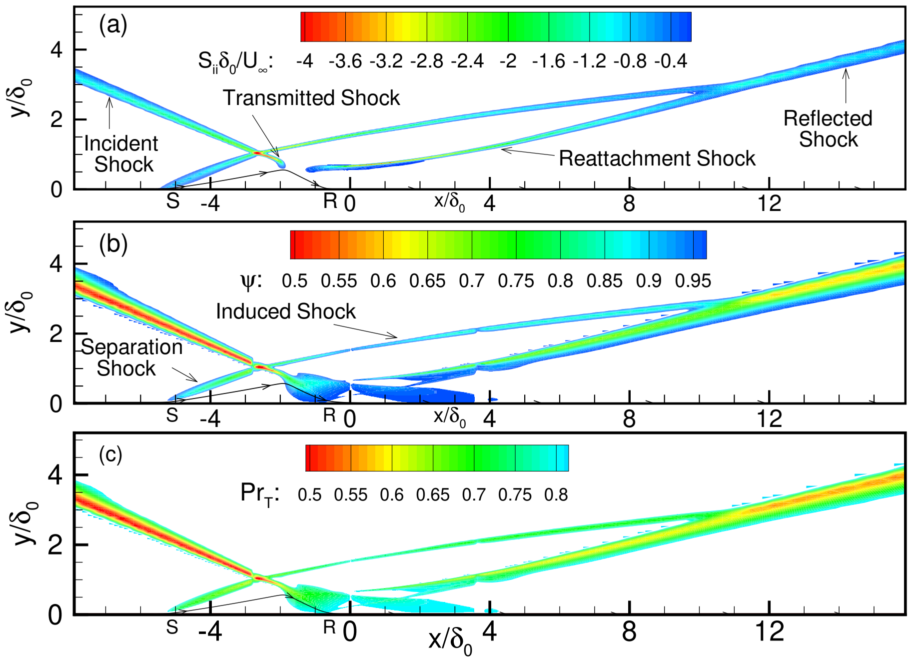

Figure 5.15: Distribution of (a) normalized mean dilatation, (b) ψ function and (c) Turbulent Prandtl number for $\beta = 14^o$ and $M_\infty = 5$.

The shock pattern computed in the 14 degree SBLI case is similar to the 10 degree case presented before. The incident, induced, transmitted, separation and reattachment shocks are identified in Fig. 5.15, along with the limiting stream line showing the extent of the separation bubble. A stronger interaction in this case results in large re-circulation region, with about $5\delta_0$ between the separation and reattachment points. Further details of the shock/expansion wave structure can be found in [60].

It is noted that the separation shock penetrates deep into the boundary layer. A closer inspection reveals that the region identified by the ψ function extends into the log region of the incoming boundary layer. The viscous sub-layer is devoid of shock waves, owing to the low Mach numbers encountered there. The near-wall shock-less region is also characterized by high transverse gradient in Mach number. Relatively smaller variation of the upstream Mach number is found in the region of the separation shock. A lack of substantial curvature of the shock wave (as seen in Fig. 5.15(a)) corroborates to this fact, and is expected to cause no major limitation to the current model without shock curvature effects. The reattachment and the induced shocks show more pronounced curvature. However, the curved regions are outside the boundary layer and are expected to have minor effect on the surface heat flux predictions.

Experimental data of wall pressure shows a distinct rise at the separation point, followed by a pressure plateau in the separation bubble. The simulation results obtained using the local form of the shock-unsteadiness k-ω model mimic this trend; see Fig. 5.16(a). The surface pressure past the reattachment point is also predicted well by the model. By comparison, the standard k-ω model gives a separation bubble much smaller than the experiments, and a steeper pressure rise on reattachment. The skin friction data also shows the same behaviour, with the local SU k-ω model predictions matching the experimental measurements well in the separation bubble and reattachment region; see Fig. 5.16(b). This coincides with the region of peak surface heat flux, and is of direct interest to the present study.

A key feature of the 14 degree SBLI case is that the reattachment shock wave in Fig. 5.15(a) is oriented parallel to the wall in the peak heat transfer region ($x \simeq 0$). The shock-normal direction is thus oriented towards the wall, such that the turbulent energy transfer in this direction has a direct influence on the surface measurement. Note that the variable Prandtl number model is based on the shock-normal component of the heat flux vector in canonical shock-turbulence interaction. It is therefore expected to capture the heat transfer mechanism directed towards the wall. A similar effect, but to a smaller extent is seen in the 10 degree SBLI case, where the reattachment shock is highly inclined to the wall and a large component of the shock-normal heat flux is in the wall-normal direction.

A second interesting aspect of the 14 degree case is that the reattachment shock is located at the edge of the boundary layer ($y/\delta_0 \sim 0.7$). This is because of the large separation bubble that moves the whole shock structure away from the wall. The reattachment shock or the reflected shock in the weaker interactions penetrates into the boundary layer and it has a direct influence on the heat transfer occurring in the vicinity of the wall. Lowering the turbulent Prandtl number at the shock, therefore, has a large reduction in

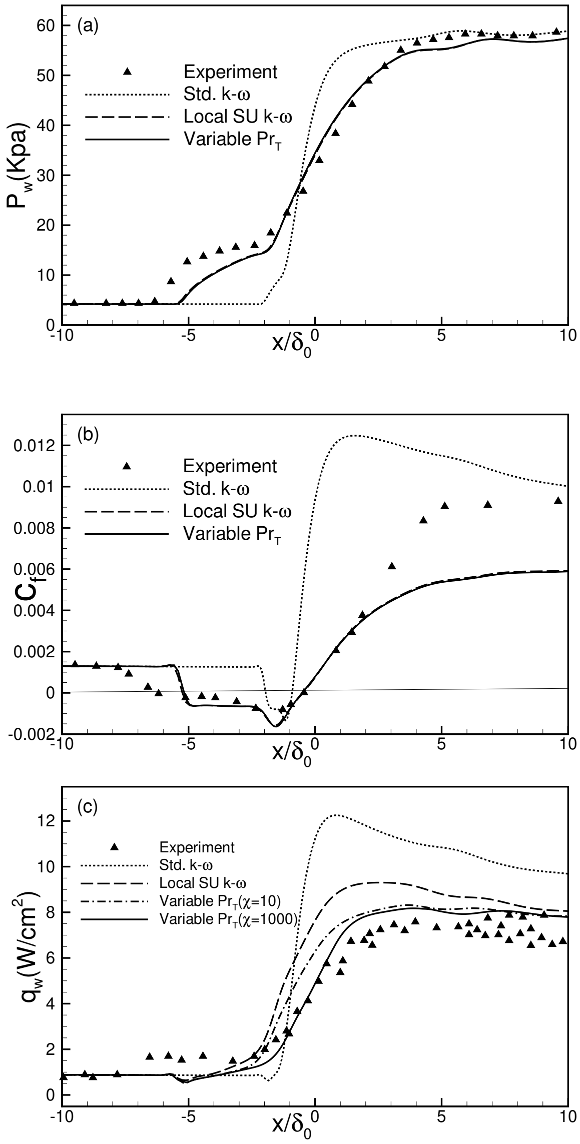

Figure 5.16: Comparison of (a) surface pressure, (b) skin friction coefficient and (c) wall heat flux for $\beta = 14^o$ and $M_\infty = 5$ using standard k-ω, shock-unsteadiness modified k-ω and variable Pr_T models with the experimental data [73].

surface heat flux compared to the SU k-ω prediction. On the other hand, the difference in the peak heat flux predicted by SU k-ω model with constant Pr_T and the current variable Pr_T version is relatively small in the 14 degree case; see Fig. 5.16(c). Also, varying the parameter χ between its limiting values of 10 and 1000 is found to have minimal effect on the surface heat flux.

The shock waves have an indirect effect on the boundary layer heat transfer via the ψ function, which takes low values in the shock waves and has an exponential relaxation back to its reference value of 1. Thus, the effect of the shock wave is transported in the downstream flow. This can be seen in Fig. 5.15(b) and 5.15(c) at the end of the transmitted shock, where low values of ψ and Pr_T are observed in the vicinity of the reattachment point R on the wall. Low values of Pr_T (in the range of 0.8) are also visible along the wall up to x $\simeq 4\ \delta_0$, where the effect of the reattachment shock is carried along the wall by the streamlines passing through the reattachment shock wave. The resulting effect on the surface heat flux can be noted in Fig. 5.16(c).

Overall, the variable Pr_T model predictions show an excellent comparison with the experimental heat flux measurements in the reattachment region and in the recovering boundary layer. Reducing the eddy viscosity by the shock-unsteadiness correction also gives a reduction in the surface heat flux. By comparison, the standard k-ω model with constant Pr_T overpredicts the peak heat flux by about 70%, and the trends are qualitatively different from that observed in the experiments. This is particularly important in light of the high values of peak heat transfer, up to eight times of the undisturbed boundary layer value, encountered in strong SBLI cases.

5.5 Summary

The physical insights from canonical shock-turbulence interaction is used to propose a variable turbulent Prandtl number model for shock-dominated flows. The model is based on linearized Rankine-Hugoniot jump conditions across a shock wave and uses model coefficients derived for the shock-unsteadiness k-ω model developed earlier. As per the analysis, the turbulent Prandtl number takes low values in shock waves, and its value decreases with increasing shock strength. A shock function is used to identify the location and the strength of the shock waves in a flow, and is computed by solving a model transport equation. The model also incorporates an exponential relaxation of the turbulent Prandtl number from its shock value to the conventional value of 0.89 away from shock waves. The shock-unsteadiness model, proposed earlier, is reformulated in terms of the shock function. This removes the upstream dependence of the model parameters, so that they can be evaluated locally at a grid point. The local form of the shock-unsteadiness model is computationally more robust and saves a considerable amount of human effort in a simulation.

The variable Pr_T model is applied, in conjunction with the shock-unsteadiness k-ω turbulence model, to oblique shocks impinging on turbulent boundary layer. Three cases with increasing shock generator angles are computed and the results are compared with the experimental measurements. It is found that the shock function can accurately capture the complex shock topology and the strength of the different shock waves in the interaction region. The low values of the turbulent Prandtl number at the shock waves result in a significant reduction in the surface heat flux prediction. The experimental data is reproduced well, both in terms of the peak heat transfer rate at flow reattachment, as well as the streamwise variation of the surface heat flux in the recovering boundary layer. The computed surface pressure and skin friction coefficient also match the experimental data better than the standard k-ω model.

Chapter 6

Modeling of Turbulent Heat Flux for Hypersonic Flows

The primary advantage of the new variable Pr_T model is its algebraic form that makes it computationally efficient and numerically robust. It is applied in the region of shock waves and the model reverts back to the constant Pr_T version other wise. The model correction increases with the strength of the interaction, such that the significant improvements are obtained in predicting the peak heat transfer rate for strong shocks. In the limit of Mach 1, the model is calibrated to give vanishing small correction, so as to revert back to standard model in the absence of shock waves.

A limitation of the model is in the fact that it uses the shock-unsteadiness parameter for purely vortical turbulence upstream of the shock [78]. This is representative of low supersonic flow interacting with shock waves, where the thermodynamic fluctuations are expected to be small. This is not the case in hypersonic flows, where the temperature fluctuations can be appreciably large compared to the velocity fluctuations. In fact, the normalized rms temperature fluctuations scale with the square of the flow Mach number relative to the normalized rms velocity fluctuations, as per Morkovin's hypothesis [56].

In this chapter, the validity of the previous variable Pr_T (chapter 5) model is extended to high Mach number flows by including the effect of upstream temperature fluctuations. The shock-unsteadiness parameter in the previous version is replaced by its counterpart [85] that includes the effect of upstream temperature fluctuations. Otherwise, the earlier variable Pr_T framework is retained, so as to take advantage of its simple algebraic form and its computational efficiency. The new model is tested over a wide range of Mach numbers for different SBLI configurations. It shows significant improvement in hypersonic cases, while collapsing back to the earlier model for lower Mach numbers.

6.1 Model development

The current heat flux model for hypersonic flows builds upon the variable Pr_T model presented in chapter 5. The key steps in the development of the earlier model is highlighted , which is based on the conservation of total enthalpy fluctuations across an unsteady oscillating shock wave.

$$T_1' + u_1' \frac{\bar{u}_1}{c_p} = T_2' + u_2' \frac{\bar{u}_2}{cp} + \xi_t \frac{(\bar{u}_1 - \bar{u}_2)}{c_p} \tag{6.1}$$

where $\bar{T}$ and $\bar{u}$ are the mean temperature and shock-normal velocity, subscript 1 and 2 represent shock upstream and downstream locations, c_p is the specific heat and ξ_t is the unsteady shock speed. Overbar is used to denote mean quantities, while prime represents turbulent fluctuations.

The above equation is written by neglecting higher-order terms involving squares of velocity fluctuations, such that the left-hand side represents the total temperature fluctuations in the upstream flow. This can be taken to be zero, assuming that Morkovin's hypothesis [56] is valid in the incoming flow. Taking a moment of Eq. (6.1) with u_2' gives a relation for the downstream turbulent heat flux

$$c_p \overline{u'T'} = -\bar{u} \left(\overline{u'^2} + \overline{u'\xi_t}(r-1) \right) \tag{6.2}$$

where r is the mean density ratio across the shock and subscript 2 is dropped for convenience. The unclosed correlation between the shock speed and the velocity fluctuations is modeled in terms of the stream-wise Reynolds stress $\overline{u'\xi_t} = b_1 \overline{u'^2}$, as per the shock-unsteadiness model of Sinha et al. [78].

Converting Eq. (6.2) into an equivalent Pr_T formulation by evaluating the thermal diffusivity and eddy viscosity in terms of the turbulent transport in the shock-normal direction gives

$$Pr_T = \frac{\nu_T}{\alpha_T} = \frac{3/4}{1 + b_1(r-1)} \tag{6.3}$$

The intermediate steps can be found in chapter 5. The above variable Pr_T model can be applied to any turbulence model. We choose the shock-unsteadiness k-ω model [79], which is known to improve separation prediction, and the associated surface pressure distribution in SBLI flows. The shock-unsteadiness parameter b_1 is obtained from linear interaction analysis [78], and is given by

$$b_1 = 0.4 + 0.6 \left(\frac{6\psi - 1}{5\psi} \right)^{5.2} \tag{6.4}$$

where ψ is a shock function computed using the mean dilatation at a shock wave (see subsection 5.3.1). It is set to 1 in the undisturbed boundary layer and takes a value 1/r at shock waves.

The shock-unsteadiness model parameter b_1 corresponds to purely vortical turbulence upstream of the shock wave [78]. This limits the applicability of the model to supersonic flows up to Mach 5. For hypersonic flows, additional fluctuations in the thermodynamic variables need to account in the boundary layer upstream of the shock interaction. Morkovin's hypothesis [56] predicts that the temperature fluctuations in high-speed boundary layers are related to the velocity fluctuations as per

$$\frac{T'}{\bar{T}} = -(\gamma - 1)M^2 \frac{u'}{\bar{u}} \tag{6.5}$$

Veera and Sinha [85] extend the original shock-unsteadiness model of Sinha et al. [78] to include the effect of upstream temperature fluctuations. They found that the shock-unsteadiness parameter is enhanced in the presence of temperature fluctuations, and is given by

$$b_1 = 0.4 + 0.6\left(\frac{6\psi - 1}{5\psi}\right)^{5.2} + 0.2(\gamma - 1)M_1^2 \tag{6.6}$$

The production of turbulent kinetic energy is also modified to include the effect of entropic production at shock waves. The model parameter b_1' is thus given by [85]

$$b_1' = \left(0.4 + 0.2(\gamma - 1)M_1^2\right)\left(\frac{1 - \psi}{5\psi}\right)^{0.3}. \tag{6.7}$$

The shock function ψ is used to compute the upstream shock-normal Mach number as per Rankine-Hugoniot relation and it is used instead of local Mach number in the upstream boundary layer. This reduces the computational effort significantly and gives up to 10% error in the shock-unsteadiness parameters b_1 and b_1' for the present cases.

Otherwise, the implementation of the variable Pr_T model remains identical to that in chapter 5. In particular, the shock-detecting function f_s is computed using the boundary layer thickness δ_0 upstream of the interaction. The value of δ_0 for each simulation is listed below. Also, Pr_T in eq. (6.3) is used with a blending function ζ (see equation 5.18) to transition smoothly to $Pr_T = 0.89$ in regions without shock waves. Fig. 6.1 shows the sensitivity study of the model parameter χ at high Mach numbers. Only the highest interaction cases of respective geometries (see section 6.2 for details) are considered here. A higher value of χ will retain the lower Pr_T value for a longer distance thus giving a lower heat flux value after the reattachment region. The sensitivity of the solution to the blending parameter χ is reported in chapter 5 for oblique shock impingement at Mach 5. At higher Mach numbers considered in this chapter, a lower sensitivity (less than 6%) is found of the wall heat flux to the variations in the model parameters.

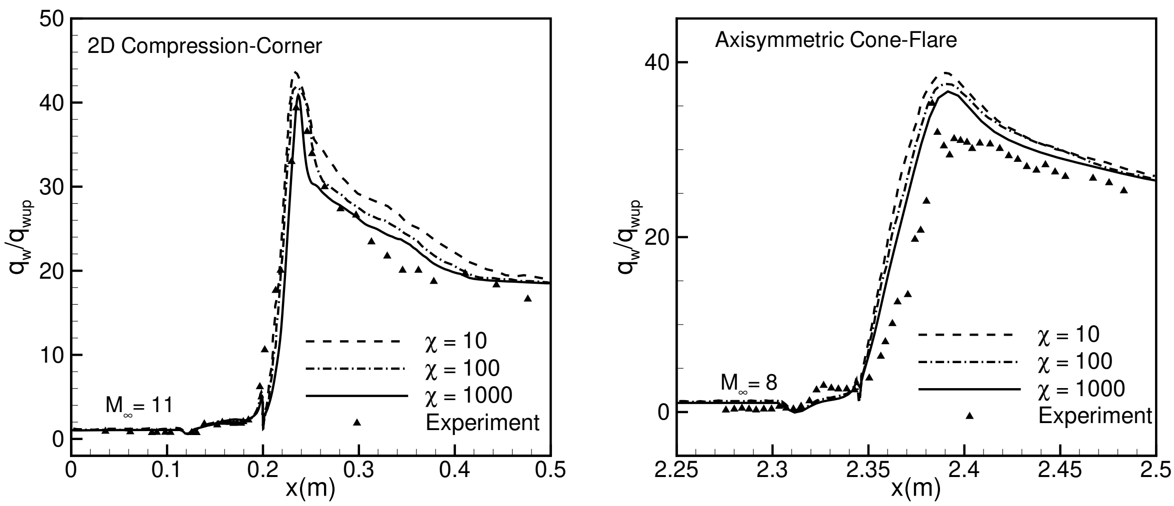

Figure 6.1: Sensitivity study of the model parameter χ for 2D compression corner (M_∞ = 11.3) and axisymmetric cone-flare (M_∞ = 8.21) geometries.

6.2 Results

The variable Pr_T model presented above is implemented in a Reynolds-averaged Navier Stokes code based on the k-ω framework and the numerical methodology is presented in chapter 3. Two-dimensional compression corner cases of Holden et al. [29] with a 1.02 m long plate followed by a 0.3 m ramp are computed for model testing. A series of tests were conducted with the ramp angle varying between 27° and 36° at free stream Mach number around 8 and a 36° ramp at Mach 11.3 (table 6.1). The plate length is long enough to have a fully developed turbulent boundary layer upstream of the interaction [29]. This eliminates any potential uncertainty in the RANS computations due to laminar to turbulent transition.

The highest temperature encountered in the simulations is around 850 K, thus justifying the perfect gas assumption employed in the governing equations. The wall temperature is reported for each case, and it is specified as an isothermal boundary condition, along with velocity no-slip, on the compression ramp. The boundary conditions on the turbulence variables are specified as per Menter [54] and given in chapter 3. The computational domain extends from the tip of the plate to the end of the ramp, where an extrapolation condition is used at the flow exit boundary. The subsequent expansion is not simulated, as it is expected to have negligible effect on the surface properties in the interaction region.

The computational grid consists of 600×250 points and it is based on a rigorous grid sensitivity study for the strongest interaction at Mach 11.3 (see Fig. 6.2). The number

Table 6.1: The freestream and wall conditions in the SBLI experiments [17] and the computed boundary layer thickness (δ_0) upstream of the interaction region.

Configurations	M_∞	ρ_∞ (kg/m^3)	T_∞ (K)	Deflection Angles	T_w (K)	Re_∞/m $\times 10^6$	δ_0 (mm)
Compression ramp	11.3	0.0825	61.0	36°	300.0	36	21
	8.2	0.4990	70.0	36°	298.0	145	17
	8.1	0.4910	71.7	33°	297.0	139	16.5
	8.3	0.5060	68.9	30°	296.0	149	15
	8.2	0.5090	71.1	27°	296.0	147	15
Cone-flare	8.21	0.0437	60.4	33°	306.5	33.5	20
	7.18	0.0572	66.6	33°	302.5	36.6	19
	6.17	0.0737	56.7	33°	297.4	44.3	17.5
	5.1	0.284	75.8	33°	294.6	118	15

of points in the wall-parallel direction is varied between 200 and 700, and the peak heat transfer rate is found to change by less than 2% beyond 600 points. The predictions are otherwise identical between the 600 and 700 point grids. An exponentially-stretched grid with 250 points is used in the wall-normal direction, and the first cell is placed at 10^{-6} m from the wall. This is equivalent to 0.4 wall units or less along the compression ramp geometry. Further refinement, both in terms of number of points and the near-wall resolution, gives a maximum of 1–2% variation in the wall heat transfer rate.

Figure 6.3 shows the computed surface pressure and heat transfer rate for the strongest interaction at Mach 11.3. The results are compared with experimental data measured along the model center line, where three-dimensional effect are found to be negligible [29]. The pressure rise at x = - 0.08 m corresponds to the separation point and it is well predicted by the current model (denoted by SU k-ω 2009) based on the shock-unsteadiness correction of Veera and Sinha [85]. The original shock-unsteadiness model (denoted by local SU k-ω and presented in subsection 2.4.6) of Sinha et al. [78] over-predicts flow separation, because of excessive damping of turbulence kinetic energy at hypersonic Mach numbers. The standard k-ω model suppresses flow separation, and results in a pressure rise close to the corner (x = 0). The current model matches the pressure plateau in the separation region, predicts a small peak at reattachment and overlaps with the pressure data measured on the ramp. The local SU k-ω model also predicts a lo-

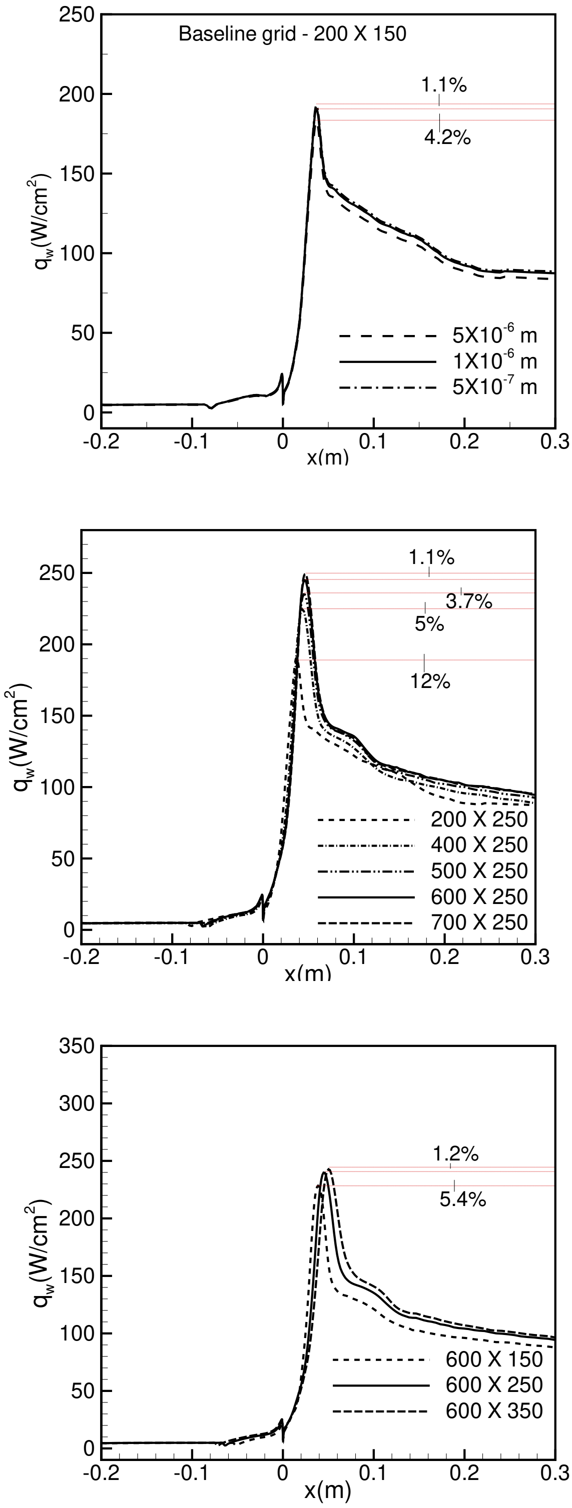

Figure 6.2: Grid refinement study of (a) near-wall resolution, (b) number of points in the streamwise direction and (c) number of points in the wall-normal direction for the compression ramp geometry at Mach 11.3.

cal pressure peak on the ramp, but its location is shifted downstream, because of a larger recirculation region.

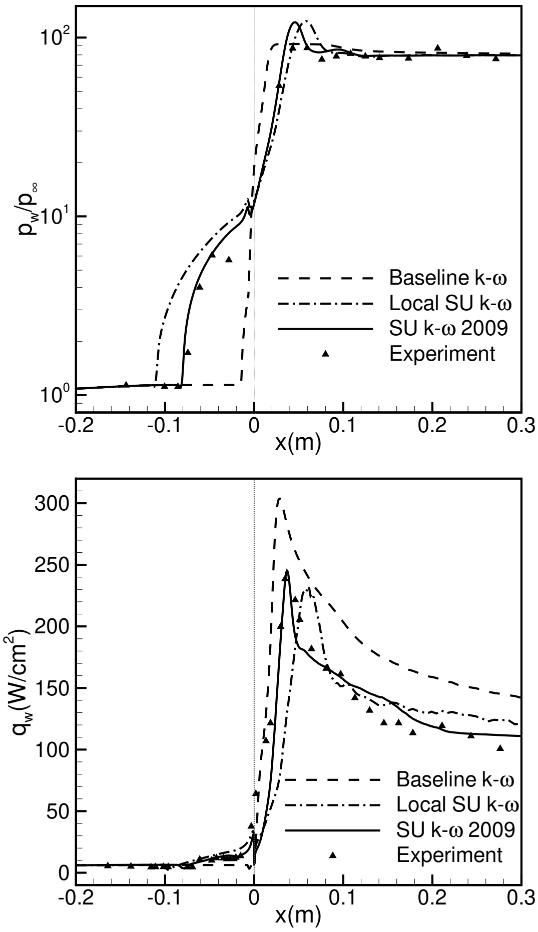

Figure 6.3: Comparison of (a) surface pressure and (b) wall heat flux for 36^o compression ramp at $M_\infty = 11.3$ using standard and shock-unsteadiness modified k-ω models with the experimental data of Holden [29].

The wall heat flux data (Fig. 6.3b) shows a modest increase at the separation point, and a steep rise at the corner. The present calculation using SU k-ω 2009, with variable Pr_T Eq. (6.3), models reproduce the experimental measurements closely. It also matches the narrow peak in wall heat flux near reattachment and the subsequent decrease in heating rate on the ramp. The local SU k-ω model along with earlier variable Pr_T model (see chapter 5) predicts a lower peak heat transfer rate and its location is shifted downstream compared to the experiment. The standard k-ω model completely misses the separation bubble, and gives a single rise in heat flux at the corner. The wall heating is over predicted by 25-30 % along the entire ramp surface. It is important to predict the correct separation point and the size of the separation bubble, as it determines the strength of the separation shock and the resulting shock-shock interaction at reattachment [61]. This has a first-order effect on the peak heat transfer rate and its location on the ramp.

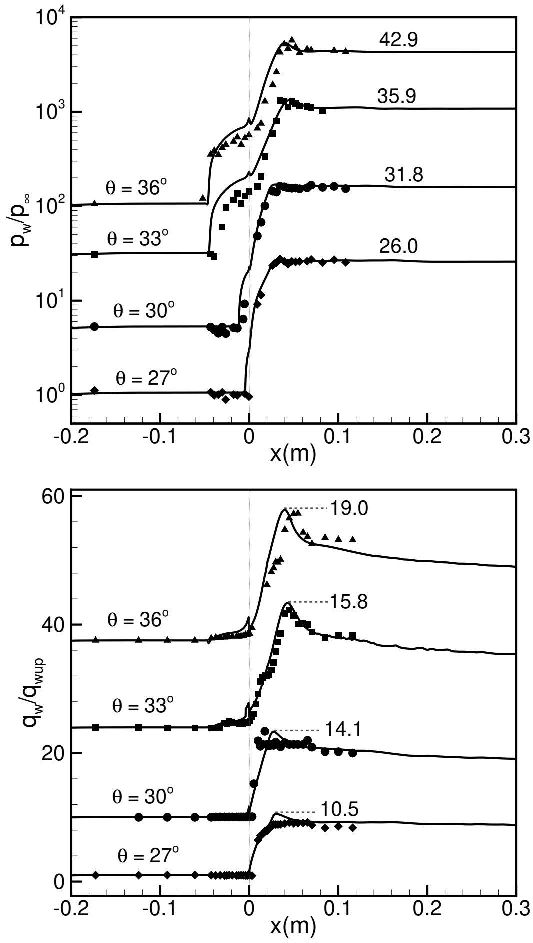

Figure 6.4: Compression ramp (a) surface pressure and (b) wall heat flux for different deflection angles at $M_\infty \simeq 8$. Computations are using SU k-ω 2009 model and compared with the experimental data [29].

Figure 6.4 is a composite figure of all the Mach 8 compression corner cases, with the ramp angle varying from 36° to 27°, computed using SU k-ω 2009 model. The heat flux data plotted in Fig. 6.4b are normalized by the respective values upstream of the interaction region. The data is offset by 9, 23 and 36 units for the 30°, 33° and 36° cases, respectively, and the peak values are marked for easy comparison. Also the pressure axis is multiplied by a factor of 5, 30 and 100 for the 30°, 33° and 36° cases, respectively, and the normalized ramp pressure is noted in Fig. 6.4a.

As expected, the separation bubble size, identified by the pressure rise upstream of the corner, moves closer to the corner as the ramp angle decreases. The weakest interaction for the 27° ramp has incipient separation. The computations match the separation location well for all the cases, except the 33° interaction. The pressure plateau in the separation bubble is over-predicted, but the peak pressure and the ramp pressure are reproduced closely. A similar trend is observed for the wall heat transfer rate (Fig. 6.4b), where the current model matches the experimentally measured peak heat flux. The only exception is the 27° case, where the model overpredicts the heat transfer on the ramp. The location of the peak heat flux is reproduced correctly in the 33° SBLI, whereas it is predicted upstream and downstream of the experimental peak in the 36° and 30° cases respectively.

Next, the axisymmetric cone-flare configurations listed in table 6.1 is considered for comparison. The geometry consists of a 2.56 m long 7° half-angle cone and a 40° flare, which gives a 33° turning angle at the cone-flare junction. The computational domain extends from the tip of the cone to the end of the flare, and the outer boundary is tailored to the inviscid cone shock. A typical grid consists of 450×150 points, with fine grid at the cone tip and the cone-flare junction, and 90 points on the flare (see Fig. 6.5 for details). Refining the grid to 850 points shows minimal changes in the solution, within 2% in the flare heat flux prediction for the strongest interaction at Mach 8.21. Similarly, increasing the number of wall-normal points from 150 to 250 gives overlapping results. The first point next to the wall is placed at 10^{-6} m, which is equivalent to 0.5 wall units or less along the cone-flare surface.

The RANS equations are solved in axi-symmetric form, with the standard, local SU and SU-2009 forms of the k-ω model. The numerical method is identical to that described above and the boundary conditions are set as per the values listed in table 6.1. The same steps are followed as delineated for the compression ramp cases. In the absence of boundary layer profile measurements upstream of the interaction, the surface heat flux measurement is matched on the cone within 7%. The flat plate heat flux data provided in the compression ramp cases is also reproduced within 10% by the computations. This is comparable to the measurement error reported in the experiments [29].

The results obtained for the strongest interaction for freestream Mach number of 8.21 is shown in Fig. 6.6. The surface pressure measurements follow the expected trend of separation pressure rise at x = - 0.04 m and a subsequent reattachment pressure rise on the flare ($x > 0$). The current model based on SU k-ω 2009 matches the pressure data on the cone and at the separation location. The pressure plateau in the recirculation bubble is under-predicted, but the solution matches the data on the flare fairly well. Excellent improvement is observed in the surface heat flux prediction (Fig. 6.6b), where the current model predictions are comparable to the experimental data on the flare. The maximum heat flux measured at x = 0.03 m is arguably matched by the computation, but the location is shifted downstream. The local SU k-ω model, on the other hand, under-predicts the flare

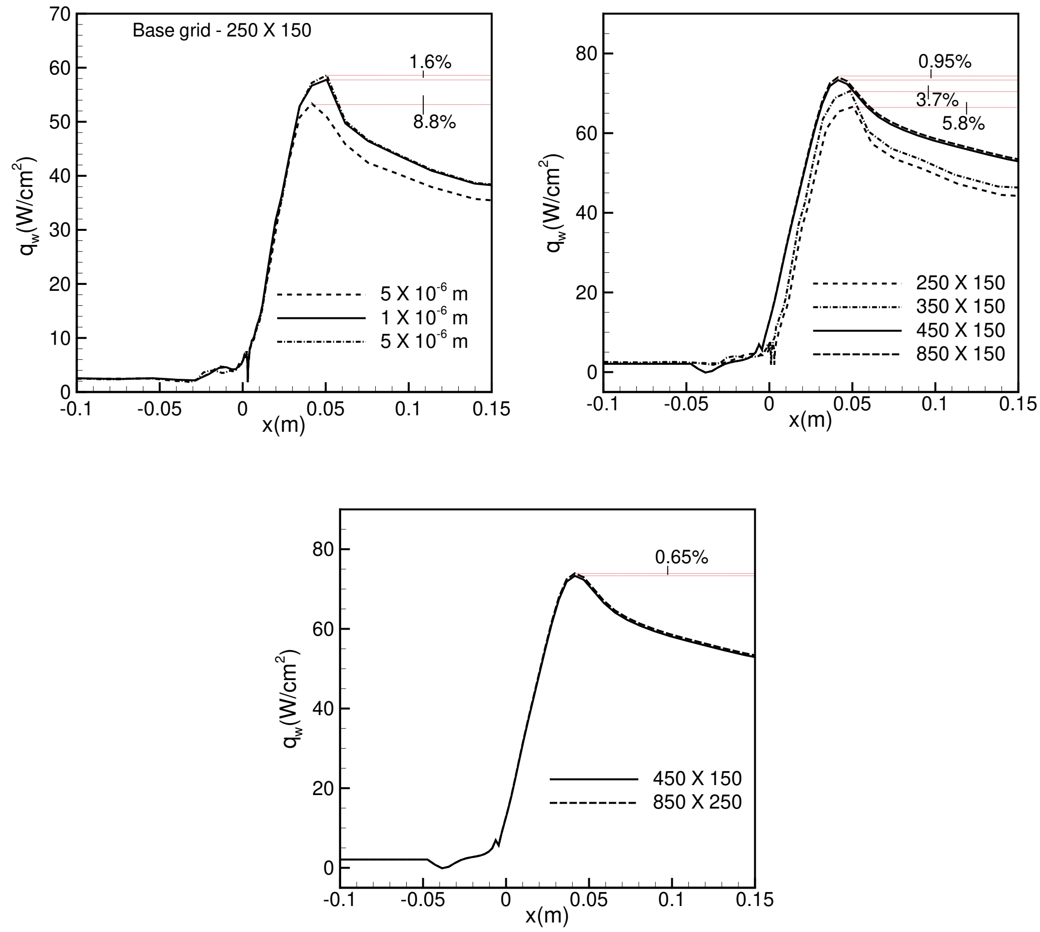

Figure 6.5: Grid refinement study of (a) near-wall resolution, (b) number of points in the streamwise direction and (c) number of points in the wall-normal direction for the cone-flare geometry at Mach 8.21.

heating rate, and the standard k-ω model grossly over-predicts it. The separation location, in the pressure plot, is also not matched by the local SU k-ω and standard k-ω models, and the trends are similar to those observed for the compression ramp flow.

Figure 6.7 compares the SU k-ω 2009 surface predictions and the experimental measurements for the remaining cone-flare cases. Once again, the pressure data is scaled up for the Mach 6 and 7 by factors of 3 and 8 respectively, while the heat flux is shifted up by 10 and 25 units respectively, compared to the Mach 5 case. The computations accurately reproduce the separation location for all the three flows. The pressure plateau in the separation bubble, the subsequent pressure rise at reattachment and the peak pressure on the flare also overlap with the experiments. The wall heat transfer data in Fig. 6.7b shows a reasonable match between the computed and measured values in the interaction region. The peak heat flux is over-predicted, but the trends in the computed solution follow the

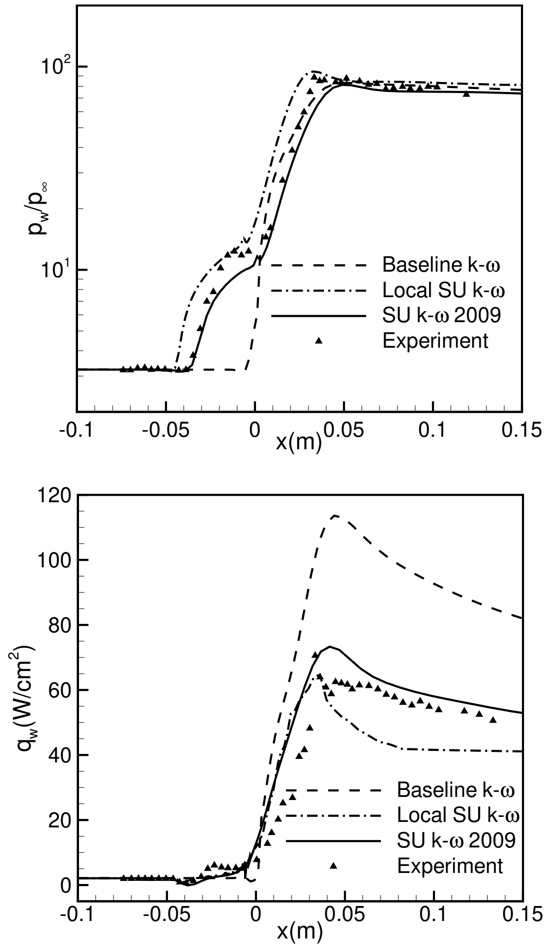

Figure 6.6: Cone-flare (a) surface pressure and (b) wall heat flux predictions at $M_\infty = 8.21$ using standard and shock-unsteadiness modified k-ω models compared with the experimental data of Holden [29].

measurements on the wall. It is interesting to note that the separation location moves downstream as the Mach number increases. This is indicative of a smaller separation bubble and an earlier reattachment on the flare. As a result, the peak heat flux location moves upstream with increasing Mach number. The SU k-ω 2009 model predicts this trend and is thus physically consistent with the experimental observations.

the SU k-ω 2009 model is next applied to the oblique shock impingement on a Mach 5 turbulent boundary layer. The experimental data is reported by Schulein [73] for a 14° shock generator angle and Reynolds number based on momentum thickness of 6982. This is one of three cases used for validating the variable Pr_T model based on local SU k-ω in chapter 5. The full details of the SBLI configuration, computational grid and boundary conditions are given in chapter 5, and are not repeated here.

Figure 6.8 shows that the surface pressure and heat transfer rate are predicted well by the local SU k-ω model, and the current SU k-ω 2009 model gives almost identical

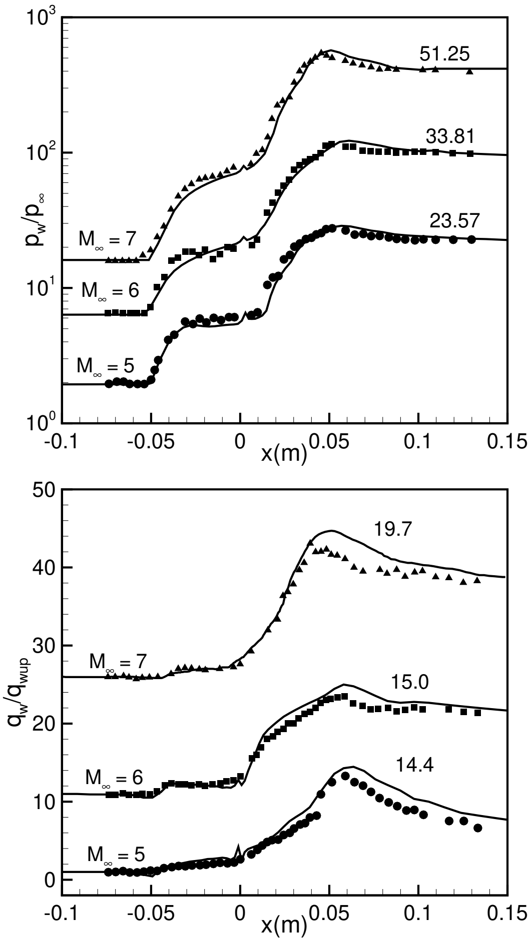

Figure 6.7: Comparison of (a) surface pressure and (b) wall heat flux for cone-flare geometry at different Mach numbers with the experiments [29].

results. Specifically, both models predict the separation pressure rise downstream of the experiment, but match the subsequent pressure rise accurately. They also give significant improvement in predicting the reattachment wall heat flux compared to standard k-ω model.

The important point is that there is less than 5% difference between the two models, and the same is true for the other Mach 5 oblique shock impingement cases reported by Schulein [73]. In fact, the current model is expected to collapse to the earlier Pr_T model (see chapter 5) for Mach numbers below 5. This is because of the fact that the extra term $(\gamma - 1)M^2$ in Eq. (6.6) has a negligible contribution in non-hypersonic boundary layers, where $1 < M < 2$ in the log layer is observed. As noted in Pathak et al. [62], the log-layer value of the turbulent Prandtl number is critical in predicting the wall heat flux accurately.

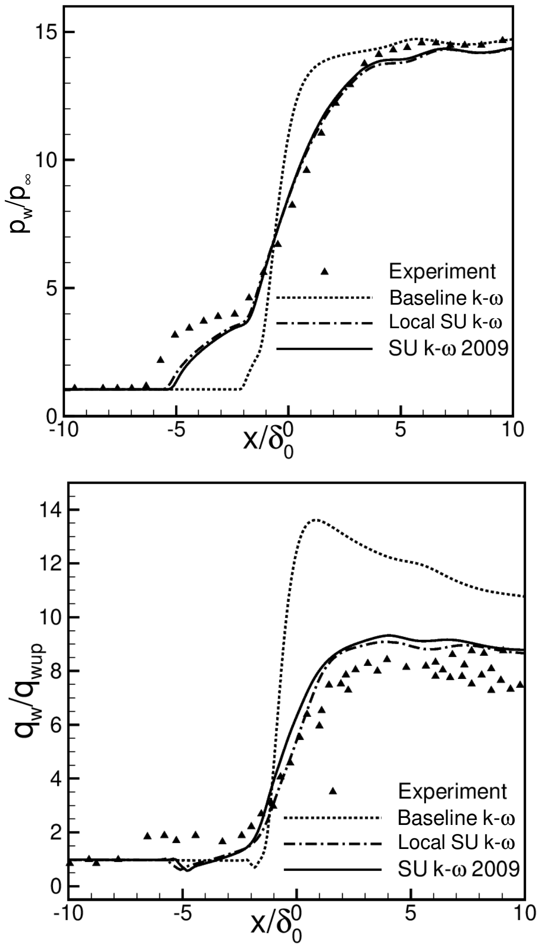

Figure 6.8: Oblique shock impingement at Mach 5: (a) surface pressure and (b) wall heat flux. Standard and SU k-ω models are compared with the experimental data of Schulein [73].

6.3 Summary

In this chapter, an extended form of variable turbulent Prandtl number model is developed for predicting the wall heat transfer in hypersonic shock-boundary layer interaction. It is an extension of the physics based model presented in chapter 5. It uses the shock-unsteadiness parameter for flows with upstream temperature fluctuations typical of hypersonic turbulent boundary layers. The new model is found to predict the peak heat transfer consistently over a range of Mach numbers and geometric configurations. It also matches the experimentally observed separation location, and gets physically consistent results with varying shock strength. Finally, the model collapses to the earlier version that has been thoroughly tested for SBLI at lower Mach numbers.

Chapter 7

Wall Heating/Cooling Effects on Surface Heat Flux

Most of our current understanding of shock wave turbulent boundary layers interaction (STBLI) is based on the results of supersonic Mach numbers (M $<$ 5) . There are very few works available in the literature which deal with hypersonic turbulent boundary layer and its interaction with the shock waves. One of the major difference between supersonic and hypersonic boundary layers is the wall temperature condition. At supersonic speeds, the surface temperature is essentially adiabatic; while at hypersonic speeds, due to considerable radiative cooling and internal heat transfer or due to necessary wall cooling to prevent melting, the surface temperatures are significantly lower than the adiabatic wall temperature. As a result, the conductive heat transfer between the boundary layer flow and the surface of hypersonic vehicles is enormous.

A limitation of the proposed model in chapter 6 is that the temperature fluctuation is modeled as per Morkovin's hypothesis [56] for the boundary layers upstream of the shock. This may not work in the presence of severe wall cooling or heating, which is measured in terms of the ratio of the wall temperature to the recovery temperature (defined as $T_r = T_\infty[1 + r_c\frac{\gamma-1}{2}M_\infty^2]$). Shock-boundary layer interaction occurring at hypersonic flight conditions usually correspond to highly cooled walls (as mentioned above). Even ground-based experimentation, for example, over flat plates at 300 K can give T_w/T_r = 0.1 for Mach numbers in the range 7–8. Experiments over heated and cooled plates have found substantial enhancement and/or reduction of the separation bubble in the interaction region [36, 90]. Similar results are also reported in direct numerical simulation, where the wall to recovery temperature is varied systematically for SBLI at supersonic Mach numbers [5, 87]. Recently, large eddy simulation is employed to explore SBLI at hypersonic Mach numbers and to design experiments involving heated/cooled walls in the HEG tunnel in DLR, Göttingen [89]. Recent experiment by Chang et al. [10] shows that the change in separation bubble size with wall heating/cooling is consistent at high enthalpy flows also. In short, there is a surge of recent interest in the study of SBLI over non-adiabatic walls, both in terms of the physics and it's potential in the control of the SBLI phenomenon. Simulating these effects accurately is an inherent part of the research effort, as the highest heating loads are reported for SBLI over highly cooled walls [5].

As wall cooling reduces the mean speed of sound ($\overline{a}$), the magnitude of turbulent Mach number (M_t) increases significantly with decreasing wall temperature and the same is shown by Duan et al. [16]. Thus the effect of upstream turbulence intensity will be a crucial factor in order to study the SBLI with non-adiabatic wall. The effect of M_t is already included in the turbulent heat flux model presented in chapter 4. In this chapter, the turbulent heat flux model (chapter 4) is used to study the effect of non-adiabatic wall on shock-boundary layer interaction in the Reynolds-average Navier-Stokes framework. The DNS data of Pirozzoli et al. [64] and Duan et. [16] for a turbulent boundary layer is also used to estimate the turbulent heat flux in the interaction region which is finally cast in a turbulent Prandtl number form and is sensitive to wall heating and cooling. The results are compared with the available DNS and experimental data.

7.1 Wall heating/cooling Effects on Heat Flux

The application of the heat flux model of chapter 4 in shock boundary-layer interaction (SBLI) will not be straight forward. The upstream temperature fluctuation in the DNS study is generated according to the formulation given by Ristorcelli et al. [68]. The analysis of turbulence level by Ristorcelli et al. [68] is similar to a turbulent boundary layer with adiabatic wall. But most of the practical application involving shock boundary-layer interaction operates with cold wall conditions, which is measured in terms of the ratio of the wall temperature to the recovery temperature (defined as $T_r = T_\infty[1 + r_c \frac{\gamma-1}{2} M_\infty^2]$ and $r_c = Pr^{1/3}$ is the recovery factor). The wall boundary conditions will also effect the shock induced heat flux specially at the reattachment point and modeling is needed for the same.

The level of upstream temperature fluctuation in a boundary-layer is not readily available in RANS simulations for non-adiabatic walls. The work of Huang et al. [31] is followed to model the upstream temperature fluctuation. The modified strong Reynolds analogy of Huang , also known as Huang's strong Reynolds analogy (HSRA), is based on the the mixing length assumption and it is found to match the DNS data well compared to any other form of the strong Reynolds analogy (SRA) [17, 64]. The full derivation of

HSRA form is given in chapter 2. As per HSRA the velocity-temperature fluctuations in a compressible turbulent boundary-layer is given as

$$\hat{A} = -\frac{\frac{T_1'}{\overline{T}_1}}{\frac{u_1'}{\overline{u}_1}(\gamma-1)M_1^2} = \frac{1}{Pr_{T,0}}\left(\frac{\partial \overline{T}_{01}}{\partial \overline{T}_1} - 1\right)^{-1}. \tag{7.1}$$

Here subscript 1 represents upstream or undisturbed boundary-layer condition and $Pr_{T,0} = 0.89$ denotes the turbulent Prandtl number in the undisturbed boundary-layer. The above equation can be simplified using the mean total temperature definition as

$$\hat{A} = -\frac{C_p}{\overline{u}_1 Pr_{T,0}}\frac{\partial \overline{T}_1}{\partial \overline{u}_1}. \tag{7.2}$$

Next the Walz temperature distribution for zero pressure-gradient turbulent boundary layer is used to calculate the upstream velocity-temperature derivative,

$$\frac{\overline{T}_1}{T_\infty} = \frac{T_w}{T_\infty} + \frac{T_r - T_w}{T_\infty}\frac{\overline{u}_1}{u_\infty} + \frac{T_\infty - T_r}{T_\infty}\left(\frac{\overline{u}_1}{u_\infty}\right)^2 \tag{7.3}$$

Using $\frac{T_r}{T_\infty} = 1 + \frac{\gamma-1}{2}r_c M_\infty^2$ relation the above equation can be simplified as

$$\frac{\overline{T}_1}{T_\infty} = \frac{T_w}{T_r}\left(1 + \frac{\gamma-1}{2}r_1 M_\infty^2\right) + \left(1 + \frac{\gamma-1}{2}r_c M_\infty^2\right)\left(1 - \frac{T_w}{T_r}\right)\frac{\overline{u}_1}{u_\infty} - \frac{\gamma-1}{2}r_1 M_\infty^2\left(\frac{\overline{u}_1}{u_\infty}\right)^2 \tag{7.4}$$

Differentiating the above equation with respect to $\overline{u}_1$ yields,

$$\frac{1}{T_\infty}\frac{\partial \overline{T}_1}{\partial \overline{u}_1} = \left(1 + \frac{\gamma-1}{2}r_c M_\infty^2\right)\left(1 - \frac{T_w}{T_r}\right)\frac{1}{u_\infty} - \frac{\gamma-1}{2}r_c M_\infty^2\frac{2\overline{u}_1}{u_\infty^2} \tag{7.5}$$

$$\Rightarrow \frac{1}{T_\infty}\frac{\partial \overline{T}_1}{\partial \overline{u}_1} = \frac{\gamma-1}{2}r_c M_\infty^2\left(\left(1 - \frac{T_w}{T_r}\right)\frac{1}{u_\infty} - \frac{2\overline{u}_1}{u_\infty^2}\right) + \left(1 - \frac{T_w}{T_r}\right)\frac{1}{u_\infty} \tag{7.6}$$

$$\Rightarrow \frac{\partial \overline{T}_1}{\partial \overline{u}_1} = \frac{\gamma-1}{2}r_c\frac{u_\infty^2}{\gamma R}\left(\left(1 - \frac{T_w}{T_r}\right)\frac{1}{u_\infty} - \frac{2\overline{u}_1}{u_\infty^2}\right) + \left(1 - \frac{T_w}{T_r}\right)\frac{T_\infty}{u_\infty} \tag{7.7}$$

$$\Rightarrow \frac{\partial \overline{T}_1}{\partial \overline{u}_1} = \frac{r_c u_\infty^2}{2C_p}\left(\left(1 - \frac{T_w}{T_r}\right)\frac{1}{u_\infty} - \frac{2\overline{u}_1}{u_\infty^2}\right) + \frac{u_\infty}{\gamma R}\frac{1}{M_\infty^2}\left(1 - \frac{T_w}{T_r}\right) \tag{7.8}$$

$$\Rightarrow \frac{\partial \overline{T}_1}{\partial \overline{u}_1} = \frac{r_c u_\infty^2}{2C_p}\left(\left(1 - \frac{T_w}{T_r}\right)\frac{1}{u_\infty} - \frac{2\overline{u}_1}{u_\infty^2} + \frac{2}{(\gamma-1)r_c u_\infty M_\infty^2}\left(1 - \frac{T_w}{T_r}\right)\right) \tag{7.9}$$

Substituting the above relation into equation 7.2 gives

$$\hat{A} = -\frac{u_\infty^2}{2\overline{u}_1}\left(\left(1 - \frac{T_w}{T_r}\right)\frac{1}{u_\infty} - \frac{2\overline{u}_1}{u_\infty^2} + \frac{2}{(\gamma-1)r_c u_\infty M_\infty^2}\left(1 - \frac{T_w}{T_r}\right)\right) \tag{7.10}$$

Here the magnitude of $Pr_{T,0}$ is equated with the recovery factor $r_c(Pr_T = r_c = 0.89)$ for a cancellation.The final expression for $\hat{A}$ becomes

$$\hat{A} = 1 - \frac{u_\infty}{2\overline{u}_1}\left[\frac{1 - \frac{T_w}{T_r}}{1 - \frac{T_\infty}{T_r}}\right]. \tag{7.11}$$

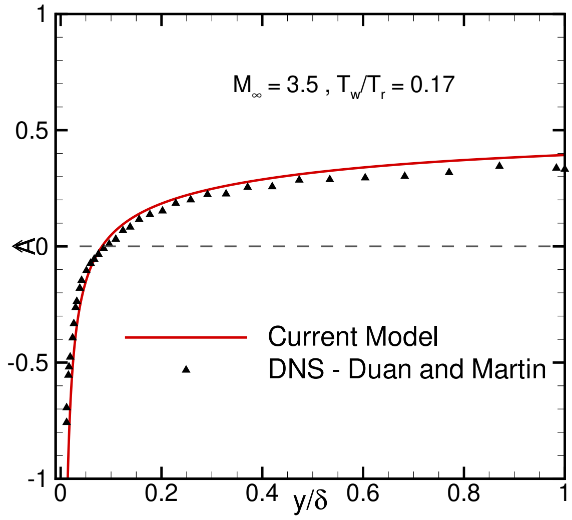

Figure 7.1: Variation of the velocity-temperature correlation $\hat{A}$ as per Eq. 7.11 in the wall normal direction for freestream Mach number 3.5 and $\frac{T_w}{T_r} = 0.17$. The model is also compared with the DNS data of Duan and Martin [17].

Note that the above expression will get back to adiabatic assumption for $T_w/T_r = 1$. The analytical solution obtained from the Walz's equation [91] for the temperature profile mostly complements the DNS and experimental data except for the very cold wall ($T_w/T_r < 0.4$) where a slight mismatch is observed at the maximum temperature location [17]. An empirical correction is proposed by Duan and Martin [17] for such cases. The analysis done by Bernardini et al. [5] also shows a disagreement between the Walz's equation and DNS data at the outer part of the boundary layer but this is because of the change in wall temperature (explained later). Figure 7.1 shows the variation of the velocity-temperature correlation $\hat{A}$ in the wall normal direction of a turbulent boundary layer for freestream Mach number 3.5 and $\frac{T_w}{T_r} = 0.17$. The model is also compared with the DNS data of Duan and Martin [17]. The current model predicts well in the near wall region as well and for $y/\delta = 0(\overline{u}_1 = 0)$ it tends to a negative value where velocity and temperature fluctuations are positively correlated. Theoretically $\hat{A} \to -\infty(\infty)$ for cold (hot) wall condition and DNS data also suggests that trend. $\hat{A}$ changes sign from negative to positive at $y/\delta = 0.08$ and the cross-over velocity can be found by setting $\hat{A} = 0$ in

Eq. 7.11. The sign change of $\hat{A}$ occur at the location of maximum temperature which is located below the sonic line. Thus the current model which is meant for only shock wave region will not be affected by the negative value of $\hat{A}$. The value of $\hat{A}$ is almost saturating to the boundary layer edge value after $y/\delta = 0.25$ and for the current SBLI simulations the edge values have been taken for the computation. The final expression for the shock-induced turbulent heat flux is given as

$$\overline{u_2'T_2'} = -\frac{\overline{u}_2}{c_p}\overline{u_2'^2}\,(1 + b_2(r-1) - \beta)\,, \tag{7.12}$$

where $\beta = \alpha r(1 - \hat{A})$. The aforementioned model accounts only the shock motion at frequencies comparable to that of the incoming turbulence. Additional low-frequency shock oscillations, observed in the SBLI, have a negligible correlation with the turbulent velocity fluctuation in the boundary layer. Such low frequency shock motion do not contribute to the $\overline{u_2'\xi_t}$ correlations. The equivalent post-shock turbulent Prandtl number is given as

$$Pr_T = \frac{3}{4}\left(\frac{1}{1 + b_2(r-1) - \beta}\right), \tag{7.13}$$

where the shock-normal Reynolds stress is modeled in terms of the Boussinesq approximation. The above expression of Pr_T is very similar to that of chapter 5,6 except the β term which combined the effect of upstream velocity and temperature fluctuations here. Also the shock-unsteadiness damping parameter is updated in order to count the turbulent Mach number effect and wall/cooling/heating effect.

$$b_2 = (0.5 + M_t^2 + 0.2A_{uT})\left(\frac{r-1}{5}\right)^{0.3}. \tag{7.14}$$

A brief review of the scalar shock function ψ is presented here to evaluate the mean density ratio at the shock region and the full analysis can be found in chapter 5. The turbulent Prandtl number is then modeled in terms of ψ. The transport equation for ψ is such that it deviates from its undisturbed value ψ_0 only in the regions of compression and gradually relaxes back from the shock value to the reference value.

$$\frac{\partial(\overline{\rho}\psi)}{\partial t} + \frac{\partial(\overline{\rho}\widetilde{u}_i\psi)}{\partial x_i} = \overline{\rho}\psi S_{ii} - \overline{\rho}(\psi - \psi_0)\frac{\sqrt{\widetilde{u}_i\widetilde{u}_i}}{L_\epsilon}, \tag{7.15}$$

where $S_{ii} = \frac{\partial \widetilde{u}_i}{\partial x_i}$ is the mean dilatation, $\sqrt{\widetilde{u}_i\widetilde{u}_i}$ is the mean velocity magnitude and $L_\epsilon = \sqrt{k}/\omega$ is the dissipation length scale in the k-ω framework. Integrating the differential equation across a shock gives the shock value ψ_s as

$$\frac{\psi_s}{\psi_0} = \frac{\overline{u_2}}{\overline{u_1}} = \frac{1}{r} \tag{7.16}$$

Thus, ψ_s is an indicator of the shock strength and an upstream undisturbed value of $\psi_0 = 1$ ensures that we get $\psi_s = 1/r$ at the shock location. Substitution of $r = 1/\psi$ in Eq. (7.13) gives an expression for turbulent Prandtl number as

$$Pr_T = \frac{3/4\zeta}{1 + b_2(\psi^{-1} - 1) - \beta} \tag{7.17}$$

where an additional factor ζ is introduced to make the formulation consistent with the conventionally accepted Pr_T value of 0.89 in boundary layers without shock waves. For vanishing shock strength in the limit $M_1 \to 1$, r $\to$ 1 and $\psi \to 1$, Pr_T should take a value of 0.89. Thus, ζ is defined as

$$\zeta = 1 + \left(\frac{0.89}{0.75}(1-\beta) - 1\right)\exp\left(\chi(1 - \frac{1}{\psi})\right). \tag{7.18}$$

such that it approaches 1 in the presence of shock waves. Here χ is model parameter and its value is equal to 1000 and sensitivity of this parameter has been checked in chapter 5.

7.2 Application to Shock/Boundary Layer Interaction

Table 7.1: The freestream and wall conditions in the DNS experiments of Bernardini [5].

Deflection angle	M_∞	ρ_∞ (kg/m^3)	T_∞ (K)	T_w (K)	T_w/T_r	H_0 (MJ/kg)	$\hat{A}$
8°	2.28	0.06	299.8	287.8	0.50	0.58	0.483
8°	2.28	0.06	299.8	431.7	0.75	0.58	0.741
8°	2.28	0.06	299.8	578.6	1.00	0.58	1
8°	2.28	0.06	299.8	809.5	1.40	0.58	1.414
8°	2.28	0.06	299.8	1097.3	1.90	0.58	1.931

The direct numerical simulations of an oblique shock impinging on a turbulent boundary layer developed over flat plat were carried out by Bernardini et al. [5] with a shock deflection angle of 8° and freestream Mach number of 2.28. The test cases consist of different values of wall to recovery temperature ratio, spanning cold (T_w/T_r = 0.5, 0.75), adiabatic (($T_w/T_r = 1$), hot (T_w/T_r = 1.40, 1.90) walls. The test conditions are given in table 7.1. The values of $\hat{A}$ at the boundary layer edge are also reported in table and these values are used in the RANS simulations. All the computations were performed with dry air and perfect gas assumption.

The computation domain is shown in Fig. 7.2 and it extends about 142 δ_{in} in the streamwise (x) direction and 12 δ_{in} in the wall-normal direction (y), with δ_{in} = 7.65mm being the reference inflow boundary layer thickness from DNS. No slip and isothermal boundary conditions are used at the wall, while extrapolation condition is applied at the exit boundary of the domain. Initially the turbulent boundary layer develops under adiabatic conditions up to x_0 and the boundary layer properties are compared with the DNS data at this location, see table 7.2. Here, δ, θ, δ^* are the boundary layer, momentum and displacement thickness respectively. The Reynolds numbers are defined as $Re_\theta = \rho_\infty u_\infty \theta/\mu_\infty$, $Re_{\delta_2} = \rho_\infty u_\infty \theta/\mu_w$, $Re_\tau = \rho_w u_\tau \delta/\mu_w$. Here subscripts ∞ and w represent the freestream and wall conditions respectively and $u_\tau = \sqrt{\frac{\tau_w}{\rho_w}}$ is the frictional velocity based on wall shear stress τ_w. The skin friction coefficient c_f is also reported in the table.

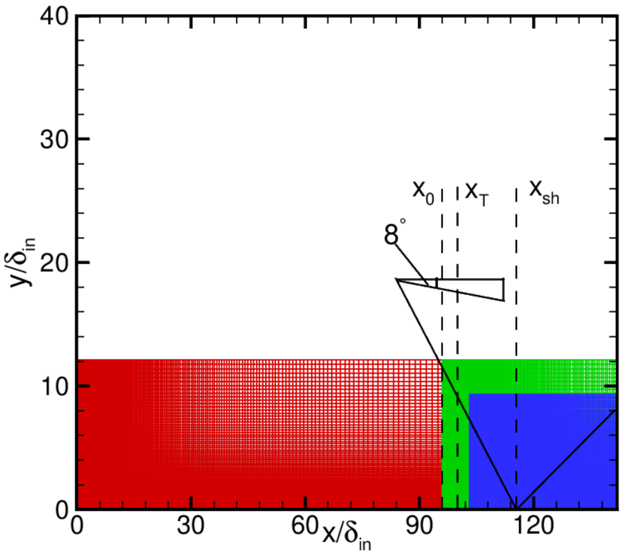

Figure 7.2: Flow configuration and computational domain under investigation.

Table 7.2: Properties of the incoming turbulent boundary layer at x_0. Here subscript 0 represents the x_0 station.

Method	δ_0 (mm)	θ_0 (mm)	δ_0^* (mm)	Re_θ	Re_{δ_2}	Re_τ	c_f (10^{-3})
DNS	11.10	0.9366	3.41	2410	1509	450	2.45
RANS	11.19	0.9405	3.48	2420	1516	458	2.48

Local cooling or heating is applied for $x > x_T$ by specifying the desired wall-to-recovery-temperature ratio $s = T_w/T_r$. To avoid a discontinuity in the wall temperature distribution, a smooth step change is prescribed according to Bernardindi et al. [5] and the same wall temperature profile is used here.

$$T_w(x) = T_r\left[1 + \frac{s-1}{2}\left(1 + \tanh\frac{2(x - x_T)}{\delta_{in}}\right)\right] \tag{7.19}$$

The transition of wall temperature from adiabatic to hot or cold is occurred between x_0 to x_T which is $4\delta_{in}$ distance apart. Figure 7.3 shows the wall temperature variation in the streamwise direction.

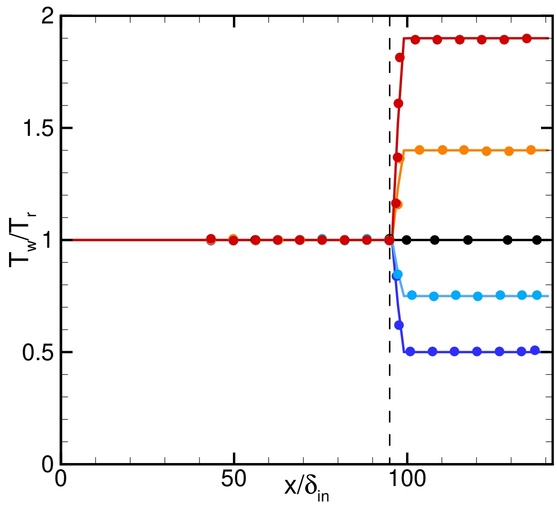

Figure 7.3: Distribution of the wall temperature as a function of the streamwise distance normalized by δ_{in}. The vertical dotted line denotes the location of the temperature step change. Here the solid line represents the RANS results and symbols denotes the DNS data from Bernardini [5]. The colour coding are : Blue $s = 0.5$, Cyan $s = 0.75$, Black $s = 1$, Orange $s = 1.4$ and Red $s = 1.9$.

7.2.1 Numerical methodology

The blue region of the computational domain in Fig. 7.2 is the final mesh used for the SBLI simulations. An inlet profile is fed at the starting of the domain and oblique shock is introduced in the simulation by locally imposing the inviscid Rankine-Hugoniot jump conditions to mimic the effect of the shock generator, and the nominal inviscid shock impingement point is $x_{sh} = 115.5\delta_{in}$; see Pasha and Sinha [60] for more details on the inlet profile generation.

The SBLI computational grid (blue region) consists of 300×400 points, with stretching functions are employed to better resolve the interaction region and to cluster grid nodes towards the wall. Refining the grid to 450×600 points shows minimal changes in the wall heat transfer solution, within 1.5% for the $T_w/T_r = 0.5$ and 1.9 cases. The first point next to the wall is placed at 10^{-6} m, which is equivalent to 0.4 wall units or less along the plate.

The two dimensional Reynolds-averaged Navier-Stokes equations (RANS) are solved for a perfect compressible gas with Fourier heat law and Newtonian viscous terms for the mean flow along with the transport equations for the turbulence quantities. The molecular viscosity μ is assumed to depend on temperature T through Sutherland's law, and the thermal conductivity is computed as $\kappa = c_p\mu/Pr$, with the molecular Prandtl number being set to Pr = 0.72. The standard $k - \omega$ model of Wilcox 1998 [92] and the shock-unsteadiness modified $k-\omega$ model of Veera and Sinha [85] along with the updated parameter b_1' (see equation 2.80) are used for turbulence closure. The turbulence models do not include any compressibility corrections, as they are found to deteriorate model predictions in the undisturbed boundary layer upstream of the interaction [12, 22]. Compressibility corrections of the form of dilatational dissipation reduce the turbulent kinetic energy in the boundary layer, and thus decrease the skin friction coefficient compared to well-established correlations for zero pressure-gradient turbulent boundary layers.

A finite volume formulation is used to discretize the governing mean flow equations fully coupled with turbulence model equations. The inviscid fluxes are solved using a modified, low-dissipation form of the Steger-Warming flux splitting method [83]. This method reduces the numerical dissipation, and is found to be useful for high-speed flows with strong shock waves and viscous-inviscid interactions with boundary layers. As a result, very thin and well-defined shock waves are captured over a few grid cells. The discretization method is second-order accurate in space; the details of the formulation can be found in Ref. [77]. The viscous fluxes and the turbulent source terms are calculated using second-order accurate central difference method. The implicit Data-Parallel Line Relaxation (DPLR) method of Wright et al. [93] is used to integrate the equations in time to reach a steady-state solution. For the turbulence quantities, the boundary conditions at the wall [54] are prescribed as $k = 0$ and $\omega = 60\nu_w/\beta_1\Delta y_1^2$, where ν_w is kinematic viscosity at the wall, $\beta_1 = 3/40$ and Δy_1 is the normal distance to the grid point nearest to the wall. Following Menter [54], the freestream conditions used for the flat plate simulations are $\omega_\infty = 10U_\infty/L = 7.91 \times 10^3 s^{-1}$ and $k_\infty = 0.01\nu_\infty\omega_\infty = 2.43 \times 10^{-2} m^2/s^2$ where L = 1 m is a characteristic length of the flat plate.

7.2.2 Surface Properties

The results for the SBLIs are reported using scaled interaction coordinates $x^* = (x - x_{sh})/\delta_0$ and $y^* = y/\delta_0$. The spatial distribution of the mean wall skin friction coefficient $c_f = 2\tau_w/\rho_\infty u_\infty^2$ is shown in Fig. 7.4. In the presence of the impinging shock,

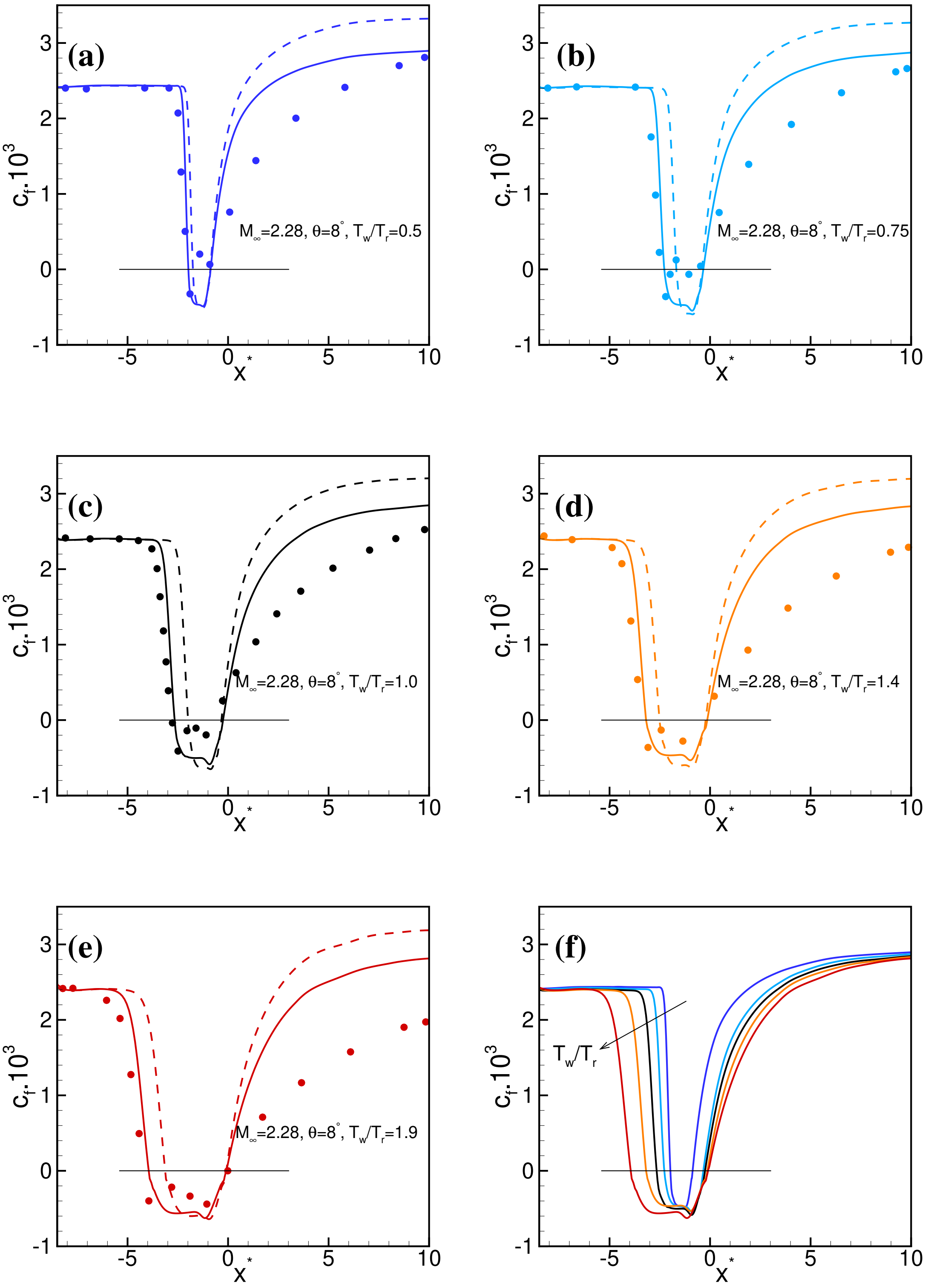

Figure 7.4: Distribution of the wall skin friction coefficient at various wall to recovery temperature ratios using standard $k-\omega$ (dashed line) and shock-unsteadiness modified $k-\omega$ model with Pr_T variation (solid line), Eq. 7.17. The results are also compared with the DNS data (symbols) of Bernardini et al. [5]. For colour nomenclature refer Fig. 7.3.

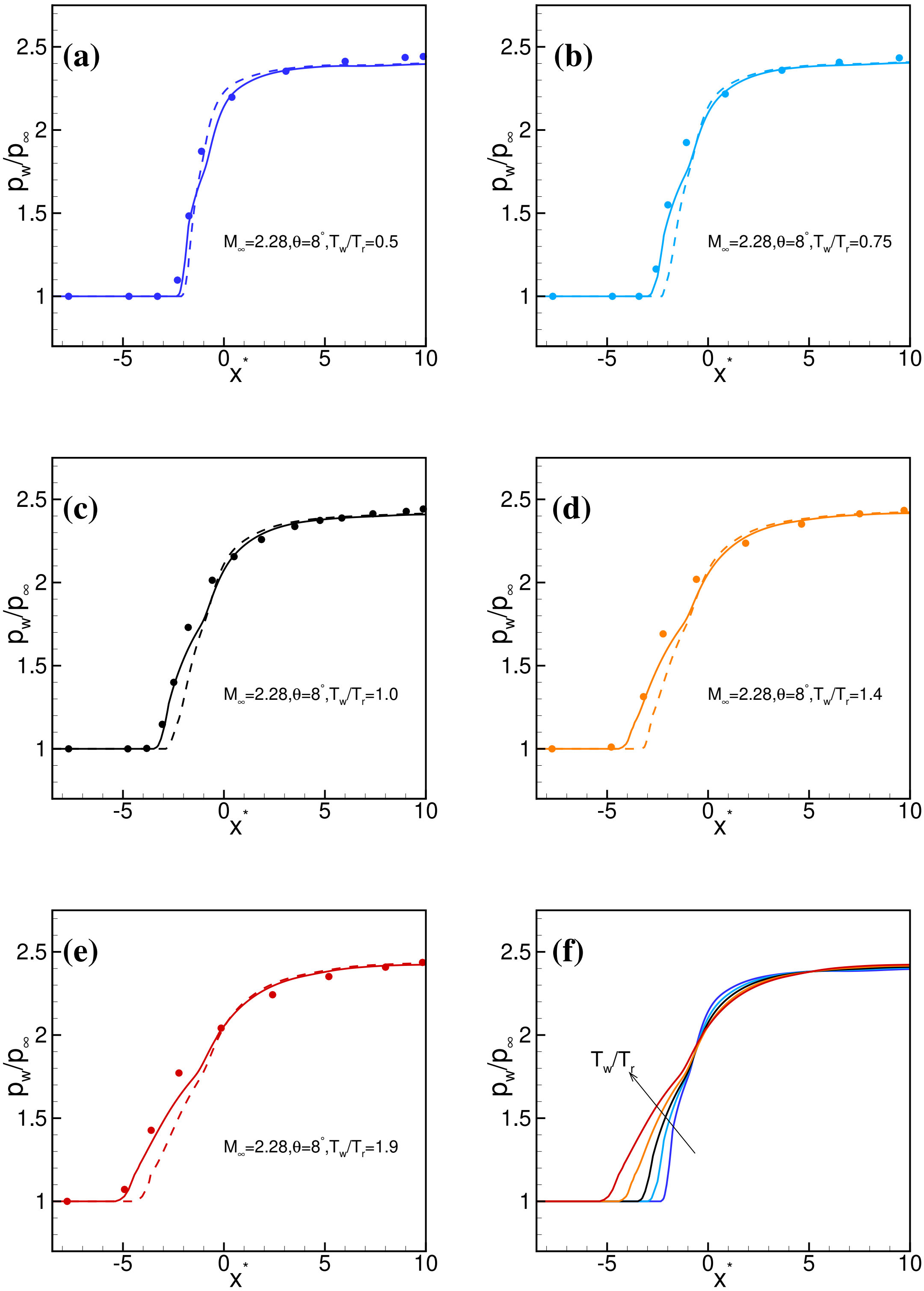

Figure 7.5: Distribution of the wall pressure at various wall to recovery temperature ratios using standard $k-\omega$ (dashed line) and shock-unsteadiness modified $k-\omega$ model with Pr_T variation (solid line), Eq. 7.17. The results are also compared with the DNS data (symbols) of Bernardini et al. [5]. For colour nomenclature refer Fig. 7.3.

the skin friction exhibits a sharp decrease at the beginning of the interaction, and for all cases mean flow separation is observed, identified by the horizontal black dashed line. Standard $k-\omega$ and the shock-unsteadiness(SU) modified $k-\omega$ model predict identical solutions in the undisturbed boundary layer. The SU modification gives a better prediction of the separation point compared to the standard $k-\omega$ and its able to mimic the DNS separation point very well for all the cases. The reattachment point is almost identical for the two models and matches the DNS data. Both the models over predict the c_f value in the post-reattachment region when compared to the DNS data with SU modification has a slightly better prediction. The difference between standard $k-\omega$ and SU $k-\omega$ increases with T_w/T_r; highest difference being observed at $T_w/T_r = 1.9$. Compared to the adiabatic case, wall cooling results in a significant reduction of separation length (-72% for s = 0.5), whereas heating the wall leads to the opposite effect (+76% for s =1.9). The location of the separation point is most affected by the wall temperature change, whereas the boundary layer reattachment is less influenced by s, being mainly controlled by the impinging shock location. An overall comparison of the wall heating/cooling on skin friction coefficient is given in figure 7.4(f).

The major influence of cooling or heating is also apparent from the mean wall pressure distribution reported in Fig. 7.5. Heating the wall shifts the beginning of the interaction upstream, leading to a smoother pressure rise. The opposite behavior occurs in the case of cooling, which produces a downstream shift of the upstream influence and a steeper variation of p_w within the interaction zone. The SU modified $k-\omega$ model is able to capture the pressure plateau well for the adiabatic and non-adibatic conditions when compared with the DNS data. Both standard $k-\omega$ and SU modified model give similar prediction in the post-reattachment region and mimics the DNS data very well. An overall comparison of surface pressure is given in figure 7.5(f) for different wall to recovery temperature ratio and upstream shift of the separation point is clearly visible with an increase in T_w/T_r.

7.2.3 Effect of wall cooling/heating on flow separation

The variation of the upstream temperature in the wall normal direction with various wall cooling/heating is shown in Fig. 7.6(a). The results are plotted at the starting of the SBLI domain; see Fig. 7.2. The near wall temperature increases with the wall heating. The maximum temperature is observed at the wall for the adiabatic and hot wall condition whereas a local temperature peak is identified just above the wall for the cold wall. Due to the low temperature, the near wall Mach number is higher for wall cooling and the sonic line moves closer to the wall, which effectively reduces the subsonic channel thickness

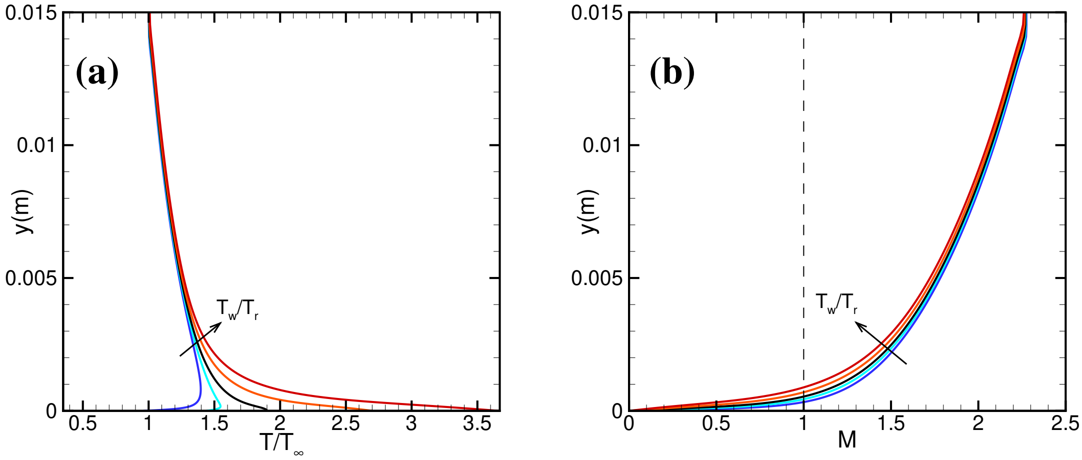

Figure 7.6: Distribution of upstream (a) mean temperature and (b) Mach number in the wall normal direction at the starting of the SBLI domain. The black dotted line in the Mach number plot represents the sonic line. For colour coding refer Fig. 7.3.

in the flow; see Fig. 7.6(b) . A higher Mach number near the wall increases the flow momentum and delay the flow separation. Also, the viscosity near the wall is low for cold wall condition. A lower viscosity increases the effective Reynolds number near the wall and hence reduces the flow separation tendency.

The wall cooling/heating not only changes the mean flow profile, it also affects the upstream turbulence. Figure 7.7 shows the the effect of wall cooling/heating on the parameter $\hat{A}$. The parameter $\hat{A}$ quantifies the upstream temperature and velocity fluctuations ratio. The magnitude of $\hat{A}$ increases with wall heating. The temperature and velocity fluctuations are always positively correlated for hot wall and a positive value of $\hat{A}$ is always obtained for hot wall condition. $\hat{A}$ value of greater than 1 also suggests that the boundary layer is dominated by the entropic mode for the hot wall condition. A higher temperature fluctuation also produced high turbulent heat flux and more heat will be convected by the turbulence eddies and the surface heat flux will be lower for the heated wall. Note that $\hat{A}$ equals to 1 for the adiabatic condition imitates Morkovin's hypothesis [56]. On the other hand, a negative correlation is found between velocity and temperature fluctuations for the cold wall condition. The crossover position ($\hat{A} = 0$) occurs close to the position of maximum mean temperature.

The standard $k - \omega$ model predicts the upstream mean profile very well and it captures the effect of wall cooling/heating on the upstream mean profile accurately. The difference between DNS and standard $k - \omega$ model is due to the upstream turbulence level. The standard $k - \omega$ model fails to capture the effect of wall temperature on shock-

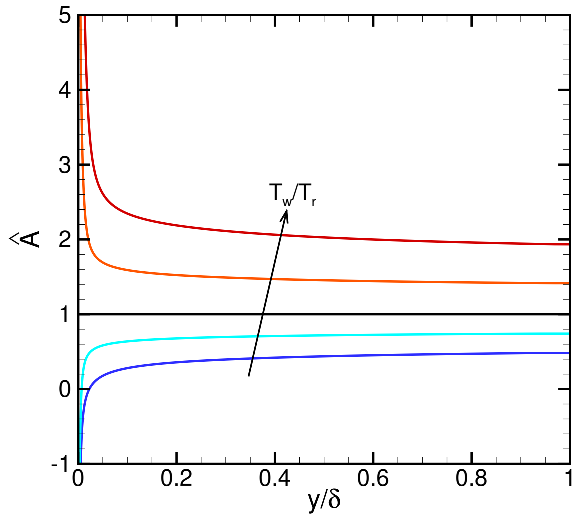

Figure 7.7: Variation of the parameter $\hat{A}$ in the wall normal direction for different wall cooling/heating at the starting of the SBLI domain. Color coding is same as Fig. 7.3.

turbulence interaction. On the other hand the SU $k-\omega$ model brings the effect of wall cooling/heating on upstream turbulence by the term $\hat{A}$ and turbulent Mach number M_t. The shock-unsteadiness damping parameter is tuned as

$$b_1' = (0.4 + M_t^2 + 0.2A_{uT})\left(\frac{r-1}{5}\right)^{0.3}. \tag{7.20}$$

Here $A_{uT} = (\gamma - 1)M^2\hat{A}$. The shock-unsteadiness damping parameter is used to limit the production of turbulent kinetic energy (TKE) across the shock and it brings the damping effect due to unsteady shock oscillation; more details can be found in [60, 70, 78]. The SU modification thus brings the effect of upstream turbulence, wall cooling/heating and shock strength together in a single model. The turbulent Mach number increases with wall cooling and the maximum value of M_t is 0.23 for $T_w/T_r = 0.5$. Hence the effect of upstream turbulent Mach number on the SU damping parameter b_1' is very small.

The variation of b_1' through the separation shock in the wall normal direction is shown in Fig. 7.8 for various wall conditions. The damping effect increases with wall heating and the maximum damping occur at the boundary layer edge. The SU modification is only applied at the shock region thus $b_1' = 0$ at the wall ($y = 0$) where the shock does not penetrates. Although b_1' varies throughout the shock wave, the variation of b_1' inside the log region (given by the black dotted line in Fig. 7.8) of the boundary layer only affects the flow separation. The value of b_1' inside the log region is comparable for the different wall cooling/heating for the current test cases.

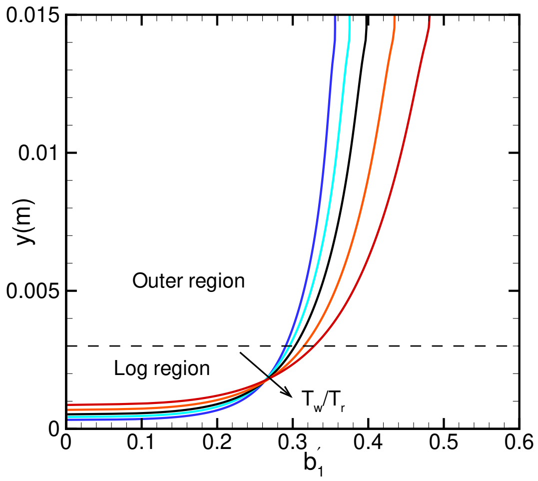

Figure 7.8: Variation of shock-unsteadiness damping parameter in the wall normal direction through the separation shock for different wall cooling/heating ratios. The color symbols are same as Fig. 7.4.

An overall comparison of the separation length computed by the two models and DNS data is shown in Fig. 7.9. The separation length is normalized by the boundary layer thickness at station x_0. Both the models predict an increase in separation size with wall heating. Standard $k - \omega$ model mostly captures the mean flow effect whereas the shock unsteadiness model captures both the effect of mean and turbulence. Thus their difference will qualitatively highlight the turbulence contribution on the overall separation. As explained earlier the turbulence contribution will be determined by the damping parameter b_1' in the log region. As the variation of b_1' is not that much inside the log region, the contribution of upstream turbulence on the overall separation is almost constant with wall cooling/heating. The overall separation due to turbulence extends about $0.2\delta_0$ for all the cases except for $T_w/T_r = 0.5$ where the effect of turbulence on the separation is much smaller and both the models predict almost identical separation.

7.2.4 Scaling of The Interaction Length

The scaling law of Jaunet et al. [36] is widely used for non-adibatic SBLI flows. The length of the interaction is normalized by the displacement thickness δ^* of the upstream boundary layer and a function g_3 which takes into account the flow deflection. From their scaling analysis, the dimensionless length of interaction is given by

$$L^* = \frac{L}{\delta^* g_3}, \quad g_3 = \frac{\sin(\beta - \theta)}{\sin\beta \sin\theta}, \tag{7.21}$$

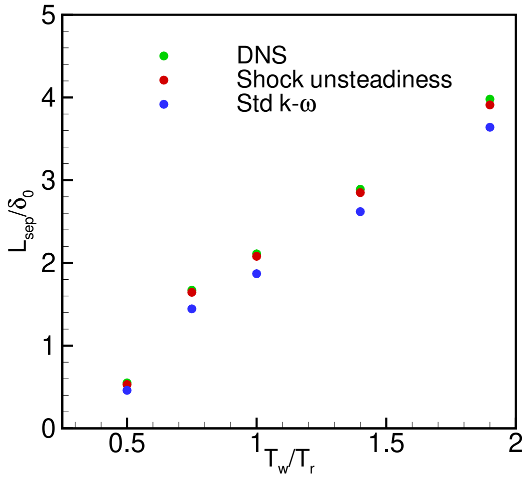

Figure 7.9: Effect of wall temperature on the separation length. The results are obtained using standard $k - \omega$ and shock-unsteadiness models. A comparison with the DNS data of Bernardini et al. [5] is also presented.

where L is the interaction length, θ and β stand for the geometric deflection and shock angle respectively. The normalized interaction length L^* is combined with the separation criterion $\Delta p/\Delta p_{sep}$, in which Δp is the shock strength and Δp_{sep} combines the effect of wall cooling/heating and freestream Mach number. The expression for Δp_{sep} is given as

$$\Delta p_{sep} = 7.14 q_\infty \sqrt{\frac{2c_{f,0}}{\sqrt{M_\infty^2 - 1}}}, \tag{7.22}$$

where q_∞ is the freestream dynamic pressure, $c_{f,0}$ is the skin friction coefficient in the upstream boundary layer.

Now for the present DNS cases of Bernardini et al. [5] the shock strength Δp is constant and Δp_{sep} captures the wall cooling/heating effect in terms of $c_{f,0}$. The scaling of Jaunet et al. [36] does not collapse the data of Bernardini et al. [5] and Souverein et al.[81] very well and a modification to the separation criterion is required in order to collapse all the data. Here $\Delta p_{sep} \propto \sqrt{c_{f,0}}$ and the wall skin friction coefficient $c_{f,0} \propto \frac{1}{Re_w^{1/5}}$ for a flat plate turbulent boundary layer. Now the wall Reynolds number $Re_w \propto \frac{\rho_w}{\mu_w}$, where ρ_w and μ_w are the density and viscosity at the wall respectively in the upstream boundary layer. According to Prandtl's boundary-layer theory, the pressure remains approximately constant in the boundary layer. Hence the wall density should be inversely proportional to the wall temperature

$$\rho_w \propto \frac{1}{T_w} \quad and \quad \mu_w \propto T_w^{0.75}, \tag{7.23}$$

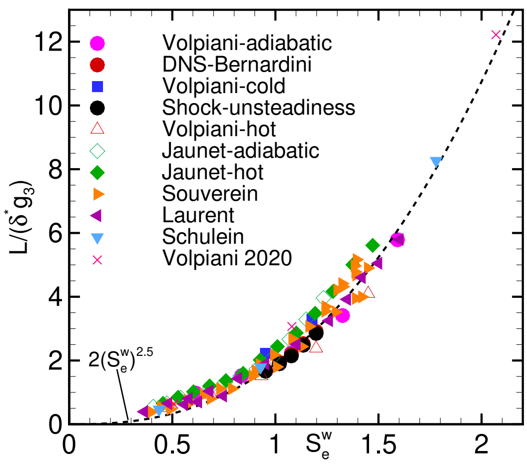

Figure 7.10: Normalized interaction length as a function of separation criterion. Compilation of results discussed in [36, 47, 73, 81, 87, 88] is also reported. Dashed line represents the best fit line (ax^b with a=2 and b=2.5).

assuming a power law relationship between the wall viscosity and temperature. Hence the Reynolds number is given as

$$Re_w \propto \frac{1}{T_w^{1.75}} \propto \frac{1}{(T_w/T_r)^{1.75}}, \tag{7.24}$$

where the recovery temperature T_r is constant. Using the above relations, we can write the skin friction coefficient as

$$c_{f,0} \propto \left(\frac{T_w}{T_r}\right)^{0.35} \tag{7.25}$$

Using Eqs. 7.22 and 7.25, we define a new separation criterion similar to the shock strength parameter of Souverein et al. [81] and Jaunet et al. [36]

$$S_e^w = \frac{13.6}{M_\infty g_3}\left(\frac{T_w}{T_r}\right)^{0.175}, \tag{7.26}$$

where the additional effects of freestream Mach number M_∞ and flow deflection g_3 are also included to scale a large number of data sets. The interaction length decreases with an increment in freestream Mach number. On the other hand the deflection angle θ increases the interaction length and decreases the parameter g_3. Hence a reduction in g_3 will results in a bigger interaction length. Thus the separation criterion S_e^w is inversely proportional to M_∞ and g_3.

The normalized interaction length is plotted as a function of S_e^w in Fig. 7.10 together with the experiments of Jaunet et al. [36] for adiabatic and heated walls, Laurent [47] for heated wall, Souverein et al. [81] for adiabatic wall, Schulein [73] for cold wall and the numerical data of Volpiani et al. [87, 88] for cold, adiabatic and heated walls. The agreement between numerical and experimental results is very good and validates the scaling law proposed herein. The DNS data of Bernardini et al. [5] and the results obtained from shock-unsteadiness correction predict almost identical interaction length. The best curve fit $\frac{L}{\delta^{*} g_3} 2(S_e^w)^{2.5}$ to the data is also presented in Fig. 7.10. Since the scaling is based on upstream quantities, it can be evaluated for the whole set of available experimental and numerical SBLIs. Note that the data from [73] and [88] does not collapse with the original scaling of [36].

7.2.5 Surface Heat Transfer

To characterize the heat transfer behavior across the interaction the spatial distribution of the Stanton number St is reported in Fig. 7.11 for all flow cases investigated here. The Stanton number is defined as

$$St = \frac{q_w}{\rho_\infty u_\infty c_p (T_w - T_r)} \tag{7.27}$$

where q_w is the wall heat flux and it is computed by Fourier law. A complex variation of the Stanton number is observed when varying the wall temperature. First St decreases to a local minimum in the proximity of the separation point, followed by a sharp rise in the reattachment zone. After the reattachment point the value of Stanton number decreases in the recovery boundary layer and reaches an asymptotic value far away from the interaction region. In the case of the heated wall ($T_w/T_r = 1.9$) a non-monotonic behaviour is observed in the Stanton number distribution. Here, the Stanton number exhibits a dip in the recovery boundary layer and then increases again, attaining a second peak in the downstream relaxation region. A strong amplification of the heat transfer rate St is found in the interaction region with respect to the reference cooled or heated boundary layers, with a maximum increase of approximately a factor of 2 for the cooled wall and 1.7 for the heated wall. The variation of the turbulent Prandtl number Pr_T in the interaction region (in the vicinity of the shock wave) directly influenced the surface heat transfer. The value of Pr_T decreases with wall heating. Reducing the Pr_T value results in a higher turbulent conductivity . An elevated turbulent conductivity leads to a higher diffusion of heat away from the wall, leading to a lower surface heat transfer for the heated wall. The new model is able to capture the peak heat transfer very well compared to the DNS data whereas the standard $k - \omega$ model over predicts the data for all the test conditions. Despite the fact that wall cooling results in a weaker interaction (as far as the separation bubble size is concerned), the reduction of the sonic line in the streamwise and wall-normal directions produces stronger temperature gradients at the wall, thus leading to larger heating rates.

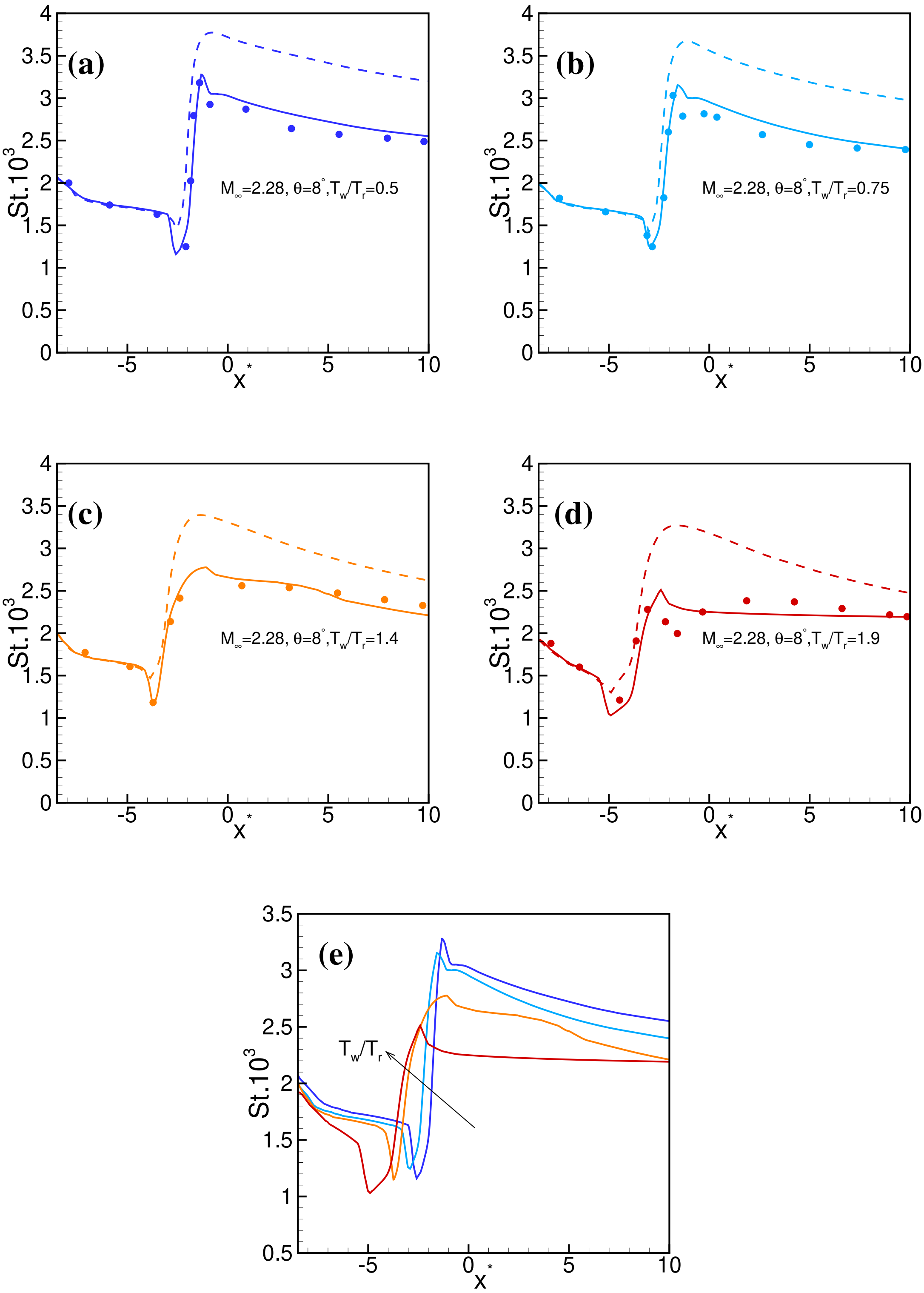

Figure 7.11: Distribution of the Stanton number at various wall to recovery temperature ratios using standard $k-\omega$ (dashed line) and shock-unsteadiness modified $k-\omega$ model with Pr_T variation (solid line), Eq. 7.17. The results are also compared with the DNS data (symbols) of Bernardini et al. [5]. For colour nomenclature refer Fig. 7.3.

7.3 Application to Hypersonic Flows

The axisymmetric cone-flare configurations of Holden et al. [29] is presented in chapter 6. Here the Mach 8 and 7 test cases are considered again for the validation of the final form of the variable Pr_T model which includes both shock and wall heating/cooling effect. The test conditions are listed in table 7.3. The geometry consists of a 2.5 m long (horizontal length) 7° half-angle cone and a 40° flare, which gives a 33° turning angle at the cone-flare junction. The computational domain extends from the tip of the cone to the end of the flare, and the outer boundary is tailored to the inviscid cone shock. The computational grid consists of 450×150 points, with fine grid at the cone tip and the cone-flare junction; see Fig. 7.12. Refining the grid to 850×250 points shows minimal changes in the solution, within 1.5% in the flare heat flux prediction for the strongest interaction at Mach 8.21. The first point next to the wall is placed at 10^{-6} m, which is equivalent to 0.5 wall units or less along the cone-flare surface. A small symmetry plane is added in front of the cone tip to avoid a stagnation point boundary condition.

	Deflection angle	M_∞	ρ_∞ (kg/m^3)	T_∞ (K)	T_w (K)	Re_∞/m $\times 10^6$	T_w/T_r	H_0 (MJ/kg)	$k_\infty, 10^{-3}$ (m^2.s^{-2})	$\omega_\infty, 10^4$ (s^{-1})
Cone-	33°	8.21	0.0437	60.4	306.5	14.30	0.38	0.87	5.00	0.54
flare	33°	7.18	0.0572	66.6	302.5	15.60	0.44	0.76	3.90	0.50

Table 7.3: The freestream and wall conditions in the SBLI experiments [29].

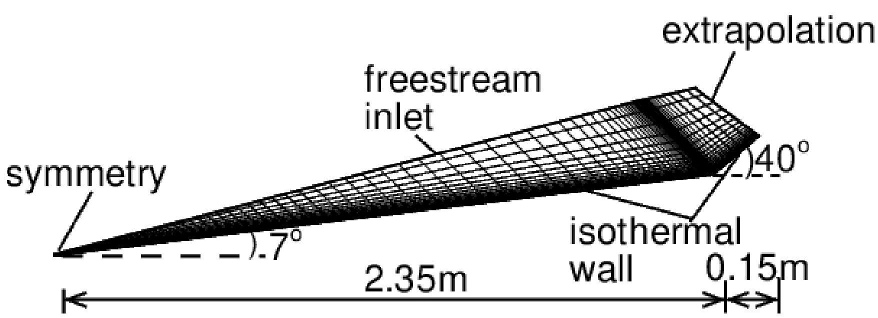

Figure 7.12: Computational mesh with boundary conditions showing every third point in each direction.

The flow topology for Mach 8.21 case is similar to that presented in Ref. [61], where an intersection of the separation shock with the reattachment shock results in a type VI shock-shock interaction. Expansion waves and high entropy shear-layer are emanated at

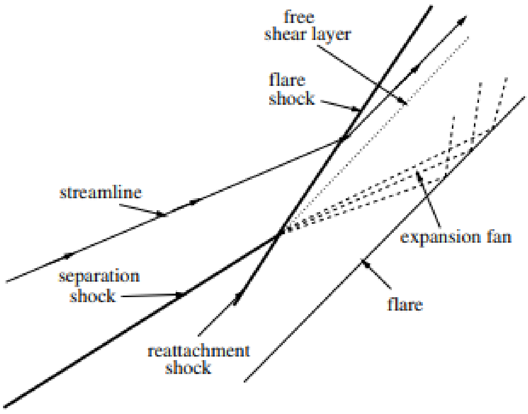

Figure 7.13: Schematic sketch of Edney type VI shock-shock interaction from Ref. [61].

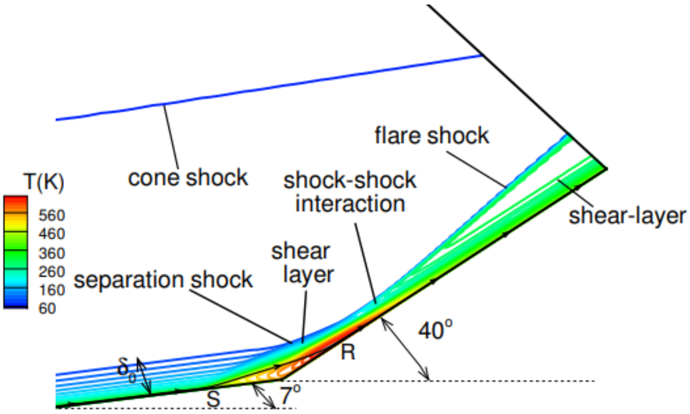

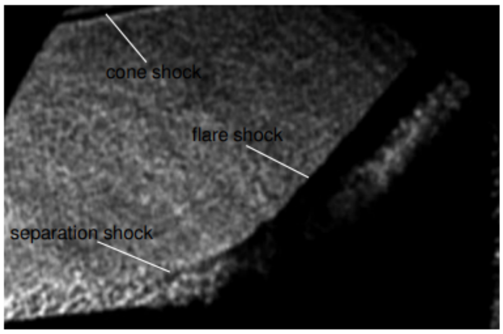

Figure 7.14: Comparison of computed temperature contours, using (a) shock unsteadiness k-ω model, and (b) experimental schlieren image [29] for M_∞ = 8.21 case.

the shock-shock interaction point; see Fig. 7.13 for further details. The computed temperature contours for Mach 8.21 case, using shock unsteadiness k-ω (2009) model is compared with the experimental schlieren image in Fig. 7.14. The shock-shock interaction does not appear to be as clear in experimental schlieren image. A thick boundary layer is formed ahead of the separation shock. The boundary-layer undergoes a compression across the separation shock and bifurcates into two parts. A part of it forms the separated region and part of it flows above separation bubble and further gets compressed across reattachment shock.

The variation of surface properties are shown in Figs. 7.15 and 7.16 for both the cases.The baseline k-ω model predicts a delayed initial pressure rise as compared to the experiment and predicts a smaller separation bubble, the new model along with shock unsteadiness k-ω (2009) model on the other hand mimics the experimental measurements closely for both cases cases. The pressure plateau between the separation (S) and reattachment (R) points is predicted accurately for Mach 7.18 case, however, it gives a smaller pressure rise at the reattachment location for the strongest Mach 8.21 interaction. The wall pressure drops slightly across the expansion waves after the reattachment region (see Fig. 7.14) and matches with experiment far downstream.

The wall heat transfer rate computed in the interaction region shows the effect of lower turbulent Prandtl number clearly. The predictions are comparable to the experimental measurements in the reattachment region and in the recovering boundary layer. The heat flux trend inside the separated region also compares well with the experimental data. By comparison, the baseline k-ω model with constant Pr_T overpredicts the peak heat flux by about 50 % and the trends at the separation point are qualitatively different from that observed in the experiments. The variation of the turbulent Prandtl number based on the shock physics and boundary layer analysis is thus found to significantly improve the heat flux predictions. The model prediction the surface heat flux is increase by 11% compared to the earlier cone-flare results presented in chapter 6 due to the wall cooling.

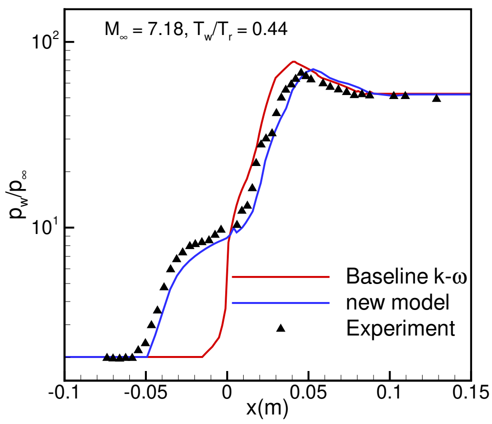

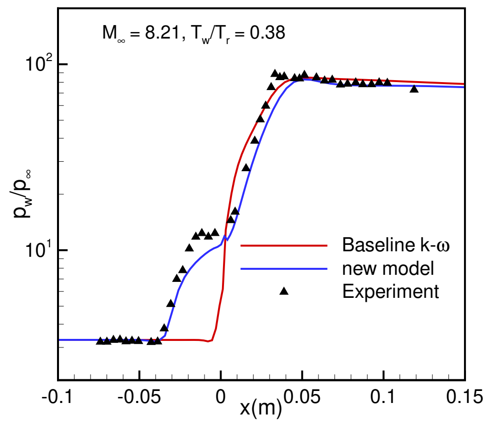

Figure 7.15: Comparison of surface pressure for M_∞ = 7.18 and 8.21 respectively, using baseline k-ω and the new variable Pr_T models with the experimental data of Holden [29].

7.4 Summary

The variable turbulent Prandtl number model is developed for predicting the wall heat transfer in shock-boundary layer interaction with wall cooling/heating effect. The current model is based on the physics of shock wave and turbulent boundary layer using DNS

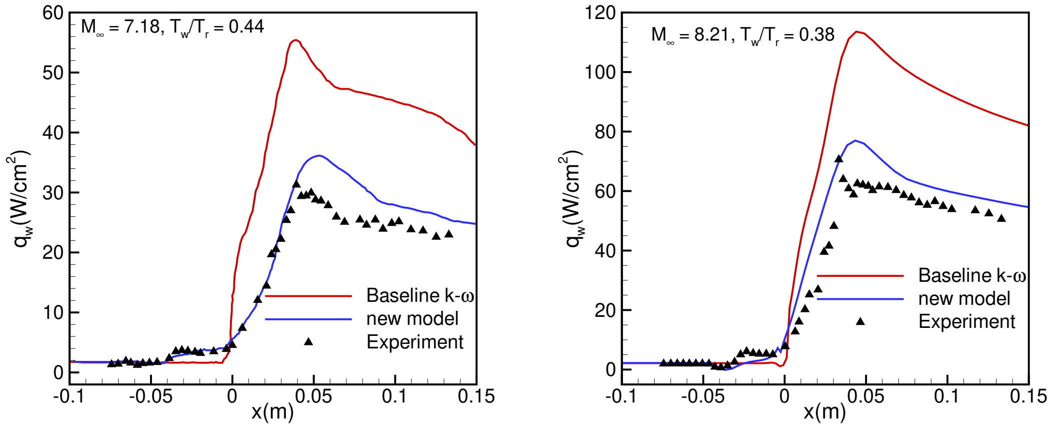

Figure 7.16: Comparison of wall heat flux for M_∞ = 7.18 and 8.21 respectively, using baseline k-ω and the new variable Pr_T models with the experimental data of Holden [29].

data The model is particularly suitable for high-speed flows with wall cooling. It uses the shock-unsteadiness parameter for flows with upstream vortical and entropic fluctuations typical of hypersonic turbulent boundary layers. The algebraic nature of the new model makes the CFD implementation easier and it can be used with any turbulence model.

Chapter 8

Conclusion and future work

In this dissertation, the turbulent heat flux generated by canonical shock-turbulence interaction is studied using DNS data, with a special emphasis on high turbulence intensity. A wide range of turbulent Mach numbers ($0.05 \leq M_t \leq 0.4$) and shock strengths ($M = 1.23, 1.50, 2.50, 3.50$) are considered, spanning both distorted shock and broken shock interactions, with shock holes. The analysis of turbulent heat flux is based on two assumptions, namely, neglecting the higher-order effects in the conservation of total temperature fluctuations and neglecting the temperature fluctuations in the upstream turbulence. It is found that the error due to the first assumption increases with M and M_t, while the magnitude of upstream temperature fluctuations, relative to the linearized kinetic energy, decreases with M and M_t. The error due to the latter assumption is higher than the former, and the dominant error scales as $[M_t(M-1)]^{-0.12}$. It is shown that the same scaling can be extended to regions of shock holes, and the error is marginally higher than that for distorted shock at identical Mach and turbulent Mach numbers.

A key feature of the work is that the turbulent statistics are computed using the threshold method that identifies the edges of the instantaneous shock wave. It is different from conventional averaging at a fixed streamwise x-location marking the edge of the mean shock wave. The threshold method eliminates the large values of turbulent statistics usually obtained by conventional averaging in the region of unsteady shock oscillations. We are thus able to directly compare with linear theory of shock-turbulence interaction and quantify the effect of the non-linear terms at the shock wave.

The analysis of turbulent heat flux is used to propose a predictive model, where the closure coefficients are a function of the shock and turbulent Mach numbers. DNS data shows that the peak heat flux generated by the shock is a function of shock strength and the turbulence intensity. The model is able to predict the DNS data, both qualitatively and quantitatively. It is a significant improvement over earlier models which include the effect of Mach number alone. We also improve upon the shock-unsteadiness model of [78] for turbulent kinetic energy amplification across a shock wave. The functional dependence of the shock-unsteadiness parameter on the turbulent Mach number is able to match the DNS data for the entire range of M and M_t considered in this work. Finally, the post-shock variation of the turbulent heat flux, including the peak and downstream decay, is reproduced by a differential equation based model. The primary limitation of the model is at low M and high M_t interactions, where the magnitude of the shock-induced turbulent heat flux is comparatively low.

The physical insights from canonical shock-turbulence interaction is used to propose a variable turbulent Prandtl number model for shock-dominated flows with few more assumptions for simplicity. The model is based on linearized Rankine-Hugoniot jump conditions across a shock wave and uses model coefficients derived for the shock-unsteadiness k-ω model developed earlier. As per the analysis, the turbulent Prandtl number takes low values in shock waves, and its value decreases with increasing shock strength. A shock function is used to identify the location and the strength of the shock waves in a flow, and is computed by solving a model transport equation. The model also incorporates an exponential relaxation of the turbulent Prandtl number from its shock value to the conventional value of 0.89 away from shock waves. The shock-unsteadiness model, proposed earlier, is reformulated in terms of the shock function. This removes the upstream dependence of the model parameters, so that they can be evaluated locally at a grid point. The local form of the shock-unsteadiness model is computationally more robust and saves a considerable amount of human effort in a simulation.

The variable Pr_T model is applied, in conjunction with the shock-unsteadiness k-ω turbulence model, to oblique shocks impinging on turbulent boundary layer. Three cases with increasing shock generator angles are computed and the results are compared with the experimental measurements. It is found that the shock function can accurately capture the complex shock topology and the strength of the different shock waves in the interaction region. The low values of the turbulent Prandtl number at the shock waves result in a significant reduction in the surface heat flux prediction. The experimental data is reproduced well, both in terms of the peak heat transfer rate at flow reattachment, as well as the streamwise variation of the surface heat flux in the recovering boundary layer. The computed surface pressure and skin friction coefficient also match the experimental data better than the standard k-ω model.

An extended form of the variable turbulent Prandtl number model is developed next for predicting the wall heat transfer in hypersonic shock-boundary layer interaction. It uses the shock-unsteadiness parameter for flows with upstream temperature fluctuations typical of hypersonic turbulent boundary layers and the temperature fluctuation is scaled as per Morkovin's hypothesis.] The new model is found to predict the peak heat transfer consistently over a range of Mach numbers and geometric configurations. It also matches the experimentally observed separation location, and gets physically consistent results with varying shock strength. The model collapses to the supersonic version for SBLI at lower Mach numbers.

The wall heating/cooling effect is also included in the final form of the variable turbulent Prandtl (Pr_T) model based on the DNS data of SBLI flows and analytical relation for turbulent boundary layer. The model is thus incorporated both the effect of shock and turbulent boundary layer. The model is particularly suitable for high-speed flows with non-adiabatic wall and it is extensively tested for a wide range of Mach numbers, Reynolds numbers, geometric configurations and wall conditions. The algebraic nature of the new model makes the CFD implementation easier and it can be used with any turbulence model.

8.1 Contributions

Overall, this dissertation discusses in detail, the analysis of turbulent heat flux in homogeneous isotropic turbulence passing through a normal shock wave and its application to shock-boundary layer interaction. The important contributions of this work are:

- Using direct numerical simulation data total temperature fluctuation is analysed across a normal shock wave and shock hole for high turbulence intensity.
- A predictive turbulent heat flux model is developed based on the DNS data and the model is tuned to capture the turbulent heat flux variation with turbulent Mach number.
- The application of the new algebraic model to SBLI shows significant improvement in predicting the surface heat flux.
- A scalar shock function is developed to capture the local shock strength and it can be used as a shock sensor. The shock function is also used to implement the existing shock-unsteadiness model locally in a CFD solver which reduced the computational time of a simulation.
- The new physics based turbulent heat flux model is able to capture both shock and wall heating/cooling effect in SBLI flows.

8.2 Future Work

Following are some of the ideas inspired by the present work that could be pursued in the future:

- The variable Pr_T model is based on the calorically perfect gas assumption, it can be extended for chemically reacted turbulent flow. The interaction of shock waves with chemically reacted turbulent boundary layer will be a nice problem to tackle. The presence of turbo-chemistry in upstream boundary layer alter the level of turbulent fluctuation and the shock turbulence interaction. The post-shock turbulence statistics is highly affected by chemical reaction.

- Applying the model to three-dimensional shock-boundary layer interaction such as scramjet intake. The current variable Pr_T model does not consider the spanwise distribution of the turbulent heat flux. But for the three-dimensional flow there may be a contrubution of spanwise heat flux on Pr_T due to the side wall effect and high shock curvature.

- The effect of surface curvature and roughness on the model prediction can be studied in detail. The variable Pr_T model is validated against the smooth wall in this dissertation. Most of the pratical application used a rough a wall and the the surface roughness create additional turbulence fluctuation in the near wall region and alter the suface properties.

Appendix A

Frame independence of ψ equation

The left hand side of Eq. 5.29 represents the material derivative of ψ. The material derivative is Galilean invariant i.e. to say that the form of the material derivative of ψ does not change under Galilean transformation from reference frame 1 given by (x, y, z, t) to reference frame 2 given by $(x^{'}, y^{'}, z^{'}, t^{'})$. Suppose that the reference frame 2 is moving with respect to the reference frame 1 at a constant velocity a, then the Galilean transformation is given by :

$x^{'} = x - at$, $y^{'} = y$, $z^{'} = z$ & $t^{'} = t$ and the velocity transforms to $U^{'} = U - a$, $V^{'} = V$ & $W^{'} = W$.

The partial derivative between the two reference frame transforms as :

$\frac{\partial}{\partial x} = \frac{\partial}{\partial x^{'}}$, $\frac{\partial}{\partial y} = \frac{\partial}{\partial y^{'}}$, $\frac{\partial}{\partial z} = \frac{\partial}{\partial z^{'}}$ and $\frac{\partial}{\partial t} = \frac{\partial}{\partial t^{'}} - a\frac{\partial}{\partial x^{'}}$ Using the above results, the

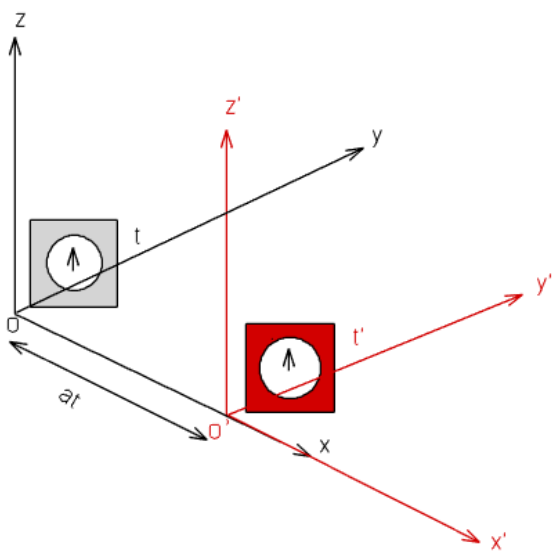

Two frame of reference relatively displaced along the x-axis.

material derivative transforms to :

$$\begin{aligned}
\frac{D\psi}{Dt} &= \rho\frac{\partial\psi}{\partial t} + \rho U\frac{\partial\psi}{\partial x} + \rho V\frac{\partial\psi}{\partial y} + \rho W\frac{\partial\psi}{\partial z} \\
&= \rho\left(\frac{\partial}{\partial t'} - a\frac{\partial}{\partial x'}\right)\psi + \rho(U' + a)\frac{\partial\psi}{\partial x'} + \rho V'\frac{\partial\psi}{\partial y'} + \rho W'\frac{\partial\psi}{\partial z'} \\
&= \rho\frac{\partial\psi}{\partial t'} + \rho U'\frac{\partial\psi}{\partial x'} + \rho V'\frac{\partial\psi}{\partial y'} + \rho W'\frac{\partial\psi}{\partial z'} \\
&= \frac{D\psi}{Dt'}
\end{aligned}$$

Hence, the material derivative of ψ does not change its form in two different inertial frames. This shows that it is Galilean invariant. Similarly it can be shown that the right hand side of Eq. 5.29 is frame independent. Hence the transport equation of ψ can be used in any inertial frames.

Appendix B

Sensitivity of threshold method

The sensitivity of different threshold limits and grid points are tabulated here for the reference.

		$\frac{T_1^{rms}}{\overline{T}_1}(\%)$				$\frac{\Delta T^{rms}}{T_1^{rms}}(\%)$			
M	$M_t =$	0.05	0.15	0.25	0.40	0.05	0.15	0.25	0.40
1.23		3.69	4.82	5.08	5.83	0.04	0.09	0.12	0.17
2.50		4.03	5.59	5.88	7.15	0.11	0.22	0.28	38
3.50		4.39	5.98	6.53	7.95	0.18	0.29	0.37	0.50

Table B.1: Variation of turbulence statistics with a threshold limit of 1%.

		$\frac{T_1^{rms}}{\overline{T}_1}(\%)$				$\frac{\Delta T^{rms}}{T_1^{rms}}(\%)$			
M	$M_t =$	0.05	0.15	0.25	0.40	0.05	0.15	0.25	0.40
1.23		3.96	5.20	5.58	6.41	0.10	0.25	0.35	0.51
1.50		4.12	5.54	5.91	7.05	0.16	0.33	0.50	0.80
2.50		4.54	6.10	6.47	7.86	0.28	0.58	0.78	1.10
3.50		4.89	6.58	7.10	8.70	0.40	0.75	1.00	1.40

Table B.2: Variation of turbulence statistics with a threshold limit of 2%.

		$\frac{T_1^{rms}}{\overline{T}_1}(\%)$				$\frac{\Delta T^{rms}}{T_1^{rms}}(\%)$			
M	$M_t =$	0.05	0.15	0.25	0.40	0.05	0.15	0.25	0.40
1.23		4.29	5.51	5.89	6.80	0.39	0.60	0.85	1.10
1.50		4.54	5.82	6.26	7.45	0.70	0.98	1.20	1.40
2.50		4.81	6.47	6.79	8.58	1.04	1.25	1.70	1.90
3.50		5.13	6.91	7.38	9.50	1.30	1.60	2.00	2.75

Table B.3: Variation of turbulence statistics with a threshold limit of 3%.

		$\frac{c_p T_1^{rms}}{\overline{u}_1 u_1^{rms}}(\%)$				$\frac{\Delta T_{0,s}^{rms}}{T_{01}^{rms}}(\%)$			
M	$M_t =$	0.05	0.15	0.25	0.40	0.05	0.15	0.25	0.40
1.23		4.28	4.07	3.84	3.61	1.00	1.30	1.75	2.00
1.50		4.09	3.89	3.62	3.49	1.45	2.00	2.50	2.90
2.50		3.91	3.75	3.55	3.31	2.50	2.80	3.40	4.00
3.50		3.78	3.59	3.43	3.18	3.10	3.50	4.00	4.80

Table B.4: Variation of turbulence statistics with a threshold limit of 5%.

		$\frac{T_1^{rms}}{\overline{T}_1}(\%)$				$\frac{\Delta T^{rms}}{T_1^{rms}}(\%)$			
M	$M_t =$	0.05	0.15	0.25	0.40	0.05	0.15	0.25	0.40
1.23		5.14	6.79	7.28	8.41	1.60	2.10	2.55	3.20
1.50		5.48	7.12	7.79	9.32	2.50	2.82	3.30	3.90
2.50		5.93	8.06	8.48	10.8	3.20	3.80	4.54	5.11
3.50		6.38	8.75	9.15	12.0	4.00	5.00	5.70	6.50

Table B.5: Variation of turbulence statistics with a threshold limit of 10%.

		$\frac{c_p T_1^{rms}}{\overline{u}_1 u_1^{rms}}(\%)$				$\frac{\Delta T^{rms}}{T_{01}^{rms}}(\%)$			
M	$M_t =$	0.05	0.15	0.25	0.40	0.05	0.15	0.25	0.40
1.23		3.15	2.95	2.80	2.65	0.34	0.51	0.73	0.90
1.50		3.06	2.83	2.59	2.48	0.60	0.86	1.03	1.15
2.50		2.97	2.71	2.43	2.35	0.85	1.07	1.41	1.62
3.50		2.79	2.56	2.27	2.22	1.11	1.37	1.71	2.40

Table B.6: Variation of turbulence statistics by shifting the shock location by three grid points (N=3) from the instantaneous shock edges.

		$\frac{c_p T_1^{rms}}{\overline{u}_1 u_1^{rms}}(\%)$				$\frac{\Delta T_{0,s}^{rms}}{T_1^{rms}}(\%)$			
M	$M_t =$	0.05	0.15	0.25	0.40	0.05	0.15	0.25	0.40
1.23		4.65	4.14	3.88	3.40	1.16	1.51	2.03	2.32
1.50		3.93	3.38	3.08	2.85	1.74	2.32	2.90	3.36
2.50		3.31	3.14	2.90	2.70	2.39	2.95	3.64	4.14
3.50		2.95	2.92	2.66	2.40	3.06	3.52	3.97	4.68

Table B.7: Variation of turbulence statistics obtained by using N = 5 in the threshold method.

		$\frac{T_1^{rms}}{\overline{T}_1}(\%)$				$\frac{\Delta T^{rms}}{T_1^{rms}}(\%)$			
M	$M_t =$	0.05	0.15	0.25	0.40	0.05	0.15	0.25	0.40
1.23		5.21	6.89	7.38	8.00	1.95	2.56	3.10	3.86
1.50		5.56	7.22	7.90	8.60	3.05	3.62	4.05	4.76
2.50		6.00	8.17	8.60	9.50	3.90	5.23	5.37	6.10
3.50		6.47	8.84	9.23	9.75	4.85	6.10	6.95	7.93

Table B.8: Variation of turbulence statistics by shifting the shock location by ten grid points (N=10) from the instantaneous shock edges.

References

[1] Babinsky, H., and Harvey, J. K., 2011, *Shock wave-boundary-layer interactions*, Vol. 32 (Cambridge University Press).

[2] Back, L. H., and Cuffel, R. F., 1976, "Shock wave/turbulent boundary-layer interactions with and without surface cooling," *AIAA J.* **14**, 526–532.

[3] Bardina, J., Huang, P., and Coakley, T., 1997, "Turbulence modeling validation," in *28th Fluid dynamics conference*, p. 2121.

[4] Barre, S., Alem, D., and Bonnet, J. P., 1996, "Experimental study of a normal shock/homogeneous turbulence interaction," *AIAA J.* **34**, 968–974.

[5] Bernardini, M., Asproulias, I., Larsson, J., Pirozzoli, S., and Grasso, F., 2016, "Heat transfer and wall temperature effects in shock wave turbulent boundary layer interactions," *Physical Rev. Fluids* **1**, 084403.

[6] Blaisdell, G. A., Spyropoulos, E. T., and Qin, J. H., 1996, "The effect of the formulation of nonlinear terms on aliasing errors in spectral methods," *Applied Numerical Mathematics* **21**, 207–219.

[7] Blevins, R. D., Holehouse, I., and Wentz, K. R., 1993, "Thermoacoustic loads and fatigue of hypersonic vehicle skin panels," *J. Aircraft* **30**, 971–978.

[8] Bose, D., Brown, J. L., Prabhu, D. K., Gnoffo, P., Johnston, C. O., and Hollis, B., 2013, "Uncertainty assessment of hypersonic aerothermodynamics prediction capability," *J. Spacecraft and Rockets* **50**, 12–18.

[9] Bradshaw, P., Launder, B. E., and Lumley, J. L., 1996, "Collaborative testing of turbulence models," *ASME digital coll.*

[10] Chang, E. W. K., Chan, W. Y., McIntyre, T. J., and Veeraragavan, A., 2021, "Hypersonic shock impingement on a heated flat plate at mach 7 flight enthalpy," *J. Fluid Mech.* **908**

[11] Chen, C. H., and Donzis, D. A., 2019, "Shock–turbulence interactions at high turbulence intensities," *J. Fluid Mech.* **870**, 813–847.

[12] Coakley, T., and Huang, P., 1992, "Turbulence modeling for high speed flows," in *30th Aerospace Sciences Meeting and Exhibit*, pp. AIAA Paper 1992–436.

[13] Dash, S. M., Brinckman, K., and Ott, J. D., 2012, "Turbulence modeling advances and validation for high speed aeropropulsive flows," *Int. J. Aeroacoustics* **11**, 813–850.

[14] Donzis, D. A., 2012, "Amplification factors in shock-turbulence interactions: Effect of shock thickness," *Phys. Fluids* **24**, 011705.

[15] Donzis, D. A., and Jagannathan, S., 2013, "Fluctuations of thermodynamic variables in stationary compressible turbulence," *J. Fluid Mech.* **733**, 221.

[16] Duan, L., Beekman, I., and Martin, M. P., 2010, "Direct numerical simulation of hypersonic turbulent boundary layers. part 2. effect of wall temperature," *J. Fluid Mech.* **655**, 419–445.

[17] Duan, L., and Martin, M. P., 2011, "Direct numerical simulation of hypersonic turbulent boundary layers. part 4. effect of high enthalpy," *J. Fluid Mech.* **684**, 25.

[18] Ducros, F., Laporte, F., Soulères, T., Guinot, V., Moinat, P., and Caruelle, B., 2000, "High-order fluxes for conservative skew-symmetric-like schemes in structured meshes: application to compressible flows," *J. Computational Phys.* **161**, 114–139.

[19] Durbin, P. A., and Zeman, O., 1992, "Rapid distortion theory for homogeneous compressed turbulence with application to modelling," *J. Fluid Mech.* **242**, 349–370.

[20] Fabre, D., Jacquin, L., and Sesterhenn, J., 2001, "Linear interaction of a cylindrical entropy spot with a shock," *Phys. Fluids* **13**, 2403–2422.

[21] Ferri, A., 1940, "Experimental results with airfoils tested in the high-speed tunnel at guidonia," *Tech. Rep.. NACA, TM 946*

[22] Forsythe, J., Hoffmann, K., and Damevin, H. M., 1998, "An assessment of several turbulence models for supersonic compression ramp flow," in *29th AIAA, Fluid Dynamics Conference*, pp. AIAA Paper 1998–2648.

[23] Gaitonde, D. V., 2015, "Progress in shock wave/boundary layer interactions," *Progress in Aerospace Sciences* **72**, 80–99.

[24] Girimaji, S. S., Jeong, E., and Poroseva, S. V., 2003, "Pressure-strain correlation in homogeneous anisotropic turbulence subject to rapid strain-dominated distortion," *Phys. Fluids* **15**, 3209–3222.

[25] Goldberg, U. C., Palaniswamy, S., Batten, P., and Gupta, V., 2010, "Variable turbulent schmidt and prandtl number modeling," *Engineering Applications of Computational Fluid Mechanics* **4**, 511–520.

[26] Griffond, J., 2005, "Linear interaction analysis applied to a mixture of two perfect gases," *Phys. Fluids* **17**, 086101.

[27] Grube, N., Taylor, E., and Martin, P., 2009, "Direct numerical simulation of shock-wave/isotropic turbulence interaction," in *39th AIAA Fluid Dynamics Conference* (San Antonio, Texas, USA). pp. 41–65.

[28] Hirsch, C., 2007, *Numerical computation of internal and external flows: The fundamentals of computational fluid dynamics*

[29] Holden, M. S., Wadhams, T. P., and MacLean, M. G., 2013, "Measurements in regions of shock wave/turbulent boundary layer interaction from mach 4 to 10 for open and "blind" code evaluation/validation," in *21st AIAA Computational Fluid Dynamics Conference*, pp. AIAA Paper 2013–2836.

[30] Honkan, A., and Andreopoulos, J., 1990, "Experiments in a shock wave/homogeneous turbulence interaction," in *21st Fluid Dynamics, Plasma Dynamics and Lasers Conference* (Seattle, WA, USA). pp. AIAA–90–1647.

[31] Huang, P. G., Coleman, G. N., and Bradshaw, P., 1995, "Compressible turbulent channel flows: Dns results and modelling," *J. Fluid Mech.* **305**, 185–218.

[32] Huete, C., Wouchuk, J. G., and Velikovich, A. L., 2012, "Analytical linear theory for the interaction of a planar shock wave with a two-or three-dimensional random isotropic acoustic wave field," *Phys. Rev. E* **85**, 026312.

[33] J. L. Brown, J. L., 2013, "Hypersonic shock wave impingement on turbulent boundary layers: Computational analysis and uncertainty," *J. Spacecraft and Rockets* **50**, 96–123.

[34] Jacquin, L., and Blin, C. C. E., 1993, "Turbulence amplification by a shock wave and rapid distortion theory," *Phys. Fluids A: Fluid Dynamics* **5**, 2539–2550.

[35] Jamme, S., Cazalbou, J.-B., Torres, F., and Chassaing, P., 2002, "Direct numerical simulation of the interaction between a shock wave and various types of isotropic turbulence," *Flow, Turbulence and Combustion* **68**, 227–268.

[36] Jaunet, V., Debieve, J. F., and Dupont, P., 2014, "Length scales and time scales of a heated shock-wave/boundary-layer interaction," *AIAA J.* **52**, 2524–2532.

[37] Johnsen, E., Larsson, J., Bhagatwala, A. V., Cabot, W. H., Moin, P., Olson, B. J., Rawat, P., Shankar, S. K., Sjögreen, B., Yee, H. C., Zhong, X., and Lele, S. K., 2010, "Assessment of high-resolution methods for numerical simulations of compressible turbulence with shock waves," *J. Computational Phys.* **229**, 1213–1237.

[38] K. Sinha, K., and Balasridhar, S. J., 2013, "Conservative formulation of the $k - \epsilon$ turbulence model for shock–turbulence interaction," *AIAA J.* **51**, 1872–1882.

[39] Kays, W. M., 1994, "Turbulent prandtl number– where are we?." *J. Heat Transfer* **116**, 284–295.

[40] Kim, J., Moin, P., and Moser, R., 1987, "Turbulence statistics in fully developed channel flow at low reynolds number," *J. fluid mech.* **177**, 133–166.

[41] Kitamura, T., Nagata, K., Sakai, Y., Sasoh, A., and Ito, Y., 2016, "Rapid distortion theory analysis on the interaction between homogeneous turbulence and a planar shock wave," *J. Fluid Mech.* **802**, 108–146.

[42] Kovasznay, L. S. G., 1953, "Turbulence in supersonic flow," *J. Aeronautical Sciences* **20**, 657–674.

[43] Larsson, J., 2010, "Effect of shock-capturing errors on turbulence statistics," *AIAA J.* **48**, 1554–1557.

[44] Larsson, J., Bermejo-Moreno, I., and Lele, S. K., 2013, "Reynolds-and mach-number effects in canonical shock-turbulence interaction," *J. Fluid Mech.* **717**, 293.

[45] Larsson, J., and Gustafsson, B., 2008, "Stability criteria for hybrid difference methods," *J. Computational Phys.* **227**, 2886–2898.

[46] Larsson, J., and Lele, S. K., 2009, "Direct numerical simulation of canonical shock/turbulence interaction," *Phys. fluids* **21**, 126101.

[47] Laurent, H., 1996, *Turbulence d'une interaction onde de choc/couche limite sur une paroi plane adiabatique ou chauffée*, Ph.D. thesis (Aix-Marseille 2).

[48] Lee, S., Lele, S. K., and Moin, P., 1993, “Direct numerical simulation of isotropic turbulence interacting with a weak shock wave,” *J. Fluid Mech.* **251**, 533–562.

[49] Lee, S., Lele, S. K., and Moin, P., 1997, “Interaction of isotropic turbulence with shock waves: effect of shock strength,” *J. Fluid Mech.* **340**, 225–247.

[50] Leger, T. J., and Poggie, J., 2014, “Computational analysis of shock wave turbulent boundary layer interaction,” in *52nd Aerospace Sciences Meeting*, p. 0951.

[51] Lele, S. K., 1992, “Shock-jump relations in a turbulent flow,” *Phy. of Fluids A: Fluid Dynamics* **4**, 2900–2905.

[52] MacCormack, R. W., and Candler, G. V., 1989, “The solution of the navier-stokes equations using gauss-seidel line relaxation,” *Computers & fluids* **17**, 135–150.

[53] Mahesh, K., Lele, S. K., and Moin, P., 1997, “The influence of entropy fluctuations on the interaction of turbulence with a shock wave,” *J. Fluid Mech.* **334**, 353–379.

[54] Menter, F. R., 1994, “Two-equation eddy-viscosity turbulence models for engineering applications,” *AIAA J.* **32**, 1598–1605.

[55] Moore, F. K., 1953, *Unsteady oblique interaction of a shock wave with a plane disturbance*, Tech. Rep. 1165 (NACA).

[56] Morkovin, M. V., 1962, “Effects of compressibility on turbulent flows,” *Mécanique de la Turbulence* **367**, 380.

[57] Moser, R., and Moin, P., 1984, “Direct numerical simulation of curved turbulent channel flow,” *Tech. Report, NASA.*

[58] Ott, J., Kenzakowski, D., and Dash, S., 2013, “Evaluation of turbulence modeling extensions for the analysis of hypersonic shock wave boundary layer interactions,” in *51st AIAA Aerospace Sciences Meeting Including the New Horizons Forum and Aerospace Exposition*, p. 983.

[59] Parent, B., and Sislian, J. P., 2004, “Validation of the wilcox k-omega model for flows characteristic to hypersonic airbreathing propulsion,” *AIAA J.* **42**, 261–270.

[60] Pasha, A. A., and Sinha, K., 2008, “Shock-unsteadiness model applied to oblique shock wave/turbulent boundary-layer interaction,” *Int. J. Computational Fluid Dynamics* **22**, 569–582.

[61] Pasha, A. A., and Sinha, K., 2012, "Simulation of hypersonic shock/turbulent boundary-layer interactions using shock-unsteadiness model," *J. Propulsion and Power* **28**, 46–60.

[62] Pathak, U., Roy, S., and Sinha, K., 2018, "A phenomenological model for turbulent heat flux in high-speed flows with shock-induced flow separation," *J. Fluids Engineering* **140**

[63] Pirozzoli, S., 2002, "Conservative hybrid compact-weno schemes for shock-turbulence interaction," *J. Computational Phys.* **178**, 81–117.

[64] Pirozzoli, S., Grasso, F., and Gatski, T. B., 2004, "Direct numerical simulation and analysis of a spatially evolving supersonic turbulent boundary layer at m= 2.25," *Phys. fluids* **16**, 530–545.

[65] Quadros, R., and Sinha, K., 2016b, "Modelling of turbulent energy flux in canonical shock-turbulence interaction," *Int. J. Heat and Fluid Flow* **61**, 626–635.

[66] Quadros, R., Sinha, K., and Larsson, J., 2016, "Kovasznay mode decomposition of velocity-temperature correlation in canonical shock-turbulence interaction," *Flow, Turbulence and Combustion* **97**, 787–810.

[67] Quadros, R., Sinha, K., and Larsson, J., 2016a, "Turbulent energy flux generated by shock/homogeneous-turbulence interaction," *J. Fluid Mech.* **796**, 113–157.

[68] Ristorcelli, J. R., and Blaisdell, G. A., 1997, "Consistent initial conditions for the dns of compressible turbulence," *Phys. Fluids* **9**, 4–6.

[69] Roy, C. J., and Blottner, F. G., 2006, "Review and assessment of turbulence models for hypersonic flows," *Progress in Aerospace Sciences* **42**, 469–530.

[70] Roy, S., Pathak, U., and Sinha, K., 2017, "Variable turbulent prandtl number model for shock/boundary-layer interaction," *AIAA J.*, 342–355.

[71] Ryu, J., and Livescu, D., 2014, "Turbulence structure behind the shock in canonical shock–vortical turbulence interaction," *J. Fluid Mech.* **756**

[72] Samtaney, R., Pullin, D. I., and Kosović, B., 2001, "Direct numerical simulation of decaying compressible turbulence and shocklet statistics," *Phy. Fluids* **13**, 1415–1430.

[73] Schülein, E., 2006, "Skin friction and heat flux measurements in shock/boundary layer interaction flows," *AIAA J.* **44**, 1732–1741.

[74] Sethuraman, Y. P. M., Sinha, K., and Larsson, J., 2018, "Thermodynamic fluctuations in canonical shock–turbulence interaction: effect of shock strength," *Theoretical and Computational Fluid Dynamics* **32**, 629–654.

[75] Shih, T. H., Liou, W. W., Shabbir, A., Yang, Z., and Zhu, J., 1995, "A new $k-\epsilon$ eddy viscosity model for high reynolds number turbulent flows," *Computers & fluids* **24**, 227–238.

[76] Sinha, K., 2012, "Evolution of enstrophy in shock/homogeneous turbulence interaction," *J. fluid mech.* **707**, 74.

[77] Sinha, K., and Candler, G. V., 1998, "Convergence improvement of two-equation turbulence model calculations," in *29th AIAA, Fluid Dynamics Conference*, pp. AIAA Paper 1998–2649.

[78] Sinha, K., Mahesh, K., and Candler, G. V., 2003, "Modeling shock unsteadiness in shock/turbulence interaction," *Phys. fluids* **15**, 2290–2297.

[79] Sinha, K., and andG. V. Candler, K. M., 2005, "Modeling the effect of shock unsteadiness in shock/turbulent boundary-layer interactions," *AIAA J.* **43**, 586–594.

[80] Smith, D. R., and Smits, A. J., 1993, "Simultaneous measurement of velocity and temperature fluctuations in the boundary layer of a supersonic flow," *Experimental thermal and fluid science* **7**, 221–229.

[81] Souverein, L. J., Bakker, P. G., and Dupont, P., 2013, "A scaling analysis for turbulent shock-wave/boundary-layer interactions," *J. Fluid Mech.* **714**, 505.

[82] Spaid, F. W., and Frishett, J. C., 1972, "Incipient separation of a supersonic, turbulent boundary layer, including effects of heat transfer," *AIAA J.* **10**, 915–922.

[83] Steger, J. L., and Warming, R. F., 1981, "Flux vector splitting of the inviscid gasdynamic equations with application to finite-difference methods," *J. computational phys.* **40**, 263–293.

[84] Thivet, F., Knight, D., Zheltovodov, A., and Maksimov, A. I., 2001, "Importance of limiting the turbulent stresses to predict 3d shock-wave/boundary-layer interactions," in *23rd International Symposium on Shock Waves, Fort Worth, TX, Paper*, 2761

[85] Veera, V. K., and Sinha, K., 2009, "Modeling the effect of upstream temperature fluctuations on shock/homogeneous turbulence interaction," *Phys. fluids* **21**, 025101.

[86] Vemula, J. B., and Sinha, K., 2017, "Reynolds stress models applied to canonical shock-turbulence interaction," *J. Turbulence* **18**, 653–687.

[87] Volpiani, P. S., Bernardini, M., and Larsson, J., 2018, "Effects of a nonadiabatic wall on supersonic shock/boundary-layer interactions," *Physical Review Fluids* **3**, 083401.

[88] Volpiani, P. S., Bernardini, M., and Larsson, J., 2020, "Effects of a nonadiabatic wall on hypersonic shock/boundary-layer interactions," *Physical Rev. Fluids* **5**, 014602.

[89] Volpiani, P. S., Wagner, A., Bernardini, M., and Larsson, J., 2019, "Using large-eddy simulations to design a new hypersonic shock/boundary-layer interaction experiment," in *AIAA Scitech 2019 Forum*, p. 0098.

[90] Wagner, A., Schramm, J. M., Hannemann, K., and andJ. P. Hickey, R. W., 2017, "Hypersonic shock wave boundary layer interaction studies on a flat plate at elevated surface temperature," in *International Conference on RailNewcastle Talks* (Springer). pp. 231–243.

[91] Walz, A., 1969, *Boundary layers of flow and temperature* (MIT press).

[92] Wilcox, D. C., 1998, "Turbulence modeling for cfd," 2nd ed. (DCW industries La Canada, CA). pp. 84–86.

[93] Wright, M. J., Candler, G. V., and Bose, D., 1998, "Data-parallel line relaxation method for the navier-stokes equations," *AIAA J.* **36**, 1603–1609.

[94] Wu, Y., Yi, S., He, L., Chen, Z., and Zhu, Y., 2015, "Flow visualization of mach 3 compression ramp with different upstream boundary layers," *J. Visualization* **18**, 631–644.

[95] Xiao, X., Hassan, H. A., Edwards, J. R., and Gaffney, R. L., 2007, "Role of turbulent prandtl numbers on heat flux at hypersonic mach numbers," *AIAA J.* **45**, 806–813.

[96] Xiong, Z., and andS. K. Lele, S. N., 2004, "Simple method for generating inflow turbulence," *AIAA J.* **42**, 2164–2166.

List of Publications

Journals:

1. **Roy, S.**, Pathak, U. and Sinha, K., "Variable Turbulent Prandtl Number Model for Shock/Boundary-Layer Interaction," *AIAA Journal*, Vol. 56, No.1, 2018, pp. 342-355.

2. **Roy, S.** and Sinha, K., " Turbulent Heat Flux Model for Hypersonic Shock-Boundary Layer Interaction," *AIAA Journal*, Vol. 57, No. 8, 2019, pp. 3624-3629.

3. **Roy, S.** and Sinha, K., " Analysis of turbulent heat flux generated by shock wave using direct numerical simulation data," Under review in *Shock Wave J.*.

4. **Roy, S.** and Sinha, K., " Turbulent Heat Flux Model for Shock-Boundary Layer Interaction with Non-Adiabatic Wall," Submitted to *Shock Wave J.*.

5. Lacombe, F., **Roy, S.**, Sinha, K., Karl, S., and Hickey, J.P., " Characteristic Scales in Shock/Turbulence Interaction," *AIAA Journal*, accepted for publication on 28th September, 2020.

6. Pathak, U., **Roy, S.**, and Sinha, K., "A phenomenological model for turbulent heat flux in high-speed flows with shock-induced flow separation," *Journal of Fluids Engineering*, Vol. 140, No. 5, 2018, pp. 1-9.

Conference proceedings:

1. **Roy, S.**, and Sinha, K., "Variable turbulent Prandtl number model applied to hypersonic shock/boundary-layer interactions," *48thAIAA Fluid Dynamics Conference*, p. 3728, 2018.

2. **Roy, S.**, Saikia, B., and Sinha, K., "Heat transfer prediction in shock-turbulent boundary layer interaction at flight enthalpy," *AIAA Scitech 2019 Forum*, p. 0339, 2019.

3. **Roy, S.**, Sinha, K., Lacombe, F., and Hickey, J.P., " Anisotropic Turbulent Heat Flux Modelling through Shock Waves," *49^{th} AIAA Fluid Dynamics conference*,2019.

4. Vemula, V. B., Raje, P., Singh, R., **Roy, S.**, and Sinha, K., "Parametric study of the performance of two-dimensional scramjet intake," 18^{th} Annual CFD Symposium, 2016.

Reports:

1. **Roy, S.** & Sinha, K., "Turbulent Heat Flux Model for Shock-Boundary Layer Interaction with Non-Adiabatic Wall," *Proc. of the 2019 Summer Progr.*, Munich, Germany, July - August, 2019. pp. 195–207.

Acknowledgements

I would like to thank Prof. Krishnendu Sinha for his technical assistance and support that has encourage me to do this work with great passion. I am grateful to him for giving his critiques on my work and for the thought provoking discussions. I would like to thank my research progress committee members: Prof. Shripad Mahulikar and Prof. Sandip Kumar Saha for their valuable feedback on my research.

I would like to express my special thanks to Dr. Yogesh Prasaad M. Sethuraman, a former Ph.D. student at the Dept. of Aerospace Engg., IIT Bombay, for providing his *direct numerical simulation (DNS)* data to post-process for the heat flux analysis in the current study.

I am also thankful to Prof. Christian Stemmer, and the participants of the 5^{th} *SFB TRR40 Summer Program 2019* at Technical University of Munich (TUM), Germany for the scintillating discussions during my visit. I would also like to thank the staff at TUM, Germany for their support and hospitality. A portion of my work was carried out there.

I thank the entire faculty and staff of the Dept. of Aerospace Engg., IIT Bombay (past and present) who supported me directly and indirectly during my Ph.D. tenure. I thank my fellow lab mates and dear friends for their amazing support over the years. A huge thanks to the open-source community for obvious reasons. Last but not the least, I thank my parents for their continuous support and encouragement during my Ph.D. at IIT Bombay. Their contribution in every aspect of my education and life, cannot be overstated.

Subhajit Roy
IIT Bombay
2021